ABSTRACT

Title of Dissertation: EFFECT OF SURFACTANTS ON DROP SIZE DISTRIBUTION IN A BATCH, ROTOR-STATOR MIXER

Gustavo A. Padron Aldana, Doctor of Philosophy, 2005

Dissertation directed by: Professor Richard V. Calabrese
Department of Chemical Engineering

Surfactants are often required to stabilize liquid-liquid dispersions produced by rotor-stator mixers. Since drops are deformed rapidly due to the high power input of these devices, the dynamic interfacial properties governed by the surfactant adsorption rate have a significant effect on the resulting drop size. The objective of this work is to develop a fundamental link between surfactant adsorption dynamics, interfacial properties, and turbulent emulsification processes in rotor-stator mixers.

The mean drop size and drop size distributions (DSD) of dilute dispersions produced by a batch rotor-stator mixer were studied. Silicone oils of various viscosities were dispersed in aqueous nonionic surfactant and aqueous methanol solutions. The aqueous methanol (clean) systems allowed comparison of surfactant-laden to surfactant-free systems with similar equilibrium interfacial tensions. The DSD were measured via a video microscopy/automated image analysis technique.

The equilibrium interfacial tension of clean and surfactant systems was measured, via a pendant drop technique, as a function of methanol and surfactant concentration, respectively. The dynamic surface tension of surfactant solutions was similarly measured. By fitting the data to the Langmuir adsorption isotherm and a long time approximation to the Ward – Tordai equation, the adsorption parameters and surfactant diffusivities were obtained. This information, with an estimate of the drop deformation timescale, allowed estimation of the surface dilational modulus (E^{sd}). This is a measure of the Marangoni stresses acting on the drop' surface due to interfacial tension gradients.

Trends observed in the mean drop size and DSD experimental results are explained in terms of the interfacial and rheological properties. Below the CMC, E^{sd} peaks and the drop size increases with concentration, despite a decrease in equilibrium interfacial tension. Above the CMC, Marangoni stresses are small but the presence of the surfactant still modifies the rheology of the interface, increasing the effective viscosity of the drops. A comprehensive set of mechanistic models for drop size in turbulent flows was developed and modified to partially account for the effect of surfactants via an appropriately defined effective viscosity. Various model choices were systematically fit to the drop size data to select the most appropriate mechanistic correlation. Normalized experimental DSD data collapsed to a single log-normal volume distribution.

EFFECT OF SURFACTANTS ON DROP SIZE DISTRIBUTIONS IN A BATCH, ROTOR-STATOR MIXER

by

Gustavo A. Padron Aldana

Dissertation submitted to the Faculty of the Graduate School of the
University of Maryland, College Park in partial fulfillment
of the requirements for the degree of
Doctor of Philosophy
2005

Advisory Committee:

Professor Richard V. Calabrese, Chair
Professor Panagiotis Dimitrakopoulos
Professor Sheryl H. Ehrman
Professor Kenneth T. Kiger
Professor Srinivasa R. Raghavan

TABLE OF CONTENTS

LIST OF TABLES

LIST OF FIGURES

LIST OF ABBREVIATIONS

A	-	Surface area, m^2
a	-	Activity, mol/l
$A_1 \ldots A_n$	-	Empirical numeric constants, dimensionless
A_d	-	Dispersed phase surface area, m^2
a_L	-	Langmuir constant (half-coverage concentration), mol/l
A_s	-	Specific surface area of the dispersion, m^2
B	-	Numeric constant, dimensionless
b	-	Radius of curvature at apex of drop, m
Bo	-	Bond number: $\Delta\rho g b^2/\sigma$, dimensionless
C	-	Concentration in bulk phase, mol/l
C_0	-	Initial surfactant bulk phase concentration, mol/l
Ca	-	Capillary number: $\mu_c \dot{\gamma} D/\sigma$, dimensionless
C_K	-	Kolmogorov constant, dimensionless
CMC	-	Critical micelle concentration, mol/l
C_μ	-	Empirical numeric constant, dimensionless
C_σ	-	Empirical numeric constant, dimensionless
D	-	Drop diameter, μm
D_0	-	Log-normal mean diameter, dimensionless
D_{10}	-	Number mean diameter of a drop size distribution, μm
D_{20}	-	Mean surface diameter of a drop size distribution, μm
D_{30}	-	Mean volume or mass diameter of a drop size distribution, μm
D_{32}	-	Sauter mean diameter (surface-weighted mean diameter) of a drop size distribution, μm
D_{43}	-	Volume- or mass-weighted mean diameter of a drop size distribution, μm
D_{AB}	-	Diffusivity coefficient, m^2/s
D_i	-	Average drop diameter of the i^{th} interval, μm
D_M	-	Diameter of mixing head flanges, m (Chapter 6)
D_{max}	-	Maximum stable diameter, μm
D_{mM}	-	Mass or volume median diameter of the distribution
$\overline{D}_n$	-	Number mean diameter (= D_{10})
D_{nM}	-	Number mean diameter of the distribution, μm
E	-	Internal energy, J (Chapter 4)
E	-	Spectral energy density function, m^3/s^2 (Chapter 3)
E	-	Surface elasticity, mN/m (Chapter 4)
E_0	-	Gibbs elasticity, mN/m
E^{sd}	-	Surface dilational modulus, mN/m
E^{ss}	-	Surface shear modulus, mN/m
F	-	Force, N
f_n	-	Continuous number frequency of the i^{th} interval, dimensionless
F_n	-	Continuous number cumulative distribution, dimensionless
$\tilde{f}_n$	-	Discrete number frequency of the i^{th} interval, dimensionless
$\tilde{F}_n$	-	Discrete number cumulative distribution, dimensionless

f_v - Continuous volume frequency of the i^{th} interval, dimensionless
F_v - Continuous volume cumulative distribution, dimensionless
$\tilde{f}_v$ - Discrete volume frequency of the i^{th} interval, dimensionless
$\tilde{F}_v$ - Discrete volume cumulative distribution, dimensionless
G - Gibbs free energy, J
g - Acceleration of gravity, m/s
H - Drop shape dependent variable (modified Bond numer), dimensionless
h - Adsorption depth, μm
HLB - Hydrophilic – Lipophilic balance, dimensionless
h_M - Height of stator head, m (Chapter 6)
HMVP - High magnification video probe
K - Turbulent kinetic energy, $kg \cdot m^2/s^2$
k - Turbulent eddy wavenumber, m^{-1}
k_a - Adsorption rate constant, m/s
k_B - Boltzmann's constant, 1.3806×10^{-23} J/K
k_d - Desorption rate constant, $mol/(m^2 s)$
L - Macroscopic characteristic length (Impeller diameter), m
ℓ - Characteristic length, m
M_r - r^{th} central moment of a discrete drop size distribution, μm^r
M'_r - r^{th} raw moment of a discrete drop size distribution, μm^r
MW - Molecular weight, g/mol
m - Mass, kg
N - Rotor speed, rpm
n - Number (exponent), dimensionless
$\vec{n}$ - Normal unit vector, m
n_D - Index of refraction, dimensionless
n_i - Number of drops in the i^{th} interval, dimensionless
P - Power dissipated by fluid, W
P - Pressure, Pa (Chapter 4)
Pe - Peclet number: UD/D_{AB}, dimensionless
P_o - Power number: $P/\rho_c N^3 L^5$, dimensionless
R - Ideal gas constant, 8.31451 J/(molK)
r - Drop radius, μm
R_1, R_2 - Curvature radii, m
Re - Reynolds number: $\rho_c N L^2/\mu_c$, dimensionless
R_H - Hydraulic radius of particle, μm
RMSD - Root mean squared difference, %
S - Entropy, J/K
T - Tank diameter, m (Chapter 5)
T - Temperature, °C or K
T - Time period, s (Chapter 3)
t - Time, s
t_D - Diffusive adsorption time scale, s
t_{dd} - Drop deformation time scale, s
t_{def} - Interface or drop deformation time scale (generic), s
t_{eddy} - Turbulent eddy lifetime, s

t_K - Kolmogorov time micro-scale, s
t_{kin} - Kinetic adsorption time scale, s
U - Fluid instantaneous velocity, m/s
$\overline{U}$ - Mean fluid velocity, m/s
u - Turbulent fluctuating fluid velocity, m/s
u'^2 - Turbulent root mean squared velocity, m^2/s^2
u_K - Kolmogorov velocity micro-scale, m/s
V - Tank volume, m^3
v - Volume (generic), m^3
$\vec{v}$ - Velocity vector, m/s
v_y^s - Surface velocity in y direction, m/s (Chapter 4)
V_d - Dispersed phase volume, m^3
Vi - Viscosity number: $\mu_d NL/\sigma(\rho_c/\rho_d)^{1/2}$, dimensionless
Vi' - Modified viscosity number: $\mu_d NL/\sigma$, dimensionless
V_i - Volume of a drop of size D_i
VM - Video microscopy
V_T - Total volume of dispersion, m^3
We - Weber number: $\rho_c N^2 L^3/\sigma$, dimensionless
x - Molar fraction, dimensionless (Chapter 4)
x - x direction, dimensionless
$\vec{x}$ - Position vector, m
$Z(j)$ - j^{th} member in a Fibonacci series

Greek Symbols

α - Characteristic shear rate (Chapter 4)
α - Flow type parameter, dimensionless (Chapter 7)
α - Numeric constant, dimensionless (Chapter 3)
β - Empirical numeric constant, dimensionless
Γ - Surface excess concentration, mol/m^2
Γ_∞ - Saturation surface excess concentration, mol/m^2
$\dot{\gamma}$ - Principal velocity gradient (shear or elongation rate), s^{-1}
δ - Rotor-stator gap width, μm
δ_D - Diffusion layer thickness, μm
ε - Turbulent kinetic energy dissipation rate, m^2/s^3
Φ - Unknown function
ϕ - Dispersed phase fraction: V_d/V_T, dimensionless
η - Kolmogorov length micro-scale, μm
μ - Dynamic viscosity, mPa·s
μ^{ss} - Surface shear viscosity, mPa·s·m
μ_c - Continuous phase viscosity, mPa·s
μ_d - Dispersed phase viscosity, mPa·s
μ_d^{eff} - Effective dispersed phase viscosity, mPa·s
μ_i - Chemical potential of i^{th} component, J/mol

μ_r - r^{th} central moment of a continuous drop size distribution, μm^r
μ'_r - r^{th} raw moment of a continuous drop size distribution, μm^r
ν - Kinematic viscosity, m^2/s
ν_c - Continuous phase kinematic viscosity, m^2/s
π - Surface pressure, mN/m
θ - Dimensionless drop deformation (strain)
ρ - Density, kg/m^3
ρ_c - Continuous phase density, kg/m^3
ρ_d - Dispersed phase density, kg/m^3
σ - Interfacial tension, mN/m (also referred to as σ_{eq})
σ_{eff} - Effective interfacial tension, mN/m
σ_g - Geometric standard deviation, dimensionless
σ_n - Number standard deviation, μm
σ_s - Normal standard deviation, μm
σ_0 - Log-normal standard deviation, μm (Chapter 2)
σ_0 - Interfacial tension of clean interface, mN/m
τ_c - Continuous phase stress, $kg/(ms^2)$
τ_d - Dispersed phase viscous stress, $kg/(ms^2)$
τ_s - Surface stress, $kg/(ms^2)$
$\tau_{xy}{}^s$ - Surface shear stress, $kg/(ms^2)$ (Chapter 4)
ω - Compression frequency, Hz

Mathematical Symbols

Δ - Difference
∇ - Gradient operator: $\nabla \equiv \partial / \partial x_i$
∇^2 - Laplacian operator $\nabla^2 \equiv \partial^2 / \partial x_i^2$
∇_s - Surface gradient operator: $\nabla_s = (I - \vec{n}\vec{n}) \cdot \nabla$ (I = identity matrix)

CHAPTER 1. INTRODUCTION

1.1. Motivation and Purpose

The dispersion of immiscible liquids by mechanical agitation is a common unit operation in the chemical process industry, and a well studied field of fluid mechanics. Its foundations date back to the 1950's and over the last decades, engineering principles have been developed and the design of mixing equipment has evolved. Nevertheless, many mixing operations are complex and demand more thorough evaluation. Failure to do so can translate into severe problems that affect the process' performance and increase its associated costs. The cost of poor mixing could be as high as $100 million per year for a company and there is an immeasurable cost of lost opportunity, where mixing problems prevent the development of new products (Paul, Atiemo-Obeng, and Kresta 2004).

High shear rotor-stator mixers are broadly used in many industries to carry out some of the most demanding mixing operations. Due to their design, high shear units dissipate the majority of their power input in a small volume, as opposed to conventionally stirred tanks, where much of the power is dissipated in the impeller region, but there is still significant dissipation throughout the tank. Because of their large and localized power investments, rotor-stator devices are often used for process intensification and to meet process objectives that cannot be achieved by other means (Myers *et al.* 1999). Some of the applications of high shear rotor-stator mixers include the production of emulsions, dispersions, and slurries in the manufacture of paints, inks, and personal care and food products; the deagglomeration of particles; and crystal size control (Calabrese 2001).

Despite their widespread application, there is a noticeable lack of fundamental knowledge to appropriately design or evaluate rotor-stator mixers. There is no theory or experimental protocol specifically tailored for these devices that would allow the prediction or assessment of their performance. This results in increased costs and time lost due to the trial and error nature of the development work done for them. Recent studies (Francis 1999; Myers, Reeder, and Ryan 2001; Padron 2001; Phongikaroon 2001), have shown similarities between their behavior and that of stirred tanks, in several aspects. This means that theories and correlations developed for stirred tanks may be used as a basis to assess rotor-stator device performance, but they still must be tested.

Many of the industrial processes that use rotor-stator mixers to produce emulsions require the use surfactants to achieve a specific property in the final product (i.e. a small drop size in emulsification processes) or to prevent particles or drops from flocculating or coalescing. However, most studies involving drop breakage in stirred tanks, rotor-stator mixers, and other dispersion devices focus on surfactant-free systems. Therefore, there is little known quantitatively about how the surfactant's presence at the liquid-liquid interface affects the drop breakup process.

When a surfactant adsorbs at a liquid interface, it modifies some of the system's properties and even creates new ones. It affects the interfacial tension, both its equilibrium value and its dynamic response to deviations from equilibrium, and it alters the rheological behavior of the interface. These phenomena have consequences on the drop deformation and breakup mechanisms, the equilibrium drop size distribution, and the stability of the dispersion. Thus, a basic understanding of the physicochemical phenomena and their effects is required. The purpose of this research is to develop a

fundamental link between interfacial properties, adsorption dynamics data, and emulsification dynamics in high shear rotor-stator mixers.

1.2. Approach

The mean drop size and drop size distribution (DSD) produced by a batch rotor-stator mixer (Silverson L4RT) for different dilute liquid-liquid systems was studied. These systems consist of silicone oils of various viscosity grades dispersed in water, aqueous surfactant solutions, and aqueous methanol solutions. The surfactants chosen for this study are Tergitol™ TMN-6, Triton™ X-100, and Triton™ X-165. These are low molecular weight, nonionic surfactants whose adsorption behavior can be characterized by the well-known Ward and Tordai (1946) approach for diffusion-controlled adsorption. The aqueous methanol systems allow comparison of the surfactant laden cases to surfactant-free systems with similar equilibrium interfacial tensions, and, as a result, allow evaluation of the effect of the presence of a surfactant.

The dispersed phase volume fraction in the liquid-liquid dispersion experiments was limited to 0.1 %v/v in all cases. Such a low value was selected for several reasons. First, the turbulent flow can be characterized by single phase theories, such as Kolmogorov's theory of local isotropy, since the amount of dispersed phase is too small to have an effect on the continuous phase turbulence. Second, the effect of surfactants on drop breakup can be isolated. Equilibrium drop size distributions are always the result of a balance between breakup and coalescence. But, at these low drop phase fractions, coalescence rates are very low and, therefore, the final drop size is mainly caused by breakup. Third, the continuous phase concentration of surfactant does not change significantly upon introduction of the dispersed phase (i.e. the continuous phase is not

significantly depleted of surfactant by adsorption at the interface or transference into the dispersed phase).

In order to quantify the effect of the surfactants, their physicochemical behavior, both equilibrium and dynamic, was examined. The equilibrium interfacial tension of silicone oil/surfactant/water and air/surfactant/water systems was measured, as well as dynamic surface tensions of the latter, via the pendant drop technique. This data allowed estimation of the critical micelle concentrations and surfactant diffusivities; as well as the surface dilational modulus, an interfacial rheology property, as a function of surfactant bulk phase concentration. With this information, the trends observed in the mean drop size and DSD data were explained. In addition, useful correlations were developed based on mechanistic theories for drop breakup in turbulent flows, which provide insight into the hydrodynamics of the process. This was accomplished by adapting proven correlations for surfactant-free systems to account for thermodynamic properties of surfactant-laden systems.

1.3. Organization of the Dissertation

This dissertation is divided into nine chapters: the present introductory chapter, three on the theories and concepts relevant to the research, one on the experimental methods employed, three that present the experimental results, and, finally, one containing the conclusions and recommendations drawn from them. Chapter 2 focuses on the characterization of the mean drop size and size distributions of dispersed phase systems. It defines different mean drop sizes and distribution functions pertinent to particulate liquid systems. It also contains a detailed description of drop size

measurement techniques and the automated image analysis technique used in this study to quantify experimental drop size measurements. The third chapter provides an introduction to turbulence and the development of mechanistic models for mean drop size for breakup of immiscible drops in turbulent flows. Important scaling parameters that allow analysis of the experimental results are also defined. Chapter 4 is about surfactants: their definition and description, their equilibrium and dynamic behavior in aqueous solutions, and their effect on the interfacial rheology and hydrodynamics of liquid dispersions. Chapter 5 includes the different experimental facilities, procedures, and conditions employed in the interfacial properties measurement and in the production of liquid-liquid dispersions and measurement of drop size.

With respect to the results, Chapter 6 covers the interfacial phenomena experiments. It contains the results of the surface and interfacial tension measurements for both clean and surfactant-laden systems and the dynamic surface tension measurements for dilute surfactant solutions. In addition, the surfactants' diffusivities and the surface dilational modulus are reported in this chapter. Chapter 7 is dedicated to the mean size and DSD results obtained from the liquid-liquid dispersion experiments. The effects of variables such as dispersed phase viscosity, surfactant concentration, and rotor speed are presented and discussed. In Chapter 8, this same data are correlated by fitting it to the mechanistic models developed in Chapter 3. This allows for significant conclusions to be drawn about the drop breakup process in rotor-stator mixers. At last, the conclusions chapter, Chapter 9, summarizes the findings of this study and proposes recommendations for future work that would complement them.

CHAPTER 2. DROP SIZE DISTRIBUTIONS AND MEASUREMENT TECHNIQUES

Dispersed fluid systems are present in many industrial applications as well as in many everyday situations, such as clouds and mists, smoke plumes, foams, emulsions, and suspensions. They are all characterized by being comprised of a continuous phase and one (or more) dispersed phase(s). The dispersed phase is present in the continuous phase in the form of finely divided particles, which may be solid (smoke and solid suspensions), liquid (mists and emulsions), or gaseous (foams or bubbly flows), with the stipulation that each particle consists on a large enough number or molecules to be considered a continuum separate from the continuous phase (Sadhal, Ayyaswamy, and Chung 1996). One of the most important characteristics of a dispersed system is its particle size, since it determines or affects many of the system's physical and chemical properties. The particles in the system may all have the same size (monodispersed system) or, as is more frequently found both in nature and industry, they made be of different sizes (polydispersed system). In monodispersed systems, only one value is needed to describe the system's particle size, a representative length common to all particles, such as the particle's diameter or radius, in case of spherical particles. In the case of a polydispersed system, mean diameters, radii, or lengths can be reported. Furthermore, a polydisperse particle size is not fully characterized unless a measure of the size distribution is also given.

The present chapter is about how the characterization of a polydispersed system's particle size may be accomplished. First, some important concepts related to particle size distributions and mean sizes will be explained. For simplification purposes, it will be

henceforth assumed that all the particles are liquid droplets, therefore spherical, and the characteristic length chosen to represent their size is the drop's diameter. This does not lessen the generality of these concepts, since they apply to particles of any shape, even amorphous ones, as long as an appropriate characteristic length is defined for them. Later, several experimental methods for determining particle size will be overviewed, emphasizing the ones used in this work.

2.1. Drop Size Distributions

A drop size distribution function is an analytical and/or graphical representation of the individual sizes of the drops in the system that allows us to think of the dispersed phase as a continuous phase (Randolph and Larson 1971). This function, however, usually cannot be measured directly and it must be constructed from associated measures of the distribution. Typically, a sample of the system, comprised of a finite number of drops, is analyzed and its results extrapolated to the whole system. The accuracy of the measured distribution will therefore depend on the representativity of the sample and the precision of the discretization. From this analysis, several mean drop sizes and other statistical parameters can be also obtained, which provide quantitative information on the drop size distribution as well.

2.1.1. Discrete Size Distributions

The simplest form of size distributions is the discrete size distribution. Basically, to obtain this distribution all the drops in the sample are categorized into small size intervals. Each interval, also referred to as a bin, is assigned a characteristic size (D_i), often equal to the average between its two limiting values. Then, the number of drops in

each interval is counted (n_i) and divided by the total number of drops. These values would be the number frequency of the interval ($\tilde{f}_n(D_i)$) and it represents the fraction of drops with sizes between the two limits of the i^{th} interval:

$$\tilde{f}_n(D_i) = \frac{n_i}{\sum_j n_j} \tag{2.1.1-1}$$

If the number frequency is plotted as a bar chart against D_i, the resulting histogram is the discrete drop size distribution of the sample. Since the number of drops in each size category was divided by the total number of particles, the sum of the number frequencies over all the intervals is equal to unity (the distribution has been normalized):

$$\sum_i \tilde{f}_n(D_i) = 1 \tag{2.1.1-2}$$

The mean drop size associated with the number frequency distribution is the number mean diameter, which is defined by:

$$\overline{D}_n = \frac{\sum_i n_i D_i}{\sum_i n_i} = \sum_i D_i \frac{n_i}{\sum_j n_j} = \sum_i D_i \tilde{f}_n(D_i) \tag{2.1.1-3}$$

Correspondingly, the number variance, which is a measure of the polydispersity of the distribution, is defined by:

$$\sigma_n^2 = \sum_i \left(D_i - \overline{D}_n\right)^2 \tilde{f}_n(D_i) \tag{2.1.1-4}$$

and it is related to the number standard deviation (σ_n) by:

$$\sigma_n = \sqrt{\sigma_n^2} \tag{2.1.1-5}$$

Drop size distributions may also be represented as a cumulative distribution, represented by $\tilde{F}_n(D_i)$. In a cumulative distribution plot, each point represents the fraction of drops with diameters equal to or smaller than D_i:

$$\tilde{F}_n(D_i) = \sum_{j}^{Di} \tilde{f}_n(D_j) \qquad (2.1.1\text{-}6)$$

Since the frequency distribution is normalized, the cumulative distribution is a curve that increases monotonically from 0 to 1. Figure 2.1.1-1 shows examples of number frequency and cumulative distributions of a random sample. The diameter at which $\tilde{F}n$ reaches the value 0.5 is called the number median diameter, D_{nM}:

$$\tilde{F}_n(D_{nM}) = 0.5 \qquad (2.1.1\text{-}7)$$

The number median diameter corresponds to a drop size such that half of the drop population is smaller and the other half is bigger than this size.

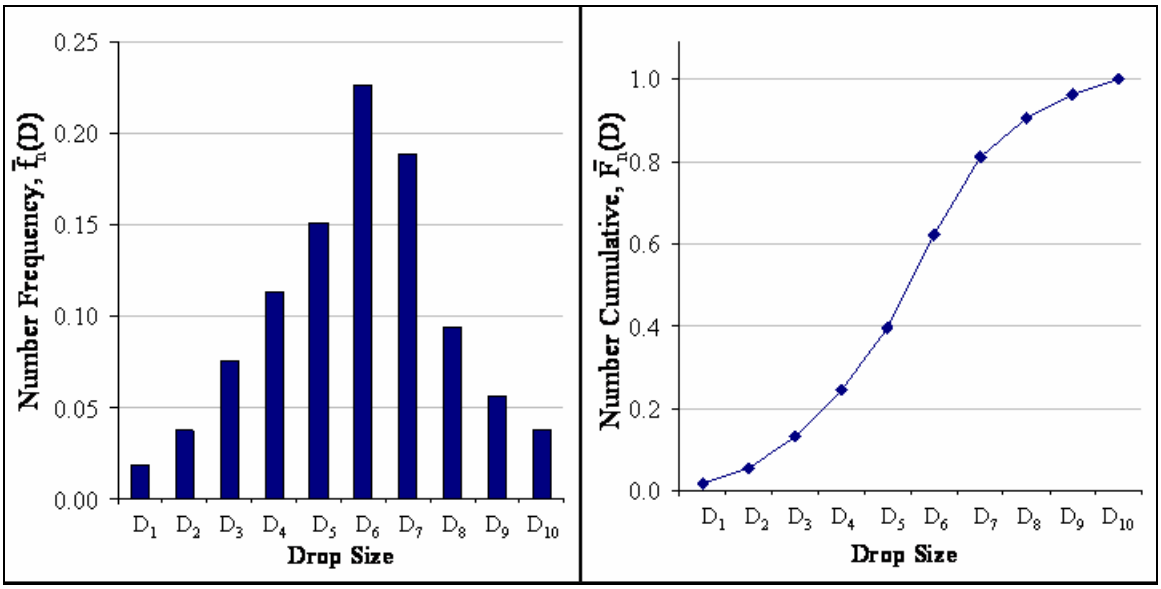

Figure 2.1.1- 1. Number frequency and cumulative discrete distributions of a random sample.

Drop size distributions may also be expressed in terms of drop volume instead of drop number. In this case, each bar in the frequency distribution represents the fraction of the total dispersed phase volume contained in drops with diameters in the size range of that particular bin ($\tilde{f}_v(D_i)$). To calculate this distribution, the volume corresponding to the characteristic drop size of the interval is multiplied by the number of drops in the bin and divided by the sum of the volumes of all bins:

$$\tilde{f}_v(D_i) = \frac{V_i}{\sum_j V_j} = \frac{\frac{\pi}{6} D_i^3 n_i}{\sum_j \frac{\pi}{6} D_j^3 n_j} = \frac{D_i^3 \tilde{f}_n(D_i)}{\sum_j D_j^3 \tilde{f}_n(D_j)} \qquad (2.1.1\text{-}8)$$

Figure 2.1.1-2 shows examples of the number and volume frequency distributions of a single sample. Likewise, a volume cumulative distribution ($\tilde{F}_v(D_i)$) can be defined, in which each point represents the dispersed phase volume fraction contained in drops of size D_i and smaller:

$$\tilde{F}_v(D_i) = \sum_j^{Di} \tilde{f}_v(D_j) \qquad (2.1.1\text{-}9)$$

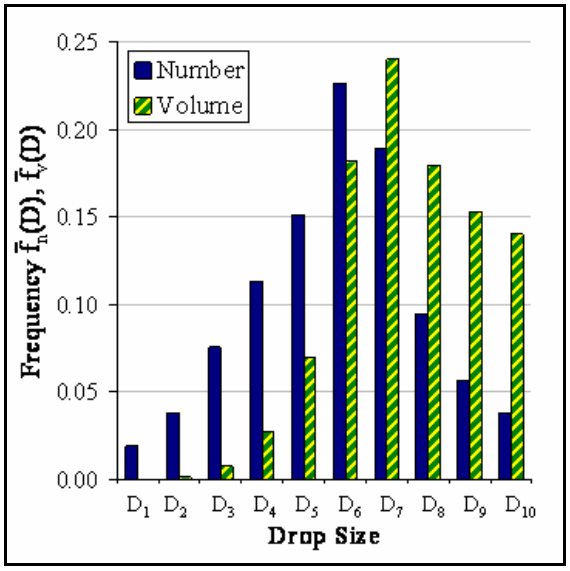

Figure 2.1.1- 2. Frequency and volume distributions of a random sample.

Since the volume and the mass of a drop are directly proportional ($m=\rho v$), volume-based distributions are also referred to as mass-based distributions.

An important aspect to be taken into account when working with discrete distributions is the bin size. If the bins are too wide, its characteristic size will hardly be representative of all the different diameters contained in it. On the other hand, if they are too narrow, it is likely that many of them will end up without any drops. A reliable way to define bin size is by using Fibonacci series to calculate the bin limits. A Fibonacci series is defined as:

$$z(j+1) = z(j) + z(j-1) \qquad (2.1.1\text{-}10)$$

For each series, the two first terms are chosen and the rest generated with the abovementioned equation. For instance, for the starting pair {1 2}, the series is 1, 2, 3, 5, 8, 13, 21, 54, …. However, regardless of the starting pair, the same asymptotic relationship is found between contiguous elements of the series ($z(j)/z(j-1) \approx 1.618$, for $j \to \infty$). Therefore, if two or more starting pairs are selected, the resulting series will intertwine to form a single sequence. Zhang, Calabrese, and Gentry (1992) found that defining bin sizes by either three or six interlaced Fibonacci series provides an excellent tool for simulation and analysis of drop breakage. This is due to the fact that the resulting series is dense enough in the lower size range to appropriately capture the features of the distribution, without increasing too fast to loose resolution in the larger range. Even broad distributions can be effectively analyzed this way, using 50 to 100 bins.

The accuracy of the size distribution also depends on sampling. The sample has to be large enough to ensure that it is truly representative of the system and also to assure that the number of drops in each bin is significant (Randolph and Larson 1971).

Phongikaroon (2001) revisited the error estimates analysis previously performed by Paine (1993) for sampling of particle size distributions, this time using interlaced Fibonacci series to define bin sizes. Both, Phongikaroon and Paine, concluded that there is a minimum number of particles that must be counted for the distribution to be statistically reliable, and that this number depends on the broadness of the distribution. For moderately polydisperse distributions, this number of the order of 1000 particles.

2.1.2. Continuous Size Distributions

If the size bins of the discrete frequency distribution are made infinitesimally small, the continuous frequency distribution is obtained:

$$f_x(D) = \lim_{\Delta D \to 0} \frac{\tilde{f}_x(D)}{\Delta D} \qquad (2.1.2\text{-}1)$$

where x is n, for number frequency distributions, and v, for volume frequency distributions. The number fraction and volume fraction of drops with diameters between D and D+dD are given by the differential quantities $f_n(D)dD$ and $f_v(D)dD$, respectively (Crowe, Sommerfeld, and Tsuji 1997). Since both $\tilde{f}_n(D)$ and $\tilde{f}_v(D)$ have been normalized, the histograms that represents the discrete frequency distributions are replaced with smooth, continuous curves that have the property that the area underneath them is equal to unity:

$$\int_0^\infty f_n(D)dD = \int_0^\infty f_v(D)dD = 1 \qquad (2.1.2\text{-}2)$$

Similarly, the discrete cumulative distributions can also be made into continuous cumulative distributions by taking their limits as ΔD approaches 0, that is, by turning the sums in equations 2.1.1-6 and 2.1.1-9 into integrals:

$$F_x(D) = \int_o^D f_x(D')dD' \qquad (2.1.2\text{-}3)$$

where, again, x stands for either n or v, whether it's a number or volume distribution, and D' is an integration variable.

Realistically, all experimentally measured drop size distributions are obtained in the form of discrete distributions, regardless of how finely discretized it may be. However, it is common practice to consider this data as values in a continuous distribution curve for analysis purposes (Crowe, Sommerfeld, and Tsuji 1997).

2.1.3. Moment-Based Mean Drop Diameters

Statistically, the moments of distributions are the basis for defining mean diameters and standard deviations (Alderliesten 1990). The general definition of the r^{th} moment of the drop diameter distribution of a particulate system is:

$$\mu'_r = \int_{-\infty}^{\infty} D^r f_n(D)dD \qquad (2.1.3\text{-}1)$$

where μ'_r is called the r^{th} raw moment (or simply r^{th} moment). If instead of a power of the diameter, the weighting function is a power of the difference between the diameter and the number mean diameter, it is called a central moment, denoted as μ_r:

$$\mu_r = \int_{-\infty}^{\infty} (D - \Delta_n)^r f_n(D)dD \qquad (2.1.3\text{-}1)$$

where Δ_n is the number mean diameter of the continuous distribution of the system. In the common case that what is actually available is the discrete frequency distribution of a sample of the system, the raw and central moments may be approximated by the following expressions:

$$M'_r = \sum_i D_i^r \tilde{f}_n(D_i) \tag{2.1.3-3}$$

$$M_r = \sum_i \left(D_i - \overline{D}_n\right)^r \tilde{f}_n(D_i) \tag{2.1.3-4}$$

respectively. From comparing equation 2.1.3-3 to equation 2.1.1-2, becomes evident that the 0^{th} order moment of a frequency drop size distribution is equal to one; and by doing so with equation 2.1.1-3, its clear that the 1^{st} moment is equal to the number mean diameter ($\overline{D}_n$). As for the central moments, from equation 2.1.3-4, the 0^{th} moment is also equal to 1, the 1^{st} moment is equal to 0, and the 2^{nd} moment is equal to the sample's variance (equation 2.1.1-4).

Several different mean drop sizes may be defined as functions of higher order moments of the distribution, each of them with different physical meanings. The general equation used to calculate this mean values is:

$$D_{pq} = \left[\frac{M'_p}{M'_q}\right]^{\frac{1}{p-q}} = \left[\frac{\sum_i n_i D_i^p}{\sum_i n_i D_i^q}\right]^{\frac{1}{p-q}} \tag{2.1.3-5}$$

for $p \neq q$, where p and q, though may be real numbers, are normally limited to integers (Alderliesten 1990). For instance, the mean diameter D_{10} may be computed as:

$$D_{10} = \frac{\sum_i n_i D_i}{\sum_i n_i} = \overline{D}_n \tag{2.1.3-6}$$

therefore, D_{10} is equal to the number mean diameter, $\overline{D}_n$, which is the arithmetic mean size of the sample, also called the length-weighted mean diameter. In the same way, D_{20} is defined by:

$$D_{20} = \left[\frac{\sum_i n_i D_i^2}{\sum_i n_i} \right]^{1/2} \qquad (2.1.3\text{-}7)$$

which is the mean surface diameter since it is the diameter associated with the mean area ($\sim D^2$) of the drops. Similarly, D_{30}, which is defined equivalently, is called the mean volume diameter. Two particularly relevant moment-based mean diameters are the D_{32} and the D_{43}. The D_{32}, also known as the Sauter mean diameter, is the surface-weighted mean diameter and it is frequently found in the spray, atomization, and liquid-liquid dispersion literature. Its physical meaning becomes clearer if its defining equation is modified as follows (Alderliesten 1991):

$$D_{32} = \frac{\sum_i n_i D_i^3}{\sum_i n_i D_i^2} = \sum_i \frac{n_i D_i^2}{\sum_j n_j D_j^2} D_i = \sum_i A_i D_i \qquad (2.1.3\text{-}8)$$

where A_i is the relative surface area of the drops in the i^{th} bin of the distribution with respect to the total surface area of the dispersed phase. This means that the D_{32} is effectively the relative area-weighted mean diameter of the dispersion. The D_{32} can also be associated with the specific surface area of the dispersion (A_s), which is the total surface area of dispersed phase per unit volume (or mass) of dispersion:

$$A_s = \frac{A_d}{V_T} = \frac{A_d \phi}{V_d} = \frac{\phi \pi \sum_i n_i D_i^2}{\pi/6 \sum_i n_i D_i^3} = \frac{6\phi}{D_{32}} \qquad (2.1.3\text{-}9)$$

where ϕ is the dispersed phase content of the dispersion – the ratio of the dispersed phase volume (V_d) to the total volume of the dispersion (V_T). D_{43} is also found, though less frequently, in dispersions literature and is the volume- or mass-weighted mean diameter.

One important property of the moment-based mean diameters is that, through Cauchy's inequality, it can be shown that:

$$D_{p-1,q-1} \leq D_{pq} \tag{2.1.3-10}$$

and that the differences between the mean diameters decrease as the uniformity of the drop sizes increases, being equal only in the case of a truly monodispersed distribution (Alderliesten 1990). Thus, the differences between the mean diameters provide an indication of the polydispersity of the sample. Another property is that they may be related by:

$$\left(D_{pq}\right)^{p-q} = \frac{\left(D_{pc}\right)^{p-c}}{\left(D_{qc}\right)^{q-c}} \tag{2.1.3-11}$$

For instance, for p = 3, q = 2, and c = 0, $D_{32}=(D_{30})^3/(D_{20})^2$. This relationship is useful when the data for the distribution is not available, but the values of two or more different mean diameters are.

2.1.4. Normal and Log-Normal Distributions

The normal, or Gaussian, distribution functions is one of the most widely used in engineering to represent a broad variety of observed data (Phongikaroon 2001). It is given by the following expression:

$$f(D) = \frac{1}{\sqrt{2\pi}\sigma_s} \exp\left[-\frac{1}{2}\left(\frac{D - D_{10}}{\sigma_s} \right)^2 \right] \tag{2.1.4-1}$$

where σ_s is the normal standard deviation. A plot of equation 2.1.4-1 results in a symmetric distribution with a "Gaussian or bell" shape, with its maximum value at D = D_{10}.

The normal cumulative distribution function is equal to:

$$F(D) = \frac{1}{\sqrt{2\pi}\sigma_s}\int_0^D \exp\left[-\frac{1}{2}\left(\frac{D'-D_{10}}{\sigma_s}\right)^2\right]dD' \qquad (2.1.4\text{-}2)$$

which yields a straight line when plotted in normal-probability coordinates (drop diameter in linear scale and F(D) in probability scale).

Even though the normal distribution is used in many engineering applications, it is seldom used in describing particle size distributions (either number- or volume-based) simply because these distributions are typically very asymmetrical, and therefore poorly fit by a bell shape (Randolph and Larson 1971). Furthermore, the normal distribution predicts finite values for negative diameters, which is not physically realistic. The normal distribution may be used, however, in the case of monodispersed systems. A particle size distribution may be considered monodispersed if it has a coefficient of variation (cv) of 0.1 or less (Crowe, Sommerfeld, and Tsuji 1997), which is defined as:

$$cv = \frac{\sigma_s}{D_{10}} \qquad (2.1.4\text{-}3)$$

One statistical distribution that is often used to represent particle sizes is the log-normal distribution(Randolph and Larson 1971). The expression for this distribution is derived from the normal distribution by replacing the drop diameter (D) with its logarithm. Therefore, the number of particles with diameters in the range from D to D+dD is given by (Crowe, Sommerfeld, and Tsuji 1997):

$$f(D)dD = \frac{1}{\sqrt{2\pi}\sigma_0}\exp\left[-\frac{1}{2}\left(\frac{\ln D - D_0}{\sigma_0}\right)^2\right]\frac{dD}{D} \qquad (2.1.4\text{-}4)$$

where D_0 and σ_0 are the log-normal mean diameter and log-normal standard deviation, respectively. A linear plot of the log-normal distribution is not symmetric about D_0 like the normal distribution is about D_{10}, it is skewed towards the larger sizes, which is what makes it suitable for representing particles. Moreover, the log-normal function is defined only for D in the interval $(0,\infty)$, which prevents it from fictitiously predicting finite frequencies for negative diameters. Figure 2.1.4-1 shows a comparison between a normal distribution curve and a log-normal distribution curve. Note that, if plotted with the drop diameter in logarithmic coordinates, the log-normal distribution has the same bell shape that the normal distribution has in linear coordinates. Consistently, the cumulative log-normal distribution is obtained by integrating the log-normal function over the drop diameter:

$$F(D) = \frac{1}{\sqrt{2\pi}\sigma_0}\int_0^D \exp\left[-\frac{1}{2}\left(\frac{\ln D' - D_0}{\sigma_0}\right)^2\right]\frac{dD'}{D'} \qquad (2.1.4\text{-}5)$$

which generates a straight line if plotted in log-probability coordinates (the drop size in logarithmic scale and F(D) in probability scale). This equation may also be expressed as:

$$F(D) = \frac{1}{2}\left[1 + \mathrm{erf}\left(\frac{\ln D - D_0}{\sqrt{2}\sigma_0}\right)\right] \qquad (2.1.4\text{-}6)$$

where erf denotes the error function which is defined as:

$$\mathrm{erf}(t) = \frac{2}{\sqrt{\pi}}\int_0^t \exp\left(\xi^2\right)d\xi \qquad (2.1.4\text{-}7)$$

The diameter at which a cumulative distribution reaches 0.5 is, by definition, its median diameter, D_M – number median, D_{nM} if the distribution is number-based, or mass (or volume) median, D_{mM}, if the distribution is mass-based (or volume-based). According to

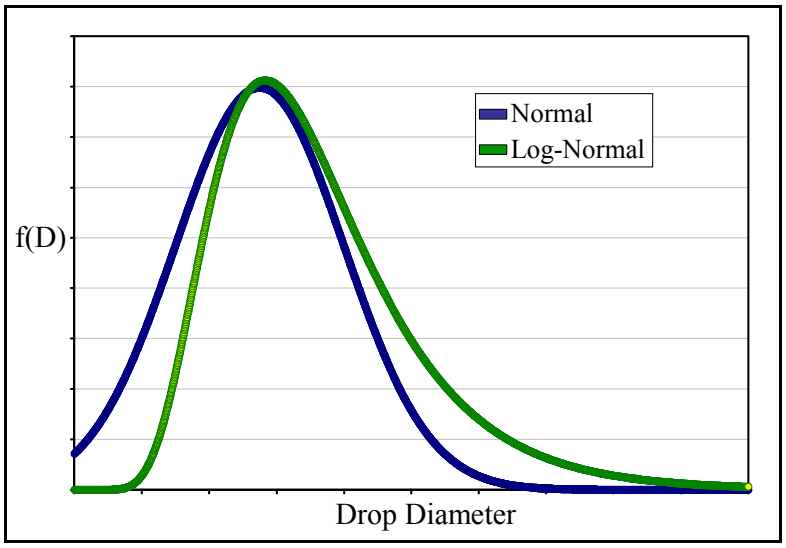

Figure 2.1.4- 1. Normal and log-normal distribution curves.

equation 2.1.4-6, this will only occur if the error function is equal to zero, which requires its argument to be also equal to zero. Thus, the log-normal mean diameter is equal to the logarithm of the median diameter of the distribution:

$$D_0 = \ln D_M \tag{2.1.4-5}$$

The log-normal standard deviation may be obtained by fitting the log-normal function to the data, or, alternatively, by the relations (Randolph and Larson 1971):

$$\sigma_0 = \ln\left(\frac{D_{84\%}}{D_M}\right) = \ln\left(\frac{D_M}{D_{16\%}}\right) \tag{2.1.4-6}$$

In particle analysis, the quantity σ_g:

$$\sigma_g = \exp(\sigma_0) \tag{2.1.4-7}$$

is frequently referred to as the geometric standard deviation, even though it is not a standard deviation in its true sense (Alderliesten 1990).

An important property of log-normal drop size distributions is that, once D_0 and σ_0 are known, the mean diameters may be obtained by the following expression(Alderliesten 1990):

$$D_{pq} = D_M \exp\left[(p+q)\frac{\sigma_0^2}{2} \right] \qquad (2.1.4\text{-}8)$$

as long as the number of drops in the sample is large (>500), σ_0 is less than 0.7, and p + q is less than 10.

There are other statistical or semi-empirical functions that can be used to represent particle sizes, such as the gamma distribution function, Rosin-Rammler distribution, or the log-hyperbolic distribution (Crowe, Sommerfeld, and Tsuji 1997). But some of them are too specific. The gamma distribution is more suited for distributions resulting from crystallization processes and the Rosin-Rammler distribution is used primarily for sprays. The log-hyperbolic function's parameters may become unstable if the tails of the distribution are not well defined. These are therefore not of interest for the present study.

2.2. Drop Size Measurement Techniques

There are many experimental techniques for measuring the drop size distribution of liquid-liquid dispersions. In the remainder of this chapter, the two methods that were employed in this dissertation, namely video microscopy and a high magnification video probe, are reviewed in detail. But first, an overview of several generally employed experimental methods will be given.

2.2.1. Common Drop Size Measurement Methods

2.2.1.1. Dynamic Light Scattering

Dynamic Light Scattering (DLS), also known as Photon Correlation Spectroscopy, is a technique for measuring sub-micron particle sizes (1 nm – 1 μm). It is based on the measurement of the variation in time of the intensity of the light scattered by the particles. These intensity variations contain information on the random motion of the particles (Brownian motion) and can be used to determine their diffusion coefficient (Hiemenz and Rajagopalan 1997). This is done by fitting the autocorrelation function of the intensity variations to a known exponential decay equation, which includes the diffusion coefficient as a parameter.

If the particles are monodisperse, and their Brownian diffusion coefficient is known, the particle size can be calculated by means of the Stokes – Einstein equation:

$$D_{AB} = \frac{k_B T}{6\pi\mu_c R_H} \qquad (2.2.1.1\text{-}1)$$

where D_{AB} is the diffusion coefficient of the particle in the continuous phase, k_B is the Boltzmann constant, T is the absolute temperature, μ_c is the continuous phase viscosity and R_H is the hydraulic radius of the particle.

When the dispersion is polydisperse, the analysis becomes more complex. A common method, introduced in 1972 by Koppel is the method of cumulants (Phongikaroon 2001). The diffusion coefficient obtained by this method is the z-average diffusion coefficient which, in turn, yields the z-average diameter when the Stokes – Einstein equation is applied. This diameter is equivalent to the D_{65} of the particle size distribution, which is heavily weighted by the biggest particles and lacks the kind of

physical interpretation associated with mean diameters based on lower moments (such as D_{10}, D_{32}, or D_{43}). The method of cumulants also generates the polydispersity index, which is related to the variance of the distribution. There are several mathematical techniques by which the information obtained by the method of cumulants can be translated into more practical data, such as the nonnegative least squares technique and the maximum entropy analysis (Hanus and Ploehn 1999; Phongikaroon 2001).

The DLS technique assumes that the measured light intensity was scattered by only one particle, therefore the sample has to be very dilute. If a significant part of the light is scattered by more than one particle before the intensity can be measured (multiple scattering), the equations no longer apply and the results are unreliable. On disadvantage of the technique is that a sample must be withdrawn from the system to perform the analysis. Droplets in this size range (1 nm – 1 μm) are usually considerably stable against coalescence if the sample is dilute. However, a surfactant is sometimes added to the sample to minimize coalescence during the analysis.

2.2.1.2. Electrical Sensing Zone Method (Coulter Counting)

The principle of electric sensing zone methods is based on the disturbance of an electrical field by a particles, previously suspended in an electrolyte, passing through a probe volume (Crowe, Sommerfeld, and Tsuji 1997). The particle suspension is passed through a small orifice while a current is established by placing electrodes at both sides of it. Each particle entering the orifice displaces a volume of electrolyte equal to its own volume, which affects the potential between the electrodes and creates a voltage pulse with an amplitude proportional to the particle volume. The method is usually calibrated with monodispersed particles of known size to obtain a calibration curve that allows

converting the pulse amplitude to particle size. A well-known instrument based on this principle is the Coulter counter, which was originally used to count blood cells.

The electric sensing method is suitable for particles in the range 0.4 – 400 μm, although particles as small as 0.1 μm have been measured under favorable conditions (Kissa 1999). The upper limit of this range is restricted by the size of the orifice and the stability of the particles in the suspension. The largest particle that can be measured is 60 – 80% of the orifice size, since larger particles will tend to block it. The measurable size range may be expanded up to 1200 μm by using multiple measurement cells with different orifice sizes.

The main sources of error for this technique are: coincidence errors, distorted pulse shape errors, calibration errors, and flocculation of the dispersion (Kissa 1999). Coincidence errors occur if two or more particles enter the sensing zone at the same time, which will be counted as a particle with a volume equal to the combination of the single volumes. Therefore, the concentration of particles in the suspension should be of the order of 10^5 particles/ml to assure that only one particle passes through the orifice at a time. If a particle passes close to the edge of the orifice, a slightly larger pulse is generated. This can be minimized by using contoured orifices and hydrodynamic flow-directing devices. Flocculation of the sample particles, and even coalescence, can occur since the sample must be pulled out of the system and it's no longer being agitated. Nevertheless, this may be avoided by adding a nonionic surfactant to the electrolyte.

2.2.1.3. Laser Diffraction

Light diffraction is a rapid technique for measuring particle sizes in the range 2 – 300 μm with adequate precision, although under certain conditions the minimum particle

size may be brought down to 0.05μm. It is based on Fraunhofer diffraction theory, which states that if the particles are larger than the wavelength of the light inciding on them, most of the light is scattered in the forward direction as the result of diffraction. This theory was described by Fraunhofer over a hundred years ago, but the complicated calculations required for the evaluation of the refraction pattern limited the application of the technique. The advent of lasers as light sources and of computers to perform the calculations has made diffraction a practical technique and nowadays there are several commercial instruments based on it (Kissa 1999).

The particles are illuminated with a collimated and vertically polarized laser beam and generate a diffraction pattern with the undiffracted beam in the center. The intensity distribution of the diffracted light is measured by a concentric ring light sensitive detector. The angle dependent intensity is transformed by Fourier optics into a spatial intensity distribution, which is proportional to the diameter of the particles. If the dispersion is polydisperse, this distribution is actually a linear superimposition of the distributions of each particle size. In the particle size range where Fraunhofer theory is valid, calibration of the method is not necessary (Kissa 1999). Furthermore, the diffraction pattern is stationary even if the particles are moving, which means that the size measurement is no affected by particle velocity. This makes the technique suitable for in-line analysis of two-phase flows (Crowe, Sommerfeld, and Tsuji 1997). In-line analysis has the additional advantage that there is no need to withdraw a sample and, therefore, sample stabilization is not an issue.

The diffraction patterns are affected by the continuous phase and the shape of the particles, since light diffraction theories assume the particle to be spherical. Also,

particles with edges or transparent may cause the appearance of false "ghost" particles in the distribution. Despite this limitations, light diffraction is widely used in industry due to its speed (the measurement usually takes only a few seconds) and convenience (bench-top size commercial analyzers are available).

2.2.1.4. Phase-Doppler Anemometry

Phase-Doppler anemometry (PDA) is one of the most advanced and accurate nonintrusive techniques to obtain particle velocities and sizes in two-phase flows (Crowe, Sommerfeld, and Tsuji 1997). The physical principle behind PDA, as well as LDA (Laser-Doppler anemometry), is the Doppler effect, which relates the interaction of light or sound waves with a moving observer or the modulation of said waves received by a stationary observer form a moving emitter. The LDA technique, however, is only capable of measuring the fluid's velocity using particles merely as tracers. PDA is an improvement over LDA which allows measurement of velocity and particle size simultaneously.

When a spherical particle passes through the measuring volume created by the intersection of two laser beams at a known angle, it scatters light. This light is received by two detectors located at different angles. The signals of this detector have a phase shift, which depends on the particle's size and composition as well as on the geometry of the detection system. The lower limit of the size range measurable with this technique is usually 2 – 5 μm. The phase difference between smaller particles is very small, and therefore difficult to measure. But improvements in optics and data processing could lower this limit considerably (Kissa 1999).

PDA is limited to spherical or nearly spherical particles with known refractive index. Other factors such as polydispersity, trajectory ambiguities (certain particle trajectories that cause scattering by other scattering mechanism than the one assumed), measurement volume variations, and very small particle sizes may impair the method's accuracy. However, this technique has the advantage of being an in situ technique. There is no need to withdraw a sample since the particles can be measured directly in the vessel or line where they are flowing. PDA instruments have become available by several commercial manufacturers and there is an ever increasing number of published papers that use the technique, which indicates its development is not over yet.

2.2.2. High Magnification Video Probe

The high magnification video probe (HMVP) is a novel technique for measuring the drop size distribution produced in situ in process vessels. The one available in this study was developed by Francis (1999). It consists of microscope objective optics housed in a stainless steel probe, attached to a CCD camera. A stroboscopic light source is used to freeze the motion of the randomly moving particles in the probe's field of view. The light is conducted by a fiber optic and transmitted through the probe. The lenses at the end of the probe focus the light into the sampling volume, illuminating the particles present in it. The light reflected from this particles is then transmitted to the CCD chip in the camera mounted on top of the probe. Figure 2.2.2-1 presents a schematic representation of the HMVP identifying its components. The images obtained through the video probe are digitized and transferred to a computer via a frame grabber, where they are later processed with an automated image analysis procedure, also developed by

Francis. Figure 2.2.2-2 shows an example of an image of soda glass particles in water obtained with the probe.

This technique is accurate in the range ~5 – 150 μm, provided that there is good phase contrast between the drops and the continuous phase. The phase contrast is quantified by the difference in refractive index, Δn_D, between the phases. For a Δn_D greater than 0.135 the minimum measurable size is 3 – 6 μm, depending on the objective's magnification power (two options are available, 20x and 40x). For lower values of Δn_D, the minimum measurable size increases significantly. For instance, for soda glass particles in silicone oil ($\Delta n_D = 0.079$) the minimum, with the 40x objective, is around 8 μm, while for silicone oil drops in water ($\Delta n_D = 0.056$), in increases to 20 μm (Phongikaroon 2001).

The main advantage of the HMVP is that it is an in situ technique; as a result, there is no

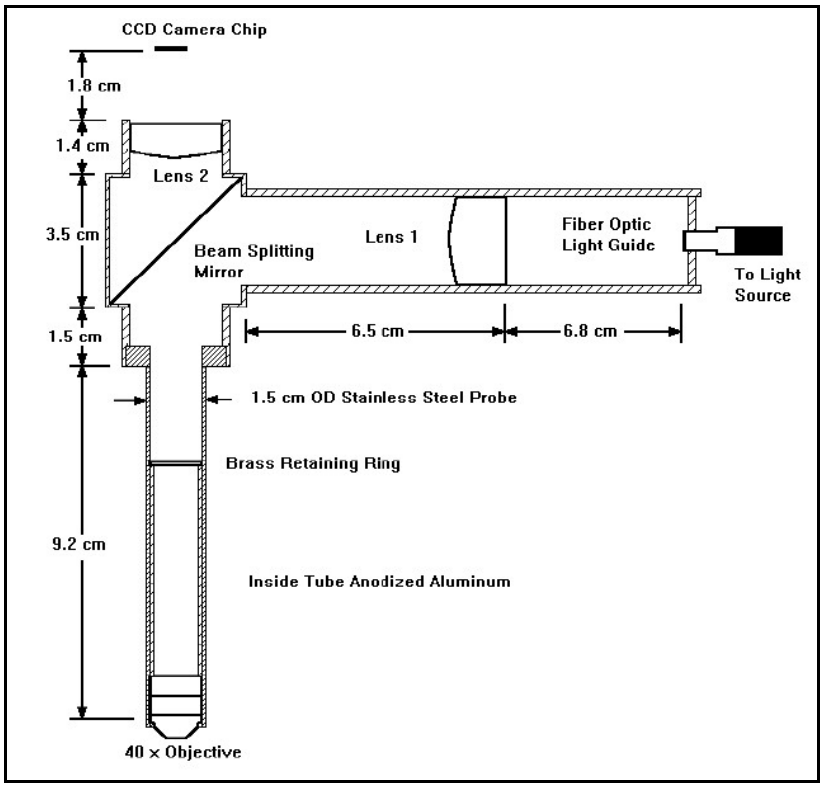

Figure 2.2.2- 1. High Magnification Video Probe (from Francis (1999)).

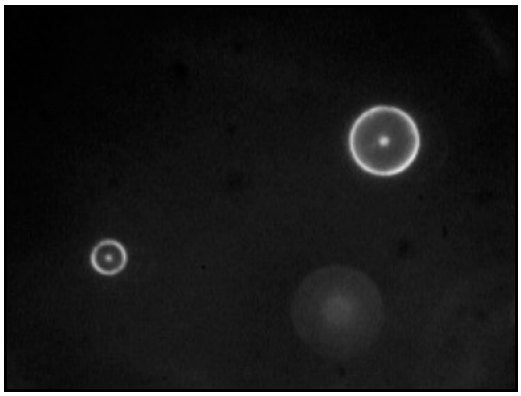

Figure 2.2.2- 2. Soda glass particles in water as observed with the video probe. (from Francis (1999)).

need to withdraw and stabilize or dilute samples of the dispersion. Its main disadvantage is its dependency on phase contrast. For the silicone oil – water systems employed in this study ($\Delta n_D = 0.056$), it is not a suitable drop size measuring technique. Consequently, the HMVP was not used to collect experimental data, but to aid in the validation of the video microscopy/image analysis system (discussed below), using dispersions of polystyrene standardized particles in water ($\Delta n_D=0.195$).

2.2.3. Video Microscopy

Optical microscopy is a very valuable tool for qualitative and quantitative analysis of dispersions. A variety of information on the size, shape, morphology, and aggregation of particles can be conveniently acquired with little time needed for sample preparation. Since individual particles can be observed and their size and shape directly examined, optical microscopy is considered the only absolute method for particle characterization (Kissa 1999). An optical microscope consists of an objective lens, an ocular lens (eyepiece), a condenser, a stage, and a telescoping drawtube. The objective lens collects the light coming from the sample and generates an image of it. The eyepiece forms a

specimen of the image provided by the objective on the retina (or photographic plate, screen, or CCD chip) and magnifies it. The condenser concentrates the light on the sample and is usually provided with a iris diaphragm to change contrast by regulating the amount of incident light on the sample. The stage is where the sample is placed and allows it to be moved sideways. The drawtube adjusts the distance between the objective and ocular lenses to focus the image.

The video microscopy (VM) technique combines the magnification power of an optical microscope with the image acquisition capability of a video camera. A number of studies have been performed comparing video microscopy to alternative methods including light scattering, Coulter counting, turbidimetry, and nuclear magnetic resonance methods. Generally, the comparison is favorable, however alternative methods are often preferred due to their higher degree of simplicity of operation (Sæther 2001). This is due to the fact that, to determine particle size distributions, a relatively large number of individual particles must be analyzed, which is usually time consuming and labor intense. However, in combination with digital image processing, such a direct imaging method becomes a powerful particle characterization technique (Crowe, Sommerfeld, and Tsuji 1997). Essentially, the apparatus consist of an optical microscope with a video camera attached to its ocular piece, which is, in turn, linked to a computer. The images of the particles observed through the microscope are automatically digitized and stored in the computer for later analysis.

As any other experimental method, the video microscopy technique has some limitations. First of all, a sample must be withdrawn from the system. Therefore, measures have to be taken to assure the stability of the sample during the analysis, e.g.

the addition of a surfactant to the sample. When the particle size approaches the wavelength of visible light (0.4 – 0.7 μm), the light diffracted by the particle may create an erroneous image (Crowe, Sommerfeld, and Tsuji 1997). Therefore, VM is only accurate in the ~1 – 200 μm range. Additionally, the sample has to be diluted enough so that images of single particles (not touching each other or superimposed) are obtained.

The specific experimental method used to obtain the images of the silicone oil drops studied in this dissertation is described comprehensively in the Experimental Methods chapter (Chapter 5). Once the images are stored in the computer's hard drive, they were analyzed in order to extract quantitative information. An automatic digital image analysis process was developed for this purpose. This process can be divided into two stages: the extraction of particle area and shape information from the images, or image analysis itself, and the examination of this information to obtain the drop size distributions and mean diameters. Both stages, as well as a validation test of the technique against the high magnification video probe, are explained in the following sections.

2.2.3.1. Image Analysis

For the first stage of the image analysis process, the software used is Scion Image, which is the Windows version of the popular NIH Image, written at the National Institutes of Health. It has a built-in function for particle analysis, however, the images have to be adequately prepared to be able to use it, and it only analyzes one image at a time. Consequently, a macro was developed to automate the particle analysis. The image preparation consists of three steps: background subtraction, grayscale normalization, and thresholding. The first or background subtraction step is done to remove from the image

any spots resultant from dirt accumulated anywhere within the optical system that may be confused with particles by the image analysis subroutine. Prior to analyzing any sample, a picture of what is seen through the microscope without the sample is taken. This image is subtracted from all the images analyzed from that sample by the macro, using Scion Image's built-in function Image Math.

The second step in the image preparation is the normalization of the image's grayscale histogram, which enhances the contrast and, therefore, makes it easier to distinguish between drops and the background of the image. The normalization is done by running a Scion Image-incorporated macro which modifies the image similarly to a regular contrast enhancement, only that it actually modifies the pixel values instead of just changing their appearance. Figure 2.2.3.1-1 shows an image of silicone oil drops in water as originally captured, as well as after background subtraction and grayscale normalization. After the image has been normalized, it is thresholded to a specific grayscale value; i.e., all the pixels that have a grayscale value above the specified threshold value are considered black (grayscale = 255), and those which grayscale is below the specification are considered white (grayscale = 0). This third step is done to

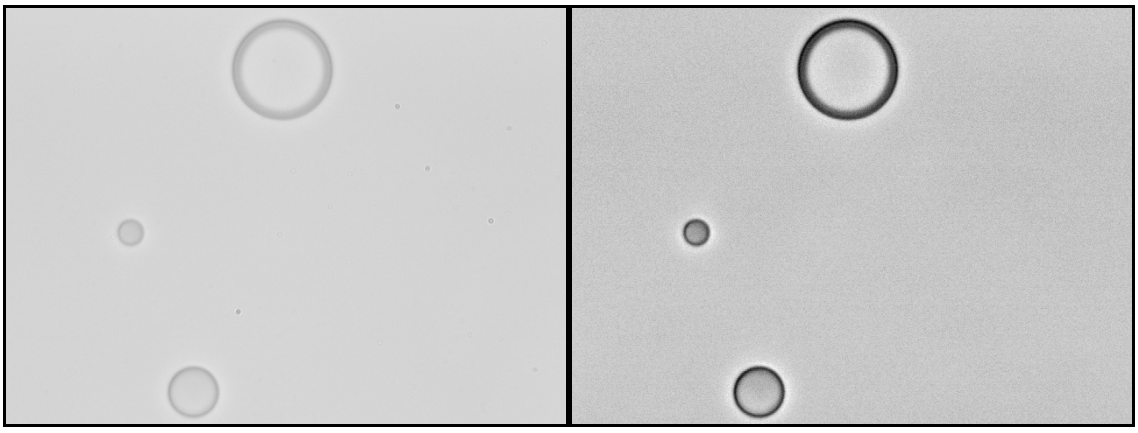

Figure 2.2.3.1- 1. Pictures of silicone oil drops in water before (left) and after (right) background subtraction and image normalization.

separate the parts of the image that correspond to drops from the background. Figure 2.2.3.1-2 presents the same picture that was shown in figure 2.2.3.1-1 after the thresholding step.

The selection of the appropriate thresholding value is crucial to the precision of the image analysis process. To this end, images of 3 polystyrene standards (Duke Scientific) with number mean diameters of 4.8, 14.9, and 26.2 μm were employed. The14.9 μm standard's images were analyzed varying the threshold value over a broad range. Figures 2.2.3.1-3 to -5 show the results of this analysis. As the threshold value increases the number mean diameter decreases, while the coefficient of variation (equation 2.1.4-3) remains practically constant until the threshold value reaches 168, when it suddenly starts to increase rapidly. This may be due to the fact that, at high threshold values a number of drops are poorly thresholded and only small fragments of these drops are measured, thus, creating a falsely larger population of small drops, which broadens the distribution. At high threshold value, some drops are not measured at all because their grayscale values are too low; therefore the total number of drops measured decreases (Figure 2.2.3.1-4). If

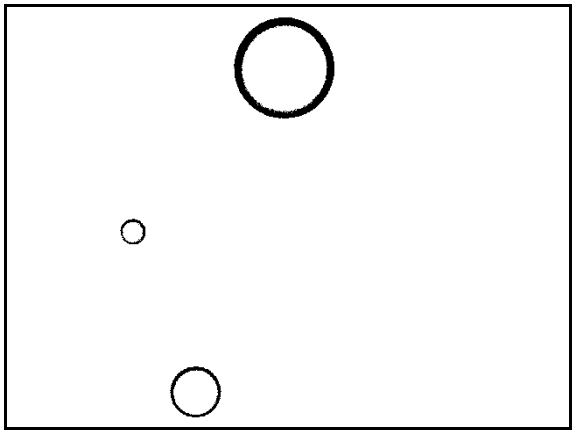

Figure 2.2.3.1- 2. Picture of silicone oil drops in water after thresholding (threshold grayscale value = 153)

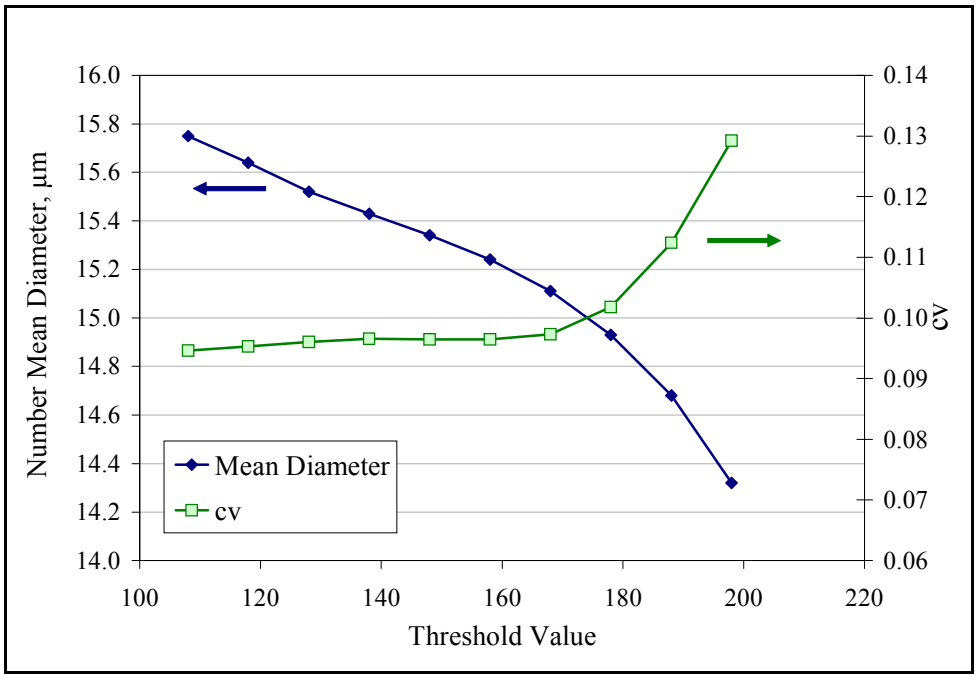

Figure 2.2.3.1- 3. Variation of number mean diameter and coefficient of variation with threshold value (14.9 µm polystyrene standard particles in water).

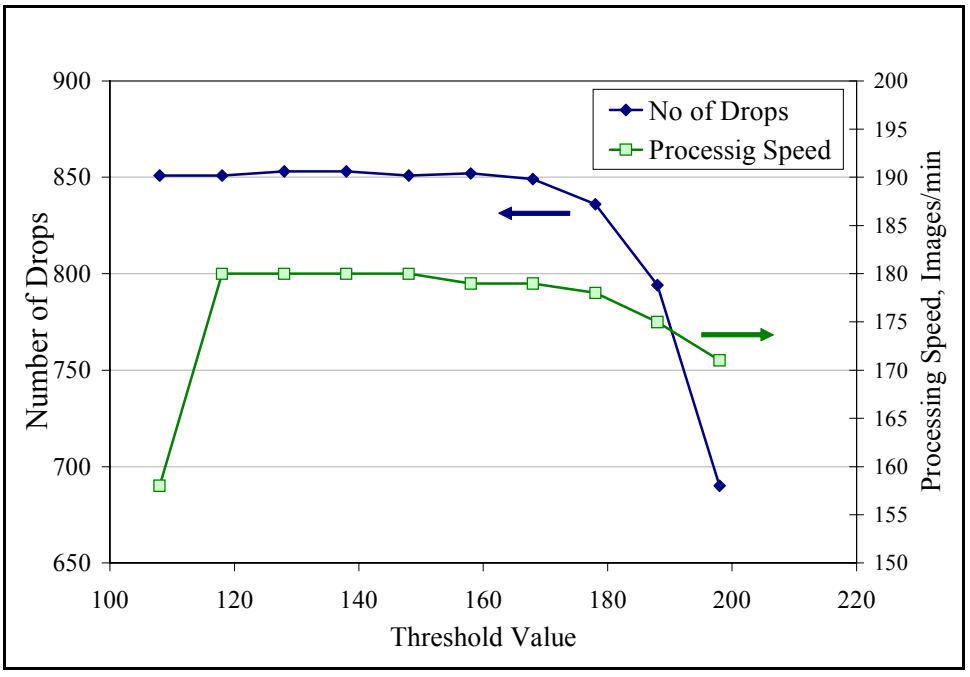

Figure 2.2.3.1- 4. Variation of the number of drops captured and the macro's processing speed with threshold value (14.9 µm polystyrene standard particles in water).

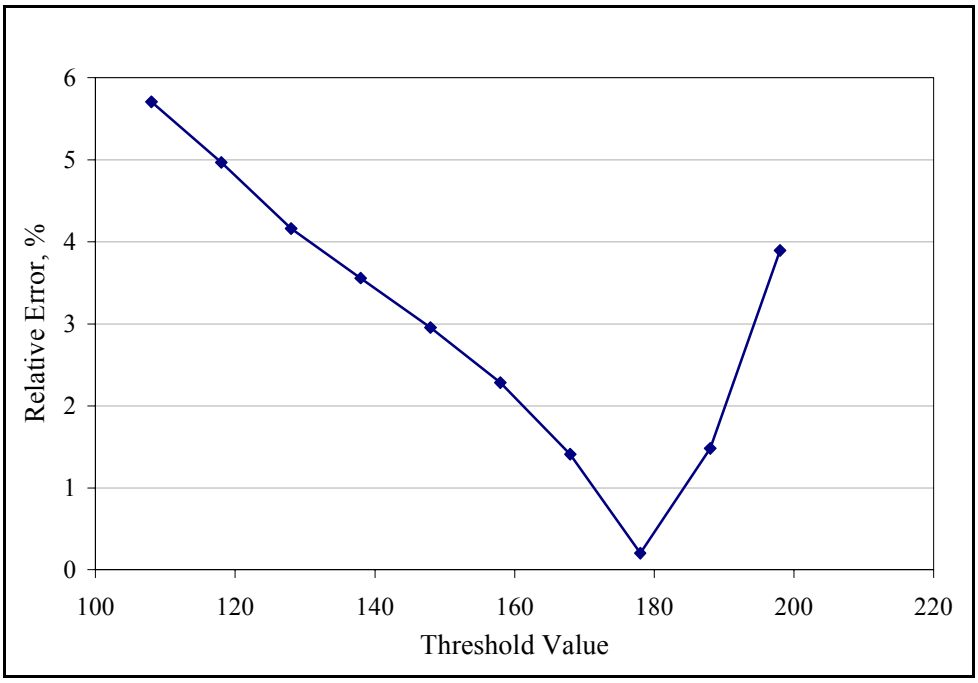

Figure 2.2.3.1- 5. Variation of relative error between calculated number mean diameter and the manufacturer's reported value with threshold value (14.9 µm polystyrene standard particles in water).

the threshold value is too low, many of the pixels of the background are captured, which increases the time necessary to analyze each image. Given these results, it seems like the optimum thresholding value would be between 128 and 168. However, according to the relative error between the calculated number mean diameter and the value reported by the manufacturer of the standard (14.9 µm), the error decreases as it approaches 180 (Figure 2.2.3.1-5). As a result, the optimum threshold range was reduced to 148 -168 (relative error less than 3%). The other two standards (4.8 and 26.2 µm) were tested in this range and it was found that even though the rest of the variables behaved in the same way, the error increased with threshold value. Consequently, the optimum threshold range was set to be 150 - 160.

Once the image has been appropriately thresholded, the built-in Particle Analysis function is called. It calculates the area and major and minor axes of the best fit ellipse of all thresholded segments of the image. To obtain this information directly in microns instead of pixels, the program requires the proper conversion factor. To obtain the conversion factors corresponding to each of the microscope's objective lenses, a stage micrometer, i.e. a microscope slide with a calibrated scale, was employed. Figure 2.2.3.1-6 shows pictures of the scale of the micrometer taken with three different lenses. The distances between the centers of the marks as well as the thickness of the marks themselves are known and NIST certified. Therefore by counting the pixels between them the pixel-micron conversion factors are easily calculated. Figure 2.2.3.1-7 shows a plot of the different conversion factors obtained for each objective lens. Figure 2.2.3.1-8 shows the same picture as in figure 2.2.3.1-3 after the final step of the image analysis process, along with a table with the results of the analysis, the area and major to minor axis ratio (M/m) of each particle.

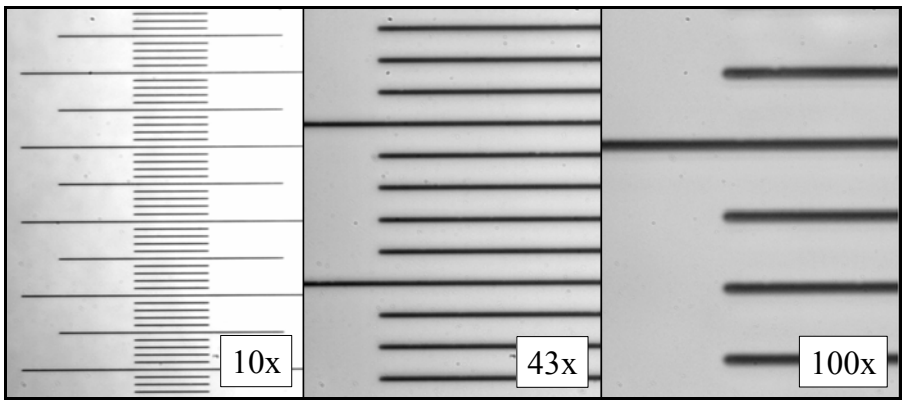

Figure 2.2.3.1- 6. Stage micrometer's scale viewed with three different objective lenses.

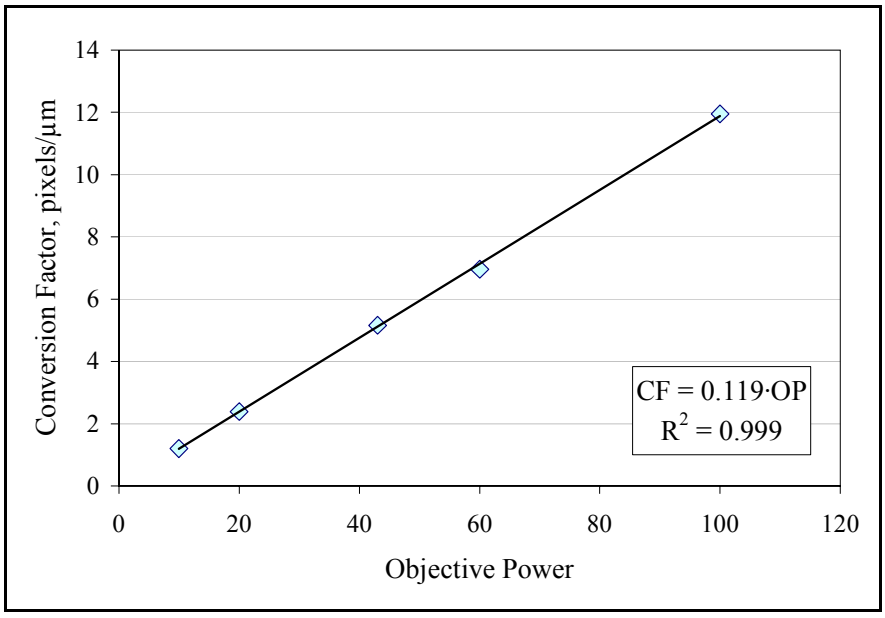

Figure 2.2.3.1- 7. Pixel-micron conversion factors for the microscope's objective lenses.

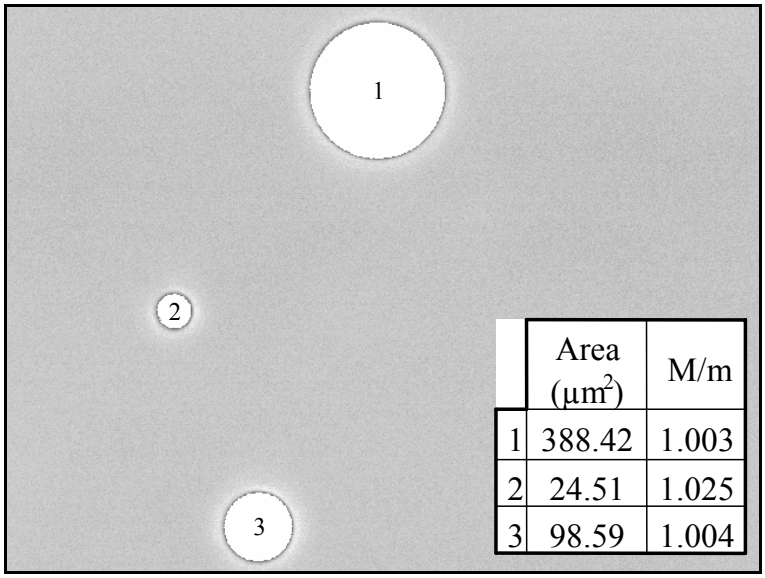

	Area (μm^2)	M/m
1	388.42	1.003
2	24.51	1.025
3	98.59	1.004

Figure 2.2.3.1- 8. Picture of silicone oil drops in water after image analysis.

To activate the macro, Scion Image for Windows hast to be running, with its "Special" menu opened, and the "Load Macro" option selected. This will open a "Load Macro File" window, where the "Macro" folder must be opened and the file "Measure

Particles" selected. After this, the "Special" menu will have three new options, and the one called "Measure Particles – VM" must be selected. At this point, the macro will start running and it will ask for the path of the folder where the images to be analyzed are stored, the number of images, and the magnification (objective lens) used. The macro processes images effortlessly, in batches at an approximate rate of 150 - 180 images/min (in a Pentium 4 computer). The output of the macro is an Excel file containing two columns, the first one with the area of each thresholded particle, and the second with corresponding major to minor axis ratio.

2.2.3.2. Data Analysis

The second stage of the image analysis process is to convert the information obtained with the Scion Image macro into drop size distributions. To this end, a macro was developed in Microsoft Excel. First, it calculates the diameter of each of the particles in the Scion Image output file, assuming it is a circle. Then, it creates a new column with the diameters of all the drops with an M/m ratio lower than 1.1. This value was chosen after analyzing several samples varying M/m. Ratios lower than ~1.05 reduce significantly the number of particles accepted, which yields unreliable average diameters. With values between 1.1 and 1.2 the number of particles vary less than 5% and the mean diameters remain constant (within <1%), but some objects that overlap or that are not appropriately thresholded are included. Therefore, 1.1 was determined to be the optimum M/m value to ensure reliable results. Then, Excel's built-in Histogram function is called to sort the diameters in this last column between pre-selected bin limits, which are based on three interlaced Fibonacci series. The output of the Histogram function is a table with one column containing the bin limits and another column with the number of drops in

each bin (n_i). The macro then computes the total number of particles and generates a new column that contains the value of the number frequency of the bin ($\tilde{f}_n(D_i)$, calculated with equation 2.1.1-1. Next, the values of $\tilde{f}_v(D_i)$, $\tilde{F}_n(D_i)$, and $\tilde{F}_v(D_i)$ are calculated through equations 2.1.1-8, 2.1.1-6, and 2.1.1-9, respectively. Columns containing the values of all distributions multiplied by 100 are also generated, which represent the distributions in terms of percentages instead of fractions. Next, the mean diameters and statistical parameters, namely D_{10}, D_{32}, D_{43}, variance, and standard deviation, are calculated via equations 2.1.3-5, 2.1.1-4, and 2.1.1-5. Finally, the maximum diameter (D_{max}) of the distribution is found and reported.

To run this macro, the Excel file containing the data from Scion Image must be opened and the button in Excel's Toolbar called "Particle Size Distribution Analysis" must be clicked (the macro must be installed and the button previously created). The whole process takes approximately 15 seconds (on a Pentium 4 computer). Figure 2.2.3.2-1 shows the output of the Excel macro, calling attention to an enlargement of the particle size distribution analysis button.

2.2.3.3. VM/Image Analysis System Validation and Error Estimation

In order to test the accuracy of the newly developed image analysis procedure, a comparison was performed between the video microscopy (VM) system and the high magnification video probe (section 2.2.2). The experiment was performed with the Silverson mixer, discussed in Chapter 5, and the dispersed phase consisted of polystyrene particles. These polystyrene particles have a broader size distribution than the standards used in the threshold analysis. Their size ranges from 1 to 15 μm, and they have $\Delta n_D =$

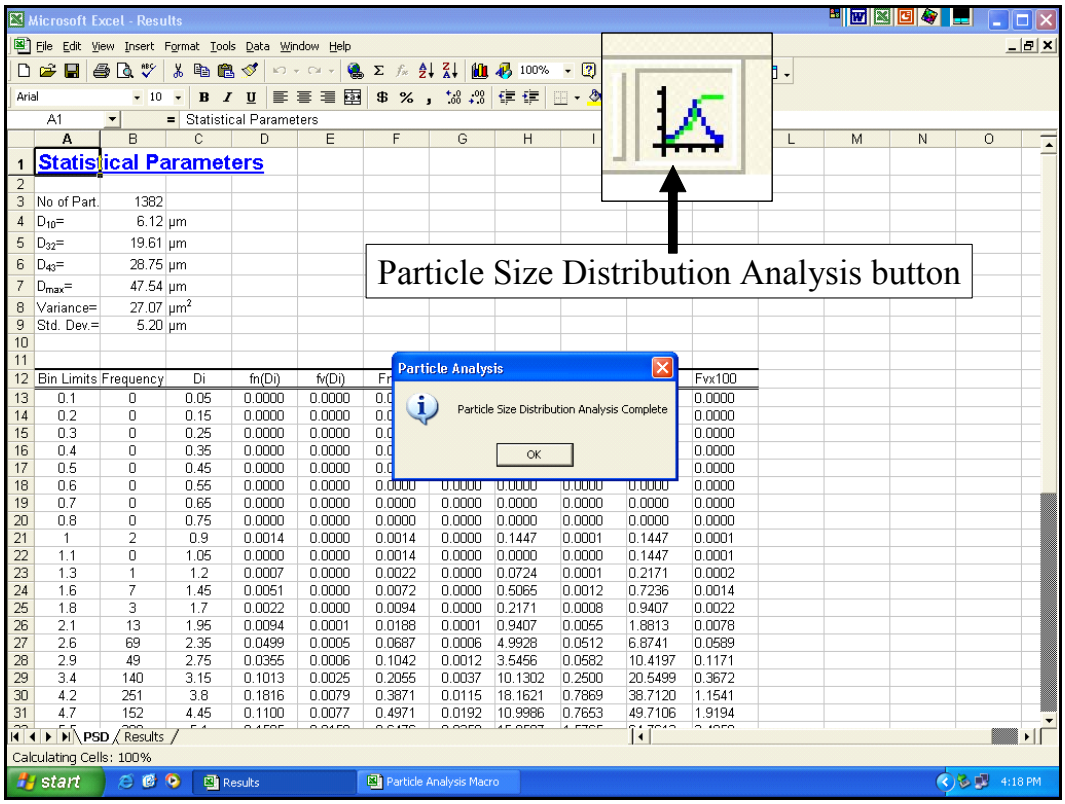

Figure 2.2.3.2- 1. Screen capture of the results of the Excel macro.

0.195 in water, making them suitable for use with the HMVP. Figure 2.2.3.3-1 shows the results of this comparison. It is evident that the volume frequency distributions, both standard and cumulative, obtained by the two methods are very similar. The video microscopy technique, however, seems to capture more small drops than the video probe. The same difference between this techniques was reported by Phongikaroon (2001). This makes sense since for the VM all particles are equidistant from the lens, while for the HMVP they are located over a sampling depth. This results in greater noise for the smallest particles.

Figure 2.2.3.3-2 shows the results for the Sauter mean diameter (D_{32}) as a function of rotor speed, obtained from two different experimental runs for 100 cSt silicone oil dispersed in pure water. The experimental conditions were the same in both

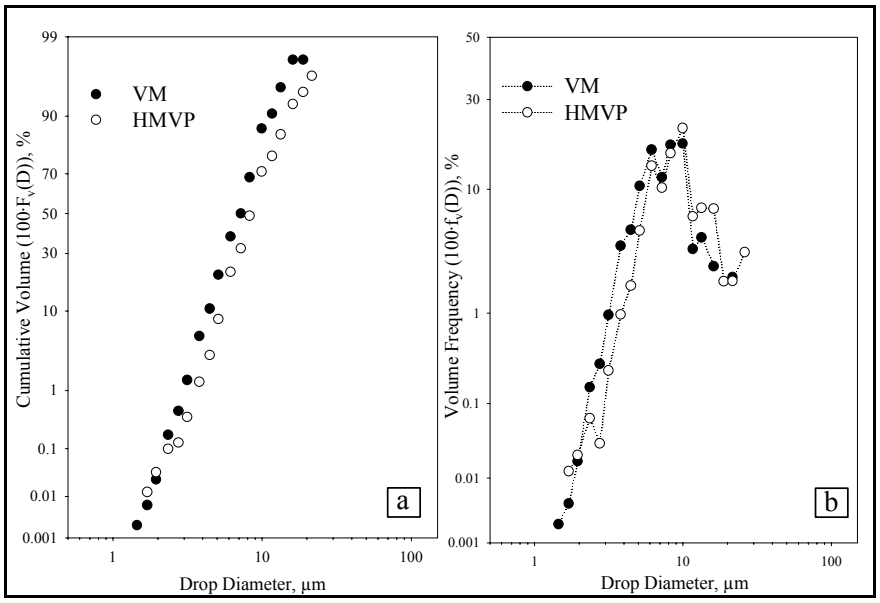

Figure 2.2.3.3- 1. Comparison between video microscopy and high magnification video probe with polystyrene particles dispersed in water. a) Cumulative volume distribution; b) Volume frequency distribution.

cases, and both sets of images were analyzed with a threshold value of 153. 10% error bars were arbitrarily included to demonstrate that the data overlap at this level of uncertainty. As shown in Figure 2.2.3.1-5, the image analysis error for this threshold value, with respect to standard particles of known size, is less than 3%. Therefore, the variation in D_{32} observed between the two runs can be attributed to the stochastic nature of liquid-liquid dispersions and the limited number of drops counted for each sample (approximately 1000, in the present case). Consequently, the results for mean drop diameters that will be presented in the following chapters should be regarded as having an error of approximately 10%.

2.3. Summary

This chapter is divided in two parts. In the first part, average drop sizes and drop distribution functions used in the characterization of dispersed systems were defined.

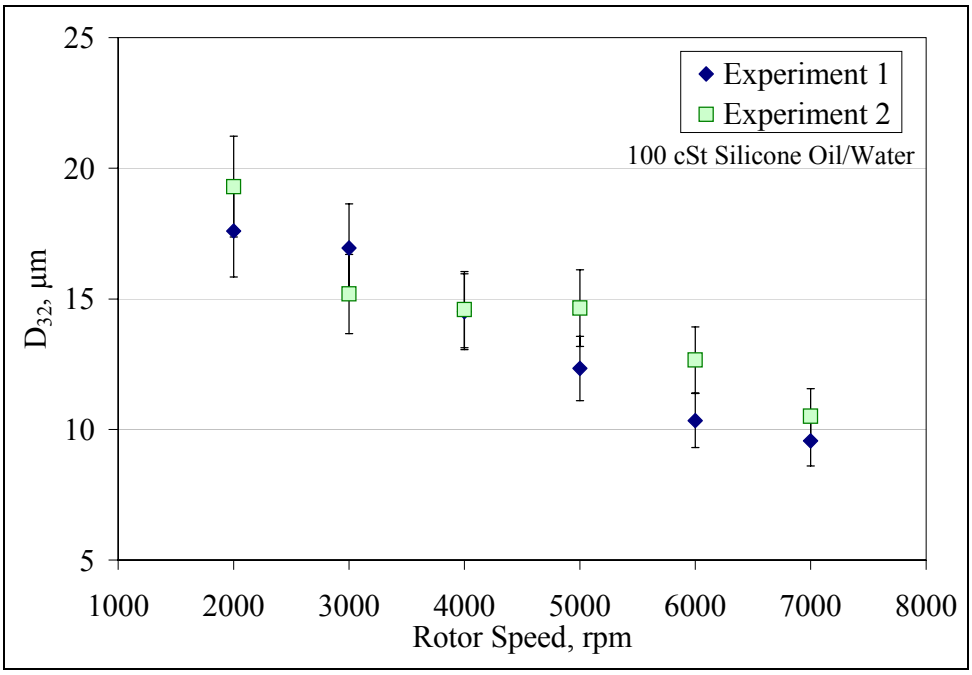

Figure 2.2.3.3- 2. Variation of Sauter mean diameter with rotor speed for 2 experimental runs with 100 cSt silicone oil in water. Error bars = 10%.

Average drop sizes based on the moments of the distribution were explained. These, particularly the Sauter mean diameter (D_{32}), will be used in the subsequent chapters to describe liquid-liquid dispersions.

The second part is dedicated to experimental methods commonly used to characterize particle size distributions. Emphasis is made on the video microscopy technique, which is the one used in the present study. Additionally, the automated image analysis procedure used to extract quantitative information from drop images is explained in detail.

CHAPTER 3. DROP BREAKUP IN TURBULENT FLOW

As previously stated, liquid-liquid dispersion is a common unit operation in the chemical, petroleum and pharmaceutical industries (Leng and Calabrese 2004). It has applications that range from heat and mass transfer processes to polymerization reactor design and crude oil treatment. In most of these cases, the drop size significantly affects the processes' efficiency and/or final product's properties. Therefore, accurate drop size prediction models are greatly desired. In the past decades, many researchers have developed models for drop breakup in turbulent flows (Kolmogorov 1949; Hinze 1955; Shinnar and Church 1960; Chen and Middleman 1967; among others), usually based on the theory of isotropic turbulence first proposed by A. N. Kolmogorov (1941). Many of these models are limited to dilute, inviscid systems at equilibrium in stirred tanks. However, several have been extended or modified to include more concentrated dispersions (Coulaloglou and Tavlarides 1976; Chatzi, Gavrielides, and Kiparissides 1989), to account for the effect of the dispersed phase viscosity (Calabrese, Chang, and Dang 1986; Wang and Calabrese 1986; Davies 1987), or to predict transient drop sizes (Kuriyama *et al.* 1996). More recently, an effort has been made to apply some of these models to high shear, rotor-stator mixing devices (Francis 1999; Phongikaroon 2001).

The objective of this chapter is to, first, provide a relatively simple introduction to the phenomenon of turbulence and some of its most basic concepts, as well as to Kolmogorov's theories for the smaller scale turbulence properties. Then, the development of mechanistic models for drop breakup in turbulent flows will be covered. Finally, a

brief discussion of the important timescales relevant to drop deformation and breakup will be provided.

3.1 Introduction to Turbulent Flows

Turbulence seems to be a ubiquitous phenomenon. It is important in many diverse and apparently unrelated fields such as meteorology, astrophysics, and several engineering specialties. In fact, almost all flows occurring in nature and in engineering practice are turbulent, laminar flow being the exception (Wallace and Piomelli 2001). Nonetheless, given its complexity, it is very difficult to define precisely. There are certain characteristics, however, that a flow must exhibit to be considered truly turbulent. The first one is randomness. Turbulent flows are time and space dependent with a very large number of degrees of freedom (Mathieu and Scott 2000). Any amount of energy put into a frictionless (very low viscosity) fluid, be it liquid or gas, is immediately distributed among all degrees of freedom, which makes turbulence, essentially, a statistical problem (Heisenberg 1948). This random nature is evidenced by measurements of instantaneous velocities in turbulent flows, which appear as randomly fluctuating signals. Even though randomness makes turbulence unpredictable in detail, statistical tools and averages may be used to describe it effectively. This randomness is rather unique, though, since in addition to the statistical random background, there are also coherent structures (e.g. vortices, ejections, and sweeps) present in most turbulent flows. These coherent structures are regular, well defined sequences of events that may still be random about their occurrence in time and space (Wallace and Piomelli 2001). Today, the coherent structures concept is being extended to include periodic structures that are forced on the

flow or created by the flow geometry, which interact with the natural structures of the flow (Kresta and Brodkey 2004).

Another important characteristic of turbulence is that it contains a wide range of coexisting space and time scales, with the smaller ones living inside larger ones (Mathieu and Scott 2000). The larger scales are usually dictated by the flow's overall geometry, while the smallest ones depend on the fluid's viscosity. The presence of these various scales is related to a third defining characteristic of turbulence, the fact that it dissipates energy. Kinetic energy is supplied to the flow by a large-scale source (a pump, for instance), which creates instabilities in the flow, generating large-scale eddies. This large-scale eddies are also unstable and they disintegrate, giving rise to, and transferring their energy to, smaller eddies, which continue doing the same, until the energy is ultimately dissipated (into heat) at the smallest scales by viscous stresses. If there is no energy supply to maintain the flow, the turbulence decays and eventually ceases (Mathieu and Scott 2000). The continuous energy transfer from larger eddies to smaller eddies is usually referred to as the "energy cascade" and is represented by the flow's energy spectrum, a plot that shows how the kinetic energy is distributed among the different scales of the flow (Bernard and Wallace 2002). Finally, there are other defining characteristics of turbulence, such as the fact that it is a continuum phenomenon - i.e. the smallest scales are orders of magnitude larger than the molecular mean free path - which means that it may be described by continuum based equations; and that it has small-scale random vorticity, and is therefore, intrinsically three-dimensional.

3.1.1. Reynolds Decomposition

Due to the random nature of turbulence, when computing turbulent motion, it is easier to decompose the instantaneous velocity into a mean motion and a fluctuating motion:

$$U = \overline{U} + u \tag{3.1.1-1}$$

where U is a fluid velocity component, $\overline{U}$ is its mean value, and u is the fluctuating velocity. This variable decomposition is known as Reynolds decomposition (after Osborne Reynolds, who first used this approach over 100 years ago). The mean velocity $\overline{U}$ is the result of some kind of averaging. There are different forms of averages used in turbulent flow analysis: ensemble average (average of the velocity component, at the same point in space and time, over several independent realizations of the flow field), spatial average (average of values at different points on a plane, at the same time), and temporal average (average of values at the same location over a sufficiently long period of time). The latter is the most commonly used, at least in experimental investigations (Bernard and Wallace 2002). The time average of the velocity component U is given by:

$$\overline{U}(\vec{x}, t) = \frac{1}{T}\int_{t-T/2}^{t+T/2} U(\vec{x}, \xi)d\xi \tag{3.1.1-2}$$

where $\vec{x}$ is the position vector in space, t is time, and T is the time period over which the average is taken. Figure 3.1.1-1 illustrates the decomposition of an instantaneous velocity component into its time-averaged mean component and fluctuating component.

In continuum mechanics, the equations that govern the motion of an incompressible, Newtonian fluid are the Navier-Stokes equation and the continuity equation, which, in index notation, are given by:

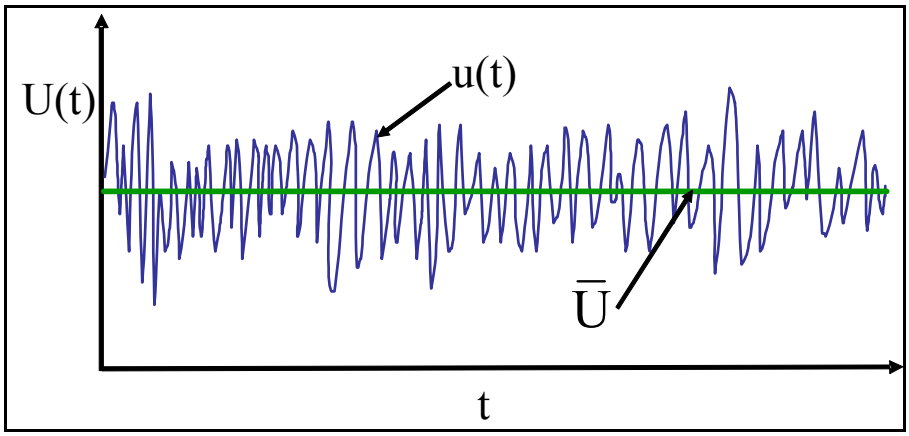

Figure 3.1.1- 1. Decomposition of the instantaneous velocity component U into a mean component ($\overline{U}$) and a fluctuating component (u).

$$\rho\left(\frac{\partial U_i}{\partial t}+U_j\frac{\partial U_i}{\partial x_j}\right)=-\frac{\partial P}{\partial x_i}+\mu\nabla^2 U_i+\rho g_i \qquad (3.1.1\text{-}3)$$

$$\frac{\partial U_i}{\partial x_i}=0 \qquad (3.1.1\text{-}4)$$

respectively, where ρ is the fluid's density, μ is its viscosity, P is the pressure, g the gravitational acceleration vector, and ∇^2 is the Laplacian operator ($\nabla^2 \equiv \partial^2/\partial x_i^2$). Applying Reynolds decomposition (equation 3.1.1-1) to all velocity components and to the pressure, and substituting them into equations 3.1.1-3 results in the so called Reynolds Averaged Navier-Stokes (RANS) equation:

$$\rho\left(\frac{\partial \overline{U}_i}{\partial t}+\overline{U}_j\frac{\partial \overline{U}_i}{\partial x_j}\right)=-\frac{\partial \overline{P}}{\partial x_i}+\mu\nabla^2\overline{U}_i-\frac{\partial\left(\rho\overline{u_i u_j}\right)}{dx_j}+\rho g_i \qquad (3.1.1\text{-}5)$$

which has the same general form as the regular Navier-Stokes equation except for the term containing $\rho\overline{u_i u_j}$, the Reynolds stresses, which is a by-product of averaging the nonlinear convection term in the Navier-Stokes equation. Physically, the Reynolds

stresses represent an additional stress due to turbulent momentum transport (Bernard and Wallace 2002). Since the Reynolds stress term is a symmetrical 2nd order tensor, it has 6 independent components, which means that the equation system comprised of the three components of the RANS equation and the averaged continuity equation, is an undetermined system, This creates the "closure problem" of turbulence, and the Reynolds stresses must, then, be calculated through independent constitutive relations in order to appropriately model turbulent flows with the RANS equation.

If the same averaging treatment is given to the kinetic energy transport equation, the following expression is obtained:

$$\frac{\partial K}{\partial t} + \overline{U}_j \frac{\partial K}{\partial x_j} = -\rho \overline{u_i u_j} \frac{\partial \overline{U}}{\partial x_i} - \varepsilon - \frac{1}{\rho} \frac{\partial \overline{p u_i}}{\partial x_i} + \nu \nabla^2 K - \frac{\partial \overline{u_j (u_i^2/2)}}{\partial x_j} \qquad (3.1.1\text{-}6)$$

where K is the turbulent kinetic energy ($K=\frac{1}{2}\overline{u_i^2}$), p is the pressure fluctuation, ν is the fluid's kinematic viscosity, and ε is the turbulent energy dissipation rate per unit mass, defined as:

$$\varepsilon = \nu \overline{\left(\frac{\partial u_i}{\partial x_j} \right)^2} \qquad (3.1.1\text{-}7)$$

The physical interpretation of equation 3.1.1-6 is that the rate of change of turbulent kinetic energy in the control volume plus the net rate of gain or loss by convection through the boundaries, is balanced by, in order, the rate of turbulent kinetic energy production, the rate of turbulent kinetic energy dissipation, the pressure work, and the viscous and turbulent diffusion through the control volume surface. The diffusion terms

being only significant very near boundaries (Bernard and Wallace 2002). The turbulent energy dissipation rate is always positive (equation 3.1-7), and therefore acts as an energy sink caused by friction (viscous forces). Of all the terms in the energy balance equation, ε is the most difficult to measure or calculate accurately. However, it is one of the most important quantities in turbulent flow analysis, as will be demonstrated in the subsequent sections.

3.2 Isotropic Turbulence

The word *isotropic*, etymologically, means "equal in all directions". Hence, the term *isotropic turbulence* is used to denote a turbulent flow field in which the statistical properties of the field are independent of the position and orientation of the coordinate axes; that is to say, symmetric with respect to any plane or rotation (Wallace and Piomelli 2001). Isotropy, however, is not to be confused with homogeneity. In homogeneous turbulence, the fluctuation statistics are the same in all spatial positions, and yet, the mean flow may be non-uniform (Mathieu and Scott 2000). Isotropy implies homogeneity, but the opposite is not true since some flows may be homogeneous in one direction and not is the others, which is incompatible with the symmetry requirements for isotropy.

One of the consequences of the symmetries of isotropy is that the mean flow must be constant (all mean flow gradients are equal to zero). In addition, the mean fluctuating velocity is the same in all directions:

$$\overline{u_1^2} = \overline{u_2^2} = \overline{u_3^2} = u'^2 \tag{3.2-1}$$

where u' is also known as the root mean squared (rms) velocity . Furthermore, under isotropic conditions, the turbulent kinetic energy equation (equation 3.1.1-6) reduces to:

$$\frac{\partial K}{\partial t} = -\varepsilon \tag{3.2-2}$$

which shows that isotropic turbulence is an inherently unsteady, decaying flow. Taylor (1935), showed that for the case of incompressible isotropic turbulence:

$$\varepsilon = 15\nu\overline{\left(\frac{\partial u_1}{\partial x_1}\right)^2} = \frac{15}{2}\nu\overline{\left(\frac{\partial u_1}{\partial x_2}\right)^2} \tag{3.2-3}$$

where $\partial u_1/\partial x_1$ is the gradient of a fluctuating velocity component in the direction parallel to it and $\partial u_1/\partial x_2$ is the gradient in one of the perpendicular directions. This simplifies to a great extent turbulence experiments and modeling, since only one fluctuating velocity gradient needs be measured or predicted to calculate ε. Figure 3.2.1-1 shows a picture (reproduced from Van Dyke 1982) of a "wrinkling" fluid surface in nearly isotropic turbulence. A fine platinum wire at the left of the picture (not seen) generates a continuous sheet of microscopic hydrogen bubbles, which is then deformed by the turbulent flow behind a grid (also to the left, not shown). It becomes evident from the picture, that the flow does not have a preferred direction under the near isotropic conditions.

Figure 3.2.1- 1. Wrinkling of a fluid surface in isotropic turbulence (Van Dyke 1982).

3.2.1. Local Isotropy

True isotropic turbulence, i.e., isotropic at all scales, is almost impossible to achieve by means other than contrived experiments or numerical simulation. It has little applicability in engineering. In 1941, Kolmogorov (1941) introduced the concept of *local isotropy*. Turbulent flows normally have high values of Reynolds number, which is defined as:

$$\mathrm{Re} = \frac{LU}{\nu} \tag{3.2.1-1}$$

where L and U are the typical length and velocity for the whole flow, respectively. Kolmogorov hypothesized that, if the Reynolds number is sufficiently high, it is very likely that there will be a small spatial domain, with linear dimensions smaller than L and not near any boundaries or flow singularities, in which the flow could be considered isotropic. Furthermore, Kolmogorov predicted that in locally isotropic turbulence the statistical characteristics of the flow only depend on the turbulent energy dissipation rate (ε) and the fluid's kinematic viscosity (ν), and that the length and time scales of the smallest eddies in the flow, the ones that dissipate energy into heat, are given by:

$$\eta = \left(\frac{\nu^3}{\varepsilon}\right)^{1/4} \tag{3.2.1-2}$$

$$t_K = \sqrt{\frac{\nu}{\varepsilon}} \tag{3.2.1-3}$$

where, η is the length scale and t_K is the time scale. However, for eddies that are large compared to η, but still very small compared to L, the flow is independent of viscosity and uniquely determined by ε. Kolmogorov's theory revolutionized the study of turbulence since it gives the small scales of the flow the character of a universal

equilibrium, whose statistical and structural properties are common to all turbulent flows (Bernard and Wallace 2002), independently of their macro-scale geometry.

One consequence of local isotropy is the existence of the "inertial sub-range", the range of small scales (smaller than L) that are characterized solely by ε. Kolmogorov determined, from dimensional analysis, that in this range the energy spectrum depends only on ε and the wavenumber (k) of the eddies (the inverse of the apparent eddy length):

$$E(k,t) = C_K k^{-5/3} \varepsilon^{2/3} \qquad (3.2.1\text{-}4)$$

where E is the energy spectral density function and C_K is the Kolmogorov constant. The prediction of the -5/3 spectrum has been verified experimentally for a wide range of turbulent flows with a typical Kolmogorov constant value of 1.4 (Bernard and Wallace 2002). In this range of the spectrum, inertial forces predominate over viscous forces. Hence the name "inertial sub-range".

The range of wavenumbers greater than η^{-1} (length scales smaller than η) is called the "viscous sub-range", since this is where the viscous dissipation of energy takes place. Heisenberg (1948) obtained that $E(k) \sim k^{-7}$, in this wavenumber range, and the expression for the energy spectral density function is (Chen 1966):

$$E(k) = \left(\frac{\alpha \varepsilon}{2\nu^2} \right)^2 k^{-7} \qquad (3.2.1\text{-}5)$$

where α is a constant. According to equation 3.2.1-5, the functional dependence of E(k) on k shifts from the Kolmogorov-predicted exponent of -5/3 to -7, indicating the dissipative effect of the viscosity at these scales. Figure 3.2-2 shows a schematic representation of a typical energy spectrum with all the ranges specified. It shows that the slope changes as the wavenumber approaches the order of magnitude of η^{-1}. Some

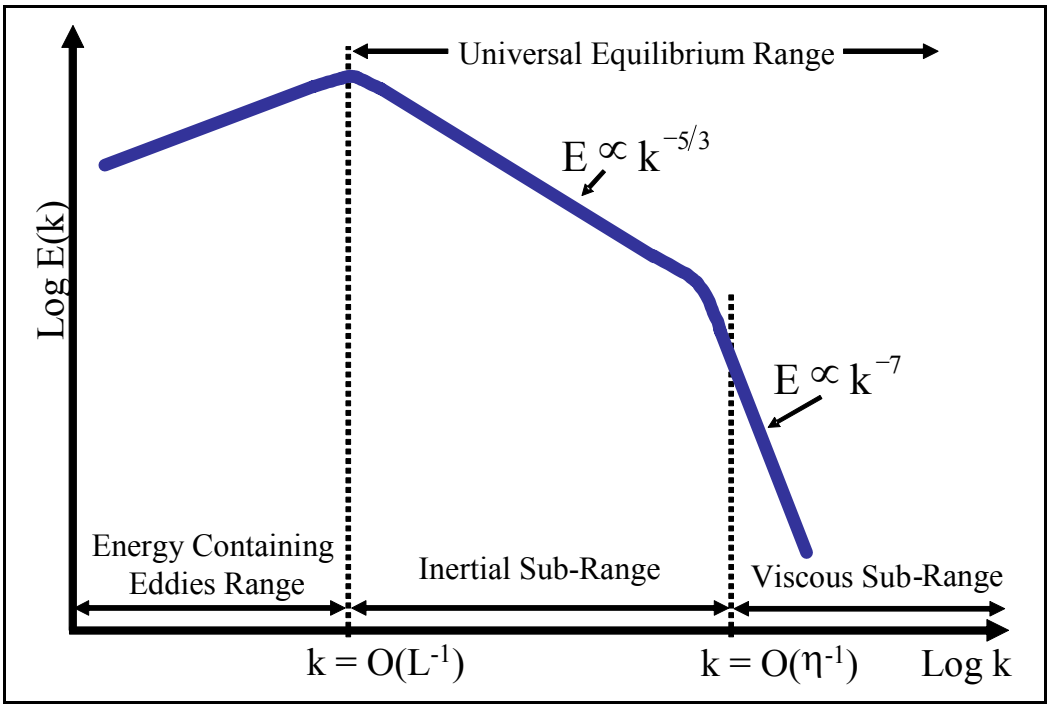

Figure 3.2.1- 2. Schematic representation of the energy spectrum of a turbulent flow.

authors actually place the dissipation limit is at $k = (5\eta)^{-1}$, where the magnitude of the viscous forces reaches 20% of that of the turbulent inertial forces (Kresta and Brodkey 2004). The difference between L and η, and therefore the length of the -5/3 range in the spectrum, increases as the Reynolds number increases.

3.3 Mechanistic Models for Drop Breakup in Turbulent Flow

Many authors have developed theoretical and/or empirical models to predict and analyze drop breakup and coalescence in turbulent mixers. In the case of dilute systems, i.e. dispersions with very low dispersed phase content ($\phi \rightarrow 0$), coalescence may be neglected, and the breakup models are based on a balance of the disruptive and cohesive forces acting on a drop in an isotropic turbulent flow field. If the drop is considered viscous ($\mu_d/\mu_c > 1$, from now on the subscripts d and c will denote the dispersed and

continuous phases, respectively), the cohesive forces that oppose the drop's deformation are those due to the interfacial tension, which tries to keep the drop's spherical from, and those due to the dispersed phase viscosity, which increases the resistance of the drop's fluid to flow, delaying the deformation. The disruptive forces are those exerted by the continuous phase on the drop. In the case of a small drop (L >> D, D being the drop's diameter) in a turbulent flow these forces are isotropic (no matter how complex the geometry) and may be inertial or viscous in nature, depending on whether the drop is in the inertial or viscous sub-range.

3.3.1. Mechanistic Models for the Inertial Sub-Range

In the inertial sub-range (L >> D >> η), the continuous phase's energy is described by the energy spectral density function of equation 3.2.1-4. The disruptive force per unit area or turbulent stress acting on a drop of diameter D is given by:

$$\tau_c = \rho_c u'^2(D) \qquad (3.3.1\text{-}1)$$

where u'(D), the rms velocity difference, is the mean velocity difference between two points in the continuous phase separated by a distance equal to D. In other words, the stress acting on the drop is equal to the dynamic pressure difference between its opposite sides, as given by Bernoulli's equation (Walstra 1983). From arguments given by Kolmogorov's (1941) theory, the mean squared velocity difference is related to the energy spectrum through:

$$u'^2(D) = \int_{1/D}^{\infty} E(k)dk \qquad (3.3.1\text{-}2)$$

Only the energy contained in eddies of size equal to or smaller than the drop (k = 1/D – ∞) are considered, since larger eddies only carry the drop rather than deform it (Leng and

Calabrese 2004). Consequently, from equations 3.2.1-4, 3.3.1-1 and -2, the expression for the stress (force per unit area) exerted by the continuous phase turbulence on the deforming drop is:

$$\tau_c \sim \rho_c \varepsilon^{2/3} D^{2/3} \tag{3.3.1-3}$$

where the symbol ~ denotes proportionality.

The surface energy of a drop is proportional to the interfacial tension between the dispersed and continuous phases. When the drop is deformed, its surface area increases and so does its surface energy. Such energy increase is thermodynamically unfavorable and, therefore, the higher the increase in surface area, the higher the force that opposes the drop deformation. In other words, smaller drops have a higher internal pressure, according to the Young-Laplace equation (see section 4.1), and hence, are more difficult to deform. Consequently, the interfacial stress that opposes the drop deformation scales with drop size as:

$$\tau_s \sim \frac{\sigma}{D} \tag{3.3.1-4}$$

where τ_s is the interfacial stress and σ is the interfacial tension.

The deformation of the drop's interface by the continuous phase's turbulent forces gives rise to viscous stresses inside the drop. According to Hinze (1955), the flow velocity inside the drop is proportional to $(\tau_c/\rho_d)^{1/2}$. Therefore, applying Newton's law of viscosity, the viscous stresses that oppose the drop's deformation are approximated by:

$$\tau_d \sim \mu_d \frac{\sqrt{\tau_c/\rho_d}}{D} \tag{3.3.1-5}$$

The maximum stable drop diameter in the dispersion (D_{max}) is that for which the disruptive and cohesive forces are at equilibrium:

$$\tau_c(D_{max}) = \tau_s(D_{max}) + \tau_d(D_{max}) \qquad (3.3.1\text{-}6)$$

By substituting equations 3.3.1-3 through -5 into equation 3.3.1-6, the following expression is obtained:

$$\rho_c \varepsilon^{2/3} D_{max}^{2/3} = A_1 \frac{\sigma}{D_{max}} + A_2 \frac{\mu_d}{D_{max}} \sqrt{\frac{\rho_c \varepsilon^{2/3} D_{max}^{2/3}}{\rho_d}} \qquad (3.3.1\text{-}7)$$

where A_1 and A_2 are arbitrary constants of proportionality (henceforth A_n, where n is an integer, will be used to designate proportionality constants. No relationship between them will be implied by the numbers). Rearranging the previous equation and solving for D_{max}:

$$D_{max} = A_3 \left(\frac{\sigma}{\rho_c} \right)^{3/5} \varepsilon^{-2/5} \left[1 + A_4 \frac{\mu_d}{\sigma} \sqrt{\frac{\rho_c}{\rho_d}} \varepsilon^{1/3} D_{max}^{1/3} \right]^{3/5} \qquad (3.3.1\text{-}8)$$

This is the representation of the mechanistic model for the maximum stable size of viscous drops that break up in dilute dispersions in the turbulent inertial sub-range. This equation, however, is difficult to use directly, mainly because of the difficulty in obtaining exact values for ε. In stirred tanks and rotor-stator mixers, the turbulent energy dissipation rate, ε, varies spatially, being higher near the mixing head than in the bulk of the fluid. The equilibrium drop size distribution will not be achieved until all drops have passed through the high energy dissipation zones, which is where ε, and therefore drop deformation, reaches its maximum. Therefore, the value of ε used in equation 3.3.1-8 should be ε_{max}. Unfortunately, the exact value of ε_{max} can be difficult to measure or predict. In geometrically similar systems, it is proportional to the average dissipation rate, $\bar{\varepsilon}$, which can be approximated as the power draw per unit mass:

$$\bar{\varepsilon} = A_5 \frac{P}{\rho_c V} \qquad (3.3.1\text{-}9)$$

The power draw (P) is equal to $P_0\rho_c N^3 L^5$ (Padron 2001), where P_0 is the power number, N is the impeller's rotational speed (in s^{-1}), and L is the characteristic length scale of the system, which for stirred tanks and rotor- stator mixers is the impeller diameter. The Reynolds number is defined as:

$$\mathrm{Re} = \frac{\rho_c N L^2}{\mu_c} \tag{3.3.1-10}$$

For high Reynolds number (>10^4), which is already a requirement to apply local isotropy theory, the Power number is constant. Since the volume of the fluid in the tank is proportional to L^3, the following expression is obtained:

$$\bar{\varepsilon} = A_5 \frac{\rho_c N^3 L^5}{\rho_c L^3} P_0 = A_6 N^3 L^2 \tag{3.3.1-11}$$

Substituting equation 3.3-11 into 3.3-8 and normalizing the drop diameter with the impeller diameter leads to:

(L >> D >> η)
$$\frac{D_{max}}{L} = A_7 \mathrm{We}^{-3/5}\left[1 + A_8 \mathrm{Vi}\left(\frac{D_{max}}{L}\right)^{1/3}\right]^{3/5} \tag{3.3.1-12}$$

where We, the Weber number, represents the ratio of the continuous phase inertial forces to surface forces acting on the drop and is defined as:

$$\mathrm{We} = \frac{\rho_c N^2 L^3}{\sigma} \tag{3.3.1-13}$$

and Vi, the viscosity number, is the ratio of the dispersed phase viscous forces to surface forces resisting drop deformation:

$$\mathrm{Vi} = \frac{\mu_d N L}{\sigma}\left(\frac{\rho_c}{\rho_d}\right)^{1/2} \tag{3.3.1-14}$$

For inviscid drops ($\mu_d \rightarrow 0$ and $\mathrm{Vi} \rightarrow 0$), the model collapses to:

$$\frac{D_{max}}{L} = A_9\left(\frac{\sigma}{\rho_c}\right)^{3/5}\varepsilon^{-2/5} = A_{10}N_{We}^{-3/5} \qquad (3.3.1\text{-}15)$$

(L >> D >> η)

which has been previously derived and validated (Shinnar and Church 1960; Chen and Middleman 1967). For highly viscous dispersed phases, τ_d is much greater than τ_s, therefore, τ_s can be neglected in equation 3.3.1-6. As a consequence, equation 3.3.1-8 is replaced by:

$$D_{max} = A_{11}\mu_d^{3/4}\left(\rho_c\rho_d\right)^{-3/8}\varepsilon^{-1/4} \qquad (3.3.1\text{-}16)$$

which for constant Power number results in:

$$\frac{D_{max}}{L} = A_{12}\left(\frac{\mu_d}{\mu_c}\right)^{3/4}\left(\frac{\rho_c}{\rho_d}\right)^{3/8}Re^{-3/4} \qquad (3.3.1\text{-}17)$$

(L >> D >> η)

Since the Reynolds number is proportional to μ_c^{-1} (equation 3.3.1-10), equation 3.3.1-17 is actually independent of the continuous phase viscosity, as it should be considering that it applies to the inertial sub-range.

This model (equation 3.3.1-12) was first derived by Calabrese *et al.* (Calabrese, Chang, and Dang 1986; Calabrese, Wang, and Bryner 1986; Wang and Calabrese 1986). They used it to correlate data obtained in a stirred tank with a Rushton turbine. Their results show that the correlation is valid for dispersed phase viscosities up to 500 cP. For higher viscosities, the behavior is more complex and not readily explainable. Nevertheless, they did find that as the dispersed phase viscosity increased, the drop size became proportional to $\mu_d^{3/4}$, as predicted by equation 3.3.1-17. The same model was also successful correlating data for breakup of viscous drops is a static mixer under turbulent flow conditions (Berkman and Calabrese 1988).

3.3.2. Mechanistic Models for the Viscous Sub-Range

When the drop size is smaller than the Kolmogorov length scale (equation 3.2.1-2), as may be the case in high energy mixing devices such as rotor-stator mixers, it falls in the viscous sub-range. In this range, the viscosity of the continuous phase is no longer negligible. Therefore, drops may be broken up by viscous stresses in addition to inertial stresses. Depending on which kind of stress is considered to predominate, the expression for the continuous phase changes. Consequently, two different sets of mechanistic models can be derived.

3.3.2.1. Inertial Stresses

Shinnar and Church (1960) proposed, based on dimensional analysis, that in this range the velocity fluctuations are given by:

$$u'^2(D) \sim \frac{\varepsilon}{\nu_c} D^2 \qquad (3.3.2.1\text{-}1)$$

This expression comes from dimensional considerations in the range of wavenumber of $O(\eta^{-1})$. As seen in Figure 3.2.1-2, this is the range where the shift from inertial sub-range to viscous sub-range occurs. Therefore, equation 3.3.2.1-1 is more likely to be valid in the range $D < \eta$, than in $D << \eta$, deep in the viscous sub-range were inertial stresses are no longer significant. The expression for the inertial stresses acting on the drop is obtained by substituting equation 3.3.2.1-1 into equation 3.3.1-1:

$$\tau_c \sim \rho_c^2 \frac{\varepsilon}{\mu_c} D^2 \qquad (3.3.2.1\text{-}2)$$

The expressions for τ_s and τ_d remain the same in this sub-range. Hence, substituting equations 3.3.1-4, 3.3.1-5, and 3.3.2.1-2 into equation 3.3.1-6 produces:

$$\rho_c^2 \frac{\varepsilon}{\mu_c} D_{max}^2 = A_{13} \frac{\sigma}{D_{max}} + A_{14} \frac{\mu_d}{D_{max}} \sqrt{\frac{\rho_c^2 \varepsilon D_{max}^2}{\rho_d \mu_c}} \qquad (3.3.2.1\text{-}3)$$

Rearranging and solving for D_{max}:

$$D_{max} = A_{15} \left(\frac{\sigma \mu_c}{\rho_c^2} \right)^{1/3} \varepsilon^{-1/3} \left[1 + A_{16} \frac{\mu_d \rho_c}{\sigma \sqrt{\rho_d \mu_c}} \varepsilon^{1/2} D_{max} \right]^{1/3} \qquad (3.3.2.1\text{-}4)$$

It's important to point out that this model, as opposed to equation 3.3.1-8, contains the continuous phase viscosity. This is to be expected since in the viscous sub-range the turbulence is no longer independent of the fluid's viscosity. Assuming that the Power number is constant, the model is simplified to:

(D < η)

$$\frac{D_{max}}{L} = A_{17} \left(We\, Re \right)^{-1/3} \left[1 + A_{18} Vi\, Re^{1/2} \frac{D_{max}}{L} \right]^{1/3} \qquad (3.3.2.1\text{-}5)$$

The derivation of this mechanistic model assumes that the stresses that deform and disrupt the drops are predominantly inertial, i.e., due to turbulent pressure fluctuations in the continuous phase. The equivalent model for the inviscid drop case is:

(D < η)

$$\frac{D_{max}}{L} = A_{19} \left(We\, Re \right)^{-1/3} \qquad (3.3.2.1\text{-}6)$$

Or in its dimensional form:

$$D_{max} = A_{20} \left(\frac{\sigma \mu_c}{\rho_c^2} \right)^{1/3} \varepsilon^{-1/3} \qquad (3.3.2.1\text{-}7)$$

In the high viscosity case, equation 3.3.2.1-4 changes to:

$$D_{max} = A_{21} \left(\frac{\mu_d^2 \mu_c}{\rho_c^2 \rho_d} \right)^{1/4} \varepsilon^{-1/4} \qquad (3.3.2.1\text{-}8)$$

Or:

(D < η)

$$\frac{D_{max}}{L} = A_{22}\left(\frac{\mu_d}{\mu_c}\right)^{1/2}\left(\frac{\rho_c}{\rho_d}\right)^{1/4} Re^{-3/4} \qquad (3.3.2.1\text{-}9)$$

assuming constant Power number. The most important difference between this equation and its equivalent for the inertial sub-range (equation 3.3.1-17) is the fact that the diameter depends on the square root of the dispersed phase viscosity instead of $\mu_d^{3/4}$.

3.3.2.2. Viscous Stresses

Equation 3.3.2.1-7 (which is comparable to one derived by Kolmogorov (1949) himself for breakage in turbulent pipe flow) has been criticized by Levich (1962) arguing that, below the Kolmogorov scale, disruptive stresses must be viscous (shear stresses) and not inertial. Even Shinnar recognized the weakness of this equation (Bourne and Baldyga 1994) and proposed an alternative based on viscous stresses. The approach proposed by Shinnar (1961) is based on the equation for the breakup of a drop due to viscous shear, originally derived by Taylor (1932):

$$\mu_c \frac{\partial v}{\partial r}\frac{D}{\sigma} = \Phi\left(\frac{\mu_d}{\mu_c}\right) \qquad (3.3.2.2\text{-}1)$$

where $\partial v/\partial r$ is the velocity gradient across the drop. The right hand side of equation 3.3.2.2-1 is the critical capillary number, which is a function of the viscosity ratio, although the exact function is unknown. The capillary number is the ratio of viscous stresses to surface stresses acting on the drop. If the capillary number is larger than its critical value (which depends, aside from viscosity, on shear rate, drop size, and interfacial tension), the drop will deform and break. Otherwise, it will deform but return to its original spherical shape after the viscous stress ceases. For inviscid drops ($\mu_d/\mu_c \rightarrow 0$) and if the densities of both fluids are similar (as is usually the case in liquid-

liquid systems), the critical capillary number may be considered a constant. Furthermore, since at the critical capillary number the drop is just about to be ruptured, it can be argued that the drop diameter in equation 3.3.2.2-1 is indeed D_{max}. Consequently, solving equation 3.3.2.2-1 for D_{max} yields:

$$D_{max} = A_{23}\frac{\sigma}{\mu_c}\left(\frac{\partial v}{\partial r}\right)^{-1} \qquad (3.3.2.2\text{-}2)$$

Following from equation 3.2-3:

$$\left(\frac{\partial v}{\partial r}\right)^{2} \approx \frac{2\varepsilon}{15\nu_c} \qquad (3.3.2.2\text{-}3)$$

Accordingly:

$$D_{max} = A_{24}\sigma\left(\mu_c\rho_c\varepsilon\right)^{-1/2} \qquad (3.3.2.2\text{-}4)$$

which, when constant power number is assumed, results in:

(D << η)

$$\frac{D_{max}}{L} = A_{25}We^{-1}\,Re^{1/2} \qquad (3.3.2.2\text{-}5)$$

According to Bourne and Baldyga (1994), this equation has a stronger physical basis than equation 3.3.2.1-6, and is therefore the recommended one to use in the viscous sub-range. However, the definitive proof is its ability to fit drop size data.

To extend this model to viscous drops a form for $\Phi(\mu_d/\mu_c)$ must be assumed. Rearranging equation 3.3.2.2-2, the following expression is obtained:

$$\mu_c\frac{\partial v}{\partial r} = A_{23}\frac{\sigma}{D_{max}} \qquad (3.3.2.2\text{-}6)$$

It's easily recognized that $\mu_c(\partial v/\partial r)$ is τ_c, by assuming that the disruptive continuous-phase stresses are predominantly viscous and simply applying Newton's law of viscosity, and that σ/D_{max} is proportional to τ_s (equation 3.3.1-4) . Therefore, choosing $\Phi(\mu_d/\mu_c) \approx$

$(1+\tau_d/\tau_s)$ and substituting it in equation 3.3.2.2-1, results in the recovery of equation 3.3.1-6. Assuming that the expression used thus far for τ_d (equation 3.3.1-5) is still valid for viscous stresses in the continuous phase and invoking again equation 3.3.2.2-3, the following equation is obtained:

$$\left(\mu_c\rho_c\varepsilon\right)^{1/2} = A_{26}\frac{\sigma}{D_{max}}\left[1 + A_{27}\frac{\mu_d}{\sigma}\sqrt{\frac{\left(\mu_c\rho_c\varepsilon\right)^{1/2}}{\rho_d}}\right] \qquad (3.3.2.2\text{-}7)$$

Solving for D_{max}:

$$D_{max} = A_{26}\frac{\sigma}{\left(\mu_c\rho_c\right)^{1/2}}\varepsilon^{-1/2}\left[1 + A_{27}\frac{\mu_d}{\sigma}\frac{\left(\mu_c\rho_c\right)^{1/4}}{\rho_d^{1/2}}\varepsilon^{1/4}\right] \qquad (3.3.2.2\text{-}8)$$

and, finally, assuming that the Power number is constant:

(D << η)
$$\frac{D_{max}}{L} = A_{28}\,We^{-1}\,Re^{1/2}\left[1 + A_{29}\,Vi\,Re^{-1/4}\right] \qquad (3.3.2.2\text{-}9)$$

This is the expression for the mechanistic model for viscous drop breakup in the viscous sub-range, assuming viscous stresses are the predominant disruptive stresses. For highly viscous drops, or a vanishingly small τ_s, equation 3.3.2.2-8 reduces to:

$$D_{max} = A_{30}\frac{\mu_d}{\sqrt{\rho_d}\left(\mu_c\rho_c\right)^{1/4}}\varepsilon^{-1/4} \qquad (3.3.2.2\text{-}10)$$

and its equivalent for the constant Power number case is:

(D << η)
$$\frac{D_{max}}{L} = A_{31}\left(\frac{\mu_d}{\mu_c}\right)\left(\frac{\rho_c}{\rho_d}\right)^{1/2} Re^{-3/4} \qquad (3.3.2.2\text{-}11)$$

The models derived in the previous sections (equations 3.3.1-12, 3.3.2.1-5, and 3.3.2.2-9) are from now on to be called “linear” models, due to the fact that they all have the general form $D_{max}/L = f(We)[1+f(Vi)]^n$. Note that the scaling of the maximum drop diameter with the Weber and Viscosity numbers, as well as with the Reynolds number

when it applies, is different depending on the nature assumed for the deforming stresses and on the turbulent sub-range. These differences allow the models to be compared against experimentally obtained values of D_{max} to determine which one – and therefore which set of physical conditions – best captures the trends observed in the data.

The maximum stable diameter in a liquid-liquid dispersion is directly proportional to the Sauter mean diameter of the drop size distribution (D_{32}). This fact has been demonstrated for both, viscous and inviscid dispersed phases, by Sprow (1967), Brown and Pitt (1972), and Calabrese, Chang, and Dang (1986), among others. Consequently, all the models derived in this and the previous sections are equally valid for D_{32}, as long as the appropriate numerical values are used for the empirical constants.

3.3.3. Alternative Mechanistic Models

The models derived in the previous section are based on a simple stress balance (equation 3.3.1-6) and assume that the drop will break as long as the disruptive stress (τ_c) is larger than the sum of the restoring stresses ($\tau_s + \tau_d$). They do not take into account the duration of the deforming stress. In a turbulent flow field, stresses are produced by the eddies in the vicinity of the drop, and eddies have a finite duration. This is of greater concern in the case of viscous drops. Their considerable internal viscous stresses resist deformation and the amount of time required to reach the drop's critical deformation. Therefore, even if τ_c is large enough in magnitude to overcome τ_s and τ_d, if it is not imposed for sufficient time, the drop may not break. One technique that several authors (Arai *et al.* 1977; Lagisetty *et al.* 1986; Clark 1988a; Das 1996) have used to account for the duration of the applied stress is to represent the deformation process with a Kelvin/Voigt element. A Kelvin/Voigt element is the combination of a Hookean spring

and a Newtonian dashpot in parallel (Figure 3.3.3-1). Both the Hookean spring and the Newtonian dashpot are fundamental rheological bodies, rather abstract concepts which have been formulated in order to describe the rheological behavior of real materials (Sobotka 1984). By combining the models of fundamental bodies, more complex rheological models are obtained for expressing the rheological behavior of material to any degree of accuracy.

The spring is the representation of the Hookean elastic solid, which is characterized by a linear stress-strain relation: the applied stress is equal to the strain multiplied by a constant elastic modulus. The Newtonian viscous liquid is represented by a dashpot, a cylinder filled with a viscous liquid in which a piston is loosely fitted. The liquid flowing around the piston (or through holes in it) offers a resistance to the applied stress proportional to the fluid's viscosity and the rate of strain. The Kelvin/Voigt element is, as already mentioned, a spring and a dashpot connected in parallel. In this configuration, the stress applied on the element is counteracted, simultaneously, by the

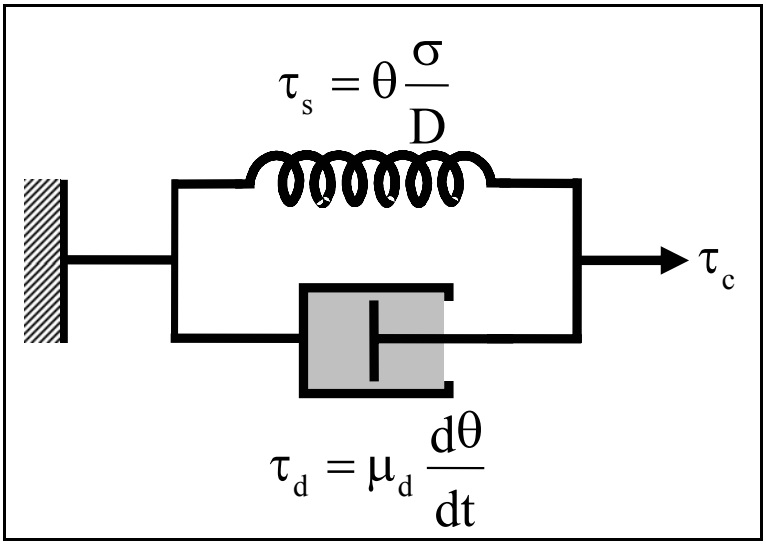

Figure 3.3.3- 1. Graphic representation of the Kelvin/Voigt element. The spring represents the "elastic" restorative force and the dashpot the "viscous" dissipative force.

spring and the dashpot and is, therefore, equal to the sum of the individual component's stresses. In the case of a deforming viscous drop, the applied stress would be τ_c, the spring's elastic modulus is the ratio of the interfacial tension to the drop diameter, and the strain is measured by the drop's deformation. Therefore, the mathematical representation of the element is (Das 1996):

$$\frac{\sigma}{D}\theta + \mu_d \frac{d\theta}{dt} = \tau_c \qquad (3.3.3\text{-}1)$$

where θ is the dimensionless deformation. This is the drop's deformation (usually measured as some sort of ratio between the major and minor axes of the deformed, elliptically shaped drop) divided by the critical deformation (the value of this deformation at which the drop breaks). By using this dimensionless deformation, the actual values of the drop deformation and critical deformation, as well as the method by which they are determined (axes ratio, critical capillary number, critical Weber number, etc), are not required. What's important is that the drop will break at $\theta = 1$, any value lower than 1 will result in the drop being returned to its spherical shape ($\theta = 0$) when the stress subsides.

Solving equation 3.3.3-1, with the initial condition $\theta(t = 0) = 0$, yields:

$$\theta = \frac{\tau_c D}{\sigma}\left[1 - \exp\left(-\frac{\sigma}{\mu_d D}t\right)\right] \qquad (3.3.3\text{-}2)$$

For the drop to break, θ doesn't only have to reach unity, but it has to do so within the lifetime of the eddy responsible for the stress that is causing the drop to deform. Thus, the maximum stable diameter is attained when these two times are equal (Das 1996):

$$t(\theta = 1) = t_{eddy} \qquad (3.3.3\text{-}3)$$

Therefore, the equation that must be solved to determine D_{max} is:

$$1 = \frac{\tau_c D_{max}}{\sigma}\left[1 - \exp\left(-\frac{\sigma}{\mu_d D_{max}} t_{eddy}\right)\right] \qquad (3.3.3\text{-}4)$$

The exact expression of this model will then depend on the expressions for τ_c and t_{eddy}, which, in turn, depend on whether the drop is in the inertial or viscous sub-range. In the latter case, it also depends on whether τ_c is assumed to be inertial or viscous in nature.

3.3.3.1. Inertial Sub-Range

For drops in the inertial sub-range ($L >> D >> \eta$), the continuous phase stress is given by equation 3.3.1-3. The eddy lifetime is defined as the characteristic period of velocity fluctuation of an eddy of size D (Coulaloglou and Tavlarides 1977):

$$t_{eddy} = \frac{D}{\sqrt{u'^2}} \sim \frac{D^{2/3}}{\varepsilon^{1/3}} \qquad (3.3.3.1\text{-}1)$$

where u' is defined by equations 3.3.1-2 and 3.2.1-4. The Kelvin/Voigt element-based model (or S&D model, for spring and dashpot) for the inertial sub-range is, in consequence:

$$D_{max} = A_{32}\left(\frac{\sigma}{\rho_c}\right)^{3/5} \varepsilon^{-2/5}\left[1 - \exp\left(-A_{33}\frac{\sigma}{\mu_d}\varepsilon^{-1/3} D_{max}^{-1/3}\right)\right]^{-3/5} \qquad (3.3.3.1\text{-}2)$$

Again, assuming constant Power number and normalizing drop size with the impeller diameter:

$$(L >> D >> \eta)\ \frac{D_{max}}{L} = A_{34} We^{-3/5}\left[1 - \exp\left(-A_{35} Vi'^{-1}\left(\frac{D_{max}}{L}\right)^{-1/3}\right)\right]^{-3/5} \qquad (3.3.3.1\text{-}3)$$

where Vi' is a modified viscosity number:

$$Vi' = \frac{\mu_d N L}{\sigma} \qquad (3.3.3.1\text{-}4)$$

3.3.3.2. Viscous Sub-Range, Inertial Stresses

In the viscous sub-range, assuming the continuous phase stresses to be inertial ($D < \eta$), the eddy life timescale is also given by $t_{eddy} = D/(u'^2)^{1/2}$, but now u'^2 is given by equation 3.3.2.1-1:

$$t_{eddy} \sim \sqrt{\frac{\mu_c}{\rho_c}}\varepsilon^{-1/2} \tag{3.3.3.2-1}$$

For these conditions, τ_c is given by equation 3.3.2.1-2, and the following model equation results:

$$D_{max} = A_{36}\left(\frac{\mu_c \sigma}{\rho_c^2}\right)^{1/3}\varepsilon^{-1/3}\left[1-\exp\left(-A_{37}\frac{\sigma}{\mu_d}\left(\frac{\mu_c}{\rho_c}\right)^{1/2}\varepsilon^{-1/2}D_{max}^{-1}\right)\right]^{-1/3} \tag{3.3.3.2-2}$$

or, for constant Power number:

$$(D < \eta) \qquad \frac{D_{max}}{L} = A_{38}\left(We\,Re\right)^{-1/3}\left[1-\exp\left(-A_{39}Vi'^{-1}\,Re^{-1/2}\left(\frac{D_{max}}{L}\right)^{-1}\right)\right]^{-1/3} \tag{3.3.3.2-3}$$

3.3.3.3. Viscous Sub-Range, Viscous Stresses

If the disruptive stresses are assumed to be viscous, then $\tau_c = \mu_c(\partial v/\partial r)$, with the velocity gradient given by equation 3.3.2.2-3. In this case, the relevant velocity scale is the Kolmogorov velocity scale:

$$u_K = \frac{\eta}{t_K} = \left(\nu_c \varepsilon\right)^{1/4} \tag{3.3.3.3-1}$$

Hence, the eddy time scale is proportional to the ratio D/u_K:

$$t_{eddy} \sim \left(\frac{\rho_c}{\mu_c}\right)^{1/4} D\,\varepsilon^{-1/4} \tag{3.3.3.3-2}$$

This results in the model for the viscous sub-range, viscous stresses being given by:

$$D_{max} = A_{40} \frac{\sigma}{(\mu_c \rho_c)^{1/2}} \varepsilon^{-1/2} \left[1 - \exp\left(- A_{41} \frac{\sigma}{\mu_d} \left(\frac{\rho_c}{\mu_c} \right)^{1/4} \varepsilon^{-1/4} \right) \right]^{-1} \qquad (3.3.3.3\text{-}3)$$

and, for constant Power number:

(D << η)
$$\frac{D_{max}}{L} = A_{42} We^{-1} Re^{1/2} \left[1 - \exp\left(- A_{43} Vi'^{-1} Re^{1/4} \right) \right]^{-1} \qquad (3.3.3.3\text{-}4)$$

3.3.3.4. Comments

The models derived in these sub-sections will be henceforth called spring and dashpot models (equations 3.3.3.1-3, 3.3.3.2-3, and 3.3.3.3-4). They have an exponential general form: $D_{max}/L = f(We)[1-\exp(f(Vi'))]^n$, as opposed to the previously defined linear models. Despite this mathematical difference, there is a striking resemblance between the two kinds of models. In all three cases (the inertial sub-range and the two viscous sub-range ones), the function of the Weber number is the same for both linear and S&D models. This means that in the inviscid drop case, both types of models reduce to the same expressions, namely equations 3.3.1-15, 3.3.2.1-6, and 3.3.2.2-5. Furthermore, in the highly viscous drop case ($\mu_d \rightarrow \infty$ or vanishingly small τ_s) the expressions resultants from the S&D models are:

(L >> D >> η)
$$\frac{D_{max}}{L} = A_{44} \left(\frac{\mu_d}{\mu_c} \right)^{3/4} Re^{-3/4} \qquad (3.3.3.4\text{-}1)$$

for the inertial sub-range,

(D < η)
$$\frac{D_{max}}{L} = A_{45} \left(\frac{\mu_d}{\mu_c} \right)^{1/2} Re^{-3/4} \qquad (3.3.3.4\text{-}2)$$

for the viscous sub-range, inertial stresses,

(D << η)

$$\frac{D_{max}}{L} = A_{46}\left(\frac{\mu_d}{\mu_c}\right)Re^{-3/4} \qquad (3.3.3.4\text{-}3)$$

for the viscous sub-range, viscous stresses. These equations are identical to those obtained from the linear models (equations 3.3.1-17, 3.3.2.1-9, and 3.3.2.2-11), except for the density ratios (which are the least significant components of the equations, considering that in liquid-liquid systems the densities are always of comparable magnitude).

It should be noted that several authors have proposed modified versions of the spring and dashpot model. Lagisetty *et al.* (1986) proposed that τ_s should not be proportional to θ, but to θ(1-θ). This is based on the argument that the surface stress should go through a maximum during the drop's deformation. That is, towards the end of the deformation process, the interfacial tension actually helps to shape the "yet unborn" daughter drops and, therefore, no longer opposes the deformation. This model was later expanded to include breakage in elongational flows (Gandhi and Kumar 1990), asymmetric binary breakage (Nambiar *et al.* 1992), the circulation of drops throughout the tank (Nambiar *et al.* 1994), and even the effect of surfactants (Koshy, Das, and Kumar 1988). Another significant modification of the model was made by Clark (1988a,b), who included an additional term in the stress balance to include the inertial force due to the acceleration of the drop's mass during elongation. All of these modifications result in much more mathematically complex expressions, which are not always better at correlating experimental data. Therefore, they will not be included in this study for purposes other than bibliographical reference.

3.3.4. Mechanistic Models in Rotor-Stator Mixers

The models developed so far are based on theories and assumptions that are considered valid for conventional stirred tanks. Padron (2001) showed that, despite the fact that in rotor-stator mixers there are several possible characteristic lengths, there is no benefit to using definitions for the Reynolds and Power numbers different than those used for stirred tanks. Furthermore, it was shown that the behavior of the Power number with respect to the Reynolds number resembles that of stirred tanks, and that the values of the Power number, albeit lower than those of impellers, are of the same order of magnitude. All this, in addition to the fact that rotor-stator devices create turbulence intense enough to warrant the local isotropy assumption, indicate that the mechanistic models should also apply to rotor-stator mixers, as long as the empirical constants are properly adjusted.

Francis (1999) obtained experimental data for drop size in dilute, inviscid dispersions in a batch rotor-stator mixer. He correlated his data to the three previously presented inviscid models (equations 3.3.1-15, 3.3.2.1-6, and 3.3.2.2-5) as well as to other models. One of the additional models is the one originally derived by Chen and Middleman (1967) for the viscous sub-range, based on the expression for the energy spectrum given by equation 3.2.1-5:

$$\frac{D_{max}}{L} = A_{47}\left(We\,Re^{4}\right)^{-1/7} \qquad (3.3.4\text{-}1)$$

The other is based on breakage due to shear in the rotor-stator gap:

$$\frac{D_{max}}{\delta} = A_{48}\,We^{-1}\,Re \qquad (3.3.4\text{-}2)$$

where δ is the rotor-stator gap width. Neither of these two models was found to correlate the data adequately. In fact, it was observed that the drop size decreased when the rotor-

stator gap width was increased, for fixed rotor speed and physical conditions, which is opposite to what equation 3.3.4-1 predicts. The models that were found to correlate the data best were the inertial sub-range model (equation 3.3.1-15) and the viscous sub-range, viscous stresses model (equation 3.3.2.2-5), depending on whether the data is fit through rotor speed or power dissipation, respectively. The reason for this ambiguity is probably the fact that the drop diameters are very near the Kolmogorov scale, and, therefore, no single breakage mechanism is dominant. An important finding of Francis's study is that the rotor-stator mixer generated a high population of small droplets, producing a log-normal drop size distribution, as opposed to the normally distributed ones previously found for stirred tanks (Chen and Middleman 1967; Calabrese, Chang, and Dang 1986; Calabrese, Wang, and Bryner 1986; Wang and Calabrese 1986).

Phongikaroon (2001) continued the work of Francis by studying the effect of the continuous phase viscosity. In conclusion, it was found that the drop size increases with μ_c, which is consistent with the viscous sub-range, viscous stresses model. However, the data were almost as well correlated by the inertial sub-range model. This strengthens the conclusion that no single mechanism is responsible for drop breakup but, rather, a combination of mechanisms. Phongikaroon (2001) also extended his study to include the effect of dispersed phase viscosity. He analyzed data corresponding to silicone oil dispersions in water, methanol, and methanol/water solutions, which allowed varying systematically μ_d and interfacial tension. These experiments were carried out in the same Silverson mixer that was used in the present study. The main findings of this work were that the drop size increases with dispersed phase viscosity and this effect intensifies as the interfacial tension decreases. For a fixed value of dispersed phase viscosity, the drop size

was found to decrease with interfacial tension. Similar trends had been found by Wang and Calabrese (1986) for stirred tanks with Rushton turbines.

Like Francis, Phongikaroon found that the drop size followed a log-normal distribution in volume, except for the highest viscosity oil (500 cP) which produced clearly bimodal distributions. With respect to the mechanistic models, Phongikaroon found that both the inertial sub-range model (equation 3.3.1-12) and the viscous sub-range, inertial stresses model (equation 3.3.2.1-5), fit the data acceptably. The former did a better job correlating the bigger drops and the latter, the smaller drops, as it would be expected. This supports the idea of a combination of breakage mechanisms. The values of the empirical constants obtained by Phongikaroon for the inertial sub-range model, however, differ significantly from those obtained by Calabrese *et al.* for stirred tanks, using the same model. The values of A_7 and A_8 (see equation 3.3.1-12) reported for the rotor-stator mixer are 0.015 and 14.8, respectively, while those for stirred tanks are 0.054 and 4.42. This means that the rotor-stator produces smaller drops for a fixed μ_d and that the effect of the dispersed phase viscosity on drop size is less pronounced in the rotor-stator device.

3.4 Drop Breakup Time Scales in Turbulent Flow

As a viscous drop is approached by an eddy, it will begin to deform. The duration of this deformation has already been defined as the eddy lifetime (equations 3.3.3.1-1, 3.3.3.2-1, and 3.3.3.3-2, for the inertial sub-range, the viscous sub-range assuming inertial stresses, and the viscous sub-range assuming viscous stresses, respectively). However, for a given turbulent stress τ_c, the higher the viscosity of the dispersed phase,

the longer it will take to deform the drop due to its resistance to flow. The drop's deformation timescale will be given by (Walstra and Smulders 1998):

$$t_{dd} = \frac{\mu_d}{\tau_c} \tag{3.4-1}$$

Consequently, the expressions for this timescale in the different turbulent regimes are:

$$(L >> D >> \eta) \qquad t_{dd} = \frac{\mu_d}{\rho_c} \varepsilon^{-2/3} D^{-2/3} \tag{3.4-2}$$

for the inertial sub-range,

$$(D < \eta) \qquad t_{dd} = \frac{\mu_d \mu_c}{\rho_c^2} \varepsilon^{-1} D^{-2} \tag{3.4-3}$$

for the viscous sub-range, inertial stresses, and

$$(D << \eta) \qquad t_{dd} = \frac{\mu_d}{\sqrt{\mu_c \rho_c}} \varepsilon^{-1/2} \tag{3.4-4}$$

for the viscous sub-range, viscous stresses.

In section 3.3.3 it was stated that for a drop to break it has to achieve its critical deformation within the lifetime of a single eddy interaction. Yet, in some cases, especially for high dispersed phase viscosity and moderate to high energy dissipation (ε), the drop deformation timescale is clearly greater (even orders of magnitude) than the corresponding eddy lifetime. The aforementioned condition for breakage, however, is based on the assumption that if the drop does not break in the eddy lifetime, it will return to its original spherical shape before being affected by another eddy. When the drop's viscosity is negligible, this is likely to be the case, but for viscous drops, this may not be the case. As the deformation timescale increases, so does the time required by the drop to relax back to the spherical shape, since this process is also hindered by the high viscosity.

Therefore, the drop could still be somewhat stretched when it starts to feel the effects of the next eddy. Some authors have even suggested that the drop is not broken up by one eddy, but by a succession of eddies passing at regular intervals, causing the drop to oscillate and then break (Walstra 1983). Whatever the case may be, the fact is that viscous drop breakage may be better scaled by t_{dd} than by t_{eddy} and, therefore, both time scales must be taken into account when analyzing experimental data.

3.5 Summary

In this chapter, a brief introduction to turbulent flows was given. The concept of local isotropy and its universal characteristics were explained based on Kolmogorov's theory. A set of mechanistic models for breakage of viscous drops in turbulent flows was derived, based on local isotropy considerations. Tables 3.5-1 and 3.5-2 presents an summary of these equations for the linear and spring and dashpot models, respectively. These equations were derived assuming that the physical properties of the fluids remain constant. They will be modified in subsequent chapters to account for dynamic phenomena related to the presence of surfactants in the system.

Table 3.5- 1. Summary of linear mechanistic models for drop breakage in turbulent flows

Model		In terms of ε	Constant P_0
Inertial Sub-Range (L << D << η)	Effect of σ and μ_d	$D_{max} = A_3\left(\frac{\sigma}{\rho_c}\right)^{3/5}\varepsilon^{-2/5}\left[1+A_4\frac{\mu_d}{\sigma}\sqrt{\frac{\rho_c}{\rho_d}}\varepsilon^{1/3}D_{max}^{1/3}\right]^{3/5}$	$\frac{D_{max}}{L} = A_7 We^{-3/5}\left[1+A_8 Vi\left(\frac{D_{max}}{L}\right)^{1/3}\right]^{3/5}$
	Inviscid limit ($\tau_s >> \tau_d$)	$D_{max} = A_9\left(\frac{\sigma}{\rho_c}\right)^{3/5}\varepsilon^{-2/5}$	$\frac{D_{max}}{L} = A_{10} We^{-3/5}$
	Viscous limit ($\tau_s << \tau_d$)	$D_{max} = A_{11}\mu_d^{3/4}(\rho_c\rho_d)^{-3/8}\varepsilon^{-1/4}$	$\frac{D_{max}}{L} = A_{12}\left(\frac{\mu_d}{\mu_c}\right)^{3/4}\left(\frac{\rho_c}{\rho_d}\right)^{3/8} Re^{-3/4}$
Viscous Sub-Range — Inertial Stresses (D > η)	Effect of σ and μ_d	$D_{max} = A_{15}\left(\frac{\sigma\mu_c}{\rho_c^2}\right)^{1/3}\varepsilon^{-1/3}\left[1+A_{16}\frac{\mu_d\rho_c}{\sigma\sqrt{\rho_d\mu_c}}\varepsilon^{1/2}D_{max}\right]^{1/3}$	$\frac{D_{max}}{L} = A_{17}(WeRe)^{-1/3}\left[1+A_{18}ViRe^{1/2}\frac{D_{max}}{L}\right]^{1/3}$
	Inviscid limit ($\tau_s >> \tau_d$)	$D_{max} = A_{20}\left(\frac{\sigma\mu_c}{\rho_c^2}\right)^{1/3}\varepsilon^{-1/3}$	$\frac{D_{max}}{L} = A_{19}(WeRe)^{-1/3}$
	Viscous limit ($\tau_s << \tau_d$)	$D_{max} = A_{21}\left(\frac{\mu_d^2\mu_c}{\rho_c^2\rho_d}\right)^{1/4}\varepsilon^{-1/4}$	$\frac{D_{max}}{L} = A_{22}\left(\frac{\mu_d}{\mu_c}\right)^{1/2}\left(\frac{\rho_c}{\rho_d}\right)^{1/4} Re^{-3/4}$
Viscous Sub-Range — Viscous Stresses (D < η)	Effect of σ and μ_d	$D_{max} = A_{26}\frac{\sigma}{(\mu_c\rho_c)^{1/2}}\varepsilon^{-1/2}\left[1+A_{27}\frac{\mu_d}{\sigma}\left(\frac{\mu_c\rho_c}{\rho_d^2}\right)^{1/4}\varepsilon^{1/4}\right]$	$\frac{D_{max}}{L} = A_{28} We^{-1} Re^{1/2}\left[1+A_{29}ViRe^{-1/4}\right]$
	Inviscid limit ($\tau_s >> \tau_d$)	$D_{max} = A_{24}\frac{\sigma}{(\mu_c\rho_c)^{1/2}}\varepsilon^{-1/2}$	$\frac{D_{max}}{L} = A_{25} We^{-1} Re^{1/2}$
	Viscous limit ($\tau_s << \tau_d$)	$D_{max} = A_{30}\frac{\mu_d}{\sqrt{\rho_d}(\mu_c\rho_c)^{1/4}}\varepsilon^{-1/4}$	$\frac{D_{max}}{L} = A_{31}\left(\frac{\mu_d}{\mu_c}\right)\left(\frac{\rho_c}{\rho_d}\right)^{1/2} Re^{-3/4}$

Table 3.5- 2. Summary of spring and dashpot mechanistic models for drop breakage in turbulent flows

Model		In terms of ε	Constant P_0
Inertial Sub-Range (L >> D >> η)	σ and μ_d	$D_{max} = A_{32}\left(\frac{\sigma}{\rho_c}\right)^{3/5}\varepsilon^{-2/5}\left[1-\exp\left(-A_{33}\frac{\sigma}{\mu_d}\varepsilon^{-1/3}D_{max}^{-1/3}\right)\right]^{-3/5}$	$\frac{D_{max}}{L} = A_{34}We^{-3/5}\left[1-\exp\left(-A_{35}Vi'^{-1}\left(\frac{D_{max}}{L}\right)^{-1/3}\right)\right]^{-3/5}$
	$\mu_d \to 0$ ($\tau_s >> \tau_d$)	$D_{max} = A_9\left(\frac{\sigma}{\rho_c}\right)^{3/5}\varepsilon^{-2/5}$	$\frac{D_{max}}{L} = A_{10}We^{-3/5}$
	$\mu_d \to \infty$ ($\tau_s << \tau_d$)	$D_{max} = A_{49}\left(\frac{\mu_d}{\rho_c}\right)^{3/4}\varepsilon^{-1/4}$	$\frac{D_{max}}{L} = A_{44}\left(\frac{\mu_d}{\mu_c}\right)^{3/4}Re^{-3/4}$
Viscous Sub-Range Inertial Str. (D<η)	σ and μ_d	$D_{max} = A_{36}\left(\frac{\sigma\mu_c}{\rho_c^2}\right)^{1/3}\varepsilon^{-1/3}\left[1-\exp\left(-A_{37}\frac{\sigma}{\mu_d}\left(\frac{\mu_c}{\rho_c}\right)^{1/2}\varepsilon^{-1/2}D_{max}^{-1}\right)\right]^{-1/3}$	$\frac{D_{max}}{L} = A_{38}(WeRe)^{-1/3}\left[1-\exp\left(-A_{39}Vi'^{-1}Re^{-1/2}\left(\frac{D_{max}}{L}\right)^{-1}\right)\right]^{-1/3}$
	$\mu_d \to 0$ ($\tau_s >> \tau_d$)	$D_{max} = A_{20}\left(\frac{\sigma\mu_c}{\rho_c^2}\right)^{1/3}\varepsilon^{-1/3}$	$\frac{D_{max}}{L} = A_{19}(WeRe)^{-1/3}$
	$\mu_d \to \infty$ ($\tau_s << \tau_d$)	$D_{max} = A_{50}\left(\frac{\mu_d^2\mu_c}{\rho_c^3}\right)^{1/4}\varepsilon^{-1/4}$	$\frac{D_{max}}{L} = A_{45}\left(\frac{\mu_d}{\mu_c}\right)^{1/2}Re^{-3/4}$
Viscous Str. (D<<η)	σ and μ_d	$D_{max} = A_{40}\frac{\sigma}{(\mu_c\rho_c)^{1/2}}\varepsilon^{-1/2}\left[1-\exp\left(-A_{41}\frac{\sigma}{\mu_d}\left(\frac{\rho_c}{\mu_c}\right)^{1/4}\varepsilon^{-1/4}\right)\right]^{-1}$	$\frac{D_{max}}{L} = A_{42}We^{-1}Re^{1/2}\left[1-\exp\left(-A_{43}Vi'^{-1}Re^{1/4}\right)\right]^{-1}$
	$\mu_d \to 0$ ($\tau_s >> \tau_d$)	$D_{max} = A_{24}\frac{\sigma}{(\mu_c\rho_c)^{1/2}}\varepsilon^{-1/2}$	$\frac{D_{max}}{L} = A_{25}We^{-1}Re^{1/2}$
	$\mu_d \to \infty$ ($\tau_s << \tau_d$)	$D_{max} = A_{51}\mu_d\left(\rho_c^3\mu_c\right)^{-1/4}\varepsilon^{-1/4}$	$\frac{D_{max}}{L} = A_{46}\left(\frac{\mu_d}{\mu_c}\right)Re^{-3/4}$

CHAPTER 4. SURFACTANTS AND INTERFACIAL PHENOMENA

Surfactants are used in a wide variety of industrial and technological applications. In many cases they are called by different names, such as: emulsifiers, demulsifiers, stabilizers, compatibilizers, dispersing agents, wetting agents, detergents, etc. Despite their many different uses, they all have one characteristic in common: a dual chemical nature that compels them to migrate to interfaces, changing system properties and creating new ones in the process. The consequences of the presence of surfactants in a fluid system affect several of its properties, both, in their equilibrium values and in their dynamic response to changes, as well as the physical and rheological properties of the system's interfaces.

The focus of this chapter will be on the diverse effects of surfactants on the interfacial properties of liquid-liquid systems. The concepts of surface and interfacial tension will be first explained, since it is mainly through these properties that surfactants affect the system. Then, the behavior of surfactants in solution will be examined, including equilibrium and dynamic aspects, as well as their influence on interfacial rheology. The physicochemical hydrodynamics of liquid drops in surfactant solutions will then be briefly considered. Finally, the chapter closes with a discussion of relevant literature on the effect of surfactants on drop deformation and breakage in liquid-liquid systems.

4.1. Surface and Interfacial Tension

The terms *surface tension* and *interfacial tension* are often used interchangeably. In fact, they both refer to the same property. Strictly speaking, however, the word surface is normally reserved for an interface between a condensed phase (solid or liquid) and a gas phase, most commonly air (Walstra 2003), whereas the word interfacial is the generic term. An interface is a region in which the properties vary from those of one phase to those of the adjoining phase (Hiemenz and Rajagopalan 1997). These transitions occur over finite distances at molecular scale, and therefore, all interfaces have a finite thickness. At larger scales, this thickness may be regarded as negligibly small and the interface may be assumed to have area, but not volume.

The surface (or interfacial) tension is a property of the interface and is responsible for a multitude of interfacial behaviors, such as the tendency of bubbles and drops to assume spherical shape, the beading of drops on solid surfaces, and the rise of liquids through capillaries (Edwards, Brenner, and Wasan 1991). It is a contract force that tends to shrink the surface and operates around its perimeter (Hiemenz and Rajagopalan 1997). This may be illustrated by means of the classic wire loop example. Figure 4.1-1 shows a loop made of thin wire with one movable side on which a liquid film has been formed by dipping the loop in said liquid. The surface tension of the film will slide the movable side inwards to minimize the film's area (assuming that this movement is frictionless), unless a force is applied to it in the opposite direction. At equilibrium (constant film area), the surface tension will be equal to the applied force divided by the length along which it acts:

$$\sigma = \frac{F}{2\ell} \tag{4.1-1}$$

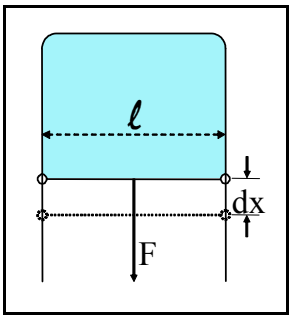

Figure 4.1- 1. Wire loop with movable side on which a liquid film was created.

where σ is the surface tension, F is the magnitude of the force, ℓ is the length of the movable wire, and the factor of 2 comes from the fact that the film has two surfaces (one on each side of the wire loop). Furthermore, if the applied force is infinitesimally larger that that required for equilibrium, the wire will be displaced a distance dx (see Figure 4.1-1). Thus, the work done by this force is:

$$\text{Work} = Fdx = \sigma 2\ell dx = \sigma dA \qquad (4.1\text{-}2)$$

where dA is the differential area created by stretching the film (again considering that the film has two sides). Therefore, the surface tension may also be defined as the work (or energy) per unit area required to create a new surface. At constant pressure and temperature, this work contributes to the differential Gibbs free energy of the system (Work = dG), so, the thermodynamic expression for surface tension is given by (Evans and Wennerström 1999):

$$\sigma = \left(\frac{\partial G}{\partial A}\right)_{T,P} \qquad (4.1\text{-}3)$$

Form a molecular point of view, surface tension can be seen as a manifestation of the differences between the energies of molecules located at the interface and in the bulk of the phase (Evans and Wennerström 1999). The energy of the molecules in the bulk is

lower because they can interact with each other; sometimes even create weak bonds between them (as in the case of water). On the other hand, at an interface, molecules are not surrounded by as many compatible molecules and, therefore, they are at a higher energetic level. Hence, molecules prefer to stay in the bulk phase to minimize their energy and work must be done to move molecules from the bulk to the surface, i.e. create new interface.

Surface tension operates on all phase boundaries, however its effect are more evident for deformable liquid interfaces (Hiemenz and Rajagopalan 1997). To achieve mechanical equilibrium on a liquid film, an equal and opposite force must be applied, as exemplified with the wire loop. In the case of a curved liquid interface, this force is due to the pressure difference operating across said interface:

$$\Delta P = \sigma\left(\frac{1}{R_1} + \frac{1}{R_2}\right) = 2\sigma H \qquad (4.1\text{-}4)$$

where H is the mean curvature of the surface. Equation 4.1-4 is known as the Young-Laplace equation and was independently derived by Young in 1805 and by Laplace in 1806. This equation is the base for several experimental methods for measuring surface and interfacial tensions, including the capillary rise method and the pendant drop method, of which the latter is explained in detail in chapter 5. For a spherical interface, such as a bubble or drop, the Young-Laplace equation reduces to $\Delta P=\sigma/2R$ ($R=R_1=R_2$), and for a planar interface, this indicates that $\Delta P=0$ ($R_1=R_2=\infty$).

4.2. Surface Active Agents

A surface active agent, or surfactant, for short, is a substance whose molecules are amphiphilic, which means that a part of them is hydrophilic (has affinity for water or

aqueous phases) and the other part is lipophilic (has affinity for oily or organic phases). This combination of antagonist affinities in the same molecule is the dual chemical nature that confers the surfactant a specific behavior when in solution. Figure 4.2-1 shows the graphic representation of a generic surfactant molecule. Note that this is just a conventionalism, surfactant molecules come in different shapes, some of which conform to this representation, but not all. What they all do have in common is a clear differentiation of their hydrophilic and lipophilic (often called hydrophobic) parts.

There are many kinds of surfactants, depending on the nature of the hydrophilic and lipophilic groups. The lipophilic or hydrophobic group is usually a long chained and/or highly branched hydrocarbon radical, normally in the range $C_8 - C_{20}$ (8 to 20 carbon atoms). These radicals frequently come from natural fatty acids, paraffins, olefins, or alcohols. Still, they may contain other structures such as alkylbenzenes, alkylnaphtalenes, partially or completely fluorinated fluorocarbons, polydimethylsiloxanes (silicone oil adducts), or high-molecular weight polyoxypropylene chains. The nature of the hydrophilic group can also be very varied. In fact, the most common surfactant classification system is based on it. According to the nature of the hydrophile, surfactants can be divided into ionics and nonionics, depending on whether or not they dissociate (ionize) in aqueous solution. Ionic surfactants can be further sub-classified into:

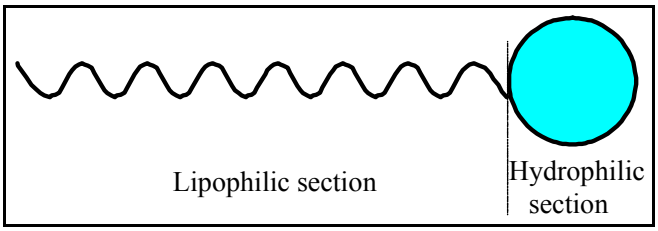

Figure 4.2- 1. Conventional representation of a generic surfactant molecule.

Anionic: the hydrophilic group acquires a negative charge (anion) when it is dissolved in water. Anionic hydrophilic groups include sulfates ($ROSO_3^-$), sulfonates (RSO_3^-), carboxylates ($RCOO^-$) and phosphates (RPO_4^-). This is the most common and oldest kind of surfactant known. Soaps are sodium or potassium fatty acid carboxylates and have been used by man for more than two thousand years. The single most studied surfactant, sodium dodecilsulfate (SDS), is a member of the sulfate esters family.

Cationic: the charge of the hydrophilic group is positive (cation). These are usually quaternary ammonium salts (R_4N^+) or derivatives of nitrogenated heterocyclic compounds. Cationic surfactants are less common and more expensive than anionic surfactants. Their economic importance has increased greatly in recent years, though, because many of them are biologically active and have proven to kill or inhibit growth of many microorganisms (Myers 1992).

Amphoteric: the hydrophile's charge can be either positive or negative depending on the pH of the solution, or it can have both charges simultaneously (these are also known as Zwitterionic surfactants). Compounds of this type include imidazoline derivatives, amino acid derivatives, and lecithins. Amphoteric surfactants represent 1% or less of the worldwide surfactant production (Myers 1992).

In the case of nonionic surfactants, the hydrophile has no charge but it is water soluble due to the presence of highly polar groups, such as polyoxyethylene ($(CH_2CH_2O)n$-H, where n is the number of ethylene oxide units), or polyols. All nonionic surfactants are synthetic, although many are derived from natural compounds such as fatty acids and sugars. They have the advantage over ionic surfactants that they are not as sensitive to the presence of electrolytes in the solution and to pH. Nonionic surfactants

include alcohol ethoxylates (alcohol adducts linked to chains of ethylene oxide of varying lengths), alkylphenol ethoxylates, polysorbates, and polyoxyethylene-polyoxypropylene block copolymers. The surfactants used in the present study, Tergitol™ TMN-6, Triton™ X-100, and Triton™ X-165, are all nonionic. The first one is an ethoxylated derivative of a highly branched alcohol, with a degree of ethoxylation of 8 (8 ethylene oxide units in its hydrophilic chain). Both Tritons are ethoxylated octylphenols with degrees of ethoxylation of 9-10 (X-100) and 16 (X-165). It must be kept in mind that, when talking about degrees of ethoxylation of commercial surfactants, the number is always an average. In reality, the surfactant sample is made up of a mixture of molecules with a broad distribution of hydrophilic chain lengths.

Another common way to classify surfactants is based on its *Hydrophilic-Lipophilic Balance*, or HLB. The concept of the HLB was first introduced by Griffin (1949) in a study aimed to reduce the amount of work involved in the selection of the appropriate emulsifier for a particular system. It was the first successful attempt to quantitatively correlate the surfactant's molecular structure with its ability to stabilize a given emulsion (Myers 1992). The HLB system consists on a set of empirical formulas by which a number, in the scale from 0 to 20, is assigned to the surfactant (Griffin 1954). Surfactants with a high HLB are considered mostly hydrophilic, while those with a low value are mostly lipophilic. These formulas were developed specifically for non-ionic surfactants used as emulsifiers. However, ionic surfactants can have their HLB value determined experimentally by comparison with nonionics, and applications other than emulsification have been related to the HLB scale. Table 4.2-1 shows the different HLB

Table 4.2- 1. HLB ranges and their applications (Myers 1992).

Range	Application
3 – 6	Water-in-Oil emulsion stabilizers
7 – 9	Wetting agents
8 – 18	Oil-in-Water emulsion stabilizers
3 – 15	Detergents
15 – 18	Solubilizers

ranges and their associated applications. The HLB scale is not exact; nevertheless, it has found extensive practical use in the selection of surfactants for specific applications.

4.3. Equilibrium Behavior of Surfactant Solutions

When a surfactant molecule is dissolved in water, the presence of the hydrophobic part of the molecule causes a distortion of the solvent structure, which increases the overall free energy of the system (Myers 1992). Driven by the need to minimize this energy, and given their amphiphilic nature, surfactant molecules will tend to move to and, subsequently, adsorb at the system's interfaces. This translates into less work being required to transport molecules to said interfaces, which, according to equation 4.1-3, decreases the system's interfacial tension. The presence of the hydrophilic part prevents the molecules from being completely expelled from the water and causes the molecules to orient themselves in such a way that the hydrophobic parts are directed away from it. This distinctive behavior is the main property of surfactants. It has numerous applications as well as many implications since it affects the system's equilibrium and dynamics, as will become evident from the discussion below.

The terms interfacial and surface tension has been used thus far to denote the system's *equilibrium* tension, which is its numeric value at the end of the adsorption process. As said before, surfactant molecules move to and, then adsorb at interfaces. The

overall process requires a finite amount of time. The terms *dynamic* interfacial and surface tension are used to refer to the variation of the property with time during the adsorption process (it is usually a curve of σ with respect to time). The shape and behavior of the σ(t) curve depends on the surfactant's adsorption dynamics, which is the subject of the later section (4.4).

4.3.1. Adsorption Equations

Before exploring the adsorption behavior of surfactants, general adsorption thermodynamics must be reviewed. The presence of an interface affects all the thermodynamic parameters of a system (Evans and Wennerström 1999). Assuming that the system can be divided into two phases, α and β, with an infinitesimally thin interface, s, dividing them, the total Gibbs energy of such system is:

$$G = G^{\alpha} + G^{\beta} + G^{s} \tag{4.3.1-1}$$

For the bulk phases:

$$G^{\alpha,\beta} = E^{\alpha,\beta} + PV^{\alpha,\beta} - TS^{\alpha,\beta} + \sum_i \mu_i^{\alpha,\beta} n_i^{\alpha,\beta} \tag{4.3.1-2}$$

and for the interface:

$$G^{s} = E^{s} + \sigma A - TS^{s} + \sum_i \mu_i^{s} n_i^{s} \tag{4.3.1-3}$$

where E is the internal energy, P is pressure, V is volume, T is Temperature, S is entropy, A is the interfacial area, σ is the interfacial tension, μ_i is the chemical potential of the i^{th} component, and n_i the number of moles of the i^{th} component. Substituting 4.3.2-2 and 4.3.1-3 into 4.3.1-1 and taking the total derivative:

$$dG = \sum_{\alpha\beta s} \left(dE + PdV + VdP - TdS - SdT + \sum_i \mu_i dn_i + \sum_i n_i d\mu_i \right) + Ad\sigma + \sigma dA \tag{4.3.1-4}$$

For a reversible process, recalling that, according to equation 4.1-2, σdA is equal to non-pressure-volume work, and employing well-known thermodynamic relationships, including the Gibbs-Dühem equation, this expression reduces to(Hiemenz and Rajagopalan 1997):

$$\sum_i n_i^s d\mu_i + A d\sigma = 0 \qquad (4.3.1\text{-}5)$$

This is the general form of the Gibbs adsorption isotherm. For a two-component system with one solvent (1) and one solute (2), equation 4.3.1-5 becomes:

$$-d\sigma = \frac{n_1^s}{A} d\mu_1 + \frac{n_2^s}{A} d\mu_2 \qquad (4.3.1\text{-}6)$$

the quantity n_i^s/A is called the surface excess concentration, an algebraic quantity that reflects concentration or depletion of a component at the interface (Evans and Wennerström 1999) and is represented by Γ_i:

$$-d\sigma = \Gamma_1 d\mu_1 + \Gamma_2 d\mu_2 \qquad (4.3.1\text{-}7)$$

The actual values of Γ_1 and Γ_2 depend on the exact placement of the mathematical interface. As aforementioned in section 4.1, interfaces have a finite thickness, but the mathematical interface is assumed to be a two-dimensional plane. Conventionally, this plane is placed so that Γ_1 is equal to 0. Therefore:

$$-d\sigma = \Gamma_2 d\mu_2 \qquad (4.3.1\text{-}8)$$

For dilute solutions, $d\mu_2$ may be approximated as $RTd\ln C_2$, where R is the ideal gas constant, T is the absolute temperature, and C is the solute molar concentration. Dropping the subscript, since now only the solute is considered:

$$\Gamma = \frac{-1}{RT}\left(\frac{d\sigma}{d\ln C}\right) \qquad (4.3.1\text{-}9)$$

This is the common form of the Gibbs adsorption isotherm. It shows that the slope of the interfacial tension vs. logarithm of concentration plot determines the surface excess concentration of the solute.

Even though the Gibbs equation is frequently called an adsorption isotherm, strictly speaking, an adsorption isotherm is an equation that relates the amount of material adsorbed directly to its concentration in solution ($\Gamma = f(C)$). The Langmuir adsorption isotherm is one of the simplest isotherms and is widely applicable to experimental data (Hiemenz and Rajagopalan 1997). It is derived assuming that the interface is solid, that both the solvent (1) and the solute (2) adsorb on it, and that both have molecules that occupy similar areas when adsorbed. The adsorption under such conditions is presented as a competition between solvent and solute for a place at the interface and may be represented by the equation (Adamson 1976):

Adsorbed solvent + Solute in solution $\leftrightarrow$ Adsorbed solute + Solvent in solution

The equilibrium constant of this process can be written as:

$$K' = \frac{a_2^s a_1^b}{a_1^s a_2^b} \qquad (4.3.1\text{-}10)$$

where a is the component's activity and the superscripts s and b stand for surface and bulk, respectively. Assuming that the surface solution is ideal (there are no lateral interactions between adsorbed molecules) the surface activities may be substituted by the components' molar fraction (Hiemenz and Rajagopalan 1997), x_1^s and x_2^s. Furthermore, $x_1^s + x_2^s = 1$ and, since the solution is dilute, the bulk activities may be approximated by the molar concentrations:

$$K' = \frac{x_2^s C_1}{(1 - x_2^s) C_2} \qquad (4.3.1\text{-}11)$$

The mole fraction of the adsorbed solute in the interface may be calculated as Γ/Γ_∞, where Γ_∞ is the saturation surface excess concentration, the value of Γ once the entire surface is covered with solute (Walstra 2003). Solving for Γ through equation 4.3.1-11:

$$\Gamma = \Gamma_\infty \frac{K'C_2/C_1}{K'C_2/C_1 + 1} \qquad (4.3.1\text{-}12)$$

Since the solution is dilute, C_1 is practically constant and thus, K'/C_1 may be assumed to be a constant. Dropping the subscript 2 and rearranging the last expression:

$$\Gamma = \Gamma_\infty \frac{C}{C + a_L} \qquad (4.3.1\text{-}13)$$

where a_L is the Langmuir constant, which, by simple examination of equation 4.3.1-13, corresponds to the half-coverage concentration (concentration of solute in the bulk for which $\Gamma = ½\ \Gamma_\infty$). Many non-ideal systems that are not expected to conform to the Langmuir equation's strict assumptions, such as in the case of polymer adsorption, nevertheless, show similar behaviors. In these cases, though, the physical significance of the constants (Γ_∞ and a_L) is dubious and they are regarded as empirical constants (Hiemenz and Rajagopalan 1997). Additionally, even though this isotherm was originally derived for adsorption at solid interfaces, it is frequently used to characterize the adsorption of low-molecular weight surfactants at liquid interfaces ((Lucassen-Reynders 1994), (Horozov and Arnaudov 2000; Ravera, Ferrari, and Liggieri 2000), to name a few).

To apply the Langmuir adsorption isotherm, the values of Γ_∞ and a_L must be determined. Since surface excess concentration can be inconvenient to measure, especially for liquid interfaces, the Langmuir-von Szyszkowski equation is commonly

used. This equation is the result of combining equations 4.3.1-9 and -13, the Gibbs adsorption equation and the Langmuir adsorption isotherm:

$$\sigma = \sigma_0 - \Gamma_\infty RT \ln\left(1 + \frac{C}{a_L}\right) \qquad (4.3.1\text{-}14)$$

σ_0 is the interfacial tension of the clean interface (no solute adsorbed). This equation has the advantage that the only physical property that must be measured is the equilibrium interfacial tension, which can be evaluated accurately. It was employed in the present study to obtain the Langmuir equation parameters form experimentally obtained surface and interfacial tension data. Equation 4.3.2-14 may also be expressed in terms of the surface pressure, π, which is defined as $\sigma_0 - \sigma$. Equations that relate π to Γ and T are referred to as surface equations of state, 2D analogies to the 3D PVT equations of state.

4.3.2. Critical Micelle Concentration

As previously mentioned, when surfactant molecules are in aqueous solution, they tend to adsorb on the interface to minimize contact between their hydrophobic part and water, causing a decrease in the interfacial tension. The fact that the surfactant molecules gather at the interface means that the surface excess concentration, Γ, is positive and therefore, according to the Gibbs adsorption isotherm (equation 4.3.1-9), the reduction in interfacial tension increases as the surfactant concentration increases. However, at a certain concentration, the surfactant molecules start self-assembling into aggregates called *micelles*. Micelles are spherical clusters of surfactant molecules with their hydrophobic groups directed towards the interior of the cluster and their hydrophilic part directed towards the water (Patist *et al.* 2002). The concentration at which this occurs is characteristic of each surfactant and is called the Critical Micelle Concentration (CMC).

At concentrations higher than the CMC, the interfacial tension remains almost constant. The common explanation for this is that the interface is completely covered with surfactant. However, the proper explanation is that, since any new surfactant added after the CMC will either join the micelles or form new ones, the chemical potential of the solution barely changes, keeping conditions at the interface almost constant (Evans and Wennerström 1999) . Figure 4.3.2-1 illustrates the behavior of surfactants at a liquid interface

The interfacial tension is not the only property of the system that undergoes an abrupt change at the CMC. Other properties with strong changes include osmotic pressure, turbidity, and conductivity (in case of ionic surfactants). CMC values obtained by different methods vary slightly, and the sharpness of the break depends on the surfactant nature. Therefore, the CMC should be regarded as a range of concentrations or an approximation, at best.

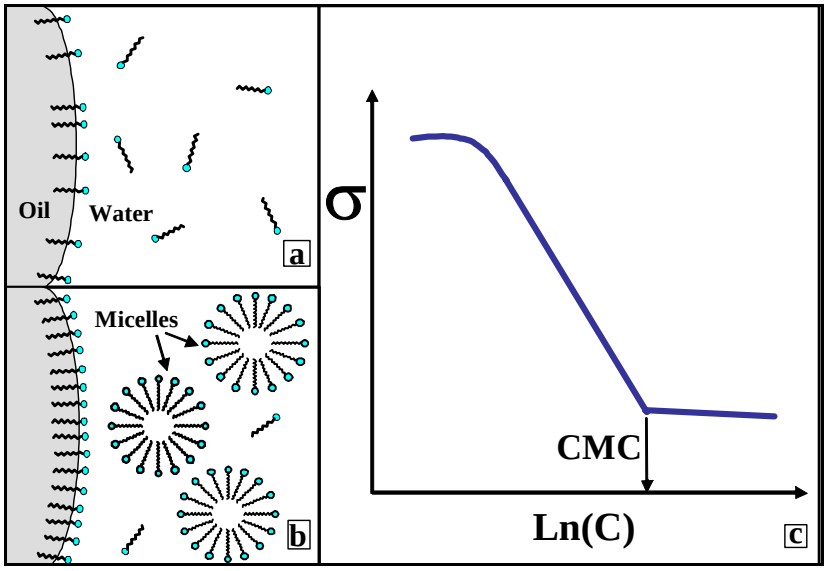

Figure 4.3.2- 1. Behavior of surfactants in a liquid-liquid system, a) concentration below the CMC; b) concentration above the CMC; c) equilibrium interfacial tension vs. logarithm of concentration curve for a typical surfactant.

If the concentration of surfactant is increased well above the CMC, the surfactants start aggregating into more complex structures, such as rod-like (cylindrical) micelles, lamellae, vesicles and liquid crystals. The concentration at which the micelles transition from spherical to cylindrical is called second CMC (CMC_{II}). The CMC_{II} doesn't affect the interfacial tension or some of the other properties affected by the CMC, but it can still be measured by methods such as the variation of the cloud point (Mu *et al.* 2001). The cloud point is a property exclusive to nonionic surfactants based on their decrease of solubility with increasing temperature. As the temperature increases, the surfactant becomes less soluble until, at a certain characteristic temperature (the cloud point), it separates from the solvent, creating a finely dispersed phase which turns the solution cloudy. The cloud point of a surfactant decreases with increasing concentration, reaches a minimum at the CMC_{II}, and increases slightly after it. The CMC_{II} may become important in turbulent emulsification processes since large, cylindrical micelles have been shown to affect the energy dissipation rate. Cylindrical micelles and polymers can deform and stretch, absorbing energy, which selectively dampens small-scale fluctuations, resulting in more anisotropic flows (van Doorn, White, and Sreenivasan 1999; Krope and Krope 2001).

4.4. Surfactant Adsorption Dynamics

The dynamics of the adsorption process is of major importance to many surfactant applications, incluiding the effects of surfactants on an emulsification process. In emulsification, drops are deformed, creating fresh interfacial area, and broken up at high rates. The size of the resulting daughter drops depends on the value of the interfacial tension during the deformation. If the surfactant adsorption is not fast enough to cover the

interfacial area as it is created, the effective or dynamic interfacial tension at the breakup point will be higher than the equilibrium interfacial tension of the system, leading to the formation of larger drops. In addition, the interfacial tension gradients created by the deformation of the interface change the interfacial rheology of the drop, which can also affect drop size as well as emulsion stability. The duration and, therefore, magnitude of the effect of these gradients depends on the surfactant's adsorption dynamics. Moreover, once the daughter drops are formed, the surfactant monolayer around them protects them against coalescence, but for this protection to be effective, the rate of surfactant adsorption should be fast enough to cover the interface during the short period between two drop collisions (Danov, Kralchevski, and Ivanov 2001). In conclusion, knowledge of surfactant adsorption dynamics is crucial in the design of surfactant-based processes and to properly interpret experimental results.

4.4.1. Adsorption Process

The process of adsorption at an interface may be divided into two coupled, time-dependent processes, the diffusion of the surfactant molecules from the bulk phase towards the interface and the actual adsorption at the interface. To explain this, consider a dilute surfactant solution with uniform concentration (below CMC) in which, at a certain instant, an interface with an insoluble phase is created. Since the energy of the system is minimized when the surfactant is at the interface, the surfactant molecules will tend to migrate towards it. The individual molecules will continue to move in all directions, but the overall flow will be from the bulk to the interface. The region of the bulk phase, with a thickness of a few molecular diameters, immediately next to the interface is called the *sub-surface* (Ward and Tordai 1946). Initially, the surfactant molecules at the sub-surface

will adsorb instantaneously, since the entire interface is available for adsorption. This sharply decreases the concentration at the sub-surface, creating a concentration gradient that further drives the diffusion of surfactant molecules. As the interface becomes fuller, there is an increased probability that a surfactant molecule will arrive at an interfacial site that is already occupied, which will make it stay longer at the sub-surface, slowing down the adsorption rate. In fact, once the interface is significantly covered, an adsorption – desorption dynamic equilibrium is established between the interface and the sub-surface. At the same time, with a non-zero sub-surface concentration, back-diffusion (diffusion from the sub-surface back to the bulk) becomes significant. The concentration at the sub-surface will continue to rise until it reaches the same value as in the bulk. At this point, diffusion ceases, since the concentration is again homogeneous, and equilibrium is attained between the interface and the bulk phase.

Although all adsorption processes include the two stages previously described, there are two limiting cases: when the exchange of molecules between interface and sub-surface is the rate-controlling (slower) step, the process is considered kinetics-controlled (also referred to as barrier-controlled). On the other hand, when the transport of surfactants towards the interface is the slow step, the process is deemed diffusion-controlled. In some cases, neither step is negligible with respect to the other and, hence, the process is mixed-controlled.

In the case of kinetically controlled adsorption, the diffusion of surfactant molecules is considered very fast compared to transfer from the sub-surface to the interface. Thus, the sub-surface concentration is constant and equal to the bulk concentration at all times, which is assumed equal to the initial concentration, C_0 (infinite

bulk phase assumption). One of the most frequently used equations to describe the transfer mechanism is the Langmuir rate equation (Dukhin, Kretzschmar, and Miller 1995):

$$\frac{d\Gamma}{dt} = k_a C_0 \left(1 - \frac{\Gamma}{\Gamma_\infty}\right) - k_d \frac{\Gamma}{\Gamma_\infty} \qquad (4.4.1\text{-}1)$$

where k_a and k_d are the adsorption and desorption rate constants, respectively. Notice that, at equilibrium ($d\Gamma/dt = 0$), equation 4.4.1-1 reduces to the Langmuir adsorption isotherm (equation 4.3.1-13) with $a_L = k_d/k_a$. Diamant *et al.* (Diamant and Andelman 1996a; Diamant, Ariel, and Andelman 2001) concluded that the adsorption of ionic surfactants, when there is no other electrolyte in solution (salt-free systems), is kinetically controlled. The strong interactions of the ions in solution drastically increase diffusion in the solution (ambipolar diffusion). However, the electrostatic repulsion from the electrically charged interface slows down the adsorption process. If the electric field is strong (as is usually the case in salt-free systems), the adsorption may be orders of magnitude slower than the diffusion. This was found to agree very well with experimental data.

4.4.2. Diffusion-Controlled Adsorption

The first physically grounded dynamic model for surfactant adsorption was derived in 1946 by Ward and Tordai (1946), and is based on the assumption that the time dependence of interfacial tension is caused by the transport of molecules to the interface, i.e. diffusion-controlled. In this model, the molecule transfer between the sub-surface and the interface is assumed to be unhindered and fast compared to the diffusion in the bulk. Therefore, the sub-surface concentration is always lower than the bulk concentration,

since the surfactant molecules are adsorbed, practically, as soon as they arrive at the sub-surface. The diffusion-controlled model may be derived from an unsteady diffusion problem. Diffusion in the bulk phase (without chemical reaction) is governed by:

$$\frac{\partial C}{\partial t} + \vec{v} \cdot \nabla C = D_{AB} \nabla^2 C \tag{4.4.2-1}$$

where $\vec{v}$ is the flow velocity vector, and D_{AB} is the binary diffusion coefficient. Assuming there is no flow and that diffusion is only in the direction perpendicular to the interface (x, with x = 0 at the interface):

$$\frac{\partial C}{\partial t} = D_{AB} \frac{\partial^2 C}{\partial x^2} \tag{4.4.2-2}$$

One of the boundary conditions for this problem is the surfactant mass balance at the interface, which in general form is (Stone 1990; Dukhin, Kretzschmar, and Miller 1995):

$$\frac{\partial \Gamma}{\partial t} + \nabla_s \cdot \left(\Gamma \vec{v}_s\right) + \Gamma\left(\nabla_s \cdot \vec{n}\right)\left(\vec{v} \cdot \vec{n}\right) = D^s_{AB} \nabla^2_s \Gamma + D_{AB} \left.\frac{\partial C}{\partial x}\right|_{X=0} \tag{4.4.2-3}$$

The sub-script (or super-script) s denotes surface properties and $\vec{n}$ is the normal unit vector. Neglecting surface diffusion and flow, both at the interface and in the bulk, the mass surfactant balance simplifies to:

$$\frac{\partial \Gamma}{\partial t} = D_{AB} \left.\frac{\partial C}{\partial x}\right|_{X=0} \tag{4.4.2-4}$$

The other boundary condition is the infinite bulk phase assumption:

$$\lim_{x \to \infty} C(x,t) = C_0; \quad \text{for } t > 0 \tag{4.4.2-5}$$

The initial conditions are a homogeneous concentration and a clean interface:

$$C(x,t) = C_0; \quad \Gamma(t) = 0; \quad \text{at } t = 0 \tag{4.4.2-6}$$

Ward and Tordai showed, through rigorous mathematical derivation, that the solution for this system of equation is:

$$\Gamma(t) = \sqrt{\frac{D_{AB}}{\pi}}\left[2C_0\sqrt{t} - \int_0^t \frac{C(0,\tau)}{\sqrt{t-\tau}}d\tau\right] \qquad (4.4.2\text{-}7)$$

where C(0,t) is the sub-surface concentration, and π is the irrational number, not the surface pressure. This approach has been used by many authors and seems to be reliable for the description of experimental observations (Ravera, Ferrari, and Liggieri 2000).

The main difficulty of using the Ward – Tordai model is that it contains the instantaneous sub-surface concentration, which is unknown. Customarily, this has been dealt with by utilizing a suitable adsorption isotherm as a boundary condition, to relate the surface excess concentration and the sub-surface concentration. Less frequently, a kinetic relation, such as equation 4.4.1-1 (Miller, Joos, and Fainerman 1994) is used. However, the practice of using an isotherm has been criticized because it relies on an equilibrium assumption (the isotherm) to solve an out-of-equilibrium, dynamic problem. Diamant *et al.* (Diamant and Andelman 1996a; Diamant, Ariel, and Andelman 2001) developed a model based on a free energy approach, which doesn't depend on equilibrium relations. They found that nonionic surfactants usually undergo diffusion-limited adsorption, provided there are no kinetic barriers at the interface, e.g. the presence of a previously adsorbed substance that would have to desorb first. They also found that when ionic surfactants adsorb is the presence of another electrolyte, the additional ions (which usually are at a much higher concentration than the surfactant) dampen the electric field in the solution, severely reducing the electrostatic interactions. Without the influence of these interactions, the time scales for this case are only slightly different than

the nonionic case, and therefore the adsorption process is also diffusion-controlled. More importantly, they concluded that using an isotherm as the boundary condition is valid as long as the process is diffusion-limited. Furthermore, the dynamic interfacial tension of a diffusion-controlled system was found to approximately obey an equilibrium equation of state (Diamant and Andelman 1996b).

Another complication of the Ward – Tordai model is that, even after assuming an appropriate isotherm, there is no analytical solution for the equation (it must be solved numerically). To overcome this, several authors (Van den Bogaert and Joos 1979; Rillaerts and Joos 1982; Fainerman, Makievski, and Miller 1994) have developed asymptotic solutions to the Ward – Tordai equation. The short times approximation, assumes that at $t \rightarrow 0$, the concentration at the sub-surface can be neglected, since not enough time has passed for a significant number of surfactant molecules to have arrived at it by diffusion. Thus, the second term in the brackets of equation 4.4.2-7 is dropped, reducing it to:

$$\Gamma(t) = 2C_0\left(\frac{D_{AB}t}{\pi}\right)^{1/2} \qquad (4.4.2\text{-}8)$$

At these short times, $\sigma_0 - \sigma$ may be approximated by $nRT\Gamma$, where $n = 1$ for non-ionic surfactants (Fainerman, Makievski, and Miller 1994). Therefore, equation 4.4.2-8 may be expressed as:

$$\sigma(t)\big|_{t\rightarrow 0} = \sigma_0 - 2nRTC_0\left(\frac{D_{AB}t}{\pi}\right)^{1/2} \qquad (4.4.2\text{-}9)$$

On the other hand, at long times when $t \rightarrow \infty$, $C(0,t) \rightarrow C_0$, so it can be factored out of the integral of equation 4.4.2-7, then:

$$\Gamma(t) = \sqrt{\frac{D_{AB}}{\pi}}\left[2C_0\sqrt{t} - 2C(0)\sqrt{t}\right] = 2\left(\frac{D_{AB}t}{\pi}\right)^{1/2}\left[C_0 - C(0)\right] \qquad (4.4.2\text{-}10)$$

For small deviations from equilibrium (Rillaerts and Joos 1982):

$$C_0 - C(0) = \frac{dC}{d\sigma}\left(\sigma - \sigma_{eq}\right) \qquad (4.4.2\text{-}11)$$

where σ_{eq} is the equilibrium interfacial tension corresponding to C_0. Then, by combining equations 4.4.2-10, 4.4.2-11, and the Gibbs adsorption isotherm (equation 4.3.1-9):

$$\sigma(t)\big|_{t\to\infty} = \sigma_{eq} + \frac{RT\Gamma^2}{C_0}\left(\frac{\pi}{4D_{AB}t}\right)^{1/2} \qquad (4.4.2\text{-}12)$$

Equations 4.4.2-9 and 4.4.2-12 may be used, under the appropriate conditions, to fit experimental dynamic interfacial tension data. If the diffusion coefficient of the surfactant is known, the goodness of fit of the data can demonstrate if the system is indeed diffusion-controlled. Conversely, if the diffusion-controlled assumption is reasonable, the experimental data may be used to obtain the diffusion coefficient. These approximations have been used in many studies of non-ionic surfactant adsorption. There is agreement that for low concentrations, the process is limited by diffusion (Göbel and Joppien 1997; Zholob, Fainerman, and Miller 1997; Horozov and Arnaudov 2000; Teipel and Aksel 2001; among others). In the present study, equation 4.4.2-12 was used to obtain the diffusion coefficients of the surfactants by fitting it to experimental dynamic surface tension data.

The ionic nature of the surfactant is not the only factor that affects its adsorption behavior. The concentration of the surfactant in the bulk phase also plays an important role. In the case of nonionic surfactants, the dependency on diffusion decreases as the bulk concentration increases, since the surfactant molecules have to travel a shorter

distance to arrive to the interface. At high enough concentrations, the controlling mechanism of the adsorption process shifts from diffusion-controlled to mixed-controlled (Lin, Chang, and Chen 1996; Dong *et al.* 2000). The HLB of the surfactant also seems to have an effect on its kinetic behavior since surfactants with only slight differences in their hydrophilic or lipophilic parts often exhibit different adsorption rates. However, in this case the relationship is more complicated because it may be influenced by the polarity of the oil phase, and hence the solubility of the surfactant in it (Hansen and Fagerheim 1998), or the branching of the hydrocarbon chain of the lipophilic part of the surfactant (Varadaraj *et al.* 1991). Furthermore, in some cases, the surfactant may undergo molecular reorientation or rearrangement which modifies its dynamic behavior (Horozov and Arnaudov 2000; Ravera, Liggieri, and Miller 2000).

4.4.3. Adsorption Time Scales

Both stages of surfactant adsorption, bulk diffusion and interfacial transfer, have associated characteristic timescales. If these time scales are known, they can be used to scale and compare the adsorption behavior of different surfactants.

For diffusion-controlled adsorption, the characteristic time depends on how effectively the interface depletes the surfactant solution and the diffusivity of the surfactant molecule (Ferri and Stebe 2000). The adsorption depth, h, is defined as the thickness of the volume adjacent to the interface that is depleted of surfactant molecules due to the adsorption (this definition assumes that the rest of the surfactant molecules in the bulk phase are not affected by this depletion). This characteristic adsorption length scale is derived from a simple mass balance: the mass of surfactant adsorbed on a differential area of the interface is ΓdA; the mass of surfactant originally in the

differential volume of thickness h, adjacent to dA is C_0hdA. Equating these two expressions results in:

$$h = \frac{\Gamma}{C_0} \tag{4.4.3-1}$$

The time scale defined by this depth and the surfactant's diffusivity would be:

$$t_D = \frac{h^2}{D_{AB}} \tag{4.4.3-2}$$

This parameter allows the prediction of adsorption behavior from equilibrium parameters (Γ and C_0) and the diffusivity, only. It provides a basis for comparing surfactants and deciding which more effectively lowers interfacial tensions. It has been shown that the surface tension equilibrates within 1-10 t_D, irrespective of the initial concentration (Ferri and Stebe 2000).

It must be pointed out that the previous derivation of h is valid only for planar interfaces. This is a valid assumption in many cases, but when the interface is that of a micron-size drop or bubble, such as in emulsification processes, the curvature of the interface cannot be neglected. Carrying out a similar mass balance on a spherical drop of diameter D yields the following expression for h:

$$h = \left(\frac{3}{4} D^2 \frac{\Gamma}{C_0} + \frac{D^3}{8} \right)^{1/3} - \frac{D}{2} \tag{4.4.3-3}$$

As the diameter of the drop increases, the value obtained from equation 4.4.3-3 approaches asymptotically the one calculated by 4.4.3-1. The diameter for which both values are the same depends on the concentration: for high concentrations they equalize at a lower diameter than for low concentrations.

If the adsorption is kinetically controlled, the timescale is the characteristics time of the solution of equation 4.4.1-1:

$$t_{kin} = \frac{\Gamma_\infty}{k_d + k_a C_0} \qquad (4.4.3\text{-}4)$$

Since t_{kin} is inversely proportional to C_0, while t_D is inversely proportional to C_0^2, the kinetic timescale decreases more gradually with increasing concentration. This is consistent with the shift in the adsorption controlling mechanism observed at high concentrations in diffusion-controlled nonionic surfactants (Lin, Chang, and Chen 1996; Dong *et al.* 2000).

The adsorption dynamics considered to this point have been derived, and applied to, surfactant solutions with sub-CMC concentrations. At concentrations above the CMC, the effect of the micellization process on the adsorption dynamics must be taken into account. Micelles are not static, they are in dynamic equilibrium with individual surfactant molecules (monomers), which are constantly being exchanged between the micelle and the bulk phase. Additionally, the micelles themselves are continuously breaking down and reaggreagating (Patist *et al.* 2002). Therefore, there are two relaxation timescales in micellar solutions: the fast relaxation time, related to the exchange of monomers between micelles and the bulk (of the order of microseconds); and the slow relaxation time, i.e. the micelle lifetime (of the order of milliseconds to minutes).

Micelles of nonionic surfactants show much longer relaxation times than for ionic surfactants, presumably due to the absence of electrostatic repulsion between the hydrophilic groups (Patist *et al.* 2002). When new interfacial area is created, the monomers in the solution will tend to adsorb on it. This disturbs the equilibrium between monomers and micelles and forces micelles to break. However, if the monomers are

depleted from the solution before the micelles break (in the case of stable micelles with high slow-relaxation times), the overall adsorption dynamics will be affected. Danov *et al.* (Danov, Valkovska, and Kralchevsky 2002) measured and compared slow relaxation times and the diffusion timescale of Triton X-100 concentrated solutions and found that the former was always smaller than the latter, but not by much. They were often within the same order of magnitude. This means that micellization – demicellization rates must be considered when interpreting adsorption processes in nonionic micellar solutions.

4.5. Interfacial Rheology

Interfacial rheology, or interfacial hydrodynamics, is the field of science concerned with the response of mobile interfaces to deformation (Edwards, Brenner, and Wasan 1991). Classical hydrodynamics often omits interfacial rheology since a precise knowledge of it is not necessary to understand basic fluid motion. However, if the system being studied has a high surface-to-volume ratio, such as in colloids (emulsions, bubbles, foams, etc) it becomes important. Furthermore, colloidal systems often contain surfactant molecules adsorbed at the interfaces, which introduce additional interfacial stresses that can have a big impact on the system's behavior.

Interfacial rheology is, in many aspects, a 2D analogue to bulk (3D) rheology, although with two significant differences. First, interfaces are always compressible, as opposed to bulk liquids which are commonly incompressible; this difference is of important in many practical cases (Miller *et al.* 1996). Second, interfaces cannot exist by themselves since they are, by definition, the boundary between two adjoining phases, so its motion is always coupled to that of the bulk phases. However, similarly to the 3D

case, interfacial rheology is concerned with the functional relationships between stress, deformation, and rate of deformation (Lucassen-Reynders 1981).

4.5.1. Rheological Properties of Surfactant Films

An interface can be deformed in two different ways; by shearing and by dilatation/compression (Walstra 2003). In the first case, the shape of the interface element being deformed changes, with constant area; in the second, the area changes, but the shape remains the same. Actually, interfaces can also be bent, but this is of no significant relevance for interfacial rheology (Langevin 2000). There are also two types of responses to deformation: elastic, when the strain is directly related to the force causing it and vanishes when said force is released; or viscous, when the strain rate is proportional to the force and the strain achieved remains after the force is removed. Consequently, there are four formal surface rheological properties: surface shear elasticity, surface shear viscosity, surface dilational elasticity, and surface dilational viscosity. In general, the deformation can be a combination of shearing and dilatation, and could produce viscoelastic responses. However, under proper conditions, they may be measured and studied individually or in known combinations.

The surface shear viscosity is the most extensively investigated of all surface rheological properties (Edwards, Brenner, and Wasan 1991). It is defined, by analogy with Newton's viscosity law, as:

$$\tau_{xy}^{s} = \mu^{ss} \frac{\partial v_{y}^{s}}{\partial x} \qquad (4.5.1\text{-}1)$$

where τ_{xy}^{s} is the surface shear stress, μ^{ss} the surface shear viscosity and v_{y}^{s} the velocity on the interface in direction y. The main cause for surface shear viscosity is friction

between neighboring adsorbed molecules (Walstra 2003). Djabbarah and Wasan (1982) found that the surface viscosity increases with decreasing average area per molecule, as well as with increasing concentration; which seems consistent with friction being its cause. Surface shear elasticity, on the other hand, is due to attractive forces between the molecules (Walstra 2003). This property, however is rarely reported and, when measured, is often in the form of a surface shear modulus (E^{ss}), a complex combination of surface shear viscosity and elasticity.

In the case of surfactant monolayers, the surface shear properties are usually considered negligibly small, at least compared to their dilational counterparts or their values for polymer or protein layers. Gupta and Wasan (1974) studied the surface shear viscosity of adsorbed films of a wide range of surfactants using a sensitive deep channel interfacial viscometer. They concluded that for most of the surfactants studied (including ionic and nonionic) the surface shear viscosity was exceedingly small, of the order of 10^{-4} sp (surface Poise, 1 sp = 10^{-3} Pa·s·m). Other authors have: (1) shown its unimportance, from hydrodynamic stability analysis; (2) found dilational properties to be several orders of magnitude greater; (3) reported maximum values of , at most, 1 sp; and (4) referred to it as "somewhat overrated in the literature" (Lucassen-Reynders 1981).

4.5.2. Surface Dilational Modulus

One fundamental difference between shear and dilational deformations is that, when an interface is sheared, the concentration of surfactant on it, i.e. Γ, remains constant. On the other hand, when the interface is dilated or compressed, Γ changes locally (decreases for dilatations and increases for compressions). This gives rise to interfacial tension gradients on the surface, which generate an additional stress on it, causing it to move in the

opposite direction to the gradient, and dragging some of the bordering bulk phases with it (Walstra and Smulders 1998). This is the so-called *Marangoni effect*, named after Carlo Giuseppe Matteo Marangoni, who first described it in 1871. Figure 4.5.2-1 is a schematic representation of the Marangoni effect in the case of a surface dilation. The interfacial tension gradients extend from the higher interfacial tension area towards the lower interfacial tension areas.

The changes in surface excess concentration due to the deformation also perturb the adsorption equilibrium between the interface and the adjoining bulk phase, creating a net flux of surfactant molecules to the interface. The adsorption of additional surfactant onto the interface relaxes the interfacial tension gradients and, thus, the Marangoni stresses. In the absence of this relaxation, the interface exhibits perfectly elastic behavior. When relaxation plays an important role, the surface shows viscoelastic behavior.

Gibbs (1878) provided a quantitative framework for the interpretation of the Marangoni effect by defining the surface elasticity as the change in interfacial tension relative to a change in surface area:

$$E = \frac{d\sigma}{d \ln A} \qquad (4.5.2\text{-}1)$$

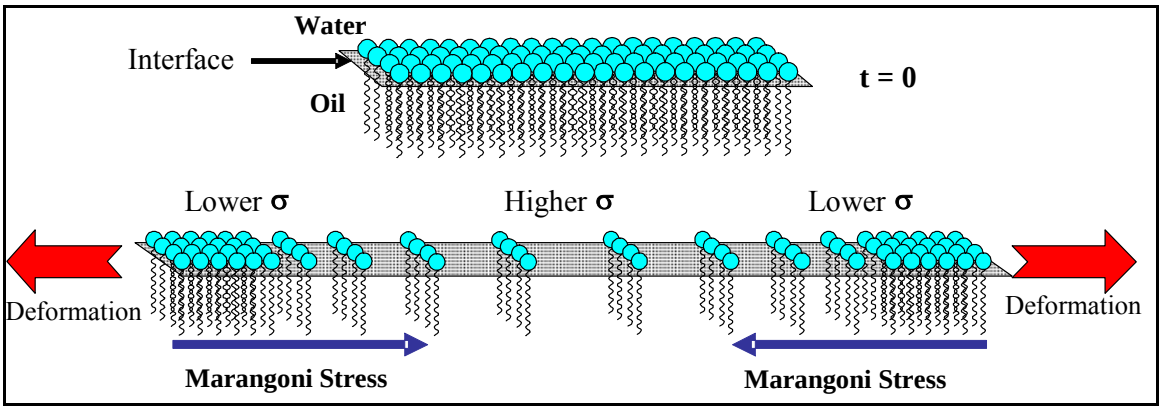

Figure 4.5.2- 1. Marangoni effect: initially (t = 0), the interface is homogenously covered with surfactant; then, the interface is dilated, creating interfacial tension (σ) gradients.

The parameter E was originally defined for soap-stabilized liquid films, but the concept has been extended to express surface tension gradients at any liquid interface (Lucassen-Reynders 1981). Even though E was defined as an elasticity, it can be expanded to include viscoelastic behavior. Lucassen and van den Tempel (1972) considered the case of a surfactant monolayer subjected to sinusoidal compression. To show this, equation 4.5.2-1 is expressed in terms of the surface pressure, π, as:

$$E = \frac{-d\pi}{d\ln\Gamma}\frac{d\ln\Gamma}{d\ln A} \tag{4.5.2-2}$$

where the first term is an equilibrium surface property and the second is a measure of the change in surface coverage with the change in area. From the surfactant mass balance at the interface, neglecting convective terms and surface diffusion, they show that:

$$\frac{1}{A}\frac{\partial(\Gamma A)}{\partial t} + D_{AB}\left.\frac{\partial C}{\partial x}\right|_{X=0} = 0 \tag{4.5.2-3}$$

By mathematical rearrangement of equation 4.5.2-3, the following expression is obtained:

$$\frac{d\ln\Gamma}{d\ln A} = -\left[1 + D_{AB}\frac{dC}{d\Gamma}\frac{(dC/dx)_{x=0}}{(dC/dt)_{x=0}}\right]^{-1} \tag{4.5.2-4}$$

Assuming there is no bulk flow, diffusion in the contiguous phase is governed by equation 4.4.2-2. After linearization, the solution to this equation is:

$$C = C_0 + Be^{nx}e^{i\omega t} \tag{4.5.2-5}$$

where B is a dimensionless constant, ω is the frequency of the compression, and n is:

$$n = (1+i)\sqrt{\frac{\omega}{2D_{AB}}} \tag{4.5.2-6}$$

Combining equations 5.5.2-2, -4, -5, and -6, the expression for E is found to be:

$$E = \frac{\frac{d\Pi}{d\ln\Gamma}}{1 + \frac{dC}{d\Gamma}\sqrt{\frac{D}{2\omega}} - \frac{dC}{d\Gamma}\sqrt{\frac{D}{2\omega}}i} \qquad (4.5.2\text{-}7)$$

Defining:

$$E_0 \equiv \frac{d\Pi}{d\ln\Gamma} \qquad \text{and} \qquad \zeta \equiv \frac{dC}{d\Gamma}\sqrt{\frac{D_{AB}}{2\omega}} \qquad (4.5.2\text{-}8a,b)$$

E may be rewritten as:

$$E = E_0 \frac{1 + \zeta + \zeta i}{1 + 2\zeta + 2\zeta^2} \qquad (4.5.2\text{-}9)$$

Lastly, the complex modulus of E, or surface dilatational modulus, is given by:

$$|E| = E^{sd} = \frac{E_0}{\sqrt{1 + 2\zeta + 2\zeta^2}} \qquad (4.5.2\text{-}10)$$

E^{sd} has, then, two components (from equation 4.5.2-9): one real, the surface dilational elasticity; and one imaginary, proportional to the surface dilational viscosity. Upon closer examination of the parameter ζ, it can be shown to be proportional to the product of the deformation frequency, ω, and the diffusion timescale (equation 4.4.3-2). Redefining h (equation 4.4.3-1) as $d\Gamma/dC$, leads to:

$$\zeta \equiv \frac{dC}{d\Gamma}\sqrt{\frac{D_{AB}}{2\omega}} = \left[\frac{2\omega}{D_{AB}}\left(\frac{d\Gamma}{dC}\right)^2\right]^{-1/2} \approx 2^{-1/2}\left(\omega t_D\right)^{-1/2} \qquad (4.5.2\text{-}11)$$

A reasonable approximation for E^{sd} is, then (Lucassen-Reynders, Cagna, and Lucassen 2001):

$$E^{sd} \approx \frac{E_0}{1 + \left(\omega t_D\right)^{-1/2}} \qquad (4.5.2\text{-}12)$$

These equations have been derived for periodic interfacial deformation of characteristic frequency ω. However, Loglio *et al.* (1991) showed, through a Laplace – Fourrier transformation analysis, that the same physical property (E^{sd}) governs both harmonic and transient surface processes. Therefore, the theory developed by Lucassen and van den Tempel (1972) can be generalized to non-periodic deformations (within the linearity of the approximation). Walstra and Smulders (1998) argue that, for emulsification processes, the timescale associated with ω can be roughly approximated by the drop deformation timescale (for now, t_{def}). This allows equation 4.5.2-12 to be expressed as:

$$E^{sd} \approx \frac{E_0}{1+\left(\frac{t_D}{t_{def}}\right)^{-1/2}} \qquad (4.5.2\text{-}13)$$

This expression for E^{sd} is convenient to explain the dependence of the modulus on surfactant concentration in the bulk phase. When the concentration of surfactant is low, the adsorption process is slow and, consequently, the adsorption timescale is large. For t_D values sufficiently larger than t_{def}, the denominator of equation 4.5.2-13 is virtually 1, and E^{sd} is approximately equal to E_0, which increases linearly with concentration. E_0, often called Gibbs elasticity, is a measure of the elasticity that the interface would exhibit in the absence of surfactant in the bulk to relax the Marangoni stresses. This parameter is sometimes confused with the surface dilational modulus, but they are equal only in the case of insoluble surfactants (surface active substances virtually insoluble in the bulk phases and, therefore, confined exclusively to the interface). As the surfactant concentration in the bulk increases, the diffusion timescale shortens, and the denominator deviates from 1, i.e. the relaxation of the Marangoni stresses by diffusion starts to

become significant. The surface dilational modulus will continue to increases until it reaches a maximum at the concentration where $t_D \approx t_{def}$. Beyond this concentration, the modulus decreases until it becomes negligible at high surfactant concentrations. This behavior is represented graphically in Figure 4.5.2-2.

For a surfactant that follows the Langmuir adsorption isotherm (equation 4.3.1-13), appropriate algebraic expressions can be found for $d\pi/d\ln\Gamma$ and $d\Gamma/dC$ (Lucassen-Reynders, Cagna, and Lucassen 2001), which, in turn, yield:

$$E^{sd} = \frac{RT\Gamma_\infty (C/a_L)}{1+\sqrt{Dt_{def}}\,\frac{a_L}{\Gamma_\infty}\left(\frac{C}{a_L}+1\right)^2} \qquad (4.5.2\text{-}14)$$

Equation 4.5.2-14 can be evaluated form surfactant equilibrium parameters, as long as the proper deformation timescale can be estimated. In chapter 3, section 4, three equations were derived for the drop deformation timescale, which depend on the turbulence regime: inertial sub-range, viscous sub-range assuming inertial stresses, or viscous sub-range assuming viscous stresses (equations 3.4-2, 3.4-3, and 3.4-4, respectively). However, as cautioned therein, these need not be the best choices for deformation timescale, since the lifetime of the turbulent eddy creating the deformation should also be taken in

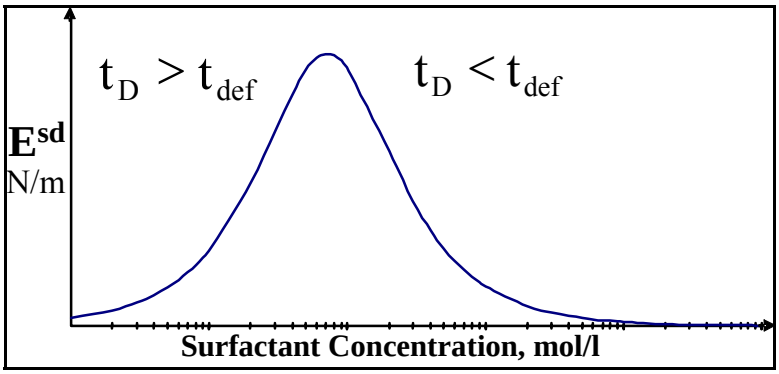

Figure 4.5.2- 2. Representation of a generic curve of surface dilational modulus as a function of surfactant bulk concentration.

consideration. This lifetime also depends on the regime, which means that there are three different expressions for this time (equations 3.3.3.1-1, 3.3.3.2-1, and 3.3.3.3-2). In order to evaluate correctly the surface dilational modulus, the appropriate deformation timescale must be chosen. In this work, equation 4.5.2-14 was used to calculate the surface dilational modulus with the 6 different possible timescales. This data were then used in correlations for the experimentally obtained drop sizes of liquid-liquid dispersion to determine the best timescale. These results are presented and discussed in Chapter 8.

Finally, it must be noted that, for the particular case of emulsification, the values of surface dilational modulus obtained through equation 4.5.2-14 should be regarded as maximum values. The derivation of this equation assumes that there is no flow in the bulk phase close to the interface. However, in emulsification, there are significant flows around the drops, especially in turbulent flows. The presence of these flows is likely to induce convective transport of surfactant molecules towards the interface, in addition to diffusion. Therefore, the Marangoni stresses would be relaxed much faster. The exact effect of surfactant convection, let alone turbulent surfactant convection, is unclear at present.

4.6. Physicochemical Hydrodynamics

Physicochemical hydrodynamics is the aggregate of problems dealing with the effect of fluid flow on chemical or physicochemical transformations as well as the effect of physicochemical factors on fluid flow (Levich 1962). The previous section was concerned with the effects of the deformation of a surfactant-covered interface and how it creates new stresses that change the rheology of the interface. In this section, it will be

shown that, when there is fluid flow in the surfactant solution next to the interface, the same doesn't need to be deformed to exhibit the Marangoni effect.

When a drop of diameter D travels through a surfactant solution, or, analogously, when a surfactant solution flows past a drop of diameter D, at large Peclet number (Pe >> 1), a diffusion layer of thickness δ_D develops near the surface of the drop. The Peclet number represents the ratio of bulk convective to diffusive fluxes (Chen and Stebe 1996), and is defined as:

$$\mathrm{Pe} = \frac{\mathrm{UD}}{\mathrm{D_{AB}}} \tag{4.6-1}$$

where U is the characteristic velocity of the flow. For a drop Reynolds number ($\mathrm{Re_D}$ = UD/ν) of less than 1, the flow is considered laminar, and the thickness of the boundary layer can be calculated precisely. For $\mathrm{Re_D} > 1$, only scaling relations in terms of order of magnitude can be developed. Independently of the value of $\mathrm{Re_D}$, the tangential velocity at the surface of the drop can be approximated (to an order of magnitude) by the velocity of the flow. Therefore, is can be shown that (Levich 1962):

$$\frac{\delta_D}{D} \sim (\mathrm{Pe})^{-1/2} \tag{4.6-2}$$

Figure 4.6-1 is an illustration of the aforementioned drop in the surfactant solution, indicating the characteristic values of the relevant variables of the system. Based on this, the following dimensionless variables may be defined:

$$\tilde{\Gamma} = \frac{\Gamma}{\Gamma_{eq}}; \qquad \tilde{C} = \frac{C}{C_0}; \qquad \tilde{t} = \frac{tu'}{D_{32}}; \qquad \tilde{v} = \frac{v}{u'}; \qquad \tilde{v}_s = \frac{v_s}{u'};$$
$$\tilde{r} = \frac{r}{D_{32}} \ (r \le D_{32}/2); \qquad \tilde{r} = \frac{r}{\delta_D} \ (r > D_{32}/2); \tag{4.6-2}$$

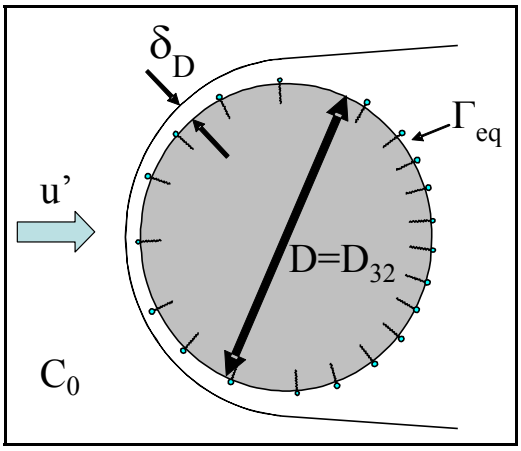

Figure 4.6- 1. Drop flowing in a surfactant solution of concentration C_0.

Where u' is the rms velocity across the drop surface (equation 3.3.1-2) and Γ_{eq} is the equilibrium surface excess concentration corresponding to C_0. In studies found in the literature, the velocity used to non nondimensionalize the surface velocity is the characteristic velocity of the flow. However, these studies were conducted in simpler laminar flows, where the choice of the characteristic velocity is clear. In this case, u' was chosen because it was considered the characteristic velocity at the drop's scale.

The mass balance for surfactant at the drop interface is given by equation 4.4.2-3. Considering that surface diffusion coefficients are usually negligible compared to bulk diffusivities, and that the adsorption depth, h, is proportional to Γ/C_0 (equations 4.4.3-1 and -3), the mass balance may be recast in dimensionless form as:

$$\frac{\partial \tilde{\Gamma}}{\partial \tilde{t}} + \tilde{\nabla}_s \cdot \left(\tilde{\Gamma}\tilde{\vec{v}}_s\right) + \tilde{\Gamma}\left(\tilde{\nabla}_s \cdot \vec{n}\right)\left(\tilde{\vec{v}} \cdot \vec{n}\right) = \left(\frac{\delta_D}{h}\right)\left.\frac{\partial \tilde{C}}{\partial \tilde{r}}\right|_{interface} \qquad (4.6\text{-}3)$$

The left-hand side of equation 4.6-3 represents the change in surface coverage due to transient and surface convection effects. More specifically, the second term corresponds to gradients in surfactant concentration at the surface due to the surfactant being "swept" by the flow along the interface caused by the bulk flow. The third term is the contribution

to gradients of surfactant surface concentration resulting from local area changes due to dilation/compression (Stone 1990). Since the Marangoni stresses are proportional to the interfacial tension gradients at the surface and (Eggleton and Stebe 1998):

$$\nabla_s \sigma = \frac{\partial \sigma}{\partial \Gamma} \nabla_s \Gamma \tag{4.6-4}$$

it can be concluded that both terms contribute to the Marangoni stresses and, therefore, these stresses act on the drop even in the absence of dilation/compression, just by the fact that it is moving in a surfactant solution. The effect of Marangoni stresses on drops, bubbles, and even large air slugs in surfactant solutions has been reported by several authors ((Stebe, Lin, and Maldarelli 1991; Milliken and Leal 1994; Eggleton and Stebe 1998; Hu and Lips 2003)). The right-hand side of the mass balance equation, on the other hand, quantifies the surfactant flux from the solution to the interface, which relaxes the Marangoni stresses. The dimensionless parameter δ_D/h, therefore, can be used to estimate the magnitude of the Marangoni effect. For $\delta_D/h << 1$, surface gradients dominate and the Marangoni stresses are present on the drop. For $\delta_D/h >> 1$, diffusion from the bulk is large enough to overcome Marangoni stresses and the drop interface is at equilibrium with the surfactant solution. This scaling parameter may help understand the effect of surfactant convection to the non-deforming drop interface, which is not included in the surface dilational modulus. The latter characterizes the role played by surfactant deformation.

4.7. Effect of Surfactants on Drop Size in Liquid-Liquid Systems

The effect of surfactants on drop size in liquid-liquid systems has been studied by different authors during the past few decades. These studies can be divided into two main

categories: Those that consider a single drop in simple shear or extensional flows, quantified the drop's deformation and critical capillary number; and those that focus on the formation of emulsions, usually in turbulent or highly inertial flows, in which average drop sizes and drop size distributions are measured.

4.7.1. Single Drop Studies

In the first category, one of the most renowned studies is that of Stone and Leal (1990), in which they extended their previous work on drop deformation and breakup (Stone, Bentley, and Leal 1986) to include the effect of insoluble surfactants. They found that the Marangoni stresses resulting from the surfactant being swept towards the drop poles by the flow made the drops harder to deform. This work was further expanded by Milliken *et al.* (Milliken, Stone, and Leal 1993; Milliken and Leal 1994) to include viscous drops and soluble surfactants. The effect of the Marangoni stresses was found to decrease with both, increasing drop viscosity and surfactant solubility. In the case of soluble surfactant, the behavior was always intermediate between the insoluble surfactant and the equilibrium interfacial tension cases, meaning that, though diminished, the Marangoni stresses were never negligible.

Eggleton and Stebe (1998) investigated the effect of kinetically controlled surfactant adsorption on the deformation of drops in extensional flow. They observed that, at low concentrations, the deformation of the drop decreases with increasing mass transfer (surfactant concentration) due to Marangoni stresses. If the concentration keeps increasing, adsorption supplies surfactant to the depleted equatorial region faster than desorption removes it from the tips, alleviating the stresses. At elevated concentrations,

the Marangoni stresses approach zero and the interface remains in equilibrium with the solution.

Janssen, Boon, and Agterof (1994a,b) examined the deformation of water drops in oil, in simple shear flow, in the presence of a nonionic surfactant. They found that the critical capillary number goes through a maximum as the surfactant concentration is increased. Furthermore, they noticed that the concentration at which the maximum was observed coincided with the one for which the surface dilational modulus (as given by equation 4.5.2-10) reaches its maximum value (see figure 4.7.1-1). They proposed the use of effective interfacial tension to correlate the data and defined it as:

$$\sigma_{eff}(C) = \sigma(C) + \beta E^{sd} \qquad (4.7.1\text{-}1)$$

The deformation timescale they used to estimate E^{sd} was the inverse of the shear rate. This approach well correlated the data obtained for viscosity ratios of 0.0013, 0.01, 0.05, and 0.152, with β values of 0.26, 0.23, 0.21, and 0.19, respectively. They argued that, given the size of their drops (~1mm), the exchange of surfactant occurs within the diffusion layer around the drop and, therefore, convection of surfactant can be neglected. They considered that for micron size drops this may not be the case and surfactant

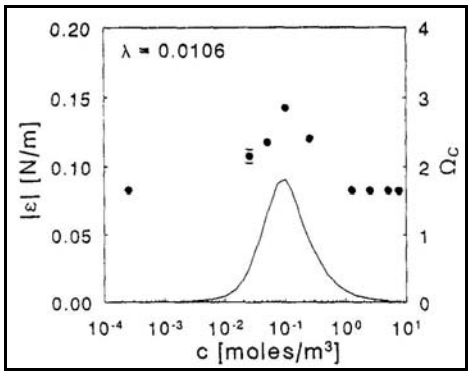

Figure 4.7.1- 1. Critical capillary number (Ω_c) and surface dilational modulus (|ε|), as functions of surfactant concentration (C). λ = viscosity ratio. (Janssen *et al.* 1994a)

convection will enhance adsorption relaxation, which will cause this approach to overestimate the effect of E^{sd}.

4.7.2. Emulsification Processes Studies

For the case of emulsification studies, where surfactant adsorption and emulsification are affected by many variables, results are varied and in some cases contradictory. Most show that the presence of the surfactant decreases the equilibrium mean drop diameter. However, the conclusions on the specific role of the surfactant and/or the mechanism by which it accomplishes that role, differ.

Konno, Arai, and Saito (1982) studied the effect of polyvinyl alcohol on drops size during the polymerization of styrene in a baffled tank with a Rushton turbine. The dispersed phase (styrene) started with a viscosity of 0.44 cP, but, as the reaction advanced, it increased to a final value of 3000 cP. They found that the drop size increased significantly when the viscosity reached 50 cP. The rate of increase depended on the dispersed phase volume fraction and on the PVA concentration. The drop size decreased with increasing PVA concentration, obtaining a constant drop size throughout the reaction for the highest concentration. They explained this effect by a decrease in coalescence rate due to faster coverage of broken drops by the PVA. Later, in a comprehensive study, Lee and Soong (1985) examined four different dispersed phases (silicone oil, kerosene, 3-cloropropene, and vinylidene chloride) in aqueous solutions with four surfactants (PVA, SDS, another nonionic, and one cationic). The dispersed phase volume fractions ranged from 2 to 20% and the experiments were carried out in a baffled tank with a six-blade impeller. The authors found that the experimental drop diameter was significantly lower than the one predicted by Hong's correlation, which is

based on clean liquid-liquid systems, using each system's equilibrium interfacial tension value. They concluded that, since the presence of the surfactant at the interface increases the time required for the liquid film between two colliding drops to drain, the rate of coalescence was decreased. Their proposed correction to the clean systems correlation consisted of including a fitting constant, which they found to have a value of 0.63, based on all their experimental data. They also found that the surfactant systems produced more uniform drop sizes, which narrows the drops size distribution.

Koshy, Das, and Kumar (1988) also argued that the effect of the surfactant in stirred-tank emulsification goes further than just lowering the interfacial tension, but they have a different explanation for this phenomenon. They argued that when a drop is approached by a turbulent eddy, it creates a depression on the drops surface which propagates across its diameter, breaking it. As the interface is stretched, interfacial tension gradient develop causing an "additional stress" that complements the turbulent stress. This stress is proportional to the difference between the equilibrium interfacial tension and the dynamic interfacial tension (the extrapolation to $t = 0$ of the $\sigma(t)$ curve). The model they developed was an extension of the S&D model by Lagisetty *et al.* (1986) with an additional term to account for this stress. They found that Lagisetty's model significantly overpredicts the drop size while their model well fits the experimental data over a broad range of surfactant concentrations. Therefore, they concluded that the extra stress generated by the surfactant plays a key role in drop breakup. While not referred to as such, it is evident that the extra stress is a Marangoni stress. However, the way they explain the drop breakage, the Marangoni stress doesn't oppose the deformation, it exacerbates it, thus producing smaller drops. The choice of this breakage mechanism,

however, is unclear. There is experimental evidence that both bubbles and viscous drops in turbulent flows undergo large scales deformations that elongate them into dumbbell-like shapes before breaking. This would result in Marangoni stresses that oppose the deformation, like those depicted in Figure 4.5.2-1. A tearing mechanism was observed by Hesketh, Etchells, and Russell (1991), but this only resulted in small fractions (~0.5%) of the drop's volume being torn away.

Chatzi, Boutris, and Kiparissides (1991) studied the effect of PVA on the transient and equilibrium D_{32} of 1% styrene-in-water dispersions in a stirred tank. They were able to fit their equilibrium data to equation 3.3.1-15 (the Weber number correlation), which was developed for clean systems, with a constant of 0.046. This value is slightly lower than the range of values reported in the literature for this correlation (0.051 – 0.081), but they attributed that to the fact that they measured the drop size through laser diffraction instead of traditional photographic methods. In the same year, Sharma, Goswami, and Rawat (1991) concluded that drop diameter correlations based on breakage by turbulent pressure fluctuations rather than viscous shear, such as those by Lagisetty *et al.* (1986), Coulaloglou and Tavlarides (1976), and others, predict the drops size of surfactant containing systems rather well, as long as the proper equilibrium interfacial tension value is used. Even though the studies mentioned so far were carried out in stirred tanks, which generate less intense turbulence than rotor-stator mixers, the rationales given by the authors for the effect of the surfactants on drop size should also apply to rotor-stators.

The only emulsification study found to take into account the effect of the rheological properties due to the presence of a surfactant is an investigation by Lucassen-Reynders and Kuijpers (1992) on water-in-oil emulsions formed with a combination

(consecutively) of an impeller and a rotor-stator mixer (Ultraturrax). It shows that drop size decreases much less with decreasing interfacial tension than expected from the Young – Laplace equation (4.1-4), especially at high surfactant concentrations. Due to this high surfactant concentration, they disregarded the possibility of coalescence (even though the dispersed phase fraction was 0.4). Therefore, they concluded that the interfacial viscoelasticty produced by the surfactant increases the effective viscosity of the drop, thus decreasing breakup and causing coarser emulsions. They defined an effective dispersed phase viscosity as:

$$\mu_d^{eff} = \mu_d + \frac{E^{sd}}{r\alpha} \qquad (4.7.2\text{-}1)$$

where r is the characteristic length scale of the drops and α is the relative rate of surface extension (approximately equal to the nominal shear rate of the flow and also used as deformation timescale to calculate E^{sd}). They found that, for their experimental conditions, the effective viscosity could be as high as ~30 times the dispersed phase viscosity, depending on the surfactant concentration (see figure 4.7.2-1) and surface

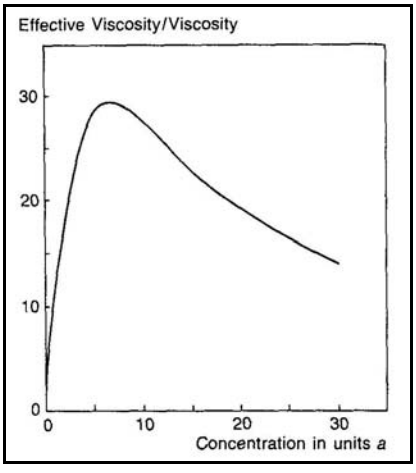

Figure 4.7.2- 1. Relative effective viscosity ($\mu_d^{eff}/\mu d$) as a function of dimensionless concentration. a=Langmuir constant (a_L) (Lucassen-Reynders and Kuijpers 1992)

activity. They argue that the conditions used in their analysis are more likely to be correct for emulsions with fairly viscous oils as continuous phase since the assumption of transport by diffusion alone holds better. They also argued that, even if inertia and turbulence are not negligible, surfactant-induced interfacial rheology should have an effect on emulsion drop size.

It is evident from the previous paragraphs that much work is still necessary to fully understand the effect of surfactants on liquid-liquid dispersions. The actual effect may even be a complex combination of some of the aforementioned factors. This lack of knowledge becomes even more patent for rotor-stator mixers given the scarce information found about them in the literature. The present study is aimed to generate practical data that would help improve this situation.

4.8. Summary

Surfactants, short for surface active agents, are a substances whose molecules are amphiphilic, a part of them is hydrophilic and the other part is lipophilic (hydrophobic). When in solution, surfactants decrease the interfacial tension of the system. This decrease depends on the surfactant's concentration and can be characterized by several adsorption equations. The adsorption process is time dependent and the variation of interfacial tension with time is an important property of surfactants. For dilute solutions of nonionic surfactants, this dynamic behavior is represented by the Ward and Tordai equation (equation 4.4.2-7)

The presence of surfactants at a liquid interface modifies its rheology. The surface dilational modulus is an important interfacial rheology parameter used to quantify the viscoelastic response of a surfactant-covered interface to a sudden expansion or

contraction. It is a measure of the Marangoni stresses acting on the interface as a result of transient interfacial tension gradients. The magnitude of the surface dilational modulus depends on the surfactant concentration and on the timescale of the deformation. Marangoni stresses may act on liquid drops flowing in a surfactant solution, even if they are not being deformed, affecting their hydrodynamic behavior.

CHAPTER 5: EXPERIMENTAL METHODS

To understand and quantify the effect surfactants on drop breakage in high shear rotor-stator mixers requires two main sets of experiments. The first set is oriented towards the characterization of the surfactants' physicochemical behavior, both equilibrium and dynamic. The second is the measurement of drop size distributions created by the mixer under different physiochemical conditions. The information obtained from the former set will be employed to analyze and interpret the data for the latter set of experiments.

The surfactant characterization consisted of the measurement and/or calculation of the different physicochemical properties that describe the interfacial phenomena acting on the system, as explained in Chapter 4. These are surface and interfacial tensions, critical micelle concentrations, cloud points, dynamic surface tension, diffusion coefficient, and surface dilational modulus. Surface and interfacial tensions were measured experimentally by means of the pendant drop technique, which will be explained here in detail. The cloud points were also measured experimentally. The rest of the physicochemical properties were mathematically derived from the surface/interfacial tension experimental data by methods introduced in Chapter 4 that will be described in the appropriate sections of the next chapter.

In order to measure the drop size distributions, dilute dispersions of immiscible liquids were formed in a batch, bench-scale, rotor-stator mixer. During the process of forming the dispersions, drops of one of the liquids were broken due to the hydrodynamic forces created by the mixer. After a long enough period of time had passed, an

equilibrium size distribution was achieved. At this point, a sample of the dispersion was withdrawn from the mixer and analyzed by means of the video microscopy technique previously described. To study the effect of the physicochemical phenomena on the drop size, the physical properties of the liquids (dispersed phase viscosity, continuous phase surfactant concentration) and the agitation conditions (rotor speed) were varied systematically.

5.1 Interfacial Phenomena Experiments

The following sections will describe the experimental equipment, materials, and procedures employed in the surfactant physicochemical characterization experiments.

5.1.1 Equipment and Materials

The most important procedure for the interfacial phenomena experiments is the pendant drop technique. The theory behind this technique is described below. Figure 5.1.1-1 illustrates the experimental setup used to perform pendant drop measurements. Drop images are captured as described below. A halogen lamp was used as light source and placed behind the drop to increase the contrast between it and the background. The drops are formed inside a glass container, which is situated inside a glass tank (aquarium). The glass tank is filled with water and equipped with a VWR Scientific heater/recirculator to maintain a constant temperature, which is monitored with an Omega HH11 handheld thermometer outfitted with a type K thermocouple. The drops were formed by means of a 500 μl Gastight® Hamilton syringe. The needle attached to the syringe could either be straight or U-shaped, depending on whether the measurement was of surface or interfacial tension. If surface tension was being measured, the needle was straight, the glass container was empty (filled with air), the syringe contained the test

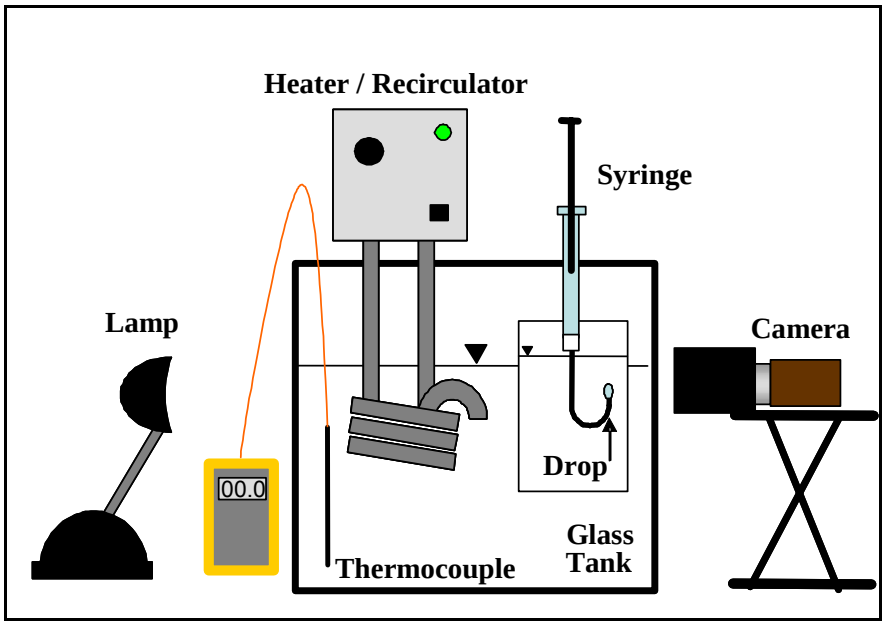

Figure 5.1.1- 1. Experimental setup used for pendant drop measurements.

liquid, and the drop hanged from the tip of the needle. In the case of an interfacial tension measurement, the needle was U-shaped, the container filled with the liquid with the highest density, the syringe contained the one with the lowest density, the drop clung to the tip of the needle, and the camera (described below) was inverted to capture an upright image of the drop. Interfacial tension could also be measured with the straight needle as long as the liquids in the container and the syringe were inverted. However, this way proved to be problematic when one of the liquids is a surfactant solution. If the surfactant solution is in the syringe, part of the surfactant molecules are transferred to the other phase, which has a much greater volume, depleting the drop of surfactant. If the surfactant solution is in the container and its volume is large enough (in this particular case it was approximately 2000 times larger than the volume of the drop), even though some of the surfactant is transferred into the drop, the concentration of surfactant in the solution remains practically constant.

The most relevant equipment used in this part of the investigation is the image acquisition system, in this case, a video camera connected to a frame grabber. The images of the drops are acquired by a Watec LCL-902 K camera. This is a black and white, ½" CCD, analog camera, which is attached to a Cosmicar TV zoom lens that enhances and allows the image to be properly focused. This particular camera has a very high sensitivity to low light levels (as low as 0.00015 lux), which is not critical to this application, but this is the same camera used with the high magnification video probe described in Chapter 2, where high sensitivity is important. The camera converts the image into a standard RS-170 analog signal, which is transmitted to an Integral Technologies FlashBus MX-332 frame grabber installed on a Pentium III personal computer. The image is displayed on the computer's monitor, where the frame grabber's application software is capable of capturing it, either on a one-image-a-time basis, or as a series of images. When the images are captured as a series, this can be a time-dependent series (each image is captured after a specified time interval has elapsed) or a manual one (each capture is triggered by clicking a button).

The liquids involved in the study are: water, methanol, and silicone oils of different viscosity grades. Deoinized water was obtained from the Bioprocess Scale-up Facility, in the University of Maryland's Chemical and Nuclear Engineering Building. It was used without any further purification or treatment. A.C.S certified methanol (99.9%) was obtained from Fischer Scientific, through the Chemistry Department's Chemistry Store. It was also used without any further treatment. Five different silicone oils were used, with nominal kinematic viscosity values of 10, 50, 100, 500, and 1000 cSt (1 cSt = 10^{-6} m^2/s). These oils are 200® Fluids, manufactured by Dow Corning. The 10 and 100

cSt samples were provided by DuPont, the 50 and 500 cSt were remnants from previous studies carried out in the lab, and the 1000 cSt sample was obtained from the Aldrich Chemical Company. As previously stated, an advantage of using silicone oils is that, even though they may have very different viscosities, their surface and interfacial tensions are virtually identical. Table 5.1.1 shows the values of the physical properties of all the pure fluids.

The three surfactants used in the study are Tergitol™ TMN-6, Triton™ X-100, and Triton™ X-165, manufactured by the Dow Chemical Company. All three are nonionic, specifically, Tergitol is an ethoxylated derivative of 2,6,8-trimethyl-4-nonanol (a branched alcohol), and both Tritons are octyl-phenol ethoxylates with different degrees of ethoxylation. Even though they are chemically very similar, they posses somewhat different physical properties (see Table 5.1.2), as well as slightly diverse adsorption behaviors (this will be shown in the results chapters).

Table 5.1.1- 1. Physical properties of the various fluids employed. (T=25°).

	Density (kg/m^3)	Dynamic Viscosity (mPa·s)	Surface Tension (mN/m)	Interfacial Tension with Water[e] (mN/m)
Water	997.05[a]	0.92[a]	71.99[d]	-
Methanol	789.67[a]	0.55[a]	22.07[d]	-
10 cSt Silicone Oil	935[b]	9.4[c]	20.1[b]	45.8
50 cSt Silicone Oil	960[b]	48.0[c]	20.8[b]	46.6
100 cSt Silicone Oil	964[b]	96.4[c]	20.9[b]	46.2
500 cSt Silicone Oil	969[b]	484.5[c]	21.1[b]	46.5
1000 cSt Silicone Oil	970[b]	970[c]	21.2[b]	46.0

[a]: Perry and Green (1999). [b]: Reported by Dow Corning Company. [c]: Calculated by $\mu=\rho\cdot\nu$. [d]: Lide (1999). [e]: Measured via pendant drop technique.

Table 5.1.1- 2. Physical and chemical properties of the three surfactants used.

	Condensed Formula	Mean Molecular Weight (g/mol)	Actives Content (%)	HLB
Tergitol TMN-6	$C_{12}H_{17}O(C_2H_4O)_8$	543[a]	90	13.0
Triton X-100	$C_8H_{18}(C_6H_4O)(C_2H_4O)_{9\text{-}10}$	624[b]	100	13.5
Triton X-165	$C_8H_{18}(C_6H_4O)(C_2H_4O)_{16}$	879 [c]	70	15.8

[a]: Flick (1993). [b]: Manufacturer's material safety data sheet.
[c]: Certificate of analysis of sample used (same sample was used in all experiments).

5.1.2 Pendant Drop Technique

The pendant drop technique is a method for determining surface or interfacial tensions based on the fact that small drops or bubbles tend to be spherical due to the predominance of surface forces over gravitational forces acting on them. However, if the drop is of a size such that surface tension and gravitational effects are comparable, the surface or interfacial tension can be determined from measurements of the shape of the drop or bubble (Adamson 1976). A drop hanging from a tip (or a clinging bubble) elongates as it increases in size because the difference in hydrostatic pressure becomes significant in comparison with that given by the curvature of the drop. If the drop's expansion is stopped before gravity overcomes the surface tension (in which case the drop falls), and the drop is left undisturbed, a force balance will be attained and the final shape of the drop will depend on its size, the density difference between drop and its surroundings, and the surface/interfacial tension. With respect to the coordinate system illustrated in Figure 5.1.2-1(a), this balance may be expressed by means of the Young-Laplace equation as follows:

$$\sigma\left(\frac{1}{R_1}+\frac{1}{R_2}\right)=\frac{2\sigma}{b}+\Delta\rho gz \qquad (5.1.2\text{-}1)$$

where R_1 is the radius of curvature on the x-z plane, R_2 is the radius of curvature on the plane normal to z, and b is the value of the radius of curvature at the apex of the drop (since the drop is symmetric, both curvature radii have the same value at the apex). If this equation is expressed as a function of the angle ϕ of Figure 5.1.2-1(a), it is called the Bashforth-Adams equation (Hiemenz and Rajagopalan 1997), which in dimensionless form is:

$$\frac{1}{R_1/b}+\frac{\sin\phi}{x/b}=2+\mathrm{Bo}\frac{z}{b} \qquad (5.1.2\text{-}2)$$

where Bo is the Bond number (ratio of gravitational to surface forces acting on the drop) and is equal to:

$$\mathrm{Bo}=\frac{\Delta\rho g b^2}{\sigma} \qquad (5.1.2\text{-}3)$$

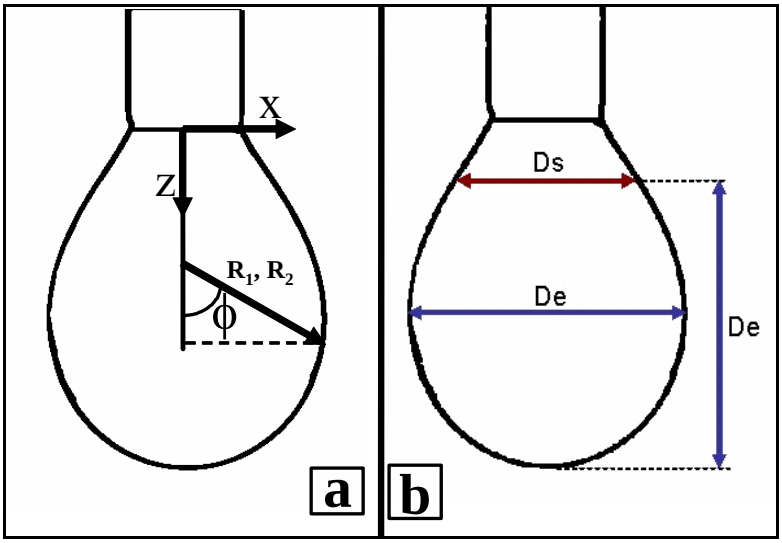

Figure 5.1.2- 1. (a) Coordinates system for the pendant drop geometry. (b) Drop measurements needed to calculate shape factor S.

Equation 5.1.2-2 can be solved numerically, with Bo and ϕ as parameters. However, the exact value of b is hard to determine. Therefore, Andreas *et al.* (Adamson 1976) developed a simplified method based on the conveniently measurable shape dependent quantity S, which in accordance to Figure 5.1.2-1(b) is defined as:

$$S = \frac{Ds}{De} \tag{5.1.2-4}$$

where De is the equatorial diameter of the drop and Ds is the diameter at a distance from the apex equal to De. The difficult to measure parameter b was combined with Bo to define a new shape dependent variable, H:

$$H = Bo\left(\frac{De}{b}\right)^2 \tag{5.1.2-5}$$

which is basically a modified Bond number. This allows the surface tension to be calculated as:

$$\sigma = \frac{\Delta\rho g De^2}{H} \tag{5.1.2-6}$$

The relationship between H and S was determined experimentally, and a set of 1/H values versus S was obtained. An extensive and reasonably accurate table of such values is found in Adamson (1976). Therefore, the only information needed to calculate the surface tension from the drop's image is De, Ds, and $\Delta\rho$.

In order to expedite the pendant drop image analysis, a Scion Image macro was developed to carry out the analysis automatically. The macro first opens the image from the specified folder, then, it performs a grayscale normalization, similar to the one explained in section 2.4.3. Next, it executes an edge detection subroutine, which is a built-in function of the software, and consists on applying a Sobel filter on the image.

This filtering generates an image comprised of the square root sum of the vertical and horizontal derivatives of the grayscale values of the original pixels. The result of this step is an image in which all the edges are considerably darkened while the rest of the image is softened. This image is then thresholded to a grayscale value of 128 and outlined, which filters out all the pixels that are not edges. Figure 5.1.2-2 demonstrates the different steps just explained. Subsequently, the program reads the x,y coordinates of all the remaining pixels, and determines the location of the rightmost and leftmost pixels as well as the apex of the drop. With this information it determines De, Ds, and consequently, S. At the same time it measures the width, in pixels, of the needle; and since the measured width, in millimeters, is requested at the beginning of the program's execution, a pixel-mm conversion factor particular to the image being analyzed is calculated. With this conversion factor, the value in pixels of De is changed into mm.

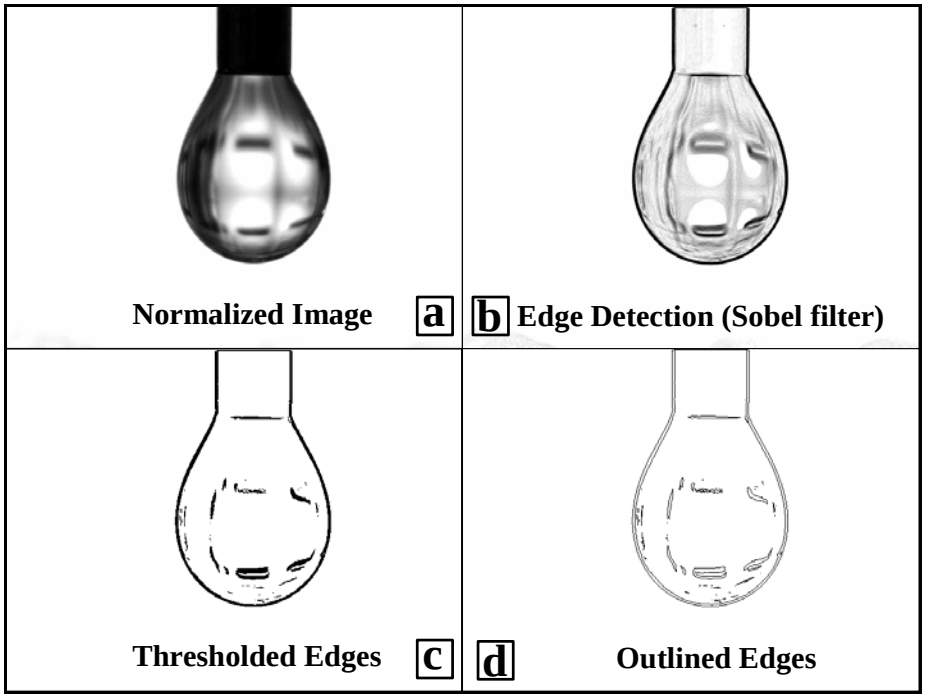

Figure 5.1.2- 2. Steps of the automated image analysis procedure (a) the original image has only been normalized, (b) after the application of the edge detection subroutine, (c) after thresholding the edges, and (d) the outline of the images are the only pixels left.

To calculate the value of H, the data from the table in Adamson (1976) was plotted and a power law regression performed to obtain an equation capable of calculating 1/H from the S value extracted from the image. Figure 5.1.2-3 shows a plot of 1/H vs. S and the power law regression curve and equation.

To corroborate the experimental setup and the image analysis procedure, the interfacial (or surface) tensions of several systems were measured, both with the straight and the U-shaped needle. At least 3 different drops of each system were analyzed and their results averaged and compared to values found in the literature. The results of this validation are reported in Table 5.1.2-1. Clearly, the method is reasonably accurate since the greatest error found with respect to the literature values was just about 5% and the standard deviations are all within 5% of the average value.

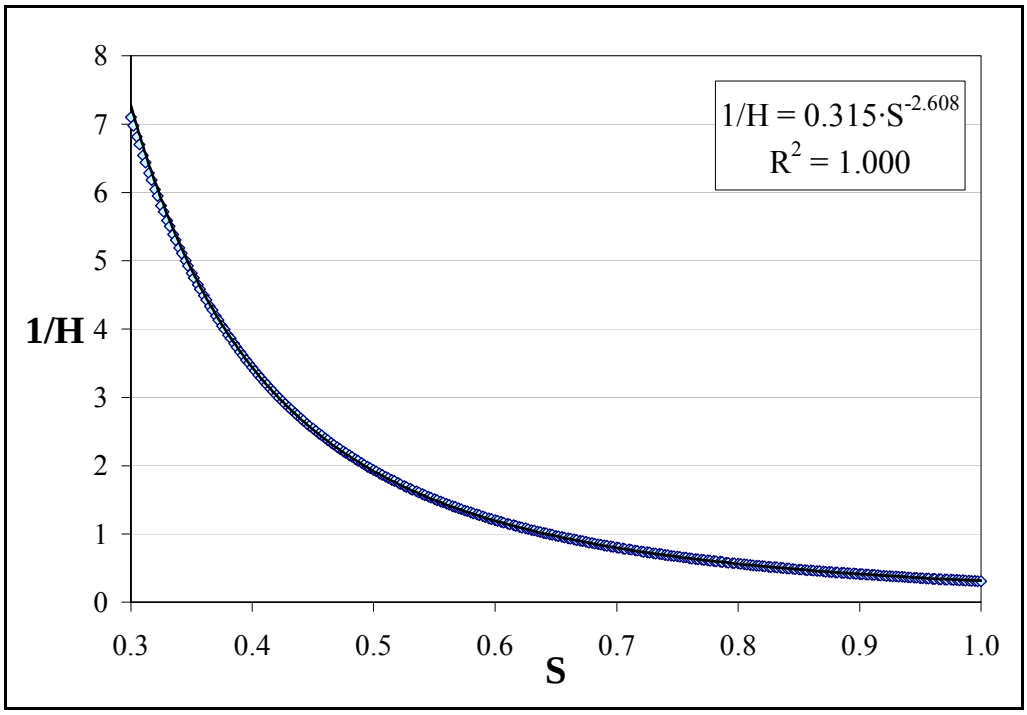

Figure 5.1.2- 3. Values of 1/H vs. S (Adamson 1976), along with power law regression curve and equation.

Table 5.1.2- 1. Validation of the pendant drop experimental technique.

System: Drop/Container fluid	Needle Shape	Interfacial Tension (mN/m)	Standard Deviation (mN/m)	Literature Value (mN/m)	Relative Error (%)
Water/Air (25°C)	Straight	72.03	1.31	71.99[a]	0.05
Air/Water (25°C)	U	71.88	1.42	71.99[a]	-0.16
Air/Methanol (25°C)	U	22.02	0.59	22.07 [a]	-0.21
Toluene/Air (25°C)	Straight	26.58	0.28	27.93 [a]	-4.83
Water/Toluene (25°C)	Straight	32.26	1.02	32.00[b]	0.81
CCl_4/Water (20°C)	Straight	44.91	0.96	45.00[c]	-0.20
Water/CCl_4 (20°C)	U	46.24	1.99	45.00 [c]	2.75

[a]: Lide (1999). [b]: Middleman (1998). [c]: Janssen and Warmoeskerken (1987)

As previously stated, the pendant drop technique is based on the equilibrium between surface and gravitational forces. For this balance to be achieved the drop must be large enough. If it is too small it will be almost fully round and this will lead to measurement errors and an incorrect interfacial tension value. This can happen when the density difference is small, as in the case of silicone oil/water systems, where the drop can be quite large to the point that they are about to fall, and still be too round. One indicator of the appropriate shape of the drop is the Bond number. If the Bond number is too low, the drop is too small, and if it is too large, the drop will simply fall. However, how low is too low cannot be predicted, it must be determined experimentally. Unfortunately, the Bond number depends on the radius of curvature at the apex (b), which is hard to quantify. One way around this is to assume that b is equal to the equatorial radius (De/2). In this case, and according to equation 5.1.2-5, the bond number can be approximated by:

$$Bo \cong \frac{H}{4} \qquad (5.1.2\text{-}7)$$

To establish the value for the critical Bond number (the minimum value to ensure that the drop is large enough to obtain a reliable interfacial tension), the tension of the 100 cSt silicone oil/water system was measured using needles of two different sizes (outer diameters of 0.82 mm and 1.27 mm), both straight and U-shaped. Since the maximum drop size attained with each needle is different, this allowed for the measurement of drops of different sizes, all at apparent equilibrium. The results of this test are plotted in Figure 5.1.2-4. It was decided from this test that only drops with Bond numbers of 0.12 or higher were acceptable and the image analysis program was modified to calculate and report the Bond number automatically. The drop images used for the validation reported in Table 5.1.2-1 were reanalyzed and they all have Bond numbers between 0.2 and 0.4.

5.1.3 Equilibrium Surface and Interfacial Tension

The equilibrium surface and interfacial tensions of surfactant and clean systems were determined through the pendant drop technique. This section will explain the procedure used to carry out these measurements, as well as the preparation of the surfactant and

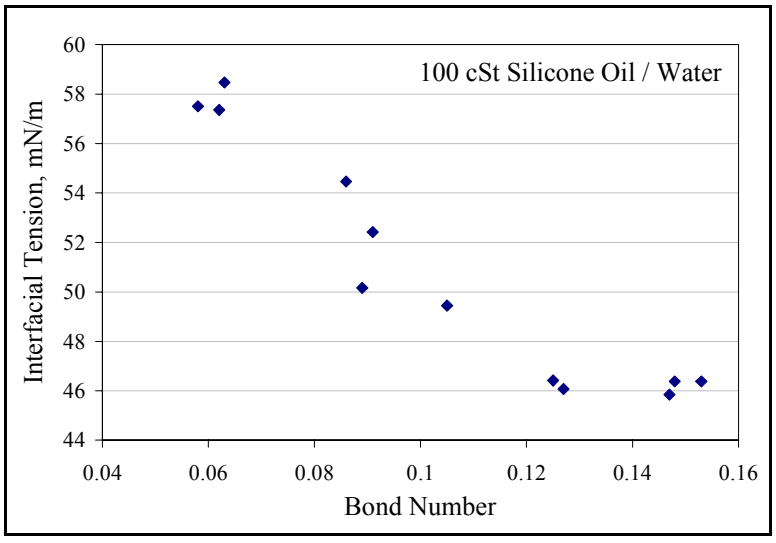

Figure 5.1.2- 4. Determination of critical Bond number for the pendant drop technique.

methanol solutions employed in them. Firstly, solutions of various concentrations of each surfactant were prepared by a volumetric method. The mass of surfactant required for the desired concentration was poured into a volumetric flask, which had been previously half-filled with warm (45 – 50°C) deoinized water and tared. A Mettler PM4000 digital balance was used for this purpose. The flask was then filled with warm water close to the mark, shaken, and left standing until the foam broke down (often overnight). At this point the flask was filled to the mark and shaken. If the surface tension of the solution was to be measured, the 500 µl syringe was filled with it and placed in the pendant drop setup (Figure 5.1.1-1).

If the measurement was of interfacial tension (with a silicone oil sample), the surfactant solution was transferred to a 250 ml rectangular glass container, which was then placed inside the glass tank (also Figure 5.1.1-1) and the syringe was filled with the silicone oil. In both cases, a small period of time, from 5 to 10 minutes, was allowed before the drop was formed so the system could approach thermal equilibrium. The temperature of the water in the glass tank was kept constant at 25.0 ±0.2 °C. At this point, a drop was formed by pressing gently in syringe's plunger. The drop was left hanging from (or clinging to) the tip of the needle for a longer period of time. This period of time was necessary to attain adsorption equilibrium of the surfactant at the interface, and it was not of a specified length. About 20 minutes after drop formation, a picture was taken and analyzed, this procedure was repeated at 10 – 15 minutes intervals until the variation of the interfacial (or surface) tension was less than 5%. Then, two more drops were analyzed using the same total period of time, and the results of the three drops were recorded and averaged. At high concentrations of surfactant, usually only half an hour

was necessary to achieve equilibrium, but at low concentration this time could be as long as an hour and a half (per drop).

In the case of clean systems, methanol/water solutions were prepared with 10, 50, and 75 %wt methanol. This solutions were prepared by weight since methanol and water form highly non-ideal solutions and their volumes are not additive (Arce *et al.* 1993). This would introduce an uncertain error if a volumetric method were used. These solutions, unlike the surfactant ones, did not produce foam. However, as a consequence of their non-ideality, they did release an appreciable amount of heat and numerous gas bubbles. Therefore, they were also let to stand for a few hours before being completed and used. The interfacial tensions of these solutions, as well as pure deoinized water and pure methanol, were then measured using essentially the same procedure described for surfactant solutions. The only difference was that since for clean systems there is no need to wait for adsorption equilibrium, the time interval between drop formation and final measurement was shortened to 15 minutes (enough to allow for thermal equilibration). Only interfacial tensions were measured with clean systems and they were done with either the straight or the U-shaped needle, whichever permitted achieving the minimum Bond number of 0.12.

5.1.4 Dynamic Surface Tension

The procedure used to measure dynamic surface tensions was basically the same as that used for equilibrium surface tensions, as previously described (section 5.1.3). The main difference was that instead of waiting to attain equilibrium before taking the pictures of the drops, these were taken continuously from the onset of drop formation. To do this, the frame grabber was programmed to take pictures at a rate of approximately 4

images per second. The image capture was started, and then the drop was quickly formed. The image capture continued for approximately 3.5 minutes (800 – 900 images). If during this time the drop fell, the frame grabber was stopped, and the process was started again. The pictures were then transferred to a Pentium 4 computer for image analysis, which was performed by the program described in section 5.1.2. This program is capable of analyzing up to 8000 images as long as they are named with the same word followed by a consecutive number. However, the analysis slows down as the number of images increases, which caused the analysis of the 800 – 900 images obtained on each experimental run to take several hours. After the analysis was completed, the data corresponding to the first few images, where the drop was still not formed, were discarded and the rest saved. This procedure was repeated twice to obtain three data sets of surface tension as a function of time per surfactant solution.

The concentration of the surfactant solution was limited to 10^{-5} mol/l to assure that the initial surface tension descent was slow enough to be captured by the described procedure. The fact that higher concentrations were not analyzed, even though they were being used in other experiments, is not important since the objective of the dynamic surface tension experiments was to obtain the surfactants' diffusivities and these do not depend on concentration. The results of both the experiments and the diffusivities calculations are presented in section 6.2.

5.1.5 Cloud Point

In order to estimate the surfactants' CMC_{II}, the cloud points of several surfactant solutions were measured according to a procedure commonly found in the literature (Koshy, Saiyad, and Rakshit 1996; Mu *et al.* 2001). First, surfactant solutions of several

concentrations were prepared following the above mentioned procedure (section 5.1.3). Then, a 2 - 3 ml sample of the solution being examined was poured into a glass test tube. The test tube was then placed in a thermostatic bath, as shown in Figure 5.1.5-1, with the temperature set to 25°C. A thermocouple was immersed into the solution and used to continuously stir the same. The bath's temperature was slowly increased by turning up the heater/recirculator's control knob, at an approximate rate of 1 – 2 °C/min. Once the solution turned hazy (the cloud point was achieved), the bath was cooled down by adding cold water until the solution was clear again. The temperature was then allowed to increase once more, but at a slower rate, to accurately record the temperature at which the solutions began to turn hazy. After the solution was completely hazy again, the heater was turned off, and the bath was cooled down slowly bay adding small amounts of cold water to it, until the solution started to clear. The temperature at which this happened was recorded, as well. The cloud point of the solution was then calculated as the average of these two temperatures. The same procedure was applied to all the surfactant solutions and curves of cloud point vs. surfactant concentration were constructed to determine the CMC_{II}. These results are reported in section 6.1.1.

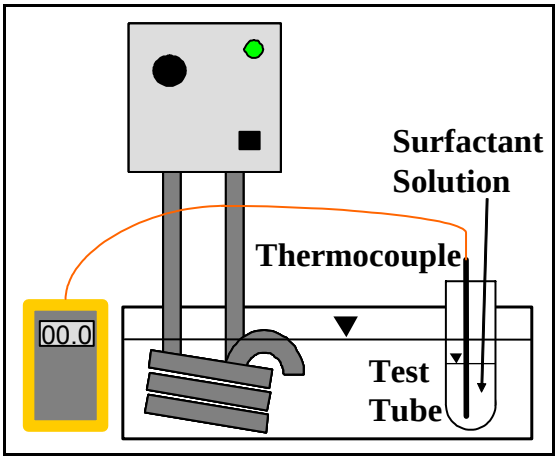

Figure 5.1.5- 1. Experimental setup for the determination of the surfactants' cloud points.

5.2 Liquid-Liquid Dispersion Experiments

The following sections will describe the equipment and experimental procedures related to the liquid-liquid dispersion experiments.

5.2.1 Equipment and Materials

The two main pieces of equipment used in the liquid dispersion experiments are the mixer, used to form the dispersions, and the microscope, used to image the drop in order to measure their size distribution. The mixer was a Silverson LR4T radial flow, high shear, rotor-stator mixer. Its mixing head consists of a four blade impeller or rotor with a diameter of 28 mm and a cylindrical stator with several openings on its side. The clearance or gap between the rotor blade tips and the stator is 0.2 mm. Figure 5.2.1-1 shows a general view of the mixer (a), as well as its mixing head (b) and a view from beneath (with the lower flange removed) where the rotor and rotor-stator gap can be observed (c). This unit has five interchangeable stators, also called heads, which differ from each other in the geometry and/or size of their openings. The only head considered in this study is the one referred to by the vendor as the slotted head, which has 16 vertical, 1.9 mm thin slots (shown in Figure 5.2.1-1(b)). The other heads available for this mixer are: the disintegrating head, with 6 round holes, the standard emulsor head, with 288 small round holes, the fine emulsor head, with 728 smaller round holes, and the square hole head, with 92, 2mm x 2mm holes. From a hydrodynamic point of view, the difference among these heads is in their power draw characteristics, evidenced by each having a slightly different power number in the turbulent regime (Padron 2001). The mixing tank is a custom-made integrated vessel made of clear glass with a volume of approximately 2 liters (Figure 5.2.1-2). The vessel's lid is made of stainless steel and is

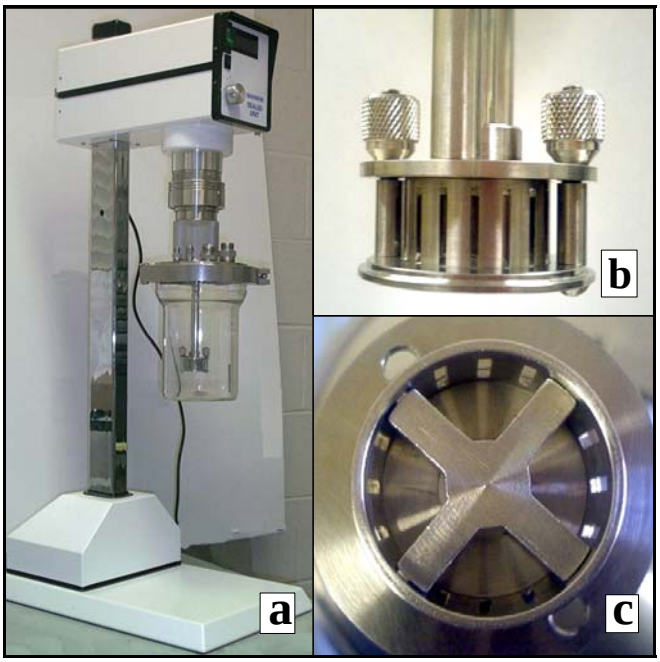

Figure 5.2.1- 1. (a) View of the Silverson LR4T mixer, (b) close up of the mixing head, (c) view from beneath the mixing head.

Figure 5.2.1- 2. Silverson's mixing tank with the mixing head in place

connected to the mixing head through 2 stainless steel rods welded to a stainless steel ring that is bolted to the base of the lid. The rotor's shaft passes through the lid and into a stainless steel cylinder which is welded to its top. Inside this cylinder the shaft goes through a mechanical seal, above which there is a water reservoir to cool down the seal while the mixer is in use. The top of the cylinder attaches to the body of the mixer and connects the rotor's shaft to the motor's shaft. The lid contains several stainless steel NPT connectors of different size threaded into its top which, among other uses, may be closed or opened to insert a thermocouple into the tank or to withdraw samples. The lid and the glass vessel both have flanges that allow them to be connected by means of a tri-clover clamp. When the tank is closed, the mixing head is fixed off-center (to avoid the formation of a central vortex when the mixer is running) at a clearance equal to 1/4 of the tank's total height, from the bottom. The impeller diameter to tank diameter ratio (D/T) is

0.25, based on the narrow section of the tank. The motor provided with this unit is a 1/3 HP, single phase motor. Its speed is variable from 100 to 9,000 rpm, depending on the load, adjustable in 100 rpm increments as regulated with a potentiometer.

The microscope is an American Optical Spencer binocular optical microscope equipped with five objective lenses: 10x, 20x, 43x, 60x, and 100x. To be able to capture digital pictures of the images obtained by this microscope, one of its eyepieces was substituted by an eyepiece base (an eyepiece with no lens) affixed to a 5 mm c-mount extension tube. This adapter allows connection of the same Watec LCL-902 K camera used for the pendant drop experiments (described in section 5.1.1). The camera sends the images, via the Integral Technologies FlashBus MX-332 frame grabber, to the Pentium III computer where they can be displayed and captured. Figure 5.2.1-3 shows the camera connected to the microscope, as well as the microscope's external light source controller. The fluids (water, methanol, and silicone oils) and surfactants employed in the liquid-

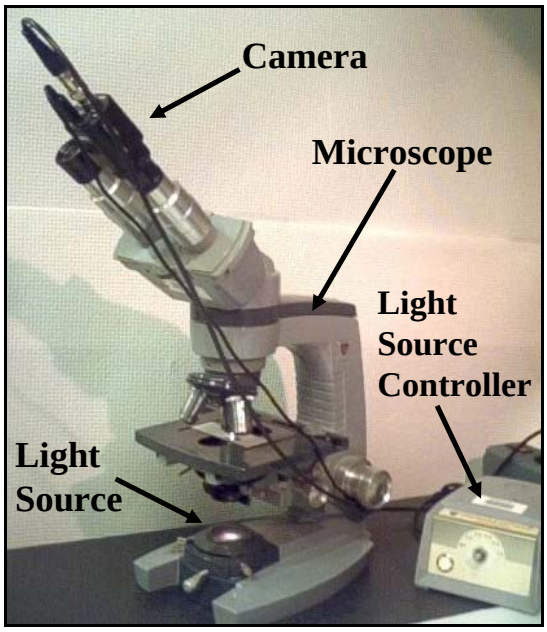

Figure 5.2.1- 3. Microscope-camera arrangement used for drop size analysis.

liquid dispersion experiments were the same as those already described for the interfacial phenomena experiments (section 5.1.1).

5.2.2 Assembly of the Experimental Apparatus

The first steps to carry out a liquid-liquid dispersion experiment were: cleaning the mixing head and tank components, preparing the solution to be used as the continuous phase (in case this phase is a surfactant or methanol solution), and assembling the mixing tank. To clean the equipment, all the components of the mixing head (rotor, stator, flange, screws, nuts, and shaft) as well as the glass vessel and its lid, were soaked. in a hot water solution containing Micro-90 (a commercial concentrated cleaning solution) and/or Alconox (a commercial powdered precision cleaner), for several hours. Afterward, all parts were rinsed thoroughly with tap water and all excess of cleaning solution and oil were manually removed. Then, they were rinsed with deoinized water. Finally, they were placed on top of paper towels to dry.

The continuous phase solutions were prepared in a similar fashion as those used for the interfacial phenomena experiments (section 5.1.3), except that a larger amount of solution (2.5 liters) was prepared for each experiment. The solution was then decanted to the glass vessel, filling it to the brim. After that, a rubber o-ring was placed on the vessel's flange. Next, the mixing head was submerged completely into the solution, while turning the rotor's shaft manually to expel all the air from inside the head. The lid was then aligned on top of the o-ring, and the clamp was placed around the vessel's and lid's flanges to seal the mixing tank. Additional solution was poured into the tank through one of the open connectors on top of the lid until all air bubbles had been evacuated and the tank was completely filled (this could be corroborated visually since the glass vessel is

transparent). In the case of surfactant solutions, since these have the tendency to form semi-stable foams, the tank was filled to the extent possible and sealed. It was then left overnight in a slanted position (wedged against a wall) before the final filling. This would give the foam time to break down and the slanted position allowed all the released air to be collected into one big bubble which was easier to expel.

Once the tank was completely filled with continuous phase, it was partially immersed in a large rectangular glass tank (aquarium), and attached to the mixer's body. Then, a type K thermocouple connected to an Omega handheld model HH11 digital thermometer was inserted into the tank trough the smaller NPT connector, and positioned so that the tip of the sensor was at the level of the mixing head. Figure 5.2.2-1 shows a diagram of the entire experimental apparatus. The heater/recirculator provided enough circulation to maintain a nearly constant temperature throughout the aquarium. When the

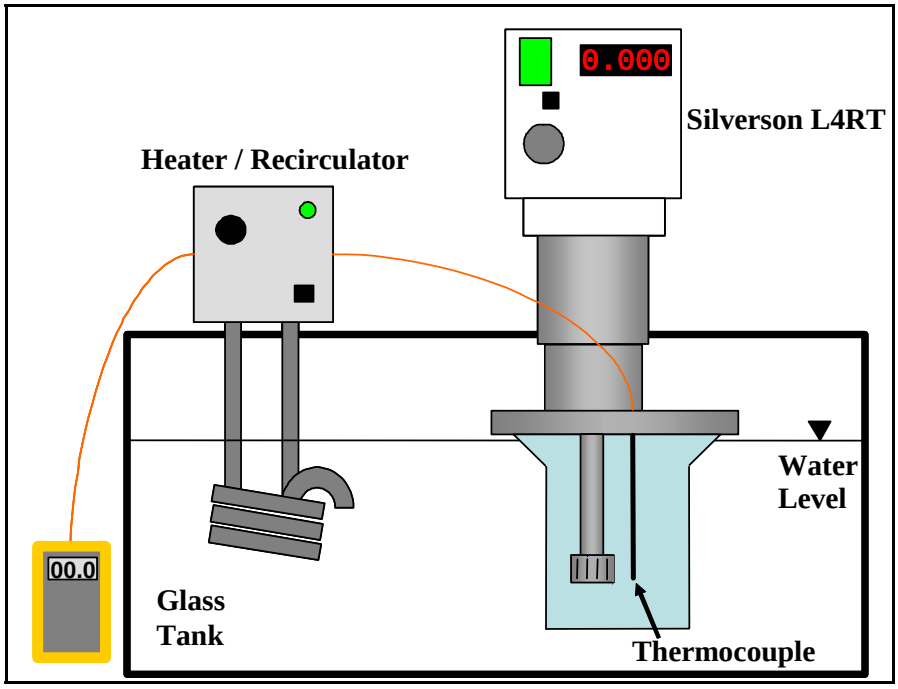

Figure 5.2.2- 1. Complete experimental setup used for liquid-liquid dispersion experiments.

mixer was run at low rotor speeds (2000 – 3000 rpm), it didn't generate enough heat to increase the temperature in the mixing tank. Since the temperature in the laboratory was below 25°C, the heater/recirculator alone was enough to keep the temperature inside the mixing tank consistently at 25 ± 1°C. At higher speeds (4000 – 7000 rpm) however, the heat generated was significant and since the heater/recirculator does not have cooling capabilities, crushed ice was added to the aquarium periodically to keep the temperature inside the mixing tank within the same range. This apparatus was housed inside the laboratory's fume hood since one of the fluids used in the continuous phase, methanol, is volatile. An additional benefit of the fume hood was that the noise generated by the mixer could be minimized by closing down the front window.

5.2.3 Procedure for Forming Dispersions

Once the mixing tank was charged with the continuous phase, assembled, and placed in the aquarium, the following procedure was followed. The mixer was turned on and set to 2000 rpm. As soon as the temperature inside the mixing tank reached its desired range (25 ± 1 °C), approximately 2 ml of the silicone oil corresponding to the particular experiment being run was injected into the tank using a 5000 μl Gastight® Hamilton syringe outfitted with a 6", 18 gauge needle (outer diameter = 1.27 mm). This amount of oil corresponds to a dispersed phase content of 0.1%v/v ($\phi = 0.001$). The oil was injected just below the mixing head, one drop at a time, or, in case of low interfacial tension systems, one short "squirt" at a time, to ensure that the entire dispersed phase immediately goes through the mixing head. About two hours were allowed to achieve the equilibrium drop size distribution. After that, a sample of the dispersion is withdrawn with a pipette (details of this procedure will be given in the next section) and the speed of

the mixer was increased by 1000 rpm. This procedure is repeated until the maximum rotor speed of 7000 rpm is reached.

In the case of the continuous phase aqueous methanol solutions, the oil was injected at a lower rotor speed (1500 – 1800 rpm). The mixer was run at this lower speed for half an hour and then it was increased to 2000 rpm. This was done because silicone oil is slightly soluble in alcohols, and therefore, putting the phases in contact before reaching the experimental conditions ensures that they will saturate with each other before the experimental conditions are set. This minimizes any effect that the solubility may have on the equilibrium drop size, i.e. drops that have already reached equilibrium size losing mass (or gaining it) due to solubilization of one phase into the other. The density difference between aqueous methanol solutions and silicone oils is small enough ($\Delta\rho \approx 1 – 36$ kg/m^3) that there was no significant risk of phase separation at the lowest rotor speed considered.

5.2.4 Sampling and Sample Analysis

The dispersion samples were withdrawn from the mixing tank using Fisherbrand® disposable serological 5ml pipettes. These pipettes were selected for sample withdrawal because they have a wide mouth (~2.2 mm inner diameter), which allows them to fill up quickly without subjecting the sample to significant shear. To take the sample, the pipette was introduced, through one of the NPT connectors, all the way to the bottom of the tank allowing it to fill up during its descent. Then it was stoppered, withdrawn from the tank, and wiped with a clean paper tissue. Before closing the NPT connector, the tank was replenished with continuous phase to evacuate the air in the mixing tank The sample was transferred to a glass vial containing a small volume of a concentrated surfactant

solution.. The concentration of the surfactant solution in the vial was such that the total sample (withdrawn volume + solution volume) would have a surfactant concentration in the range 50 – 100xCMC (samples for experiments run at 100xCMC did not require any more surfactant). Next, a few drops of the sample were placed on a microscope slide which was then positioned under the microscope so that images of the drops may be captured.

The microscope slides had been previously customized to handle dispersion samples by placing three stacked layers of adhesive tape at their end and close to their center (see Figure 5.2.4-1). The sample was placed between the stacked tape layers and then a cover glass was placed on top so that it rested on the tape. This prevented the oil drops in the sample from being compressed by the cover glass's weight, which would have resulted in erroneous drop diameter measurements. The space created by the tape stacks had a height of approximately 180 μm, which was enough to accommodate even the largest oil drops created during these experiments.

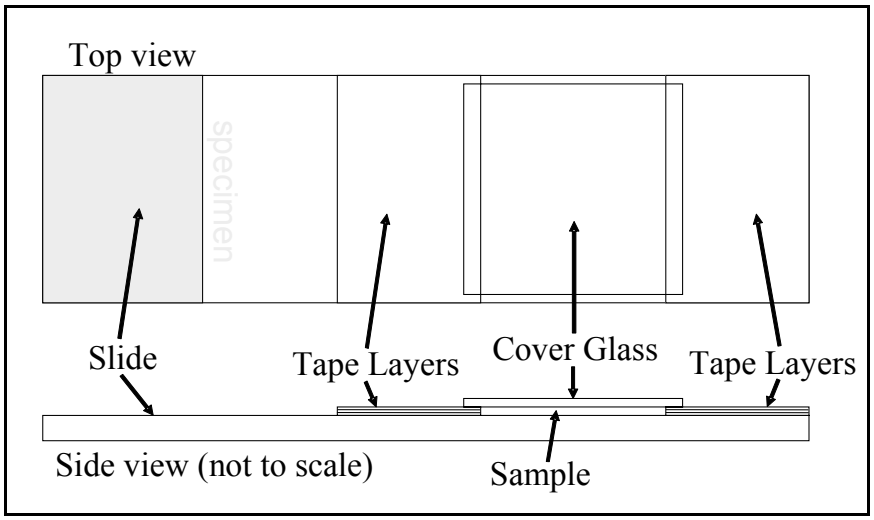

Figure 5.2.4- 1. Schematic representation of a customized microscope slide.

The slide was placed under the microscope in such a way that the upper-left corner of the sample region was directly under the objective lens and the image was focused until the oil drops were clearly visible on the computer display. After the first image was captured, the slide was moved (using the microscope's stage control knobs) towards the microscope (the image would scroll down in the computer screen), until the next drop or group of drops was within the field of view. At this point, the image was refocused (if necessary) and a new picture taken. The slide was continually scrolled (and pictures taken) in the same direction until its lower edge was reached. Then, the slide was scrolled towards the left a distance equal to or larger than the field of view, and then in the opposite direction as before, until the upper edge of the slide was reached. The slide continued to be systematically scrolled in this way until a sufficient number of drops had been captured or until the lower-right corner of the sample was reached; in which case a new slide was prepared to continue the image acquisition. Care was taken not to capture images with air bubbles in them, since they would be considered drops by the image analysis software. Air bubbles were easily distinguishable from oil drops, under the microscope. They showed as considerably thicker circles, compared to the thin ones shown in Figure 2.2.3.1-1, corresponding to oil drops. Additionally, air bubbles were always moving fast, oil drops moved slower or not at all.

Drop image capture was accomplished using the FBG application (part of the frame grabber's application software). The images were saved in an appropriately identified folder on the computer's hard drive, and the capture mode was set to manual. Each capture was triggered by clicking on the "grab" button and the picture was automatically saved giving the file the name "figure" followed by a consecutive number,

starting from 000. Enough images were captured to ensure a count of at least one thousand drops. These images were later analyzed using the image analysis procedure described in section 2.2.3

5.3 Summary

This chapter described in detail the experimental methods and equipment used in the present study. The interfacial phenomena experiments were conducted via a pendant drop technique. This technique is based on an equilibrium between surface or interfacial tension and gravitational forces acting on a static drop hanging from a needle. The procedure used to measure equilibrium and dynamic interfacial and surface tensions of surfactant and clean systems was explained. Including the procedure by which the aqueous surfactant and aqueous methanol solutions were prepared. Additionally, the method used to estimate the CMC_{II} of the surfactants, which is based on the measurement of their cloud points, was described.

The procedures involved in the liquid-liquid dispersion experiments were also described. These included cleaning and assembling of the mixing vessel, formation of the dispersions, sample withdrawal, and sample analysis.

CHAPTER 6. INTERFACIAL PHENOMENA EXPERIMENTAL RESULTS

The results of the previously described interfacial phenomena experiments are presented in this chapter. These results constitute a comprehensive characterization of the interfacial behavior of the surfactants employed in this study, both equilibrium and dynamic, and of the clean methanol/water/silicone oil systems. First, the equilibrium surface and interfacial tensions of surfactant-laden and clean methanol/water systems will be reported. The fit of the surfactant data to the Langmuir – von Szyszkowski equation of state is also shown. Then, the dynamic surface tension results are described, along with the outcome of the surfactant diffusion coefficient calculations. The Langmuir parameters obtained from equilibrium measurements and the aforementioned diffusivities are then combined, along with timescale estimation equations derived in chapter 3, to predict values for the surface dilational modulus of the aqueous surfactant/oil interfaces. Finally, the physicochemical hydrodynamics of translating oil drops in surfactant solutions is addressed.

6.1. Equilibrium Surface and Interfacial Tensions

The equilibrium behavior of three different systems was measured: aqueous surfactant/air, aqueous surfactant/silicone oil, and aqueous methanol/silicone oil. The results for all three will be presented in the following sections, along with comparison to literature values, when possible.

6.1.1. Surface Tension of Surfactant Systems

Figure 6.1.1-1 shows the equilibrium surface tension as a function of surfactant bulk concentration for Tergitol TMN-6, Triton X-100, and Triton X-165. Each data point is the average of 3 – 5 measured values and their variation is represented by vertical error bars. Clearly, the three surfactants show the expected behavior: the surface tension decreases with increasing concentration until it reaches a constant value when the critical micelle concentration is exceeded. The CMC were calculated by extrapolating the best linear regression of the 3 or 4 data points before the slope break, and intersecting it with the linear regression of the points after the break. The results are presented in Table 6.1.1-1. The solid lines in Figure 6.1.1-1 are the best fit to the Langmuir – von Szyszkowski equation of state (equation 4.3.1-14). By fitting this equation to the data, the values for

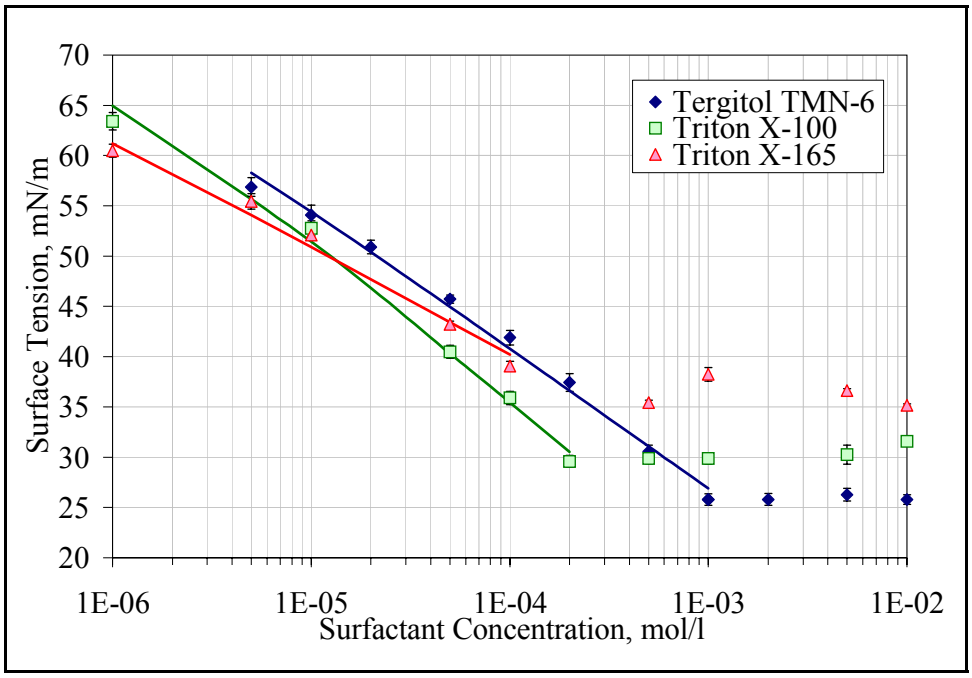

Figure 6.1.1- 1. Equilibrium surface tensions for the three surfactants. Solid lines are the best fit to the Langmuir – von Szyszkowski equation of state (T = 25°C).

Table 6.1.1- 1. Critical micelle concentration, saturation surface excess concentration, and Langmuir constant for surfactants at the water/air interface (T = 25°C).

	CMC mol/l	Γ_∞ mol/m^2	a_L mol/l
Tergitol TMN-6	1.03×10^{-3}	2.44×10^{-6}	5.77×10^{-6}
Triton X-100	2.19×10^{-4}	2.87×10^{-6}	5.91×10^{-6}
Triton X-165	1.44×10^{-4}	1.88×10^{-6}	1.09×10^{-7}

the saturation surface excess concentration (Γ_∞) and the Langmuir constant (a_L) were obtained for each surfactant. The results are also presented in Table 6.1.1-1.

The surface tension values obtained for Triton X-100 are within 2 to 8% of the values reported by Göbel and Joppien (1997) over the range 10^{-5} – 5×10^{-4} mol/l, measured with the pendant drop technique as well as with a Wilhelmy plate. The CMC value obtained by the same authors for Triton X-100 is 2.63×10^{-4} mol/l, and the one reported by Lin, McKeigue, and Maldarelli (1990) is 2.3×10^{-4} mol/l, both consistent with the one found in the present study. There is also good agreement between the calculated values of Γ_∞ and a_L and the ones found by Lin, McKeigue, and Maldarelli (1990) of 2.91x10-6 mol/m2 and 6.62x10-6 mol/l, respectively; and to a lesser degree with those of Ravera *et al.* (1997) of 3.2×10^{-6} mol/m^2 and 1.4×10^{-6} mol/l. The only values known for Tergitol TMN-6 are those reported by the manufacturer for the CMC (0.058 %wt ~ 1.07×10^{-3} mol/l) and for the equilibrium surface tension at 0.1 %wt (26 mN/m), both of which compare well to the values in Table 6.1.1-1 and Figure 6.1.1-1. No reported values were found for Triton X-165 for any of these parameters.

Figure 6.1.1-2 shows the variation of the cloud point with surfactant concentration for Tergitol TMN-6 and Triton X-100. The minima in these curves indicate the location of the second critical micelle concentration. The value found for Tergitol is

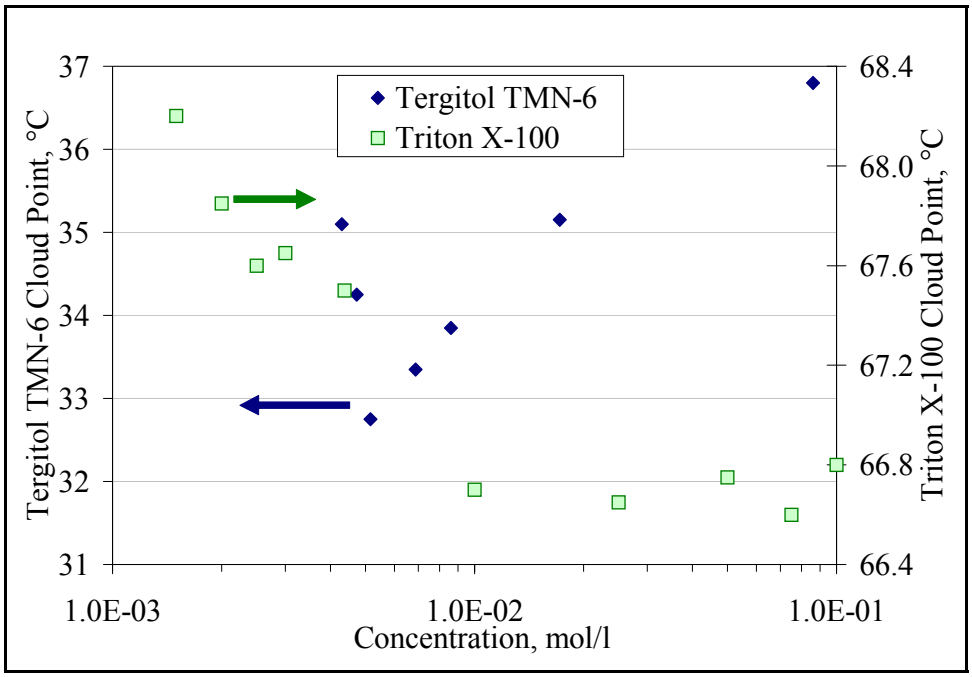

Figure 6.1.1- 2. Cloud point vs. surfactant concentration for Tergitol TMN-6 (left scale) and Triton X-100 (right scale).

approximately $5x10^{-3}$ mol/l ($CMC_{II} \approx 5xCMC$) and the one for Triton is close to 0.02 mol/l ($CMC_{II} \approx 90xCMC$). Values of CMC_{II} between 2 and 3 %wt (0.03 – 0.04 mol/l) have been reported for Triton X-100 (Koshy, Saiyad, and Rakshit 1996; Qiao and Easteal 1998). The cloud point of Triton X-165 is higher than 100°C (Flick 1993), therefore immeasurable. Based on these findings the maximum concentrations to be used in the liquid-liquid dispersion experiments were set to 5xCMC for Tergitol and 100xCMC for both Tritons.

6.1.2. Interfacial Tension of Surfactant Systems

Figure 6.1.2-1 is equivalent to Figure 6.1.1-1 but for interfacial tension at the water/silicone oil interface. The CMC and Langmuir – von Szyszkowski parameters were similarly computed for these systems and are reported in Table 6.1.2-1.

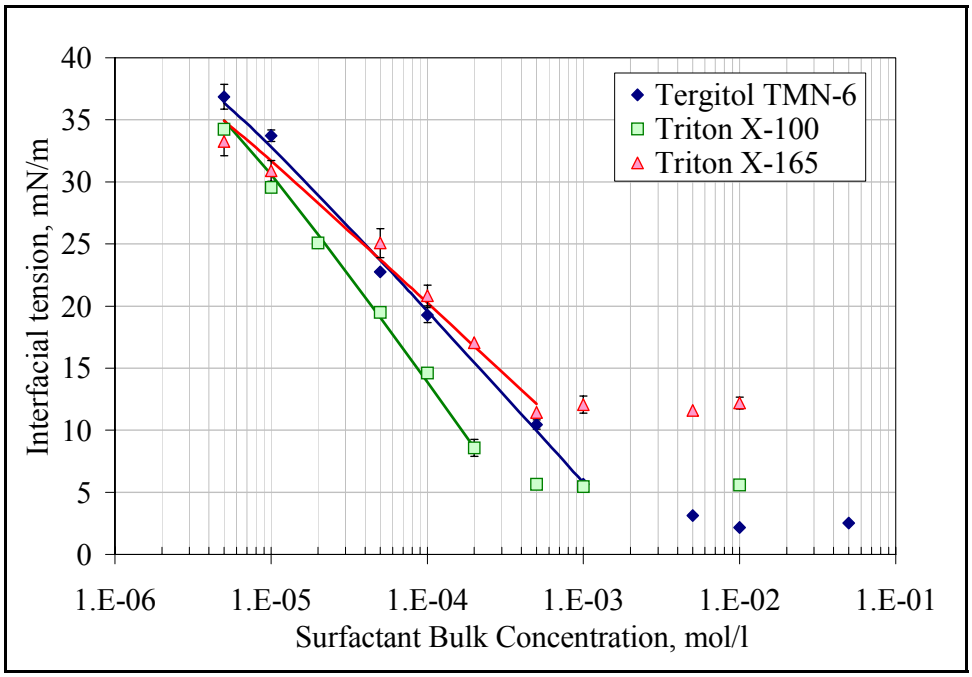

Figure 6.1.2- 1. Equilibrium interfacial tensions (water/100 mPa·s silicone oil) for three surfactants. Solid lines are the best fit to the Langmuir – von Szyszkowski equation of state (T = 25°C).

Table 6.1.2- 1. Critical micelle concentration, saturation surface excess concentration, and Langmuir constant for surfactants at the water/silicone oil interface (T = 25°C).

	CMC mol/l	Γ_∞ mol/m^2	a_L mol/l
Tergitol TMN-6	1.72×10^{-3}	2.43×10^{-6}	1.21×10^{-6}
Triton X-100	3.02×10^{-4}	3.09×10^{-6}	1.50×10^{-6}
Triton X-165	4.63×10^{-4}	2.05×10^{-6}	6.04×10^{-7}

Unfortunately, interfacial properties studies with silicone oils are scarce in the literature and, as a result, there are no comparative values available. However, some comparisons with the water/air results are possible. The general trends observed are fairly similar between the two systems and the above-CMC values are of the same order (Triton X-165 > Triton X-100 > Tergitol TMN-6). The increase in the saturation surface excess concentrations and CMC is consistent with a change in orientation of the molecule due to

an increase in affinity of the surfactant for the non-aqueous phase (Hansen and Fagerheim 1998). This is to be expected since, in liquid-liquid systems, surfactants are usually soluble, at least to some extent, in both phases. An implication of this dual solubility is that surfactants may actually transfer from one phase to the other. This behavior is characterized by the partition coefficient. This parameter was measured here experimentally, but the results were not very conclusive since only the order of magnitude of the coefficient could be approximated. Nevertheless, these approximated values indicated that it was reasonable to neglect the effect of partitioning the liquid-liquid dispersion experiments. The details of the partition coefficient measurement and the analysis of results are given in Appendix A.

The values of equilibrium interfacial tension plotted in Figure 6.1.2-1 were measured for the 100 cSt silicone oil. Nevertheless, the equilibrium interfacial behavior of silicone oils, in the viscosity range used in this study, is independent of viscosity. Figure 6.1.2-2 shows the interfacial tension of silicone oils of various viscosity grades against water, air, and aqueous surfactant solutions at concentrations below and above their respective CMC. It is evident form this graph that any effect that oil viscosity may have on the equilibrium interfacial tension can be neglected.

6.1.3. Interfacial Tension of Clean Systems

The interfacial tension of surfactant-free aqueous methanol/silicone oil systems is presented in Figure 6.1.3-1 as a function of methanol concentration. The observed non-linear behavior is caused by the also non-linear variation of the density of water/methanol solutions with methanol concentration (Arce *et al.* 1993). However, it is also noticeable that the viscosity of the oil, again, plays no role on its interfacial behavior.

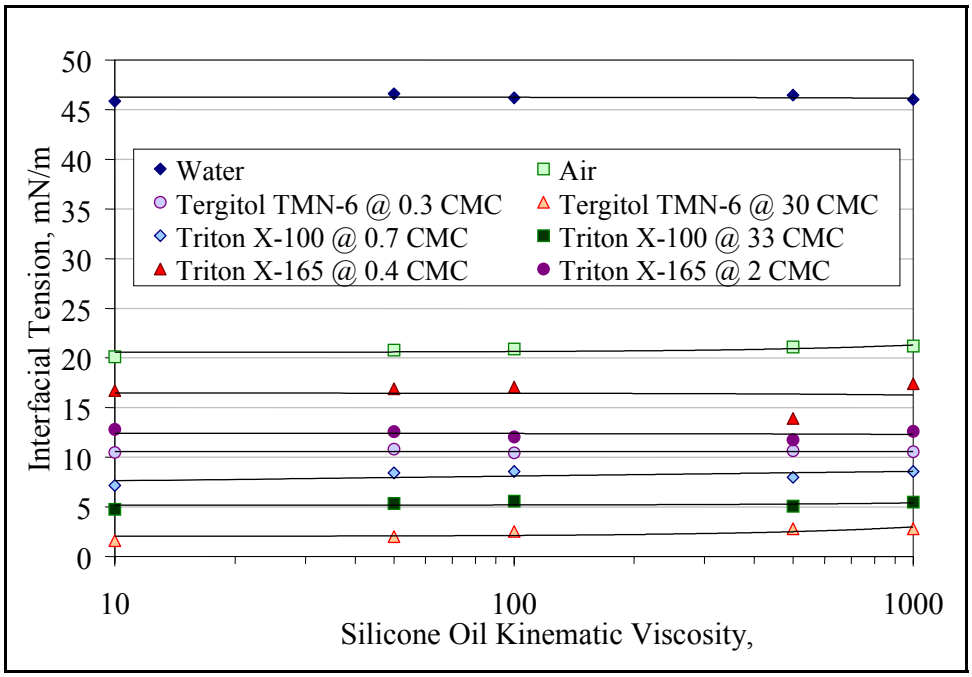

Figure 6.1.2- 2. Interfacial tension of silicone oils against different phases. The values for air are those reported by the manufacturer, the rest were measured via the pendant drop technique (T = 25°C).

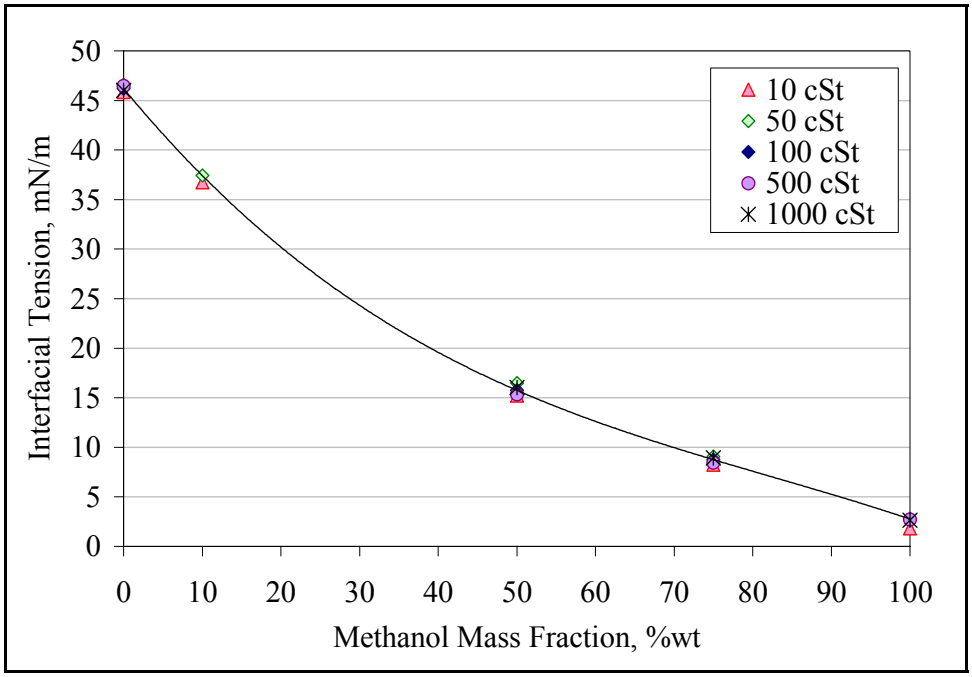

Figure 6.1.3- 1. Equilibrium interfacial tension of aqueous methanol/silicone oil systems (T = 25°C).

These values compare relatively well with those reported by Wang and Calabrese (1986) for the same systems (within 2 – 5 % for the range 0 – 50 %wt; 24 % for 75 %wt). There is a discrepancy with these author's data for pure methanol, with their value being less than half of the one reported here. This discrepancy may be due the difference in experimental technique since Wang and Calabrese used a du Noüy ring method. The present value of 2.7 mN/m agrees better with the value reported by Phongikaroon (2001), 2.1 mN/m, measured also with a pendant drop technique.

6.2. Dynamic Surface Tension and Diffusivity

The dynamic surface tension of surfactant solutions was measured according to the experimental method described in Chapter 5 and the data were fit to the long times approximation of the Ward – Tordai equation (equation 4.4.2-12) to estimate the surfactant diffusion coefficient in aqueous solutions. The use of this equation presupposes that the adsorption is diffusion-controlled. As indicated in chapter 4, this assumption is reasonable for nonionic surfactants at concentrations well below the CMC. A fixed concentration of 10^{-5} was chosen for all surfactant solutions to ensure the applicability of the assumption and to obtain a variation of surface tension with time that is slow enough to be adequately captured with the employed experimental technique. It is assumed that the diffusion coefficient so obtained is independent of surfactant concentration so that the result can be applied at arbitrary concentration.

To verify that the data obtained is consistent with the long times approximation, the surface tension was plotted against the inverse of the square root of time. According to equation 4.4.2-12, this should result in a straight line that intersects the coordinate axis at the corresponding equilibrium value. Figure 6.2-1 shows this plot for the Triton X-100

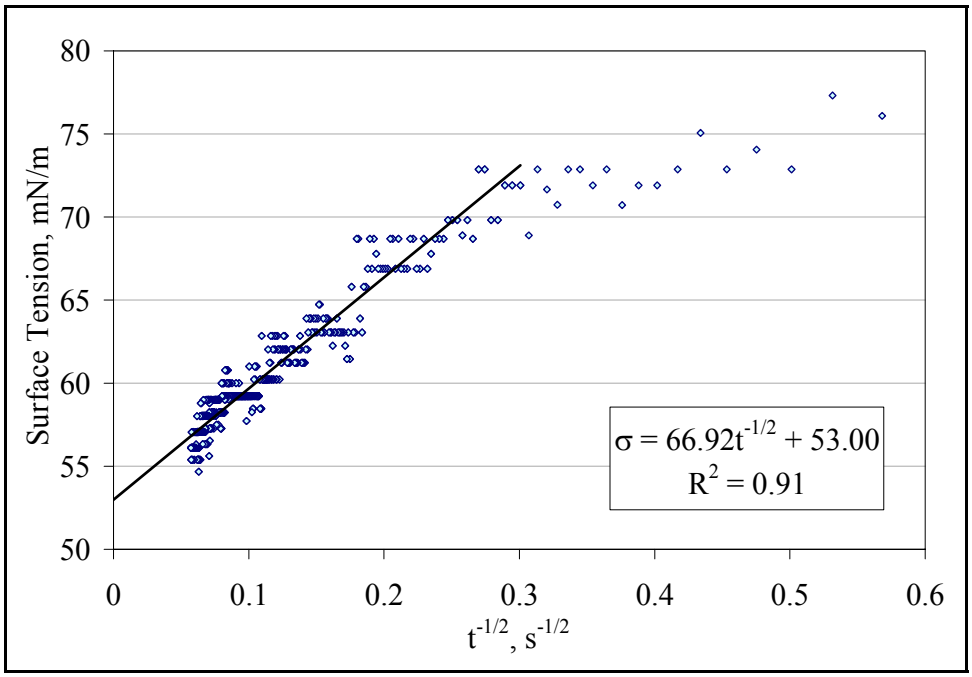

Figure 6.2- 1. Fit to the Ward – Tordai long times approximation equation for a Triton X-100 solution. $C_0 = 10^{-5}$ mol/l, T = 25°C.

solution. It shows that as time increases ($t^{-1/2} \rightarrow 0$), the data does fall fairly well on a straight line and its intersection value, 53.00 mN/m, is practically the same as the equilibrium surface tension value of 52.8 mN/m obtained for this surfactant concentration. The diffusion coefficient could very well be obtained from this linear fit. However, given the scatter seen in the data, it was preferred to fit equation 4.4.2-12 to the $\sigma(t)$ data by converging on the diffusion coefficient that gave the least total error between experimental and calculated values of $\sigma(t)$ (excluding the data points that did not fall in the linear region of the $\sigma(t^{-1/2})$ plot). This fit is shown in figure 6.2-2. The initial data points, aside from not conforming to the long times approximation, may also contain significant error, as evidenced by the fact that values above 72 mN/m, (corresponding to pure water) were obtained. This may be due to vibrations originating during the manual formation of the drop.

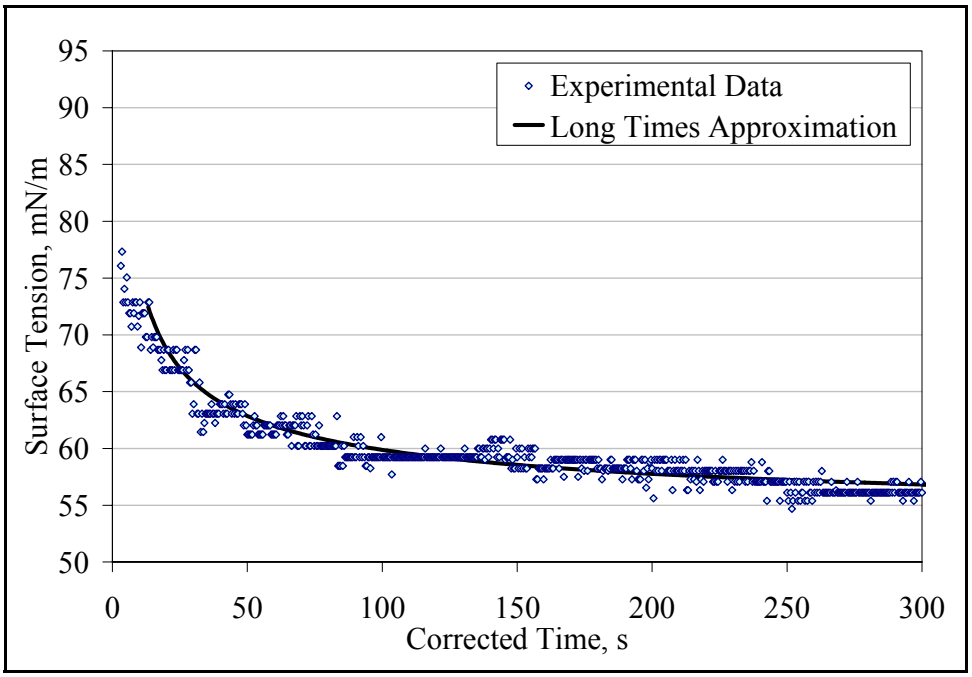

Figure 6.2- 2. Dynamic surface tension of a Triton X-100 solution. $C_0 = 10^{-5}$ mol/l, T = 25°C.

To attain the highest image capture rate, the frame grabber was set at AFAP (as fast as possible), which doesn't allow specification of the exact time interval between images. The time associated with each data point was obtained from the time information record of the computer for each consecutive drop image. A plot of elapsed time against image number was constructed for each experiment to obtain a correction factor that allows transforming the image number into real time (the linear regression coefficients of these plots were always between 0.99 and 1).

The curve fitting procedure was done in triplicate for each surfactant solution. The values used for the surface excess concentration were calculated through the Langmuir isotherm (equation 4.3.1-13) using the corresponding Γ_∞ and a_L constants reported in Table 6.1.1-1. The average diffusion coefficients, so determined, are given in Table 6.2-1, along with the surfactants molecular weight to show that, as expected, the

molecular diffusivity decreases as the molecular weight increases. The diffusivity of Triton X-100 has been measured by several authors. Figure 6.2-3 shows a comparison of the value reported herein and some from the literature. Even though there are large discrepancies in the data, the present value is within the same range, at least, to an order of magnitude approximation.

Table 6.2- 1. Average diffusion coefficients and molecular weights of the three surfactants (T=25°C)

	D_{AB} ($x10^{-10}$) m^2/s	MW g/mol
Tergitol TMN-6	8.10 ± 1.6	543
Triton X-100	5.02 ± 0.04	624
Triton X-165	1.15 ± 0.30	879

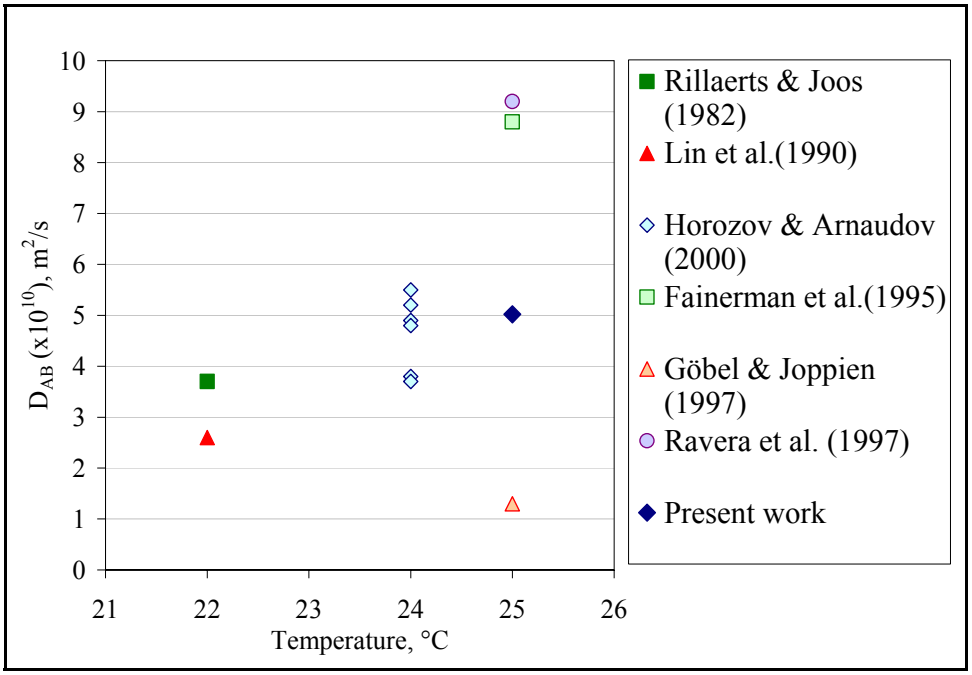

Figure 6.2- 3. Diffusion coefficients reported for Triton X-100. Comparison with literature data.

6.3. Prediction of Surface Dilational Modulus

Once the equilibrium behavior and the diffusion coefficient of the surfactants are known, the surface dilational modulus (E^{sd}) can be predicted through equation 4.5.2-14, as long as a suitable deformation timescale can be determined. The expressions for the possible deformation timescales in turbulent liquid-liquid dispersions were defined in chapter 3 (equations 3.3.3.1-1, 3.3.3.2-1, 3.3.3.3-2, and 3.4-2 thru -4, depending on turbulence regime and the use of the eddy lifetime or the drop deformation timescale). One common factor in all these equations is the turbulent energy dissipation rate, ε. Therefore, the appropriate values of ε must be determined first, regardless of the timescale ultimately used.

The average energy dissipation rate in the tank, $\bar{\varepsilon}$, can be approximated by equation 3.3.1-9. However, this approximation doesn't take into account the dissipation rate's broad spatial variation throughout the tank. As explained in chapter 3, the drop size in a turbulent dispersion scales better with the maximum dissipation rate, achieved near the impeller, instead of the volumetric average. An estimation of the order of magnitude of ε_{max} can be obtained using the impeller swept volume instead of the total tank volume (Kresta and Brodkey 2004). Using previously obtained power draw data for the Silverson L4RT mixer and stator head used in this study, both average and maximum dissipation rates were calculated. The actual power (P) data, corresponding to that of Figure 4.3-2 in Padron (2001), was used in equation 3.3.1-9 (assuming $A_3 = 1$) for the calculation, instead of the average power number of 2.1, reported in the same reference. The results of these calculations are presented in Figure 6.3-1. The impeller swept volume was estimated as the mixing head volume, delimited by the diameter of the flanges of the

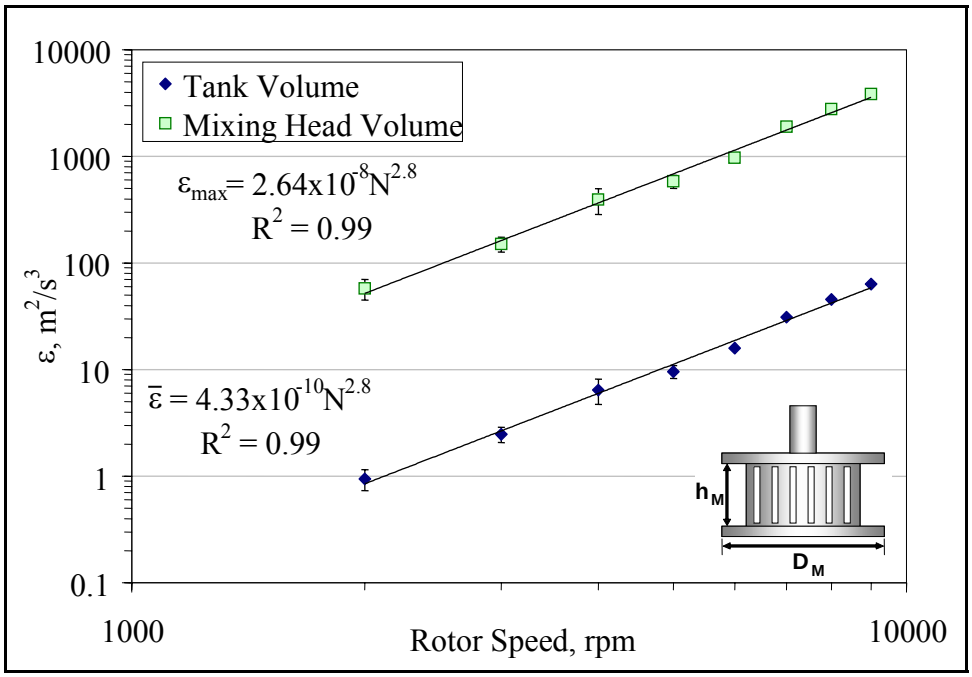

Figure 6.3- 1. Average and maximum turbulent kinetic energy dissipation rates calculated from power draw data for the Silverson L4RT mixer.

mixing head, D_M, and the height of the stator, h_M (see insert in Figure 6.3-1). The reported ε values are proportional to, roughly, N^3; which agrees with the assumption made in equation 3.3.1-11. ε_{max} was used to estimate the deformation time scales and, thus, the surface dilational modulus. Henceforth, when the turbulent energy dissipation rate is used, it will implicitly refer to ε_{max} and to the values herewith shown.

Figure 6.3-2 shows the calculated surface dilational modulus for Tergitol TMN-6, Triton X-100 and Triton X-165 for a specified set of conditions (drop diameter, oil viscosity, ε, turbulence regime, and timescale). All curves show the behavior described in Chapter 4: an initial increase with concentration until a maximum value is reached and then a decrease to negligible values. The maximum values of E^{sd} achieved for each surfactant are in the order of their diffusivities. The larger the diffusion coefficient, the

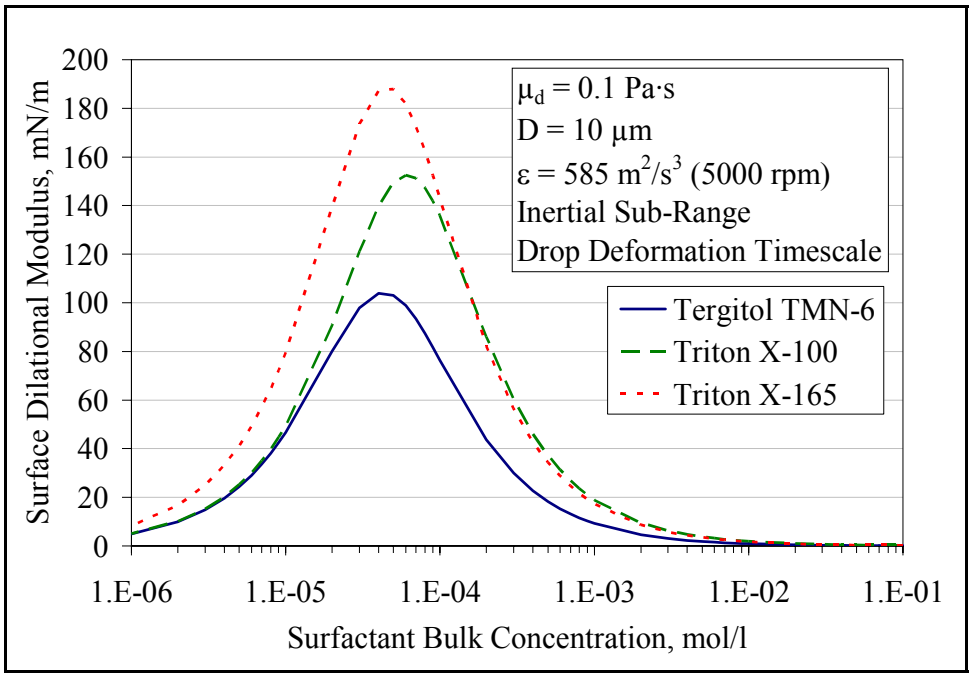

Figure 6.3- 2. Surface dilational modulus, E^{sd}, as a function of surfactant concentration for three surfactants.

lower the maximum, because the Marangoni stresses are relaxed by diffusion of surfactant molecules from the bulk phase. The maximum values also depend on the magnitude of the deformation timescale because more rapid deformations (lower timescales) are more likely to be over before enough surfactant has adsorbed and, therefore, the Marangoni stress relaxation will be lower. The deformation timescale depends on the oil viscosity, the drop size, ε, the turbulence regime, and the assumed timescale. Drops of lower viscosity and larger size are deformed faster; therefore E^{sd} increases with drop diameter and with decreasing viscosity. The larger the energy dissipation rate, the faster the interface is deformed; hence E^{sd} is proportional to ε. The effect of the regime and timescale are shown in Figures 6.3-3 and 6.3-4. The eddy lifetimes tend to be lower than drop deformation (drop stretching) timescales for all regimes, but the difference decreases for lower viscosity oils.

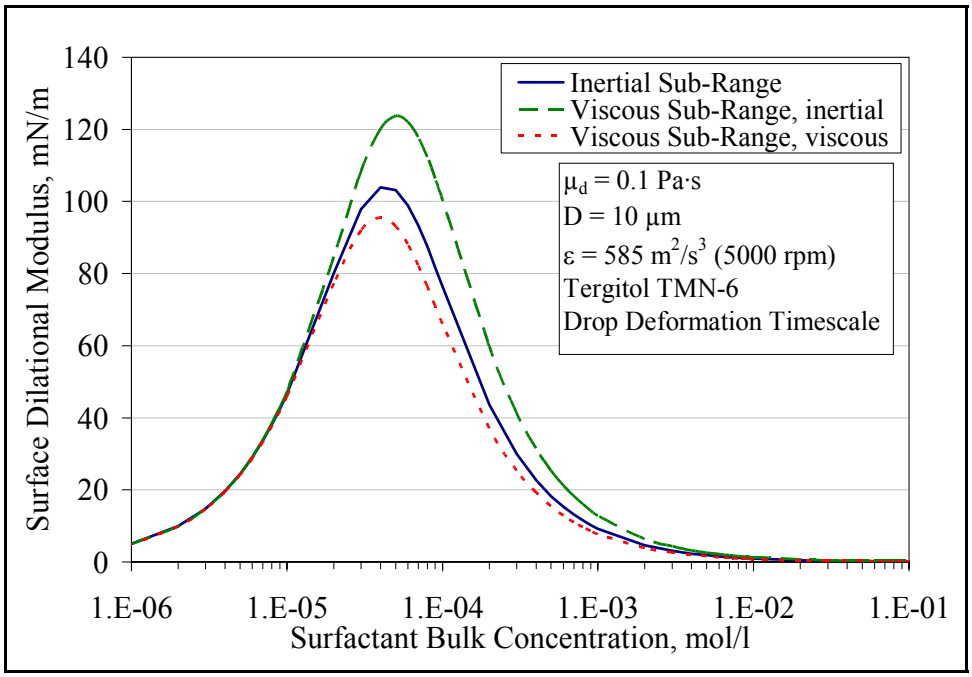

Figure 6.3- 3. Surface dilational modulus, E^{sd}, vs. surfactant concentration for Tergitol TMN-6 for the different turbulence sub-ranges.

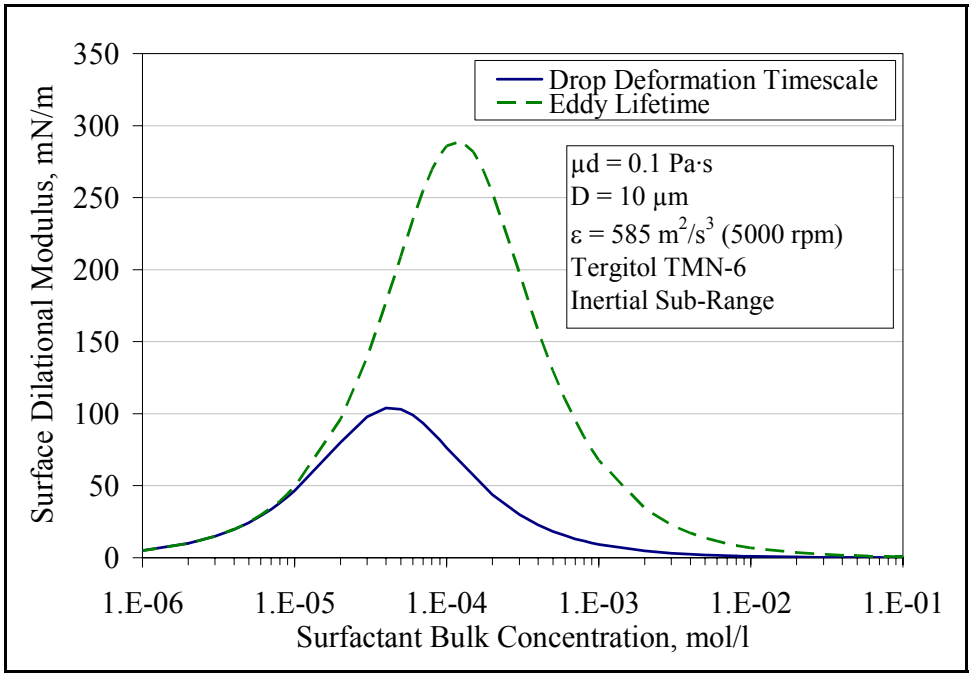

Figure 6.3- 4. Surface dilational modulus, E^{sd}, vs. surfactant concentration for the two possible types of deformation timescale.

The location of the maximum, i.e. the concentration at which the maximum E^{sd} is reached, is approximately the same for all three surfactants (see Figure 6.3-2). The exact concentration depends on the values of the aforementioned parameters, but it was found to range approximately from $3x10^{-5}$ to $1.5x10^{-4}$ mol/l, reaching extreme values of 10^{-5} and $2x10^{-4}$ mol/l under certain combinations. This means that the maximum E^{sd} is always reached at concentrations below the CMC. The maximum location of each surfactant relative to the others remains the same regardless of the particular conditions.

Experimentally measured values of the surface dilational modulus reported in the literature vary from 1 to 1000 mN/m, depending on surfactant parameters and the rate of deformation used. Most of these studies were done for the water/air interface (Lucassen-Reynders and Wasan 1993). Lucassen and van den Tempel (1972) reported a decrease in the maximum E^{sd} and the concentration at which it is achieved for decanoic acid at the water/air interface as the deformation timescale increased. This agrees qualitatively with the behavior predicted by equation 4.5.2-14. More recently, Jiang, Chiew, and Valentini (1992) measured the dilational modulus of Triton X-100 at the air/water interface by studying the damping of capillary waves. They found a maximum of about 40 mN/m at a concentration of approximately $2x10^{-5}$ mol/l and a deformation frequency of 150 Hz. Using the parameters for air/water interfaces reported in Table 6.1.1-1, the maximum value obtained from equation 4.5.2-14, for an equivalent deformation timescale of 0.0067 seconds, is 54 mN/m at a concentration of $9x10^{-5}$ mol/l. Even though there are numerical differences this comparison shows that the approach presented here, despite being based on ideal behavior (Langmuir adsorption), can produce reasonable estimates of the surface dilational modulus. Similar conclusions were drawn by Bonfillon and Langevin (1993),

who measured the viscoelasticty of Triton X-100 monolayers at the water/dodecane interface through longitudinal wave damping and compared their results to the Lucassen – van den Temple equation (4.5.2-10). This study was limited, however, to large concentrations (mostly post-CMC) and low deformation frequency (0.6 Hz).

Equation 4.5.2-14 will later be used in combination with the mechanistic model equations derived in Chapter 3 to correlate experimental drop size data for surfactant systems. This results, as well as a detailed explanation of the approach used, will be presented and discussed in Chapter 8.

6.4. Physicochemical Hydrodynamics

In chapter 4, the parameter δ_D/h was introduced as a scaling factor for Marangoni stress relaxation for a spherical drop moving through a surfactant laden solution. The diffusion layer thickness, δ_D, depends on the drop size, the diffusion coefficient, and the characteristic velocity of the flow. The adsorption depth, h, depends on the equilibrium surface excess concentration and the surfactant bulk concentration. Figure 6.4-1 shows δ_D/h as a function of surfactant concentration for typical conditions: a 10 μm drop, in the flow generated by the mixer at 5000 rpm. The characteristic velocity was assumed to be $\varepsilon^{1/3}D^{1/3}$, as given by equations 3.2.1-4 and 3.3.1-2. Strictly, this assumption is valid for the inertial sub-range, but it can provide an order-of-magnitude approximation in the viscous sub-range. It is evident from the plot that at the highest concentrations the value of δ_D/h barely reaches unity. The maximum δ_D/h calculated varying the drop size and ε within experimental conditions was 4. This means that Marangoni stresses are acting on the drops as they translate in the surfactant solution, even if they are not being deformed.

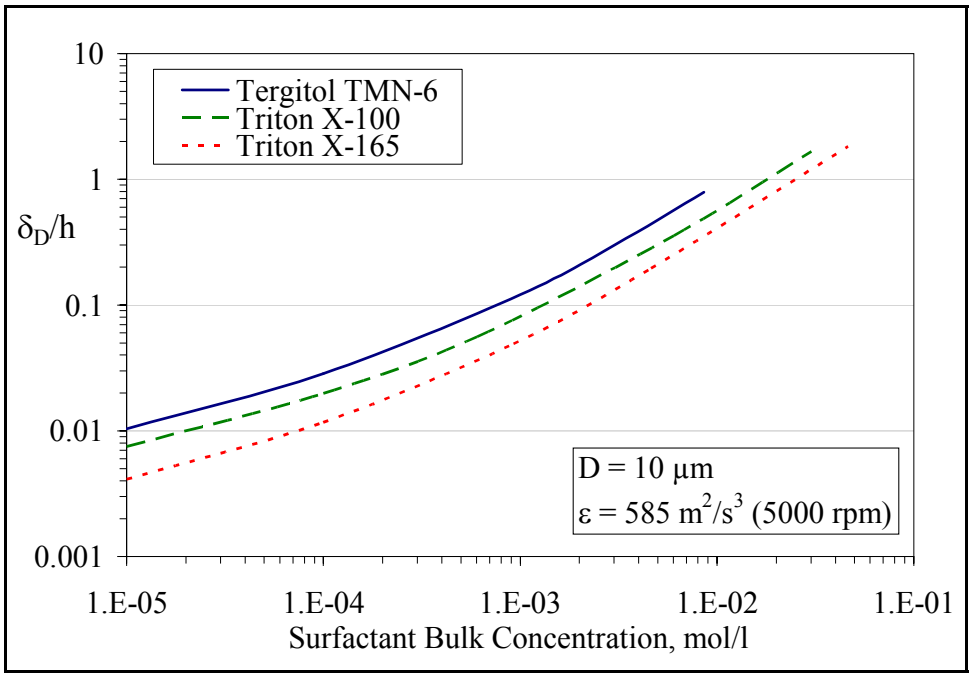

Figure 6.4- 1. Ratio of diffusion layer thickness to adsorption depth as a function of surfactant bulk concentration.

6.5. Summary

This chapter presented the results obtained for the interfacial phenomena experiments. Equilibrium and interfacial tensions for surfactant-laden systems, as well as for clean systems were measured. They show satisfactory agreement with the behavior predicted by the Langmuir – von Szyszkowski equation of state. In addition, some of these results were favorably compared to available literature values. The dynamic surface tension of dilute surfactant solutions was found to follow the trend indicated by the long times approximation of the Ward and Tordai equation. This confirms that the adsorption process under such conditions is diffusion-controlled and allowed estimating the surfactant diffusion coefficients.

The surface dilational modulus was calculated through equation 4.5.2-14, using the results of the equilibrium and dynamic surface/interfacial tension experiments.

Previously obtained power draw data were employed to estimate the deformation timescales for the different turbulence sub-ranges. The calculated E^{sd} values show the expected trend, attaining maxima at concentrations below the CMC for a wide range of experimental conditions. They were also satisfactorily compared to literature data. This shows that the approach used here to predict this interface rheological property is adequate, despite the assumptions made during its derivation (Chapter 4). From a physicochemical hydrodynamic analysis, it was shown that Marangoni stresses may be acting on drops in surfactant solutions even if they are not being deformed.

CHAPTER 7. LIQUID-LIQUID DISPERSION EXPERIMENTAL RESULTS

The present chapter contains the results of the liquid-liquid dispersion experiments previously described. Results for clean systems will be presented first. These include all experiments carried out with pure water or aqueous methanol solutions as the continuous phase. Then, results for the surfactant laden systems will be shown. In both cases, the effect of predominating properties and variables, such as dispersed phase viscosity, methanol or surfactant concentration, and rotor speed will be shown and discussed, as well as explanations for the observed trends.

The Silverson L4RT mixer has several interchangeable stator heads. However, as mentioned in the experimental methods chapter, the only stator head considered in the present study was the slotted head. Therefore, in all the results presented in this chapter, the use of this head will be implied. Previous studies included the effect of the stator head geometry on mean drop size diameter (Francis 1999; Phongikaroon 2001) and power draw (Francis 1999; Padron 2001).

7.1. Clean Systems

As previously mentioned, clean systems include all the experiments in which the continuous phase is either water or aqueous methanol solutions. Since most of the results are in terms of the Sauter mean diameter (D_{32}), the relationship between D_{32} and the maximum stable drop diameter of the dispersion (D_{max}) will be examined first. Then, the effect of physical properties and experimental variables will be discussed.

7.1.1. Relationship between D_{32} and D_{max}.

Figure 7.1.1-1 shows the plot of Sauter mean diameter against maximum measured diameter for the clean systems experiments. A linear regression analysis, forcing the intercept through the origin of coordinates, yielded a proportionality constant of 0.39 between these two diameters, with a coefficient of determination (R^2) of 0.82. This value is somewhat lower than the 0.44 reported by Francis (1999) and Phongikaroon (2001) for rotor-stator devices. It is also considerably lower than the average values reported for stirred tanks: 0.64 by Chen and Middleman (1967), 0.72 by Brown and Pitt (1972), and 0.61 by Calabrese, Chang, and Dang (1986). This last difference is indicative of the propensity of rotor-stator mixers to produce dispersions with relatively larger populations of smaller drops, compared to conventional stirred tanks.

Compartmentalizing the data into different dispersed phase viscosity grades (Figure 7.1.1-2) shows that there is a dependency of the proportionality constant between D_{32} and D_{max} on the viscosity of the drops. In the lower viscosity range, 10 cSt – 100 cSt, the value of the constant is 0.42 – 0.45 (not counting the inexplicably low value of 0.33 obtained with the 50 cSt data set), which is very close to the 0.44 reported by Francis (1999) for inviscid dispersed phases. In the 500 – 1000 viscosity range the constant reduces to 0.35 – 0.36. A comparable decrease was observed by Calabrese, Chang, and Dang (1986) in stirred tanks, with D_{32}/D_{max} decreasing from ~0.6 to ~0.5 for the higher viscosity oils (5000 and 10,000 cSt, in their case). An additional data set corresponding to 10,000 cSt silicone oil in water produced a constant of 0.31, which, despite the scatter (R^2 = 0.37, only three points available), substantiates the dependency on dispersed phase viscosity. This viscosity-dependent behavior will be

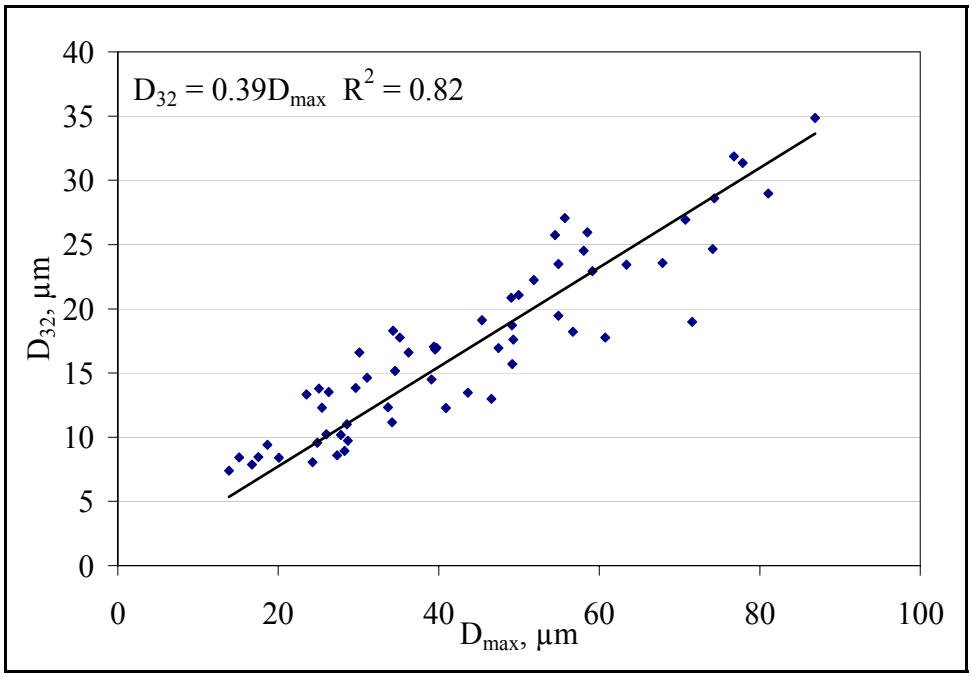

Figure 7.1.1- 1. Sauter mean diameter (D_{32}) vs. maximum stable diameter (D_{max}) for clean systems, showing the best fit linear regression through all data points (forced through origin).

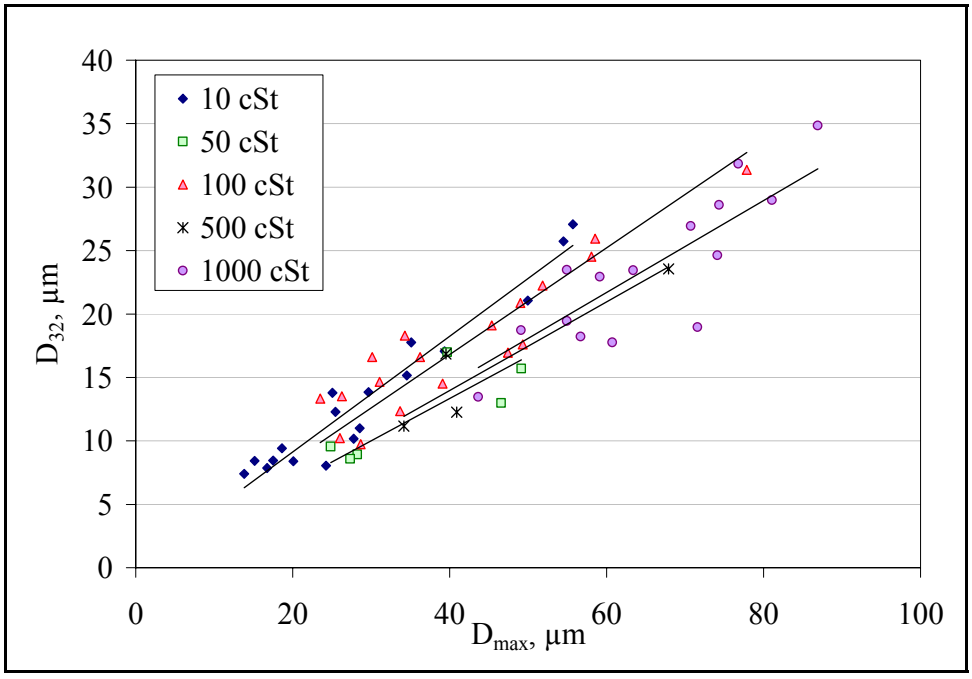

Figure 7.1.1- 2. D_{32} vs. D_{max} plot showing best linear regressions for all five silicone oil viscosity grades. 10 cSt: $D_{32} = 0.45D_{max}$ (R^2=0.93), 50 cSt: $D_{32} = 0.33D_{max}$ (R^2=0.65), 100 cSt: $D_{32} = 0.42D_{max}$ (R^2=0.83), 500 cSt: $D_{32} = 0.35D_{max}$ (R^2=0.85), 1000 cSt: $D_{32} = 0.36D_{max}$ (R^2=0.73)

explained in more detail in the following section, where the effect of dispersed phase viscosity is discussed.

7.1.2. Effect of Dispersed Phase Viscosity

Figure 7.1.2-1 shows the variation of the Sauter mean diameter of silicone oils in pure water for the dispersed phase viscosity and rotor speed ranges studied. As expected, the mean drop size decreases as the rotor speed, and thus the energy dissipation rate, increases. In the viscosity range from 10 to 100 mPa·s (or cSt) there is little variation in drop size with respect to drop viscosity, especially for the lower rotor speeds. For stirred tanks (equipped with a Rushton turbine), in this same viscosity range, the increase in mean diameter with μ_d is considerably more appreciable; with an increase in D_{32} of up to ~40% (Wang and Calabrese 1986).

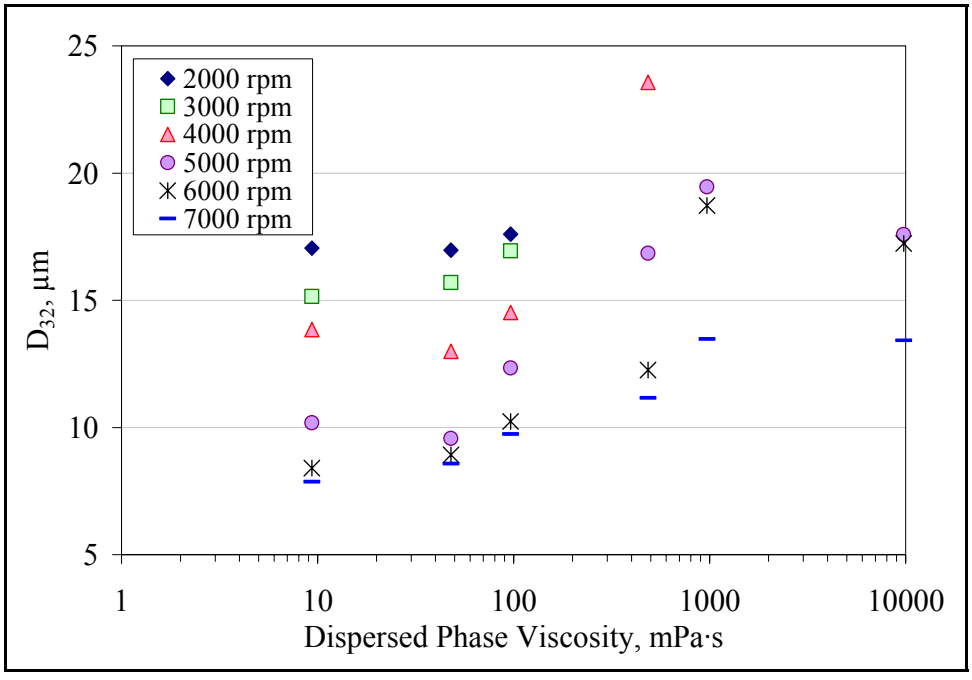

Figure 7.1.2- 1. Sauter mean diameter of silicone oil-in-water dispersions as a function of dispersed phase viscosity for all rotor speeds.

Francis (1999) obtained $D_{32} \sim 16\mu m$ for chlorobenzene ($\mu_d \approx 1$ mPa·s) dispersed in water with a rotor-stator device at 2500 rpm, which is very similar to the values in Figure 7.1.2-1 for 10 cSt oil at comparable speeds. However, the interfacial tension of the chlorobenzene/water system is slightly lower (37 mN/m, compared to 46 mN/m of silicone oil/water), which means that his mean drop size should be somewhat smaller. Nevertheless, this could be due to the fact that he used the High Magnification Video probe to measure drop size, which loses accuracy for drops below ~5 μm (see Chapter 2). Therefore, the lower size tail of the drop size distributions may have been cut off, producing higher mean values.

After 100 mPa·s, the increase in D_{32} with dispersed phase viscosity becomes steeper. However, for the highest viscosity values, 1000 and 10,000 mPa·s, the drop size does not increase anymore and remains approximately constant. This behavior has not been observed in stirred tanks for similarly viscous silicone oils (previous rotor-stator studies did not include oil viscosities in this range). Nevertheless, it could be explained by considering the deformation of drops under simpler flow conditions.

Bentley and Leal (1986) studied drop deformation and breakup under different flow conditions by means of a computer controlled four-roll mill apparatus. This allowed them to accurately control the flow pattern and change it from simple shear flow to purely extensional (hyperbolic) flow. Figure 7.1.2-2 shows a summary of their results for the critical capillary number for different flow patterns: $\alpha = 1$, represents extensional flow. Decreasing values of α mean transition from extensional to simple shear flow ($\alpha=0$). The continuous lines are predictions based on the small deformation theory of

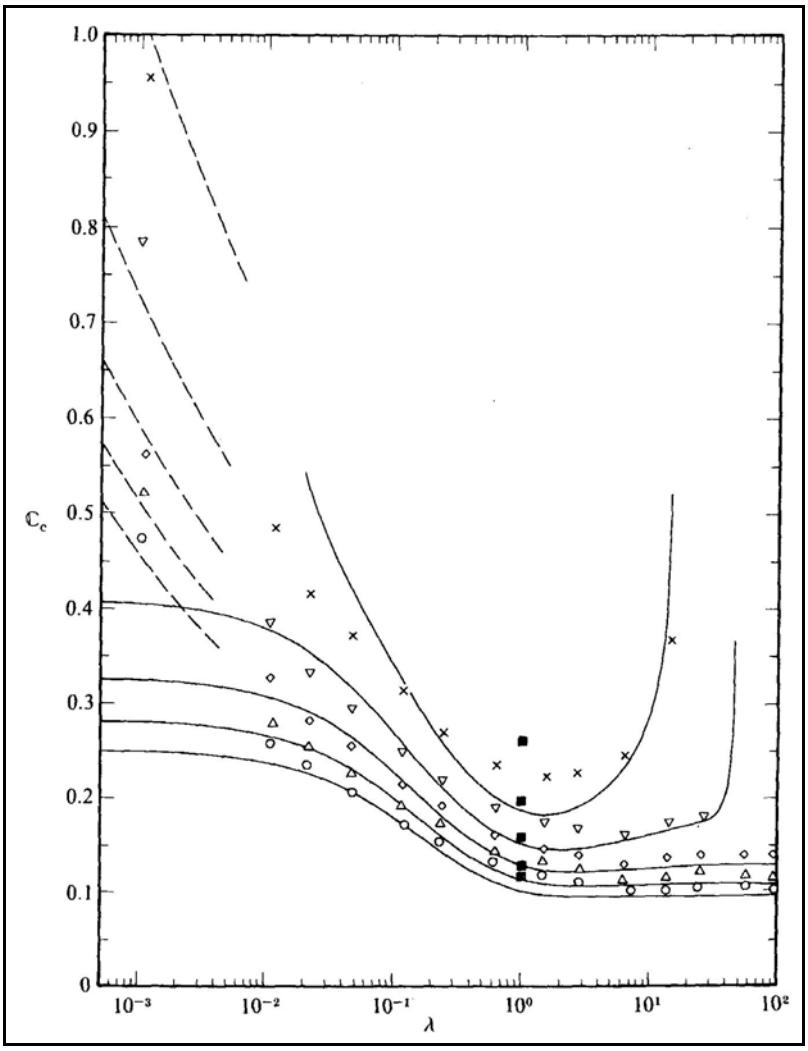

Figure 7.1.2- 2. Critical capillary number as a function of viscosity ratio (λ) for different flow types: ○, α=1.0; △, α=0.8; ◇, α=0.6; ▽, α=0.4; ×, α=0.2; ■, Numerical; —, small deformation theory; – –, large deformation theory. Reproduced from Bentley and Leal (1986). See text for explanation.

Barthès-Biesel and Acrivos (1973); the dashed lines are predictions from the large deformation theory of Acrivos and Lo (1978); and the black squares are theoretical predictions by Rallison (1981). As indicated by this plot, the critical capillary number remains constant for viscosity ratios greater than 3, in the purely extensional case (α = 1).

The capillary number is defined as:

$$Ca = \frac{\mu_c \dot{\gamma} D}{\sigma} \qquad (7.1.2\text{-}1)$$

where $\dot{\gamma}$ is the principal velocity gradient (shear or extension rate). The fact that its critical value remains constant means that, for constant interfacial tension, continuous phase viscosity, and flow conditions, the maximum stable drop size becomes independent of the dispersed phase viscosity. Therefore, if the flow is mostly extensional, the size of the drops remains constant as the viscosity of the dispersed phase increases, for $\mu_d/\mu_c > 3$. On the other hand, if shear is significant, the size of the drops should increase with μ_d/μ_c, due to the higher critical capillary number, but the extent of the increase depends on the how close the flow is to a pure simple shear flow.

Turbulent flows are neither simple shear nor purely extensional flows, but they are better approximated by the latter. Simple shear flows are not very realistic, since they require that only one velocity gradient be present. Whenever there are two or more velocity gradients acting simultaneously (as in the case of 3D turbulent flows) the flow is closer to being extensional than simple shear. The fact that, for viscosity ratios between 10 and 1000, the drop size increases (Figure 7.1.2-1, since $\mu_c \approx 1$) could be interpreted as meaning that the breakage behavior is between that for simple shear and that for extensional flows ($0 < \alpha < 1$, following Figure 7.1.2-2). By the same token, the steady drop size after 1000 cSt, may indicate a shift in the mechanism towards a more purely extensional behavior. In turbulent flows, the drops are stretched by eddies that have a limited lifetime. The drop also has a deformation timescale, t_{dd} (see Chapter 3, section 3.4), which, for these highly viscous oils, is orders of magnitude larger than the eddy lifetime. Therefore, a drop may be just starting to return to its original shape when it

encounters another eddy, and so on. Hence, the drops are effectively stretched by a succession of eddies into a long thread; which would be comparable to being stretched by an extensional flow. In stirred tanks, this may not be seen since energy dissipation rates are smaller and drop sizes are larger; which translates into considerably larger eddy lifetimes but only slightly larger deformation timescales (for a fixed μ_d). Therefore, there is an increased probability that even highly viscous drops will be broken by a single eddy (higher shearing conditions).

Studies of viscous oil dispersions in stirred tanks (Calabrese, Chang, and Dang 1986; Wang and Calabrese 1986) have shown a change in the drop size distributions (DSD) with increasing oil viscosity. The DSD for low viscosity oils is normally distributed (normal "Gaussian" distribution in volume), but for high viscosities (1000 – 10,000 cSt) the distribution becomes log-normal and, in some cases, bimodal, indicating a larger production of small drops. Figure 7.1.2-3 shows the DSD of the different silicone oils in water, at 6000 rpm, obtained in the present study. The fact that all distributions are linear, or almost linear, in this plot (probability scale in the y-axis and logarithmic scale in the x-axis) signifies that they are log-normal in volume. However, it is noticeable that as the dispersed phase viscosity increases, the DSD curve tends to bend slightly (compared to the 10 cSt curve), which indicates that in rotor-stators there is also a somewhat larger production of small drops by highly viscous oils. This is consistent with the smaller D_{32}/D_{max} values obtained for high viscosity oils (see previous section).

This higher production of smaller drops may be explained by examining the drop breakage mechanism. Viscous drops usually elongate into dumbbell-shaped bodies: two bulbous ends united by a thin liquid thread. After a certain time period, the thread

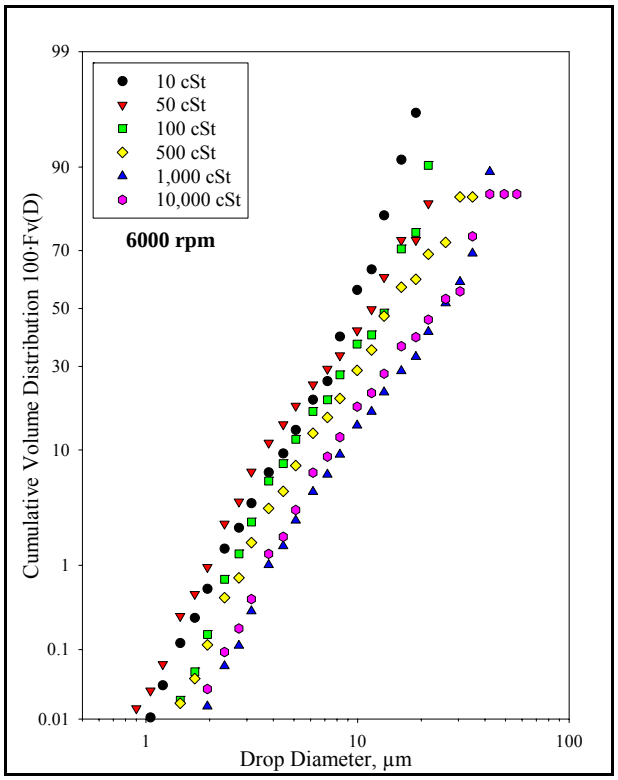

Figure 7.1.2- 3. Cumulative volume drop size distributions for silicone oils of different viscosities in water at 6000 rpm.

becomes unstable and the dumbbell breaks up into two daughters with one or more smaller satellites between them. As the viscosity of the oil increases, the stability of the liquid thread increases, which allows it to be further stretched before breakup occurs (Janssen and Meijer 1993). Figure 7.1.2-4 shows how a viscous liquid thread is broken by the onset of a sinusoidal instability (also known as Rayleigh instabilities, after Lord Rayleigh, who first observed them in 1892). As seen, the thread breaks at several points depending on the instability's wavelength and amplitude. Instabilities develop more slowly for higher viscosities. Therefore, the higher the dispersed phase viscosity, the longer the thread will become before breaking. The longer the thread, the larger the number and smaller the size of satellite drops resulting from a single breakup event. This

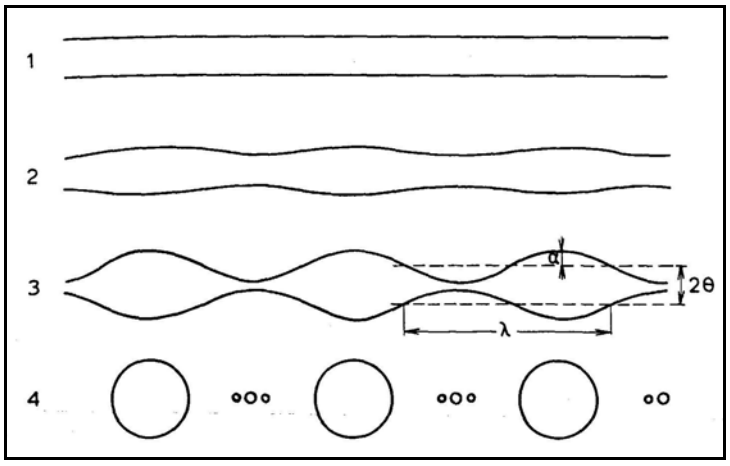

Figure 7.1.2- 4. Instability-induced breakage of a liquid thread. θ = initial thread radius, α = instability amplitude, λ = instability wavelength. Reproduced from (Walstra 1983)

is consistent with the "ligament stretching" breakage mechanism described by Ali *et al.* (1981) and Chang *et al.* (1981) for viscous drops in stirred tanks. They observed that the velocity gradient stretches the drops into ligaments or elongated sheets which fracture into small droplets when the stretching became sufficient to create unstable interfacial conditions.

As mentioned before, in stirred tanks, the DSD is sometimes bimodal for high viscosity oils dispersed in water (Wang and Calabrese 1986). On possible explanation for why this is not observed in the present study is that the drop sizes attained in stirred tanks is at least an order of magnitude larger that the ones obtained here (for 1000 cSt silicone oil: $D_{32StirredTank} \approx 300 - 2000$ μm; $D_{32rotor\text{-}stator} \approx 13 - 20$ μm). However, the size of the satellite drops formed in both types of mixers are probably of the same order of magnitude, since their size depends on the thickness of the viscous thread at breakup and this is mostly dictated by oil viscosity and interfacial tension. Therefore, the mean sizes of the daughter drop population and of the satellite drop population are considerably closer and they do not show as distinct peaks in the distribution.

A final concern is the rheological behavior of highly viscous silicone oils. Certain grades of silicone oil exhibit weak elastic behavior. However, these are commercially sold as Newtonian standards (Calabrese, Chang, and Dang 1986). A measure of the relative significance of elastic effects can be obtained by estimating the Deborah number, De. This is defined as the ratio of the elastic relaxation time of the oil to the characteristic time for the deformation of a viscous drop, t_{dd}. Following the analysis of Calabrese, Chang, and Dang (1986) the Deborah number for conditions similar to those for the 10,000 cSt oil was estimated to be approximately $De \leq 0.02$. It is highly unlikely that the lower viscosity grades would show a greater elastic behavior Therefore, elastic effects can be considered unimportant for the oil viscosity range considered in this study.

7.1.3. Effect of Methanol Concentration in the Continuous Phase

In chapter 6, it was shown that the interfacial tension of silicone oil/aqueous methanol systems decreases as the concentration of methanol increases (see Figure 6.1.3-1). Therefore, it would be intuitively expected to observe a decrease in the mean drop size as the concentration of methanol in the continuous phase increases, since the resistance to breakage due to surface forces diminishes. This behavior has indeed been observed, even for highly viscous silicone oils, in stirred tanks (Wang and Calabrese 1986) and in previous rotor-stator studies (Phongikaroon 2001). However, as Figures 7.1.3-1 and 7.1.3-2 indicate, this was not the behavior obtained in the present case. Figure 7.1.3-1 illustrates the variation of the number mean diameter (D_{10}), the Sauter mean diameter (D_{32}), the volume-weighted mean diameter (D_{43}), and the maximum stable drop diameter (D_{max}) with respect to the methanol concentration (in weight percent) for 10 cSt silicone oil at low and high rotor speed. Figure 7.1.3-2 shows similar plots for 100

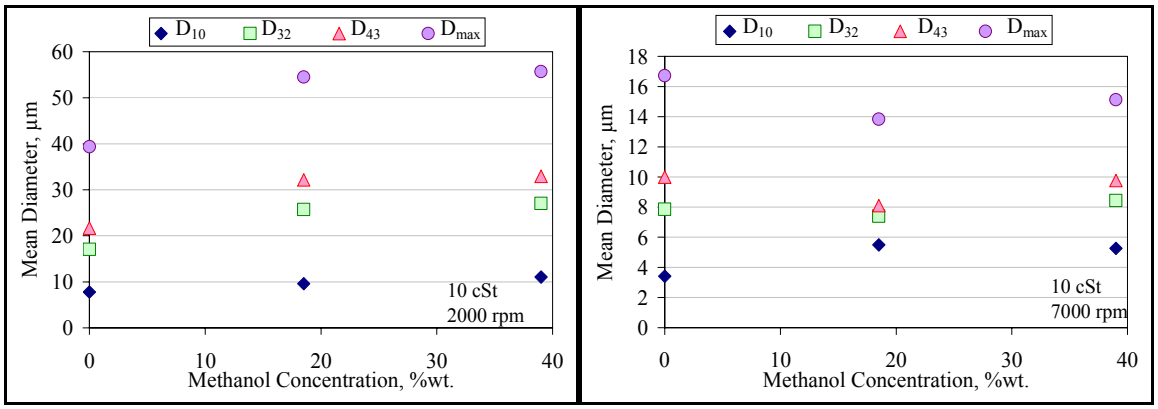

Figure 7.1.3- 1. Mean and maximum diameters for 10 cSt silicone oil as a function of methanol concentration in the continuous phase, at 2000 (left) and 7000 (right) rpm.

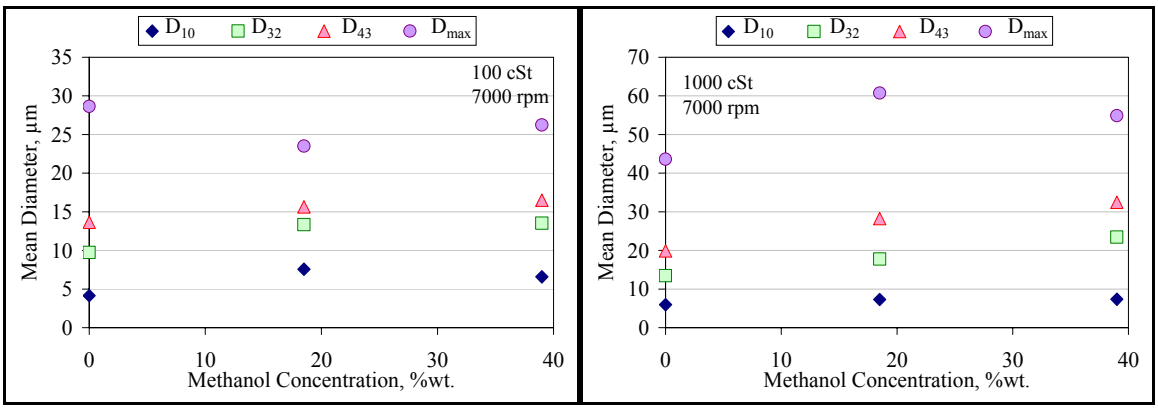

Figure 7.1.3- 2. Mean and maximum diameters for 100 (left) and 1000 (right) cSt silicone oils as a function of methanol concentration in the continuous phase, at 7000 rpm.

and 1000 cSt silicone oils at high rotor speed. It is evident from these plots that the general tendency is for the drop size to increase, or to remain almost constant, with increasing methanol concentration, despite the fact that the interfacial tension is reduced by more than half ($\sigma_{0\%MeOH}$ = 46 mN/m, $\sigma_{39\%MeOH}$ = 20 mN/m). The fact that similar trends are observed for all the mean diameters (D_{pq}) indicates that this trend is not due to a change in the form of the DSD. The relative increase in drop size with respect to the behavior in pure water is greater for higher viscosities and for lower rotor speeds. The latter trend is better appreciated by reference to Figure 7.1.3-3, which shows the Sauter

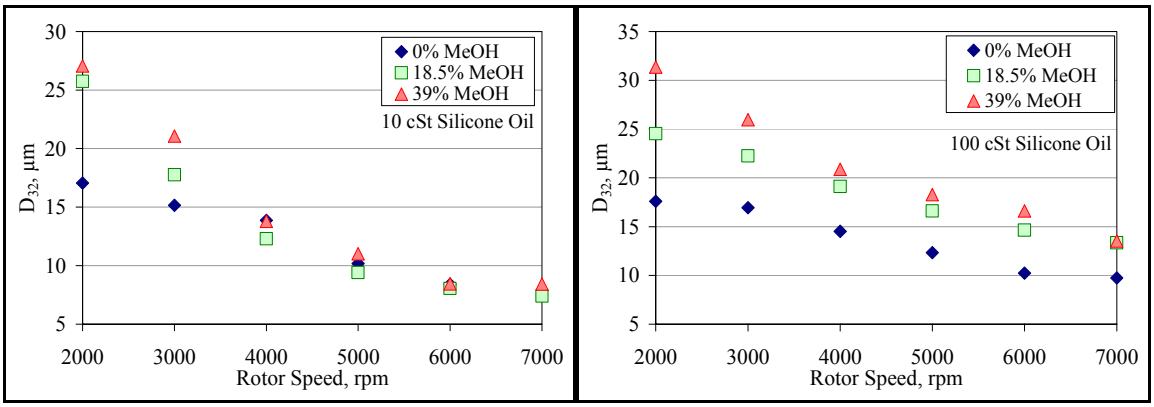

Figure 7.1.3- 3. Sauter Mean Diameter for 10 (left) and 100 (right) cSt silicone oil as a function of rotor speed.

mean diameter as a function of rotor speed for two different oil viscosities. For the 10 cSt silicone oil and high rotor speed (> 5000 rpm) there is no significant difference between the drop size obtained in water and the one obtained in methanol solutions.

Examining the mechanistic models developed in Chapter 3, this behavior could possibly be explained if the systems were already at the high viscosity limit. In this case, the drop size is independent of interfacial tension and scales with a negative power of the continuous phase density. The actual value of the exponent of ρ_c depends on the turbulence sub-range: -⅜ for the inertial sub-range (equation 3.3.1-16), -½ for the viscous sub-range, predominated by inertial stresses (equation 3.3.2.1-8), and -¼ for the viscous sub-range, viscous stresses (equation 3.3.2.2-10). The density of methanol solutions decreases with increasing concentration of the alcohol ($\rho_{c0\%MeOH}$ = 997 kg/m^3, $\rho_{c18\%MeOH}$ = 969 kg/m^3, and $\rho_{c39\%MeOH}$ = 934 kg/m^3). Therefore, in the high viscosity limit, a slight increase of drop size with methanol content would be expected. Nevertheless, the dispersed phase viscosities in question seem too low to be at the viscous limit, at least

judging by results obtained in stirred tanks (Calabrese, Chang, and Dang 1986; Wang and Calabrese 1986).

One convenient way to assess whether the behavior corresponds to the viscous limit or not is by plotting the maximum stable diameter against the turbulent energy dissipation rate, ε. In the viscous limit, D_{max} scales with $\varepsilon^{-1/4}$, independently of the turbulence sub-range (see again equations 3.3.1-16, 3.3.2.1-8, and 3.3.2.2-10). Figure 7.1.3-4 shows these plots for water (0% methanol). The exponents on ε were obtained by a power law regression, and based on their values (≤ ¼) it appears that they are close to the high viscosity limit. As previously mentioned, in stirred tanks this behavior is not observed for such relatively-low viscosities. However, in rotor-stator mixers the energy dissipation rate is much higher, which produces much higher continuous phase stresses and, hence, much higher viscous resistance within the drops ($\tau_d \sim \tau_c^{1/2}$). This could result

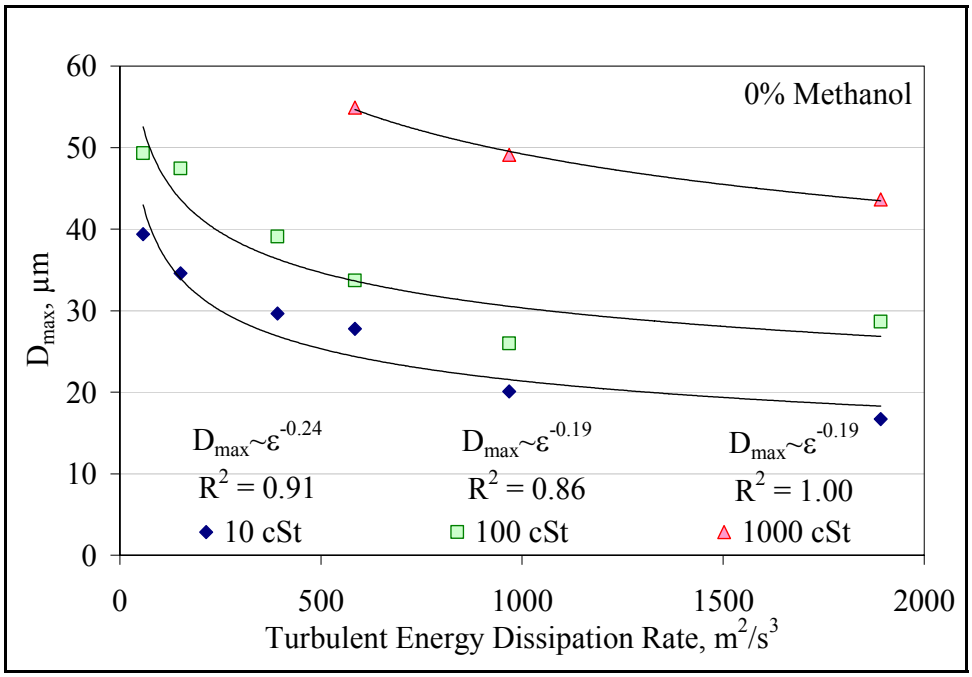

Figure 7.1.3- 4. Maximum diameter as a function of the turbulent energy dissipation rate for silicone oils in water. Solid lines indicate the best power law fit.

in high viscosity behavior being displaced toward lower dispersed phase viscosity. However, performing the same analysis on methanol-containing systems shows an incongruent result. Figure 7.1.3-5 presents the same plots for 39% methanol, where an increase in the exponents on ε for 10 and 100 cSt is shown. The 10 cSt silicone oil shows proportionality with $\varepsilon^{-2/5}$, which is the expected behavior for the low viscosity limit in the inertial sub-range, according to equation 3.3.1-15. The exponent found for this oil in 18.5% methanol solution (not shown in graphs) is 0.36, and those for 100 cSt are 0.26 for 18.5% (not shown) and 0.33 for 39% (Figure 7.1.3-5). Thus, there seems to be a shift from highly viscous behavior towards inviscid-like behavior as the methanol content of the continuous phase is increased (or σ decreased). This is the opposite to what current mechanistic theories predict and to what has been observed for similar systems in stirred tanks (Wang and Calabrese 1986) and rotor-stator mixers (Phongikaroon 2001). The

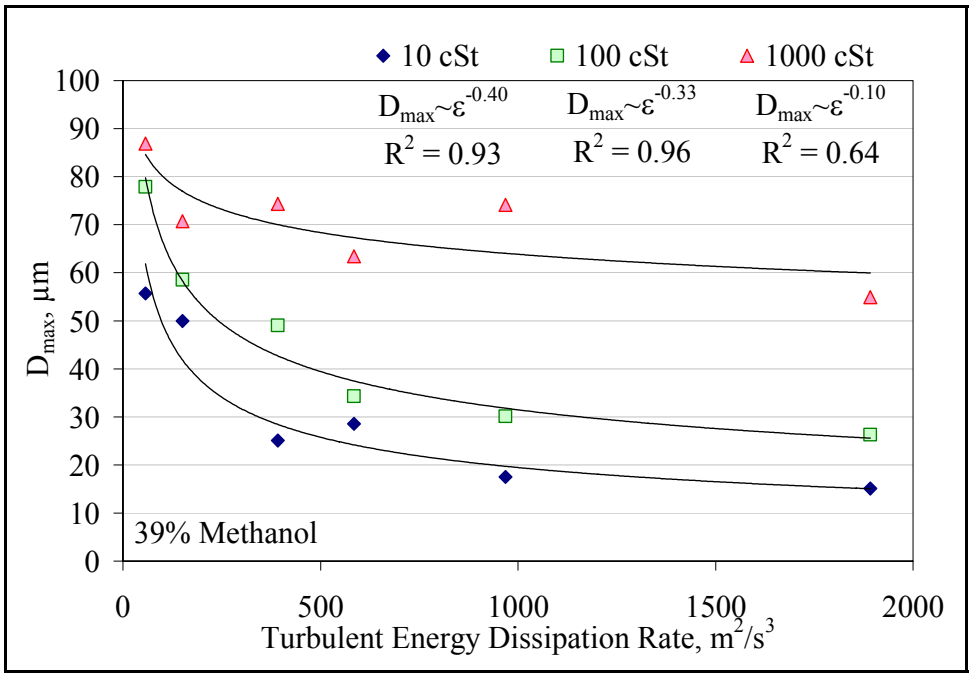

Figure 7.1.3- 5. Maximum diameter as a function of the turbulent energy dissipation rate for silicone oils in 39% methanol. Solid lines indicate the best power law fit.

behavior of the 1000 cSt silicone oil, on the other hand is quite different. It starts close to the viscous limit for pure water ($\sim\varepsilon^{-0.19}$), and then changes to $\sim\varepsilon^{-0.1}$ for both methanol concentrations. Except for the fact that the magnitude of the exponent on ε is lowest for the highest drop viscosity, this behavior is not readily explainable by any of the mechanistic models, and may indicate a shift towards a different kind of breakage mechanism.

Note that the equations that were referenced in the previous analysis correspond to the "linear" mechanistic models. In Chapter 3, section 3.3.3, alternative models, the so-called "spring and dashpot" models, were introduced. However, in the viscous limit, the S&D models predict that D_{max} is proportional to $\rho_c^{-3/4}\varepsilon^{-1/4}$, irrespective of the turbulence sub-range. Therefore, if the same thought exercise is carried out with respect to the S&D equations, similar conclusions would result.

Figure 7.1.3- 6. contains the normalized cumulative number and volume frequency distributions for 100 cSt silicone oil drops in water and methanol solutions, at a rotor speed of 2000 rpm. It is at the lowest speeds that the largest anomalies discussed above occur. The number distributions were normalized with the number mean diameters (D_{10}) of each case, and the volume distributions with the Sauter mean diameters. The curves for water and methanol solutions collapse very well into a single curve, in both cases. This indicates that the increase seen in drop diameter with methanol concentration is not due to an anomalous behavior in the tails of the distribution (low diameter and high diameter extremes of the curve). For instance, it rules out the possibility of the increase being the result of an abnormally large number of big drops, or of a conspicuous lack of small drops. It also lowers the possibility of it being caused by random experimental

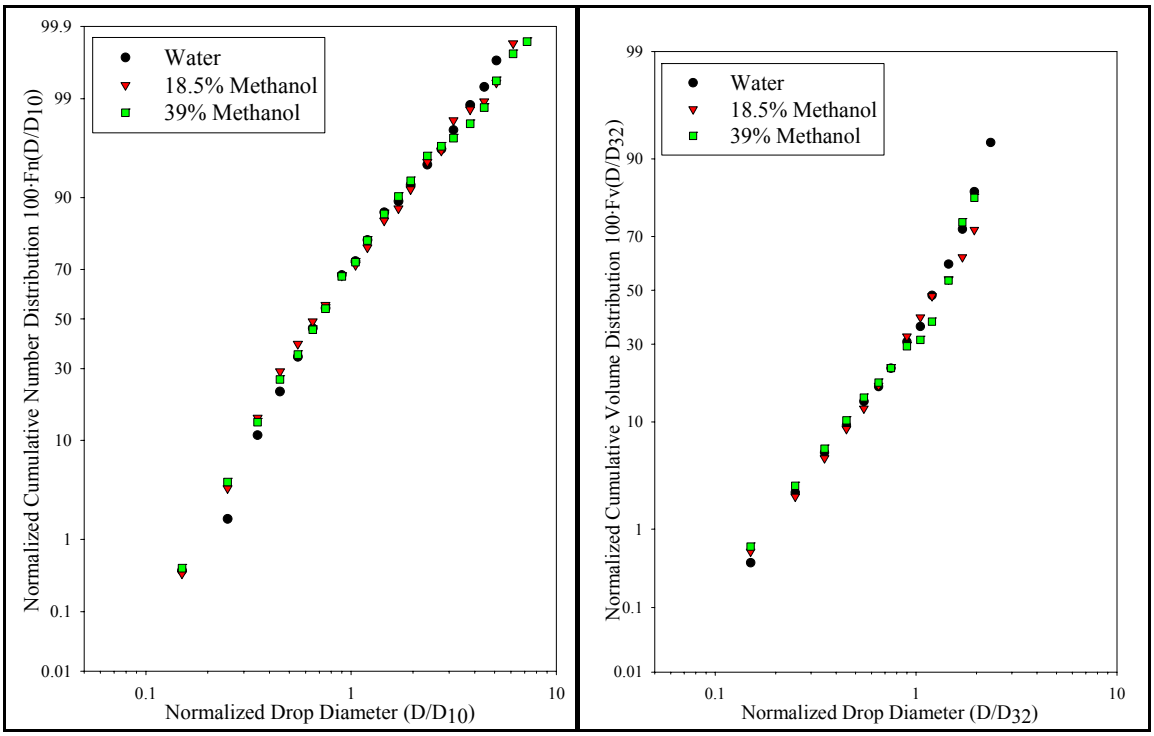

Figure 7.1.3- 6. Normalized cumulative number (left) and volume (right) drop size distributions for 100 cSt silicone oil at 2000 rpm.

error or a shift in breakup mechanism. Similar curves were obtained for 10 and 1000 cSt silicone oils.

7.1.3.1. Systematic Analysis of Potential Uncertainties in Mean Drop Size Data

Sample Coalescence

Several other potential causes for the observed trends were investigated. First, the possibility of coalescence in the sample was considered. This was thought of as a possible cause since there is evidence that surfactants do not exhibit interfacial activity in short-chain alcohols (Ray 1971) and in ethanol solutions with concentrations greater than 20 – 25% (Becher and Trifiletti 1973). Therefore, the drops could undergo significant coalescence while being analyzed if they remain in a methanol-rich environment. Coalescence was indeed observed under the microscope while measuring drops of 100

cSt silicone oil in 100% methanol. For this reasons, the samples for silicone oil/aqueous methanol systems were diluted with surfactant solution to a volume such that the final concentration of methanol was below 10%. This is actually the reason why methanol concentrations in the DSD experiments were limited to ~40%. Higher methanol content would require such large dilutions that the drop size measurement would become quite difficult. Each microscopy slide would contain considerably less than 1000 counts of drop size.

Methanol and water form highly non-ideal solutions (Arce *et al.* 1993), and mixing them releases enough heat to increase the sample's temperature a few degrees. Again, to insure that the sample was representative of conditions in the vessel, the vial with the surfactant solution was chilled in ice prior to the sample dilution to minimize any effects that this increase in temperature could have. With all the measures taken to dilute and stabilize the sample, it is unlikely that coalescence was significant and , therefore, it may be excluded as the cause of the drop size increase with increasing methanol content.

Sampling Error

Sampling error was considered as another possible cause. The differences in density between the dispersed and continuous phases could cause the drops to stratify vertically, creating "zones" of different mean drop sizes within the tank. If this occurs, removing the sample from different zones could produce erroneous drop size measurements. However, this was discarded as a potential source of error based on a sampling analysis done early in this investigation. Three samples where taken from the tank with a 500 cSt silicone oil dispersion in water ($\Delta\rho \approx 28$ kg/m^3) at 4000 rpm: one

from the top of the tank, one from the discharge of the mixing head, and one allowing the pipette to fill up continuously from the moment it was introduced in the tank until it reached its bottom (as described in section 5.2.4). Figure 7.1.3.1-1 shows the results obtained from the three samples, as well as a diagram indicating where the samples were acquired. Evidently, the drop size distributions do not show significant differences. If such level of homogeneity is observed for water as the continuous phase, it would be expected to be equally good or better for methanol solutions since the density differences between them and silicone oils are approximately equal or smaller ($\Delta\rho \approx 1 - 36$ kg/m^3).

Image Analysis Error

The possibility of a systematic error in the automated image analysis was also tested. In methanol systems, the contrast between the oil drops and the background of the

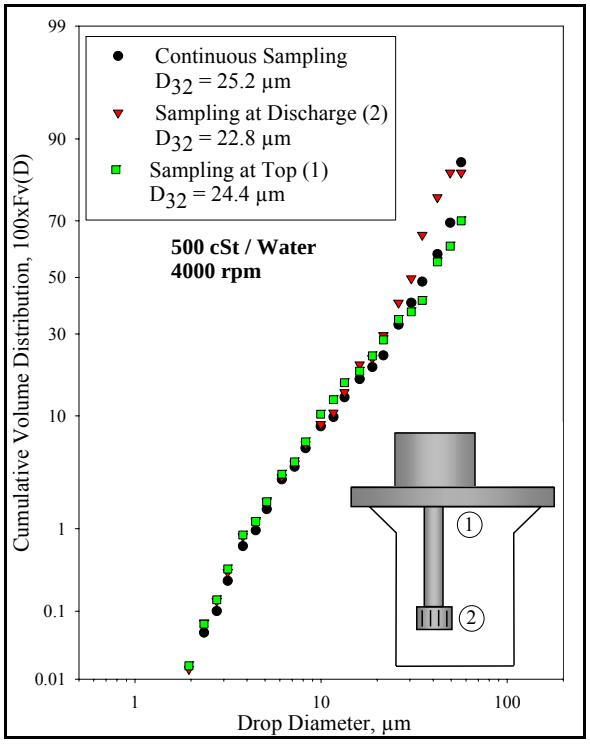

Figure 7.1.3.1- 1. Sampling analysis results. The samples were taken from the top of the tank (1), the discharge of the mixing head (2), and in a continuous manner, as explained in Chapter 5, section 5.2.4.

image is slightly lower than in pure water. This could result in some of the smaller drops being ignored by the automated image analysis procedure (see Chapter 2) due to poor thresholding. The probability of this happening is low since the grayscale of each image is normalized to enhance contrast (see Figure 2.2.3.1-1). However, to rule this out definitively, the images of selected, unidentified samples were given to Dr. Phongikaroon to be analyzed using his methodology (Phongikaroon 2001), which relies on manually selecting the drops to be measured. This way, a blind test comparison could be made between both methods. The results for D_{32} of this comparison test are show in Figure 7.1.3.1- 1. Similar results were obtained by both approaches for D_{10}, D_{43}, and the distributions' standard deviations. The results for D_{max} show slightly larger numeric deviations, but the trend to increase with increasing methanol concentration is also present. The small numerical differences could be attributed to the fact that the manual method counted only 500 drops per sample, while the automated one counted over 1,100

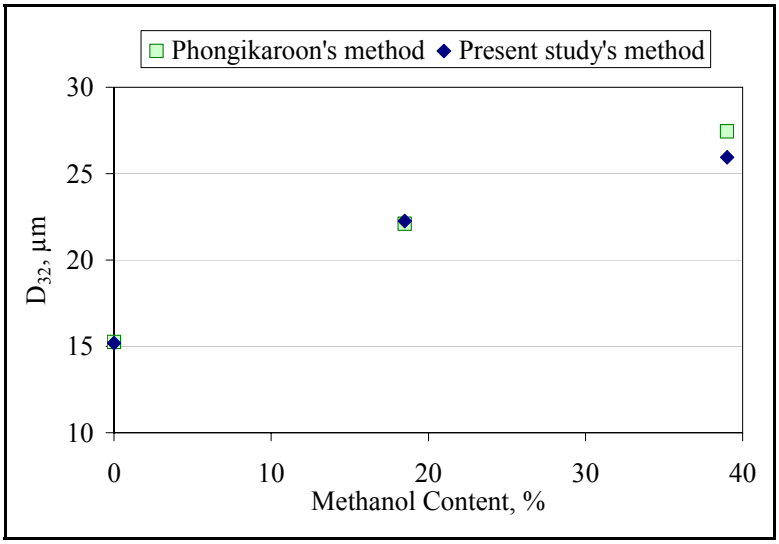

Figure 7.1.3.1- 2. Comparison between Phongikaroon's (2001) manual image analysis method and the present study's automated method. Samples correspond to 100 cSt silicone oil in aqueous methanol, at 3000 rpm.

drops per sample. Clearly, the differences observed between the two analysis methods are negligible. Therefore, the observed experimental trends cannot be attributed to image analysis error.

Ostwald Ripening

Finally, the possibility of Ostwald ripening affecting the drop size was studied. Ostwald ripening is a mass transport process where small drops are dissolved in and transported through the continuous phase with their material transferred to larger drops. The cause of this phenomenon is that the solubility in the continuous phase of material in a drop increases as the curvature of the interface increases (Weiss, Canceliere, and McClements 2000). The fact that silicone oils are slightly more soluble in methanol solutions than in water could cause Ostwald ripening to become significant, increasing the size of the larger drops of the dispersions.

Francis (1999) developed an Ostwald ripening model to estimate the lifespan of small drops (<1μm) of anisole and chlorobenzene in water. Using the same approach, the problem was recast to estimate the growth of large drops due to Ostwald ripening, in a period of 2 hours. Physical properties such as diffusion coefficients, solubilities and even molecular weights, are difficult to find for silicone oils. Hence, the model was applied to chlorobenzene drops. By doing this, although the numerical results would not correspond to the real systems, some general information could be extracted concerning trends with variables such as initial drop diameter and rotor speed. According to the model's results, the growth of drops due to Ostwald ripening should be considerably larger for dispersions with a smaller initial mean drop size and should increase with rotor speed. These trends go against what is observed experimentally, since the effect should then be larger for the

least viscous 10 cSt oil (smaller initial drop diameter) and for 7000 rpm versus 2000 rpm; which is exactly the opposite of what is shown in Figure 7.1.3-3. Hence, the observed increase in drop size with methanol concentration cannot be brought about by Ostwald ripening.

Summary

At this point, a satisfactory explanation for the observed effect of methanol concentration is still elusive. Therefore, a direct comparison between clean and surfactant-laden systems may not be possible, as originally intended. However, the exhaustive analysis done on both data and experimental methods, reassures our confidence in the results obtained in this study; including those for surfactant systems, since the experimental methods and data analysis procedures were essentially the same. The fact that some of these results are not yet understandable only confirms the assertion that much fundamental research is still needed to appropriately evaluate rotor-stator mixers (see Chapter 9, section 9.6 “Recommendations for Future Work”).

7.2. Surfactant Systems

The results for surfactant laden systems will be reported in the following sections. As was the case of clean systems, the discussion will start with the relationship between the Sauter mean diameter and the maximum diameter. Then, it will move on to the effect of surfactant concentration in the continuous phase and, thus, of interfacial rheology.

7.2.1. Relationship Between D_{32} and D_{max}

Figure 7.2.1-1 presents the Sauter mean drop diameter vs. maximum stable drop diameter plot for surfactant-containing systems, along with the linear regression analysis

through all data points and forced through the origin. The value obtained from said analysis for D_{32}/D_{max} is 0.40, with a coefficient of determination of 0.79. This value is, basically, the same than that found for clean systems (0.39), although with a slightly higher scatter. With respect to dispersed phase viscosity discrimination, the trends are comparable to those for the clean systems data (Figure 7.2.1- 2). In the 10 – 100 cSt range, the proportionality constant is 0.43 – 0.50, a little higher than the clean systems case. This apparent increase could be interpreted as an indication of narrower size distributions, especially in the 10 cSt case (constant = 0.50). It could also mean that the presence of surfactant inhibits, to some extent, the formation of satellite drops during breakup of low viscosity drops. However, there is no further evidence to support this conjecture.

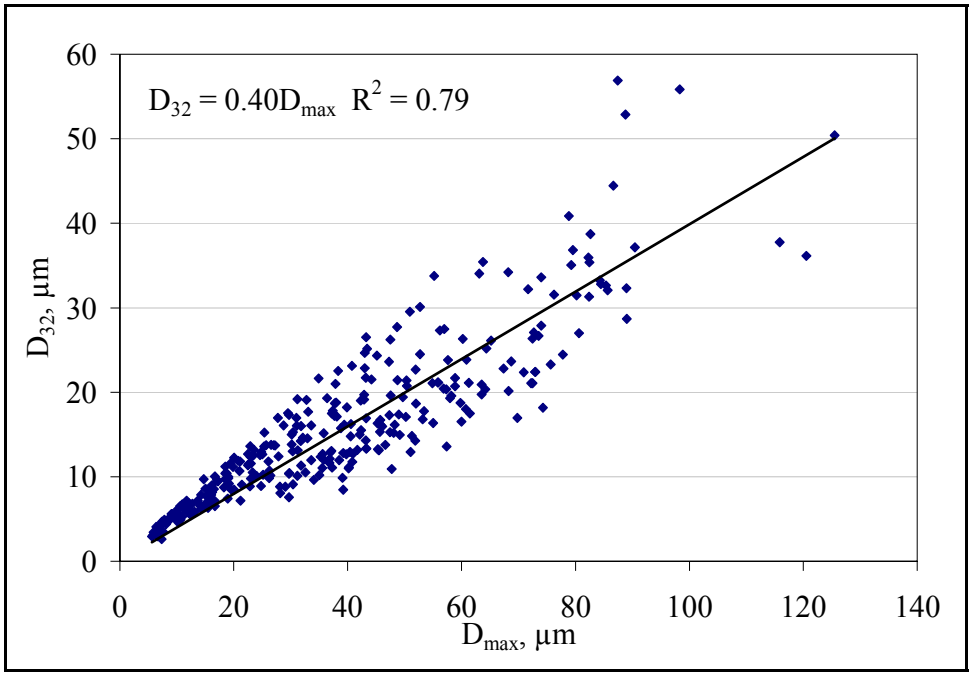

Figure 7.2.1- 1. Sauter mean diameter (D_{32}) vs. maximum stable diameter (D_{max}) for surfactant systems, showing the best fit linear regression through all data points and forced through the origin.

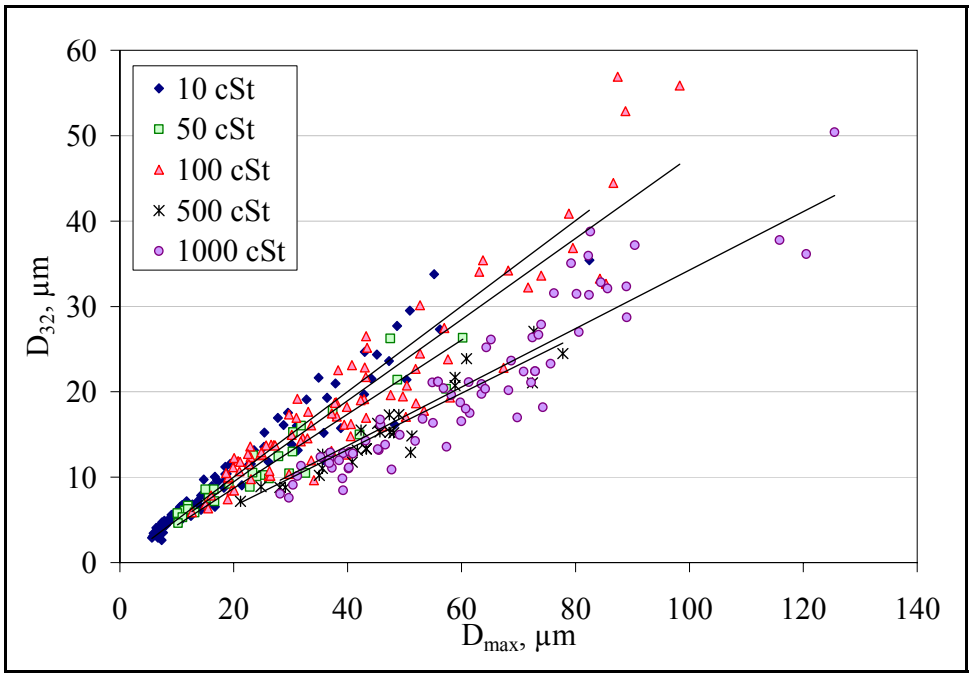

Figure 7.2.1- 2. D_{32} vs. D_{max} plot showing best linear regressions for all five viscosities. 10 cSt: $D_{32} = 0.50 D_{max}$ (R^2=0.92), 50 cSt: $D_{32} = 0.43 D_{max}$ (R^2=0.88), 100 cSt: $D_{32} = 0.47 D_{max}$ (R^2=0.86), 500 cSt: $D_{32} = 0.33 D_{max}$ (R^2=0.88), 1000 cSt: $D_{32} = 0.34 D_{max}$ (R^2=0.85)

In the high viscosity range (500 – 1000 cSt), the opposite trend is observed: the constant decreased slightly to 0.33 – 0.34. This can be related to the production of a larger number of smaller drops (satellites), particularly at high surfactant concentrations. The behavior of high viscosity, high surfactant concentration systems will be discussed more thoroughly at the end of the next section.

7.2.2. Effect of Surfactant Concentration and Interfacial Rheology

The following figures illustrate the effect of surfactant concentration on the Sauter mean diameter of silicone oil dispersions. Figures 7.2.2-1 and 7.2.2-2 show the results for all silicone oil viscosities in the case of Tergitol TMN-6 at low and high rotor speeds, respectively. Figures 7.2.2-3 and 7.2.2-4 are the equivalent plots for Triton X-100, and

Figures 7.2.2-5 and 7.2.2-6 for Triton X-165. Several observations can be made from these graphs. First, it is evident that, in most cases, the drop size undergoes a maximum as the concentration of surfactant increases. The maximum is generally located at 10^{-4} mol/l, regardless of the surfactant being considered. This is remarkably consistent with the maximum found for the calculated surface dilational modulus, as previously reported in Chapter 6, section 6.3. The increase in drop size with increasing surface dilational modulus agrees with the conclusions of Milliken and Leal (1994), and Eggleton and Stebe (1998), who found that at low surfactant concentrations, the Marangoni stresses cause the critical capillary number of deforming drops to increase. On the other hand, Milliken *et al.* also found that the effect was less noticeable at higher viscosity ratios ($\mu_d/\mu_c > 10$). This can be explained by the fact that they only studied the case of purely extensional flow, in which case the critical capillary number tends to a constant value for high viscosity ratios (see Figure 7.1.2-2).

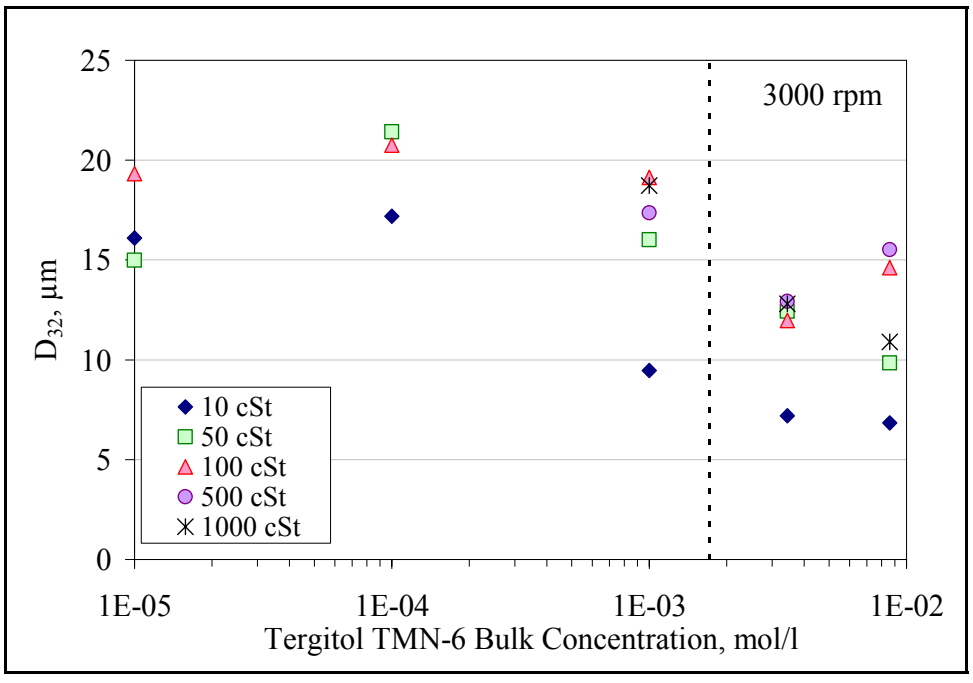

Figure 7.2.2- 1. Variation of D_{32} with Tergitol TMN-6 concentration for all silicone oil viscosities at low rotor speed. Dotted line: CMC.

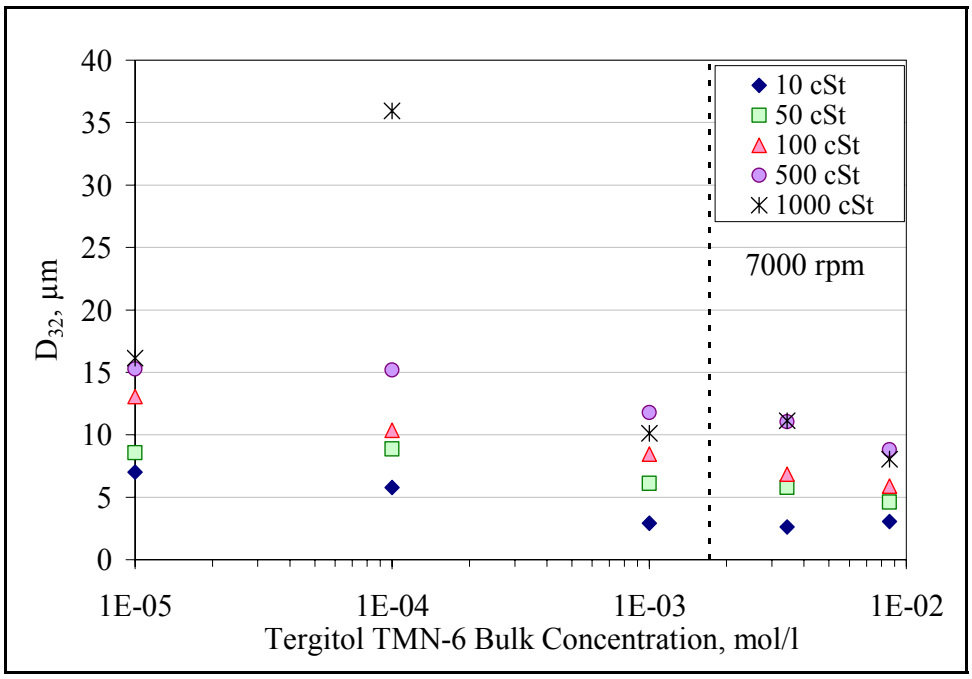

Figure 7.2.2- 2. Variation of D_{32} with Tergitol TMN-6 concentration for all silicone oil viscosities at high rotor speed. Dotted line: CMC.

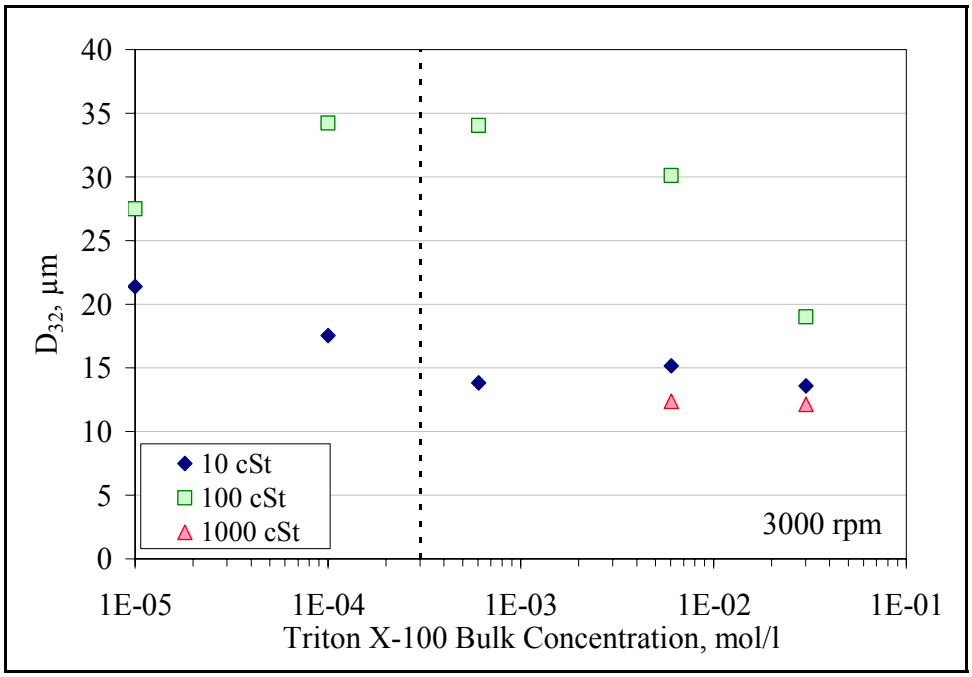

Figure 7.2.2- 3. Variation of D_{32} with Triton X-100 concentration for all silicone oil viscosities at low rotor speed. Dotted line: CMC.

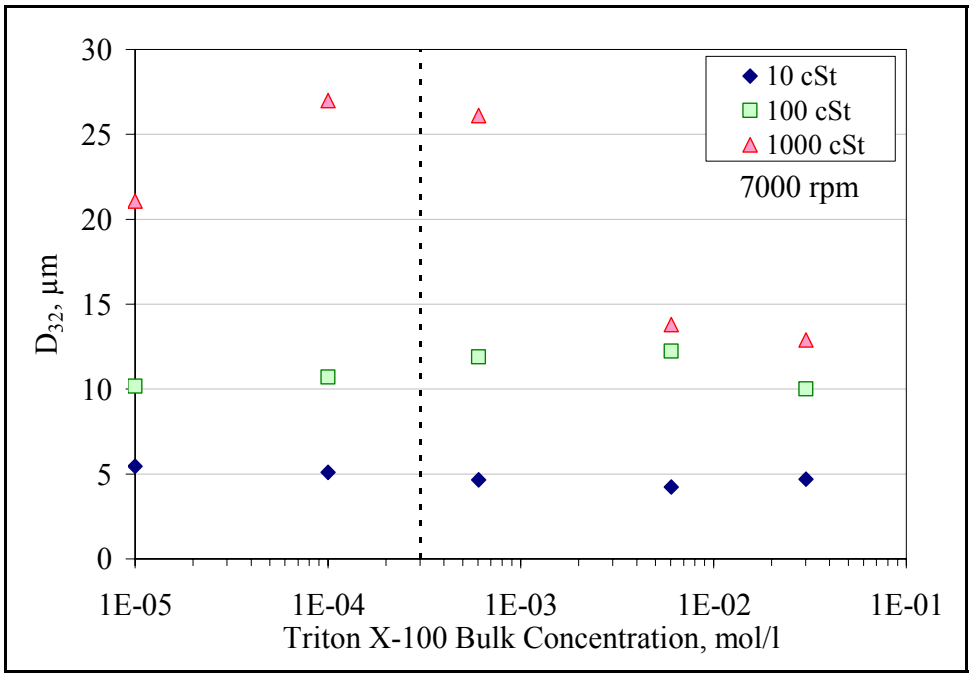

Figure 7.2.2- 4. Variation of D_{32} with Triton X-100 concentration for all silicone oil viscosities at high rotor speed. Dotted line: CMC.

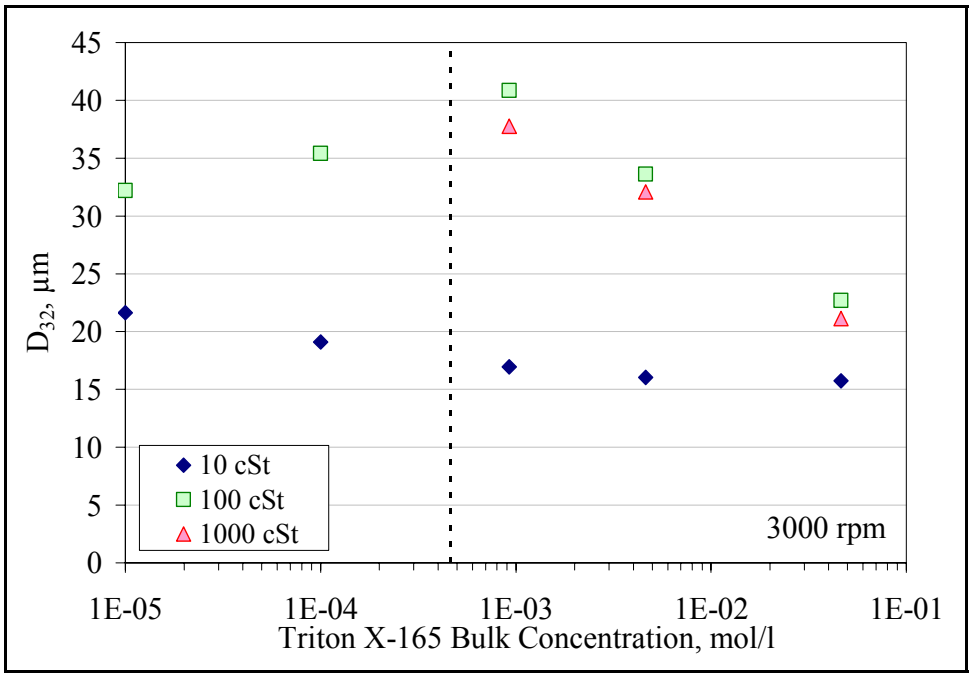

Figure 7.2.2- 5. Variation of D_{32} with Triton X-165 concentration for all silicone oil viscosities at low rotor speed. Dotted line: CMC.

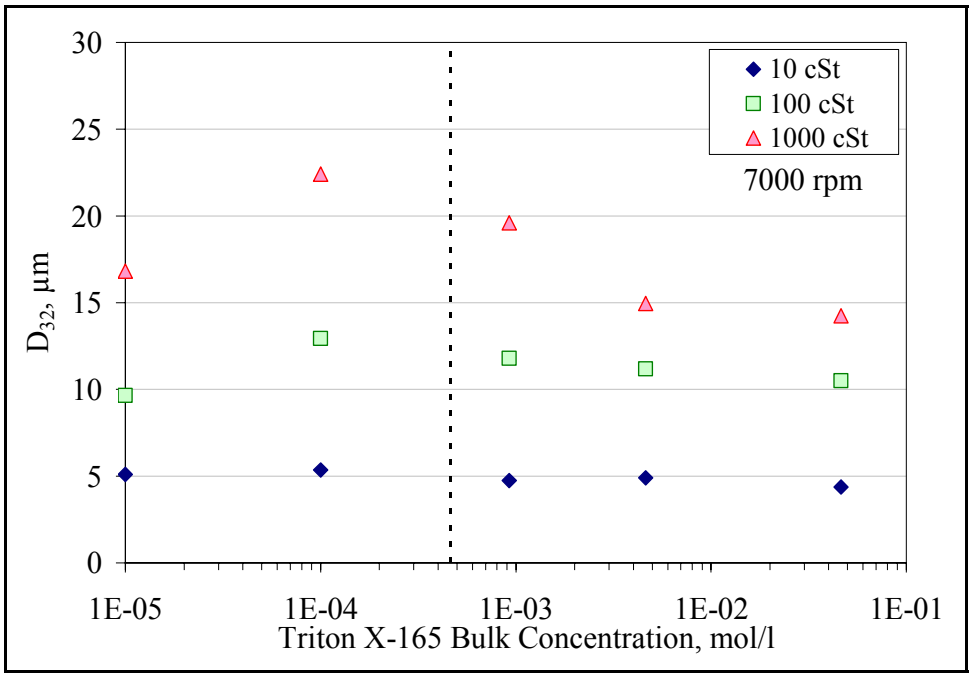

Figure 7.2.2- 6. Variation of D_{32} with Triton X-165 concentration for all silicone oil viscosities at high rotor speed. Dotted line: CMC.

As reported in Chapter 4, Janssen, Boon, and Agterof (1994a,b; 1997) found a correlation between a maximum in critical capillary number with a maximum in surface dilational modulus, for simple shear flows and plane hyperbolic flows, although to a lower degree in the latter case. They observed an increase in the maximum value of the capillary number with viscosity ratio, even though they studied viscosity ratios in the range 0.0013 – 0.152, where the critical capillary number decreases with increasing viscosity ratio. This is the reason why they proposed the effective interfacial tension approach (equation 4.7.1-1) instead of the effective dispersed phase approach (equation 4.7.2-1) of Lucassen-Reynders and Kuijpers (1992). It also suggests that if the increase in viscosity ratio was made in the range where the critical capillary number increases with it ($\mu_d/\mu_c \sim 1$ and higher), the effect of the surface dilational modulus could be even higher; which agrees with the results shown in Figures 7.2.2-1 thru -6, where the increase in the

maximum D_{32} is quite sensitive to the dispersed phase viscosity. Consequently, it can be concluded that interfacial rheology does have a significant effect on drop deformation and breakup, with the Marangoni stresses and, thus, the surface dilational modulus apparently dominating the behavior for low surfactant concentrations.

Another important observation is that there is a notable difference in the behaviors of low, moderate, and high viscosity oils in the whole concentration range. The lower viscosity oil (10 cSt) only exhibits the maximum in drop diameter in a small number of cases. In addition, for low rotor speed, the drop size remains constant at concentrations above the CMC; while for high rotor speed, it remains almost constant in the whole concentration range. The moderate viscosity oil (e.g. 100 cSt) clearly shows a maximum at low speeds but it disappears, or lessens considerably, at high rotor speed. The drop size remains almost constant after the CMC is reached, at high speed; but at low speed it is noticeably not constant.

There is no data for high viscosity oils (500 and 1000 cSt) at low rotor speed and surfactant concentrations less than ~10^3 since the initial drop size obtained with these oils (size of drops ejected from the stator slots right after injecting the oil) was so large (visible to the naked eye) that the flow at 2000 rpm is not strong enough to prevent them from floating to the top of the tank. Therefore, the initial rotor speed for experiments with these conditions was is the 4000 – 5000 rpm range. At low surfactant concentrations (10^{-5} – 10^{-4} mol/l) and high speeds, the 1000 cSt silicone oil produced the largest drop sizes and the most evident maxima. However, at high concentrations (~ CMC or higher), the drop size is about the same, sometimes even smaller, than the one obtained with lower viscosity oils, despite the viscosity being one to two orders of magnitude larger.

Consequently, the effect of the presence of surfactant seems to be related to the dispersed phase viscosity, even at high concentrations where the surface dilational modulus is negligibly small and, thus, equilibrium-like behavior would be expected.

The apparently low sensitivity of the 10 cSt silicone oil to the surface dilational modulus contradicts the behavior predicted by equation 4.5.2-14 if the drop deformation timescale, t_{dd}, (equations 3.4-1) is used, as suggested by Walstra and Smulders (1998). This timescale is proportional to the dispersed phase viscosity and is therefore lower for the lowest viscosity oil. This translates into a greater calculated surface dilational modulus, which should cause a larger effect on drop size. However, Hansen, Peters, and Meijer (1999), while studying the effect of surfactants on the stability of a fluid filament embedded in a viscous fluid, concluded that the disturbance to the surface tangential velocity created by the Marangoni stresses does not propagate into inviscid fluids. Thus, the dilatational surface elasticity does not affect inviscid systems and the effect of the surfactant is limited to lowering the interfacial tension. Even though their study was on the stability of a liquid thread, this conclusion could also apply for the case of a deforming drop; in which case, it would explain the increase of the effect of the surface dilational modulus with oil viscosity.

7.2.2.1. High Surfactant Concentration

Although at concentrations close to and above the CMC the drop size tends to decrease or remain constant with increasing surfactant concentration, the values of the Sauter mean diameter remain relatively close to the drop size of the corresponding oil dispersed in pure water. This can be observed in Figures 7.2.2.1-1 to -3, which show the variation of D_{32} with rotor speed for all surfactants and surfactant concentrations, and

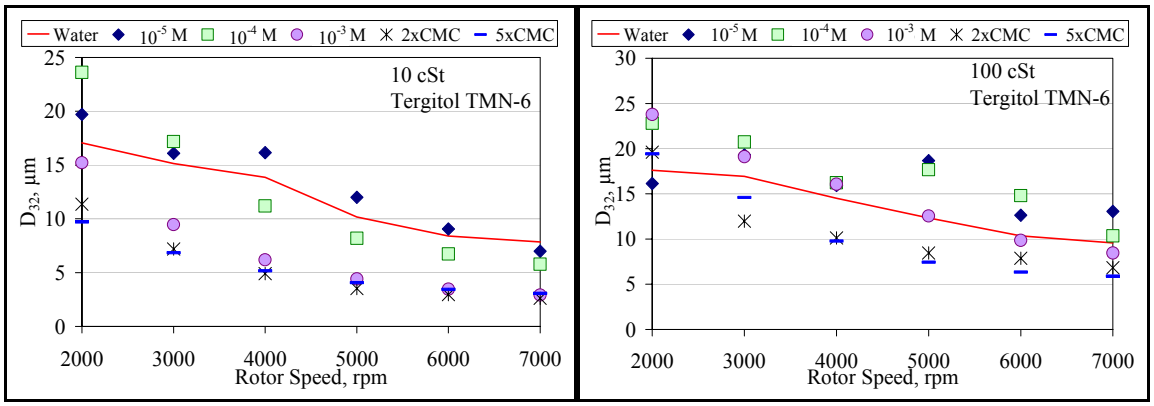

Figure 7.2.2.1- 1. D_{32} against rotor speed for 10 (left) and 100 cSt (right) silicone oils at all Tergitol TMN-6 concentrations. Continuous line: same oil in clean water. M = mol/l

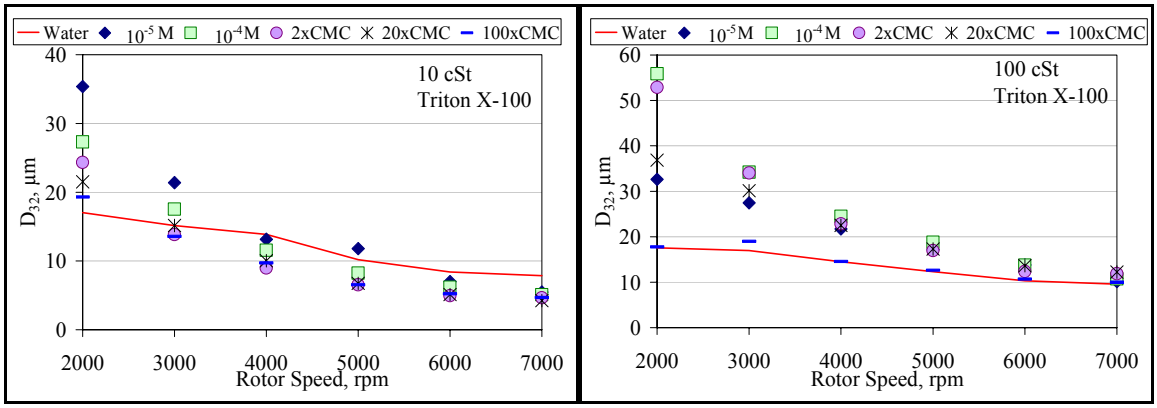

Figure 7.2.2.1- 2. D_{32} against rotor speed for 10 (left) and 100 cSt (right) silicone oils at all Triton X-100 concentrations. Continuous line: same oil in clean water. M = mol/l

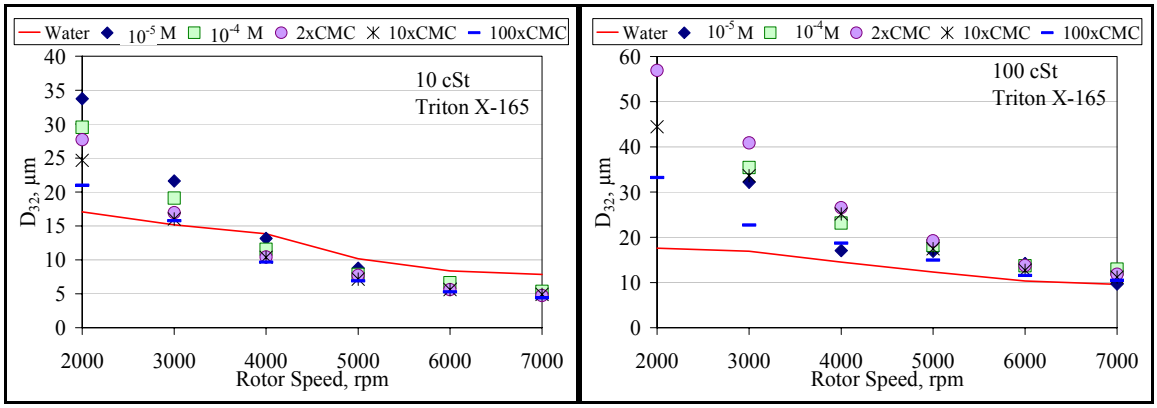

Figure 7.2.2.1- 3. D_{32} against rotor speed for 10 (left) and 100 cSt (right) silicone oils at all Triton X-165 concentrations. Continuous line: same oil in clean water. M = mol/l

where the continuous line represents the pure water case. The trends with respect to rotor speed are consistent in that, for all surfactants and surfactant concentrations, the mean drop size decreases as the rotor speed increases. In the case of Tergitol TMN-6, the drop size obtained for high concentrations (above CMC), is lower than the values for clean water, although not by much. However, in the case of both Triton X surfactants and 100 cSt silicone oil, the drop size of surfactant systems is always equal or larger than that for water, despite the facts that at high concentrations the surface dilational modulus is negligible (< 1 mN/m) and the equilibrium interfacial tension is less than $1/4^{th}$ of the clean interface value (46 mN/m). Another interesting observation is that At low rotor speeds, the Triton X surfactants seem to be more sensitive to rotor speed, exhibiting much steeper initial slopes than the Tergitol and clean water cases.

There are some possible explanations for the apparently small decrease in drop size at high surfactant concentrations. It could be the result of slower adsorption dynamics due to the presence of micelles or a shift in the adsorption mechanism from diffusion-controlled to mixed-controlled. As explained in Chapter 4, section 4.4.3, the presence of micelles, especially nonionic micelles, may hinder the adsorption process. When new surface area is created, the micelles dissociate before the monomers can adsorb. If the deformation is faster than the micelles' slow-relaxation time, the only surfactant molecules available would be the ones already in monomeric form. Therefore, the effective adsorption timescale would remain practically constant above the CMC. In this case, the equilibrium value of the interfacial tension may never be achieved in the timescale of the deformation and the surface dilational modulus would remain at a finite value. The relaxation time is characteristic of each surfactant and that may explain why

with Tergitol TMN-6 the drop size is reduced at high concentrations but not with the Tritons. However, there is no available data on the relaxation times of these surfactants at present. Therefore, it is not known if the difference between them can effectively be explained from this standpoint.

A shift in adsorption mechanism could have similar effects. Nonionic surfactants have been reported to undergo such shifts at concentrations of the order of the CMC or higher (Lin, Chang, and Chen 1996; Dong *et al.* 2000). This means that the kinetic timescale (equation 4.4.3-4) may no longer be negligible in the high concentration range, and have a limiting effect on the overall adsorption dynamics. Any adsorption delay or time-related effect would, however, affect all silicone oils equally since the adsorption dynamics is independent of oil phase viscosity and all silicone oils have the same equilibrium interfacial behavior (see Chapter 6, section 6.1.2). As indicated in the previously referenced figures, this is not the case, since the observed behavior is different for the different viscosity oils, with the 10 cSt oil achieving drop sizes smaller than in water with all surfactants.

Another possible explanation is that the drop size in some surfactant laden system is larger than that for pure water, even at high surfactant concentration, due to a higher surfactant-induced interfacial shear viscosity. As aforesaid in Chapter 4, section 4.5.1, the surface shear viscosity of low molecular weight surfactants (as those used in this study) is usually considered negligibly small. However, most of the studies on interfacial shear viscosity found in the literature focus on planar interfaces in air/water or systems containing inviscid oil phases (most commonly hexane, toluene, or other light hydrocarbons). Edwards and Wasan (1988a,b) found that the intrinsic rheological

properties of liquid interfaces (shear and dilational viscosities of surfactant-free interfaces) depend on the curvature of the interface. Through dimensional considerations, they showed that surface curvature has such a marked effect on surface viscous stresses, that even very small surface rheological coefficients may result in considerable surface stresses for highly curved interfaces. On the other hand, Wasan, Gupta, and Vora (1971) determined that the interfacial velocity of clean liquid-liquid systems decreases as the viscosity ratio of the bulk phases increases. They say that this can be translated into an increase of the intrinsic surface shear viscosity of the interface with viscosity ratio. More recently, Pozrikidis (1994) carried out a numerical study of the effect of surface viscosity on the deformation of liquid drops, for the case of isotropic interfacial tension (no Marangoni stresses). He concluded that increasing the surface viscosity makes the drop behave more like a rigid particle and reduces the deformation.

Even though the previously cited studies focus on intrinsic interfacial viscosity instead of on surfactant-induced viscosity, it stands to reason that the presence of a surfactant on the interface would exacerbate the effect of surface shear viscosity observed on them because that is what the presence of surfactants do to the surface shear viscosity of planar, inviscid interfaces. Consequently, the surface shear stresses acting on surfactant-covered, viscous, spherical, micron-sized droplets may be considerably higher than those predicted by the conventionally-measured, low interfacial shear viscosity coefficients as applied to planar interfaces. This possible explanation for the higher-than-expected drop size values measured in concentrated surfactant solutions makes sense from the standpoint that it allows for the differences observed between the different viscosity oils. Furthermore, it may explain the higher D_{32} vs. rpm slopes obtained for the

Triton X surfactants since many surface layers are pseudoplastic (shear-thinning) (Erni *et al.* 2003; Walstra 2003).

7.2.2.2. Low Dispersed Phase Viscosity

To be able to better discern which possible explanation – limiting effects on adsorption dynamics or surface shear viscosity – is more suitable, it must be ascertained how close to, or far from, equilibrium-predicted behavior the high concentration data really are. Seeing as the 10 cSt data is the one apparently closer to equilibrium behavior (constant drop size above the CMC in all cases and drop size reduction, with respect to the clean water case, for all surfactants), the next part of the analysis will focused on this low viscosity data.

As previously stated, in the low surfactant concentration range, the data corresponding to the 10 cSt oil seems to be the least affected by the surface dilational modulus. However, a closer examination of this data indicates that it may still be of significance. Figure 7.2.2.2-1, shows the variation of mean drop size with rotor speed for concentrations of 10^{-3} mol/l for Tergitol TMN-6 and 2 times the CMC for Triton X-100 (6.04×10^{-4} mol/l). At these concentrations, both surfactants exhibit the same equilibrium interfacial tension: 5.6 mN/m. However, the drop size obtained for TX-100 is always greater than that for Tergitol. This difference may be explained by the difference in the values for the surface dilational modulus that these two conditions show, as seen in the bottom part of Figure 7.2.2-1. The E^{sd} for the Triton concentration is approximately three times higher than that for Tergitol (68 versus 20 mN/m) Therefore, even though the equilibrium interfacial tension is the same in both cases, the Marangoni stresses are significantly smaller for Tergitol and, thus the drop diameter is lower.

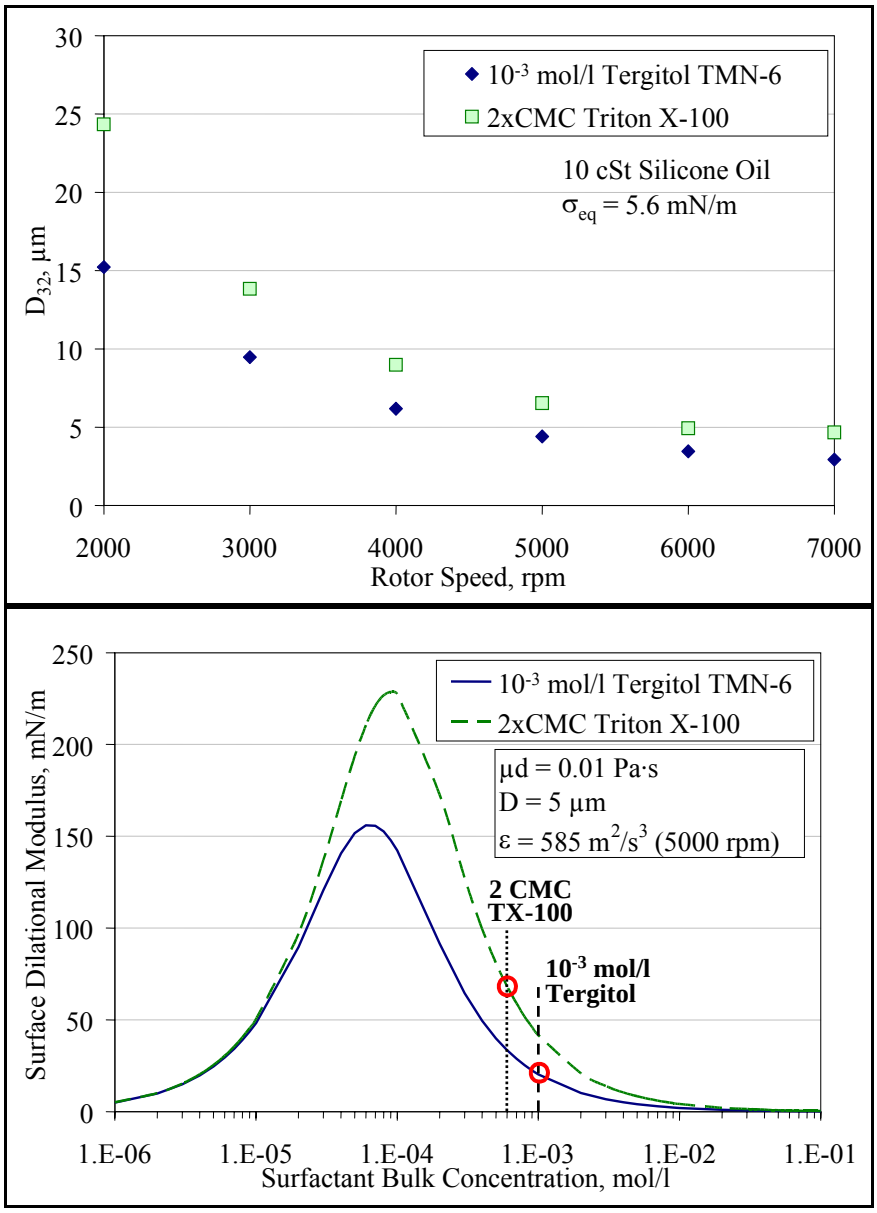

Figure 7.2.2.2- 1. Top: variation of D_{32} with rotor speed for 10^{-3} mol/l Tergitol TMN-6 and 2xCMC Triton X-100 (σ_{eq} = 5.6 mN/m, in both cases). Bottom: Variation of E^{sd} with surfactant concentration for Tergitol TMN-6 and Triton X-100, emphasizing the difference between the two conditions of the upper graph.

At higher surfactant concentrations, the effect of the surface dilational modulus seems to become negligible, as predicted, and the drop size is determined by equilibrium conditions. For low dispersed phase viscosities and equilibrium interfacial conditions, the drop size should scale with a positive power of the interfacial tension, according to

equations 3.3.1-15, 3.3.2.1-7, or 3.3.2.2-4, depending on whether the drops are in the inertial or viscous sub-range, and in the latter case, if the predominating stresses are inertial or viscous in nature. In other words:

$$\frac{D_{32}}{D_{32(0)}} \approx \left(\frac{\sigma_{eq}}{\sigma_0} \right)^n \qquad (7.2.2.2\text{-}1)$$

where $D_{32(0)}$ is the Sauter mean diameter for the same oil in clean water at the same rotor speed, σ_{eq} is the corresponding equilibrium interfacial tension, σ_0 is the clean interfacial tension, and n is 3/5 for the inertial sub-range, ⅓ for the viscous sub-range, inertial stresses, and 1 for the viscous sub-range, viscous stresses. Table 7.2.2.2-1 shows the averaged $D_{32}/D_{32(0)}$ for 10 cSt oil in surfactant solutions at the highest concentration of each surfactant and compares it to the corresponding $(\sigma_{eq}/\sigma_0)^n$ values (note: only the values corresponding to 5000 – 7000 rpm were included in said average since this is the range in which possible equilibrium behavior is observed). Clearly, the drop sizes obtained under these conditions are almost exactly the size predicted for drops broken up by sub-Kolmogorov (viscous sub-range) inertial stresses, and at interfacial equilibrium. The Kolmogorov microscale (equation 3.2.1-2), calculated with the maximum energy dissipation rate (Figure 6.3- 1), for these rotor speeds is in the range ~ 4.5 – 6 μm. The

Table 7.2.2.2- 1. Average relative Sauter mean diameter for 10 cSt silicone oil in highly concentrated surfactant solutions, compared to equilibrium-predicted interfacial tension ratios for the inertial sub-range (3/5 exponent), the viscous sub-range, inertial stresses (1/3) and viscous sub-range, viscous stresses (1).

Surfactant (Concentration)	$\overline{D_{32}/D_{32(0)}}$ [a]	$(\sigma_{eq}/\sigma_0)^{3/5}$	$(\sigma_{eq}/\sigma_0)^{1/3}$	(σ_{eq}/σ_0)
Tergitol TMN-6 (5xCMC)	0.40	0.18	0.39	0.059
Triton X-100 (100xCMC)	0.61	0.28	0.49	0.12
Triton X-165 (100xCMC)	0.62	0.44	0.63	0.25

[a]: averaged from the values for 5000, 6000, and 7000 rpm

drop sizes (D_{32}) in question are in the range 2.6 – 4.4 μm, which means that they are indeed in the viscous sub-range, although just barely. However, the important point here is that they indicate that the interfacial tensions are at, or very close to, equilibrium values for all surfactants, at least when the concentration and the rotor-speed are high. This agrees with the results presented on Figure 6.4-1, which shows that for the highest surfactant concentrations the parameter δ_D/h reaches values close to unity. This means that for these concentrations equilibrium interfacial behavior is possible since the Marangoni stresses can be rapidly relaxed by diffusion of surfactant molecules from the continuous phase. Hence, it is unlikely that the seemingly high drop sizes obtained for the higher viscosity oils are the product of limited adsorption dynamics. As mentioned above, equilibrium interfacial behavior is independent of oil viscosity; therefore, if the 10 cSt oil does not show signs of an adsorption dynamics change, the rest of the silicone oils should also not experience one. Therefore, the reason why the drop sizes of higher viscosity oils do not fall to the equilibrium-estimated level is most likely related to an increase in surface shear viscosity caused by the presence of surfactant at the interface.

Possibly, surface viscosity-related behavior is observed even in the 10 cSt silicone oil if the whole range of rpm is considered. The different behavior that both Triton X surfactants display in the low speed range (2000 – 4000) was already shown by the higher slopes that they exhibit in Figures 7.2.2.1-2 and 7.2.2.1-3. However, it is better appreciated in Figure 7.2.2.2-1, where the D_{32} of the drops obtained with the highest concentration of each surfactant is plotted against the turbulent energy dissipation rate. The Tergitol curve shows proportionality to $\varepsilon^{-1/3}$, which is the behavior predicted by equation 3.3.2.1-7 for the viscous sub-range assuming breakage by inertial stresses. This

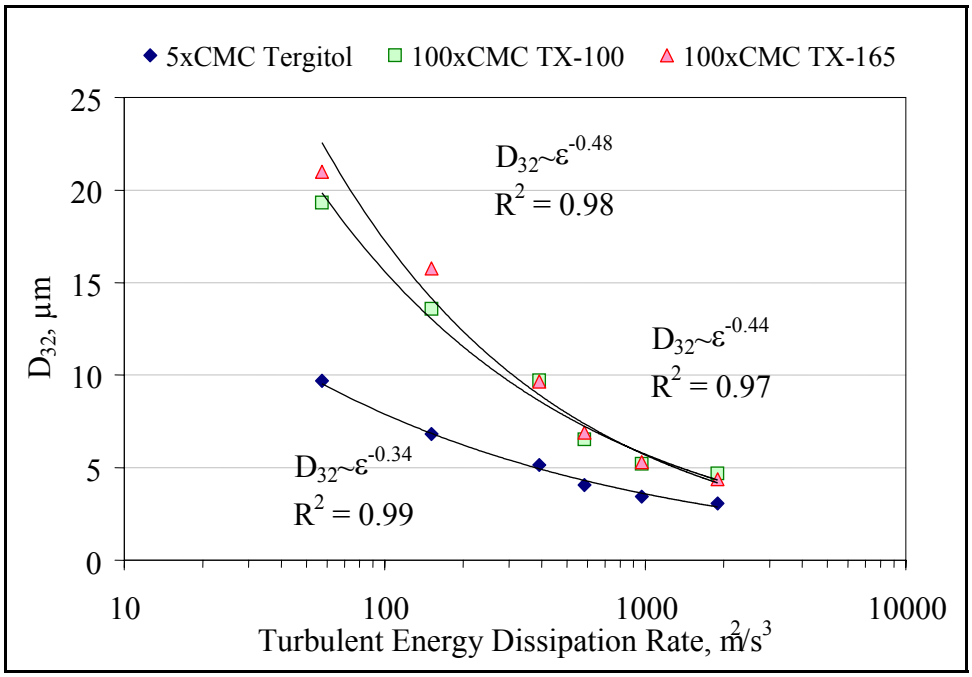

Figure 7.2.2.2- 2. Sauter mean diameter against energy dissipation rate for 10 cSt silicone oil at the highest concentration of each surfactant.

corroborates the fact that for this oil, inviscid-like equilibrium behavior is attained. The slopes of both Tritons are higher: $\varepsilon^{-0.44}$ for X-100 and $\varepsilon^{-0.48}$ for X-165. Conversely, if only the high rpm data is considered for these surfactants, the exponents fall down to -0.28 for X-100 and -0.38 for X-165, which are considerably closer to the theoretical -⅓ value. Hence, the higher drop size obtained at low rpm could be due to a higher and shear-thinning interfacial viscosity. This does not explain, however, why the drop size obtained with Triton X-100 is so close to the one obtained with X-165, despite the fact that its equilibrium interfacial tension is half of that for X-165 (5.6 and 11.8 mN/m respectively).

7.2.2.3. High Dispersed Phase Viscosity and High Surfactant Concentration

The highest deviations from predictable behavior are observed for the high viscosity, high surfactant concentration cases (1000 cSt silicone oil at post-CMC concentrations). Under such conditions, the resulting drop size is approximately equal to,

or even lower than, the ones obtained with lower viscosity oils. All mechanistic models predict that drop size scales with a positive power of the dispersed phase viscosity (exponents range from ⅓ to 1). Furthermore, as shown in Figure 7.2.2.3-1, at the highest surfactant concentrations the drop size becomes virtually insensitive to the turbulent energy dissipation rate (and, thus, to rotor speed). So far, the behavior with respect to rotor speed remains unexplained. Curiously, this behavior bears a resemblance to that observed for the same oil in methanol solutions, where the drop size becomes independent of the energy dissipation rate (see Figure 7.1.3-5). Conversely, though, the drops size in that case increases as the interfacial tension decreases. Therefore, the apparent similarity could just be a coincidence. On the other hand, it is possible that the reason for the lower-than-expected D_{32} for the high viscosity oil is related to the constant drop size observed for the 1000 – 10,000 cSt oils in water (see section 7.1.2).

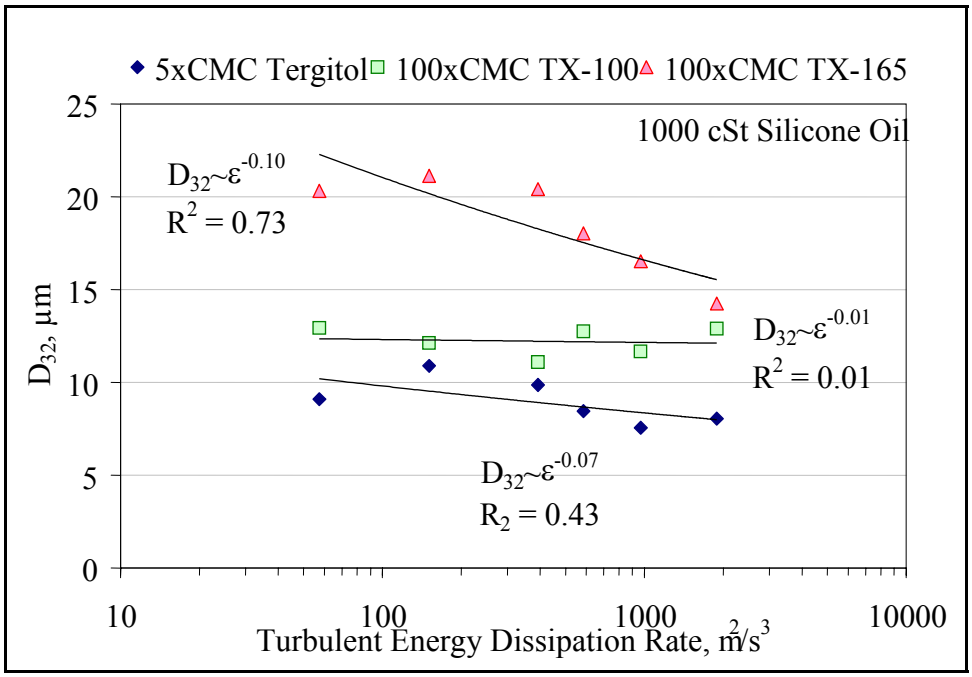

Figure 7.2.2.3- 7. Sauter mean diameter against energy dissipation rate for 1000 cSt silicone oil at the highest concentration of each surfactant.

At these surfactant concentrations, as evidenced from the 10 cSt oil analysis, the interface behaves like it is at equilibrium and, therefore, the drops are covered with surfactant even during deformation. In a previous section of this chapter, it was explained how high viscosity oils deform into bulbous ends united by a viscous thread and that the higher the drop viscosity, the longer this thread gets before breaking. Hajiloo, Ramamohan, and Slattery (1987) studied the effect of interfacial viscosities (dilational and shear) on the stability of a liquid thread, via a linear stability analysis. The case they considered was that of a rapidly adsorbing surfactant, so that the Marangoni stresses may be neglected; which is similar to having a high surfactant concentration. They concluded that the growth rate of the instabilities moves towards zero as the surface viscosities increase and, therefore, the effect of increasing interfacial viscosities is the tendency to stabilize the thread. As previously mentioned, a more stable thread translates into a longer thread and, thus, a more extensional flow-like behavior. Consequently, the effect of a higher interfacial viscosity due to the presence of surfactant at the interface could be analogous to having a larger bulk phase viscosity. This would explain the drop size attaining an apparent constant size, as in the case of 10,000 cSt oil in water (see section 7.1.2), but at a much lower dispersed phase bulk viscosity, μ_d.

Figure 7.2.2.3-2 contains the average drop size, over the entire ε range, for the same cases presented in Figure 7.2.2.3-1 (1000 cSt at the highest concentration of each surfactant), against the equilibrium interfacial tension of each surfactant for post-CMC concentrations. It shows that the drop size scales linearly with the interfacial tension. While in the right direction, this is not the behavior predicted by the mechanistic models of chapter 3. However, it must be recalled that these models account for the effect of the

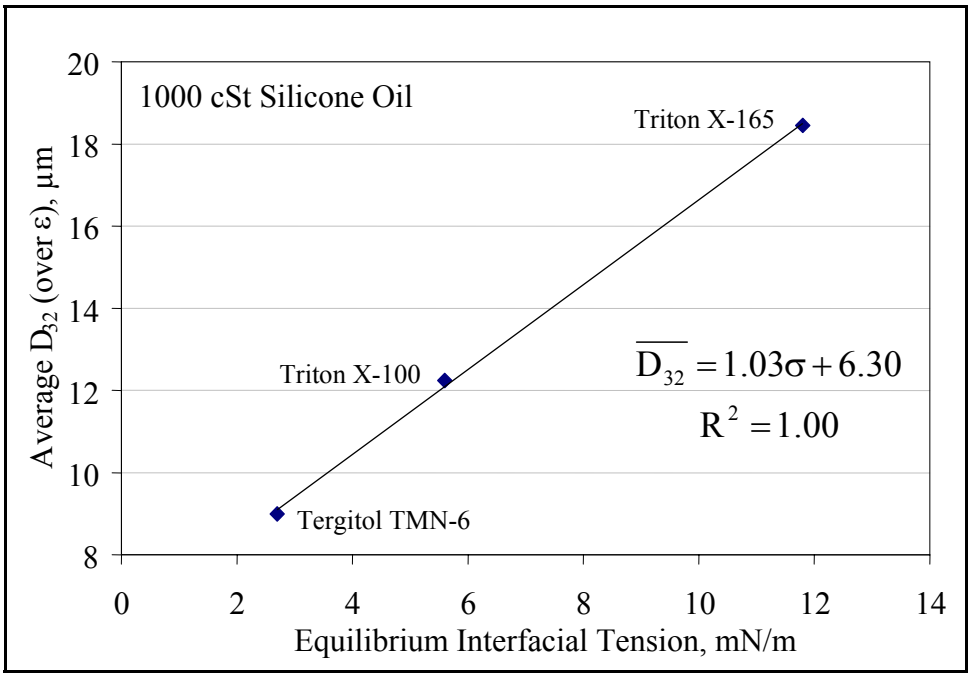

Figure 7.2.2.3- 8. D_{32} averaged over all ε values (from Figure 7.2.2.3-1) as a function of the equilibrium interfacial tension of each surfactant at post-CMC concentrations.

dispersed phase viscosity as an additional viscous shear stress on the drop (equation 3.3.1-5). If the drop is stretched by an extensional flow, the drop size should behave closer to what is indicated by the capillary number, defined in equation 7.1.2-1. This means that for constant dispersed phase viscosity and flow conditions (the flow conditions are not really constant since ε varies, but the D_{32} was averaged over all ε values), the drop size should be directly proportional to the interfacial tension ($D \sim \sigma$). Therefore, the behavior shown in Figure 7.2.2.3-2 supports the theory of a shift towards extensional flow-like behavior, in this case, due to a higher interfacial viscosity.

7.2.3. Drop Size Distributions

The previous section focused on the effect of surfactant on the mean drop size of silicone oil dispersions. Now, the attention will be on the effect that the presence of surfactants

has on the drop size distribution. Figure 7.2.3-1 shows the drop size distributions of three silicone oils (10, 100, and 1000 cSt) in Tergitol TMN-6 solutions at low concentration (10^{-5} mol/l), for all rotor speeds. As seen, the 10 cSt oil's distributions are practically parallel to each other, and they shift towards smaller sizes as the rotor speed increases. For the higher viscosity oils, there is a slight bend in the curves, similar to that observed for the pure water cases (Figure 7.1.2-2), especially in the 1000 cSt oil at lower rotor speed. This indicates the presence of the relatively larger population of smaller drops, suggested by the lower D_{32}/D_{max} observed for larger μ_d. Furthermore, Figure 7.2.3-1 shows that the effect of increasing rotor speed is less significant for the higher viscosity oils. Figure 7.2.3-2 is a similar plot, but in this case for highly concentrated surfactant solutions (Tergitol TMN-6 at 5xCMC). The 10 cSt distributions are no longer parallel, but tend to converge in the smaller drop size range. This means that the high concentration of surfactant increases the monodispersity of the distributions as the rotor-speed increases. This is consistent with the increase in D_{32}/D_{max} observed for this oil in surfactant systems (section 7.2.1), since a higher D_{32}/D_{max} denotes a narrower distribution. By comparing these DSD to the ones at low surfactant concentration (Figure 7.2.3-1) is evident that for higher rotor speeds the size of the smaller drops of the distributions is approximately the same, while the larger drops do get reduced in size. This indicates that this particular oil achieves an equilibrium drop size that seems to be at the limit of what the mixer can produce under the experimental conditions of the present study. This explains why the distributions narrow at high surfactant concentrations. However, this could also be due to the fact that the drop size is nearing the limit for the video microscopy technique (~1 μm).

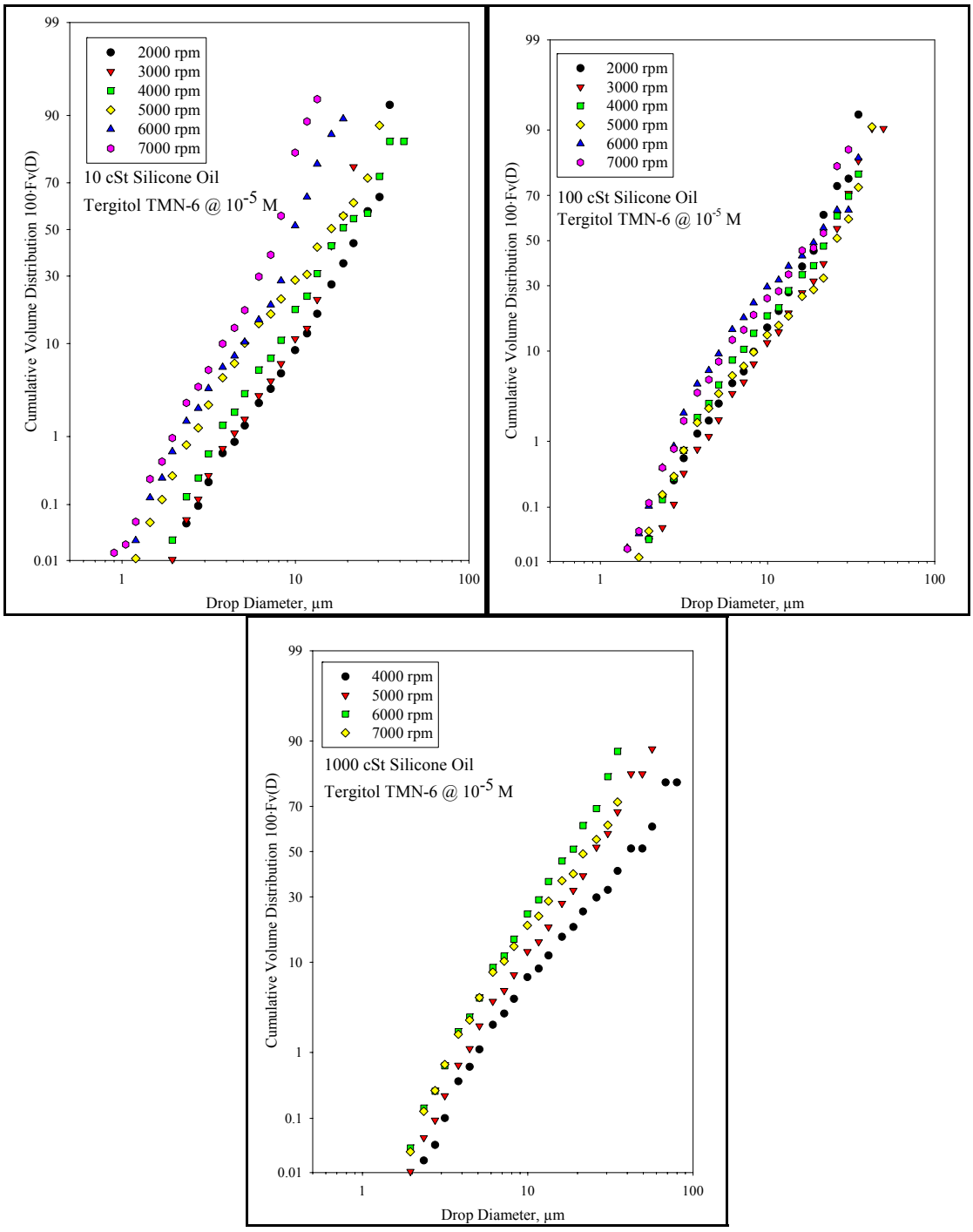

Figure 7.2.3- 1. Cumulative volume drop size distributions of 10 (top, left), 100 (top, right), and 1000 cSt (bottom) silicone oils dispersed in 10^{-5} mol/l Tergitol TMN-6 solutions.

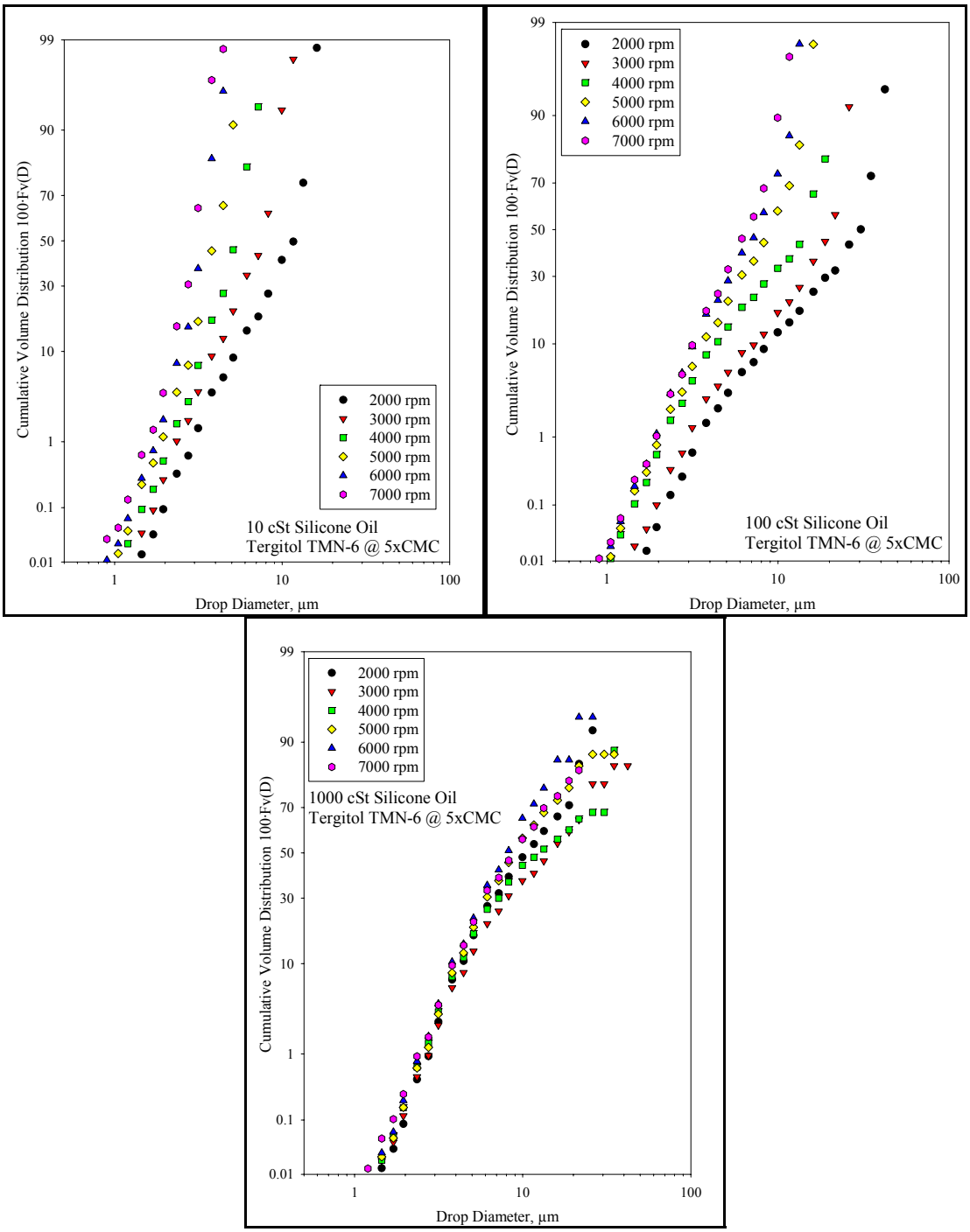

Figure 7.2.3- 2. Cumulative volume drop size distributions of 10 (top, left), 100 (top, right), and 1000 cSt (bottom) silicone oils dispersed in 5xCMC Tergitol TMN-6 solutions.

In the 100 cSt case, the effect of high surfactant concentration at low rotor speed is to increase the population of smaller drops, thus increasing the curvature in the

functional form of the DSD. However, at high rotor speed, the opposite effect is seen, the DSD curves are straighter than they were at low concentration. This could explain the fact that for this viscosity grade, there is also an increase in the proportionality constant between D_{32} and D_{max}. However, at present there is no adequate explanation for this phenomenon.

For the highest viscosity oil, the change in shape of the DSD is most evident, as rotor speed only affects the size of the largest drops. This agrees with the hypothesis of a larger production of satellite drops due to the longer elongation of the liquid thread caused by surfactant-enhanced stability. It is also evident that the dependency on rotor speed is minimum for the high concentration, high viscosity case. The 1000 cSt distributions shown in Figure 7.2.3-2 correspond to the samples for 5xCMC Tergitol TMN-6 presented in Figure 7.2.2-11, where the lack of dependence on rotor speed, or in this case turbulent energy dissipation rate, is also manifested.

The preceding observations were made on the basis of the Tergitol TMN-6 distributions presented in Figures 7.2.3-1 and -2. However, similar trends are observed for Triton X-100 and Triton X-165. Figures 7.2.3-3 and -4 show selected drop size distributions obtained with these surfactants, for all drop viscosities, and low and high concentrations, at a fixed rotor speed of 5000 rpm. In these plots, however, aside from the behavior already described, it is also seen that at high surfactant concentrations the distributions corresponding to 100 and 1000 cSt overlap. This is consistent with the behavior observed for the D_{32} of these oils at the same surfactant concentration, described in the previous section and shown in Figures 7.2.2-3 thru 7.2.2-6.

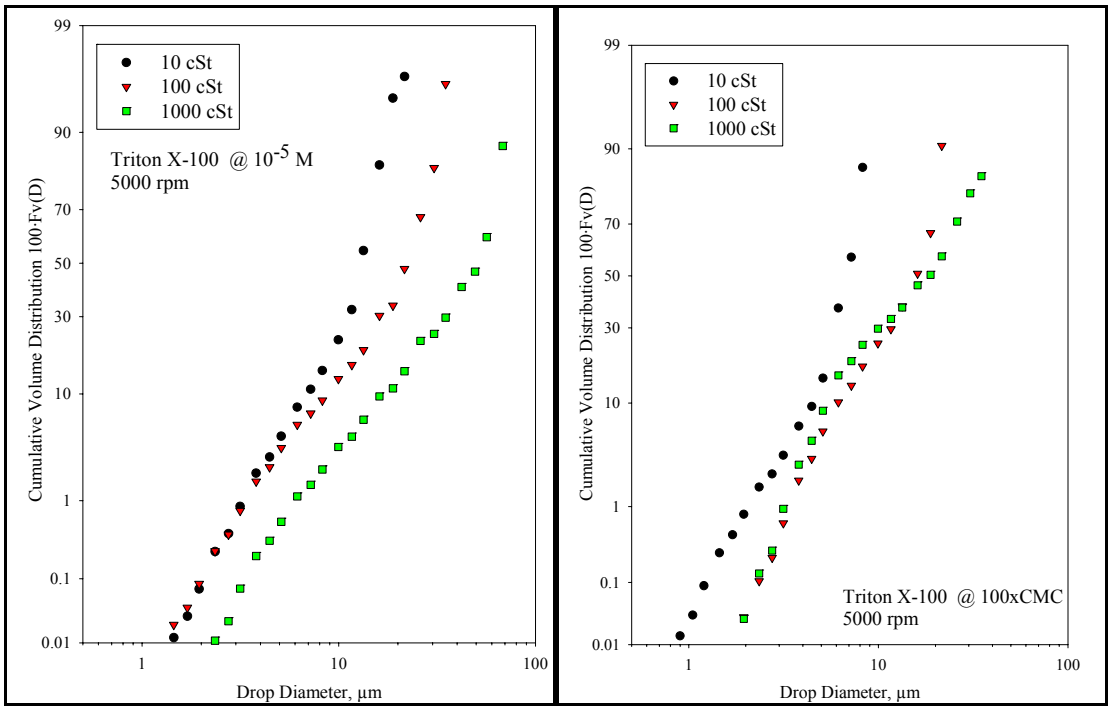

Figure 7.2.3- 3. Cumulative volume drop size distributions of 10, 100, and 1000 cSt silicone oils dispersed in 10^{-5} mol/l (left) and 100xCMC (right) Triton X-100 solutions at 5000 rpm.

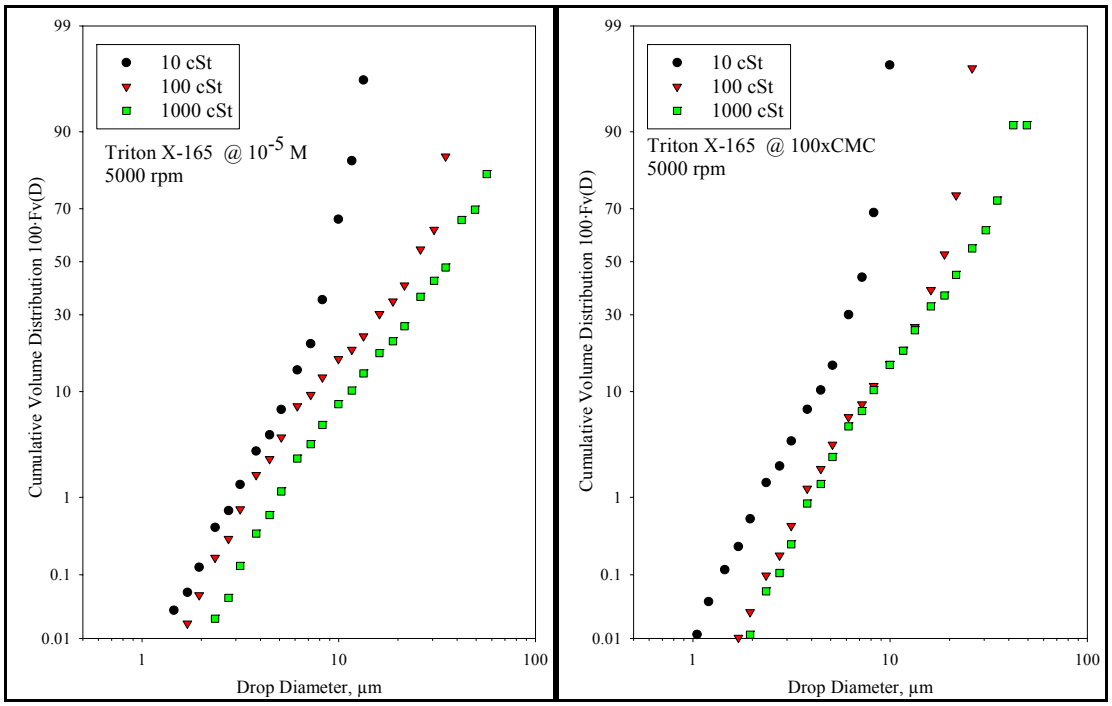

Figure 7.2.3- 4. Cumulative volume drop size distributions of 10, 100, and 1000 cSt silicone oils dispersed in 10^{-5} mol/l (left) and 100xCMC (right) Triton X-165 solutions at 5000 rpm.

7.2.4. Possible effect of Surfactant Convection

So far, the transport of surfactant to the interface by convection has been neglected. The previous analysis of the effect of the surface dilational modulus on drop size is based on the calculated values for this property that were presented in Chapter 6. The equations used were derived from the theory of Lucassen and van den Tempel (1972), as explained in Chapter 4; which assumes that the surfactant is transported solely by molecular diffusion and that there is no bulk flow in the surfactant solution. Evidently, that is not the case in emulsification processes, especially ones in which the flow is turbulent. According to Walstra and Smulders (1998), convection is the only significant surfactant transport mechanism in emulsification and diffusion is negligible. They admit that the surface dilational modulus may be estimated by Lucassen and van den Tempel's approach (presented in Chapter 4, section 4.5.2), but that it should be regarded as an approximated value.

The only way to formally introduce convection into the equations for the surface dilational modulus is to include the convective terms in the governing equations (equations 4.4.2-2 and 4.5.2-3). This would complicate greatly the derivation since the flow fields, both in the bulk and at the interface, would have to be solved simultaneously with the mass balances. However, by examining the length and timescales related to the adsorption process, a criterion for the relative magnitude of the two transport mechanisms can be established

The two characteristic length scales were introduced in Chapter 4. One is the adsorption depth, h (equation 4.4.3-3); the other is the diffusion layer thickness, δ_D (equation 4.6-2). The former determines the distance that surfactant molecules must

travel to get to the drop's surface; the latter is the thickness of the region around the drop in which diffusion is dominant. These two length scales are independent of each other: h depends mainly on the surfactant's equilibrium conditions (i.e. surfactant concentration), while δ_D is determined by hydrodynamics. Figure 7.2.4-1 shows an idealized schematic representation of drops in two different conditions: on the left, the adsorption depth is equal or smaller than the diffusion layer ($\delta_D/h \geq 1$), and on the right, the adsorption depth is larger than the diffusion thickness ($\delta_D/h < 1$). In the first case, all the surfactant adsorbed on the drops comes from within the diffusion layer. Thus, diffusion is the dominant transport mechanism and the adsorption timescale is given by equation 4.4.3-2. In the second case, surfactant molecules are convected by the flow from the bulk to the diffusion layer and, then, it diffuses through it to the drop surface. Therefore, the adsorption timescale has a convective component, given by the distance that the surfactant is convected ($h-\delta_D$) and the flow's characteristic velocity (u'); and a diffusive

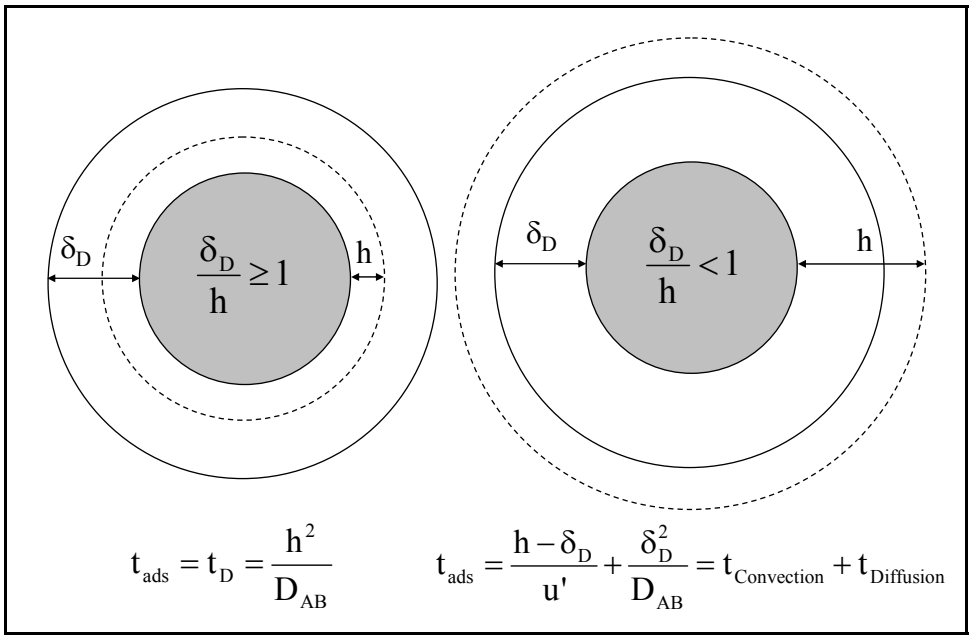

Figure 7.2.4- 1. Schematic representation of a drops, diffusion layers and adsorption depths

component given by the diffusion layer thickness and the surfactant's diffusivity (D_{AB}). The total adsorption times for the two limiting cases are given in Figure 7.2.4.1. It is seen that the physicochemical parameter δ_D/h can be employed to determine whether diffusion is the only significant transport mechanism or if convection should be considered. Moreover, in the latter case, if the ratio between the two components of the adsorption timescale can be estimated, it can give an idea of how significant convection is compared to diffusion. For the range of variables in the present study, $t_{Convection}/t_{Diffusion}$, given by:

$$\frac{t_{Convection}}{t_{diffusion}} = \frac{(h - \delta_D)D_{AB}}{u'\delta_D^2} \qquad (7.2.4\text{-}1)$$

reaches maximum values of O(1) for the lowest surfactant concentrations (10^{-5} mol/l), which produces the lowest δ_D /h values (see Figure 6.4-1). This means that, even when surfactant convection is significant, diffusive transport is never negligible. This is further evidenced by the fact that in the lower concentration range, the surface dilational modulus has an appreciable effect on drop size, as shown in the previous sections.

7.3. Summary

The mean drop size of liquid-liquid dispersions of silicone oil in water produced by rotor-stator mixers increases with increasing dispersed phase viscosity, for low to moderately high viscosity values. This increase is less pronounced that that observed for similar oils in stirred tanks. For high drop viscosity, however, the behavior changes and the drop size becomes independent of dispersed phase viscosity. This is not explained by the mechanistic models previously derived. However, it could be explained by a shift towards a more extensional flow-like behavior caused by the long deformation timescales of highly viscous drops. The addition of methanol to the continuous phase, although

decreasing the interfacial tension of the system, increases the mean drop size of the dispersion. This behavior is contrary to what is predicted by mechanistic theories and has yet to be satisfactorily explained. However, there is confidence that it is not due to flaws in the experimental data.

The mean drop size is significantly affected by the presence of surfactants in the continuous phase. This effect depends on the surfactant concentration range and dispersed phase viscosity. At low surfactant concentrations, the Marangoni stresses acting on the drop due to surfactant-induced interfacial tension gradients dominate the behavior of the mean drop size. The D_{32} increases with increasing surfactant concentration until it reaches a peak. This occurs at surfactant concentrations similar to those at which the surface dilational modulus attains its maximum value, as shown in Chapter 6. Therefore, E^{sd} may be used to characterize the behavior the mean drop size of liquid dispersions in dilute surfactant solutions.

At high surfactant concentrations the Marangoni become negligible, but the surfactant still has an effect on drop size. At low dispersed phase viscosity, behavior consistent with the equilibrium interfacial tension is observed, for high rotor speed. However, at lower rotor speeds, the surfactant seems to increase the surface shear viscosity and causes shear thinning behavior. At high dispersed phase viscosity, the drop size becomes independent of rotor speed. The apparently higher surface shear viscosity increases the effective drop viscosity and induces a shift towards more extensional flow-like behavior, consistent with the observed for high oil viscosity in water. Additionally, the number of small drops (satellites) in the DSD increases for high surfactant concentration and oil viscosity. This is also consistent with the extensional flow behavior.

CHAPTER 8. DROP SIZE CORRELATIONS

In this chapter, the DSD data presented previously will be correlated by fitting it to mechanistic models for mean drop size in turbulent dispersions. These correlations are of high practical interest since they allow the prediction of DSD from physical properties data and operational conditions. From a more fundamental point of view, they also provide valuable insight into the mechanics of drop breakage in turbulent dispersions. By fitting the data to different models, or variations thereof, conclusions may be drawn about the dominating forces acting during the deformation and breakup process.

The chapter will begin with a description of the methodology employed to include the effect of the presence of surfactants into the models, as well as the criterion used to evaluate model accuracy. Then, the data fitting for the D_{32} correlations will be presented and discussed. Finally, a correlation for the drop size distribution, based on the log-normal cumulative distribution function, will be developed from the experimental data.

8.1. Sauter Mean Diameter Correlations

8.1.1. Methodology

The mechanistic models derived in Chapter 3 presuppose that the fluids are pure and free of any surface active material. Therefore, they implicitly assume that all the physical properties remain at their equilibrium or nominal values. This is not necessarily the case when there is a surfactant present in the system. The approach chosen to include the effect of surfactants is based on the hypothesis that drop breakup in the presence of a surfactant can be evaluated from equilibrium relations, provided that some appropriately

defined, effective physical properties are used (Janssen, Boon, and Agterof 1994b). In this particular case, the effective property will incorporate the surface dilational modulus, E^{sd}, in order to introduce the effect of interfacial rheology into the model. It must be noted that a more complete approach would include the effect of the surface shear viscosity as well. However, this property cannot be predicted from equilibrium behavior, like the surface dilational modulus, and presently there is no experimental data available.

Two variations of this approach can be found in the literature, as referenced in Chapter 4. One utilizes an effective dispersed phase viscosity and the other an effective interfacial tension. The first one, proposed by Lucassen-Reynders and Kuijpers (1992), is based on the fact that the surface dilational modulus represents the viscoelastic resistance to movement of the interface and corresponds to an apparent interfacial dilational viscosity of magnitude E^{sd}/α, where α is the relative rate of interface extension ($\sim\omega$, in the equations of Chapter 4). They argue that the total resistance of the dispersed phase would be determined by the sum of the dispersed phase bulk viscosity and the interfacial viscosity which results in equation 4.7-2. As explained previously, in the present case the surface dilational modulus calculated from equation 4.5.2-14 should be regarded as a limiting value, the actual value during emulsification could be smaller due to convection of surfactant to the interface. Consequently, the effective dispersed phase viscosity to be used with the models is defined as:

$$\mu_d^{eff} = \mu_d + C_\mu E^{sd} \frac{2t_{def}}{D_{32}} \qquad (8.1.1\text{-}1)$$

where C_μ is an empirically adjustable constant and t_{def} is the chosen deformation timescale (t_{dd}, the drop deformation timescale, or t_{eddy}, the eddy lifetime)

The other variation is that proposed by Janssen, Boon, and Agterof (1994b). They chose to define an effective interfacial tension (equation 4.7-1) instead of using an effective dispersed phase viscosity because they considered the low viscosity ratio range ($\mu_d/\mu_c < 1$), where an increase in μ_d would actually decrease the critical capillary number. Even though this is not the case in the present study, it is an approach worth examining. Therefore, the effective interfacial tension to be used here is defined as:

$$\sigma_{eff} = \sigma + C_\sigma E^{sd} \qquad (8.1.1\text{-}2)$$

where C_σ is also an empirically adjustable constant. Note: the two approaches are always used independently: whenever the effective viscosity is used, the interfacial tension is assumed to be at equilibrium and, vice versa.

There are three different linear models, equations 3.3.1-12, 3.3.2.1-5, and 3.3.2.2-9; one for each turbulence sub-range: inertial sub-range, viscous sub-range assuming inertial stresses, and viscous sub-range assuming viscous stresses, respectively. For each of these models there is an equivalent spring and dashpot model: equations 3.3.3.1-3, 3.3.3.2-3, and 3.3.3.3-4, respectively. As mentioned, there are two possible timescales for the deformation, t_{dd} and t_{eddy}. Also, there are the two possible approaches, μ_d^{eff} and σ_{eff}. This allows for 24 possible combinations. Thus, in the following section, the best set of conditions to fit the data will be determined by a process of systematic elimination.

The main criterion for the selection of the best set of conditions was the root mean squared difference (RMSD) between the experimental dimensionless diameter, $(D_{32}/L)_{exp.}$, and the dimensionless diameter, $(D_{32}/L)_{calc,}$ calculated from the resulting correlation:

$$\mathrm{RMSD} = 100\mathrm{x}\sqrt{\frac{\sum_{i}\left(\frac{\left(D_{32}/L\right)_{exp.} - \left(D_{32}/L\right)_{calc.}}{\left(D_{32}/L\right)_{exp.}}\right)_{i}^{2}}{N}} \qquad (8.1.1\text{-}3)$$

where N is the number of data points. A lower RMSD value (in %) indicates a higher accuracy for the evaluated correlation. It should be noted that this criterion alone may not be satisfactory. In some cases, where the RMSD of two or more correlations are close (within a few %), additional arguments were made to select the best fit.

The calculated values were computed through a program written in Matlab (Appendix B), which obtains D_{32}/L by an iterative procedure that also calculates E^{sd} at each step (E^{sd} also depends on D_{32}). The values for the empirical constants of the mechanistic models were found by changing the general form of the models from $D_{32}/L = A_1 f(We)[1+A_2 f(Vi)]^n$ to $(D_{32}/L)^{1/n} f(We)^{-1/n} = A_1^{1/n} + A_1^{1/n} A_2 f(Vi)$, where f(We), f(Vi), and n are different for each model, but known (see Table 3.5-1). Making this change allowed calculating the values for A_1 and A_2 from the linear regression of a plot of $(D_{32}/L)^{1/n} f(We)^{-1/n}$ versus f(Vi), using physical properties and experimental drop size data. The values so obtained for the constants vary with C_μ or C_σ, since they modify physical properties included in f(We) and f(Vi). Therefore, the value for C_μ or C_σ was varied over the range 0 – 1 to obtain corresponding values for A_1 and A_2. The values for all constants were input into the Matlab program and it calculated D_{32}/L for all the different experimental conditions as well as the RMSD. The optimum constants values were those that minimized the RMSD of the correlation.

8.1.2. Surfactant Systems

8.1.2.1. Individual Models

Figure 8.1.2.1-1 shows the goodness of fit of the linear model for the inertial sub-range (equation 3.3.1-12, also found in Table 3.5-1) using both effective property approaches (σ_{eff} and μ_d^{eff}). The corresponding equations are:

$$\frac{D_{32}}{L} = 0.086 We^{-3/5}\left[1 + 0.229 Vi\left(\frac{D_{32}}{L}\right)^{1/3}\right]^{3/5};\ \sigma_{eff} = \sigma + 0.029 E^{sd} \quad (8.1.2.1\text{-}1)$$

(L >> D >> η)

$$\frac{D_{32}}{L} = 0.079 We^{-3/5}\left[1 + 0.089 Vi\left(\frac{D_{32}}{L}\right)^{1/3}\right]^{3/5};\ \mu_d^{eff} = \mu_d + 0.055 E^{sd}\frac{2t_{dd}}{D_{32}} \quad (8.1.2.1\text{-}2)$$

with RMSD values of 55.3 and 38.3%, respectively. Figure 8.1.2.1-2 presents a similar pair of plots, but for the viscous sub-range, inertial stresses, linear model (equation 3.3.2.1-5, also in Table 3.5-1). In this case the equations are:

$$\frac{D_{32}}{L} = 0.276(We\,Re)^{-1/3}\left[1 + 0.369 Vi\,Re^{1/2}\left(\frac{D_{32}}{L}\right)\right]^{1/3};\ \sigma_{eff} = \sigma + 0.17 E^{sd} \quad (8.1.2.1\text{-}3)$$

(D < η)

$$\frac{D_{32}}{L} = 0.201(We\,Re)^{-1/3}\left[1 + 0.296 Vi\,Re^{1/2}\left(\frac{D_{32}}{L}\right)\right]^{1/3};\ \mu_d^{eff} = \mu_d + 0.109 E^{sd}\frac{2t_{dd}}{D_{32}} \quad (8.1.2.1\text{-}4)$$

with RMSD of 50.7 and 33.6%, respectively. The equivalent graphs for the viscous sub-range, viscous stresses linear model (equation 3.3.2.2-9 and Table 3.5-1) are shown in Figure 8.1.2.1-3. The equations in this case are:

$$\frac{D_{32}}{L} = 0.015 We^{-1}\,Re^{1/2}\left[1 + 0.187 Vi\,Re^{-1/4}\right];\ \sigma_{eff} = \sigma + 0.028 E^{sd} \quad (8.1.2.1\text{-}5)$$

(D << η)

$$\frac{D_{32}}{L} = 0.014 We^{-1}\,Re^{1/2}\left[1 + 0.069 Vi\,Re^{-1/4}\right];\ \mu_d^{eff} = \mu_d + 0.046 E^{sd}\frac{2t_{dd}}{D_{32}} \quad (8.1.2.1\text{-}6)$$

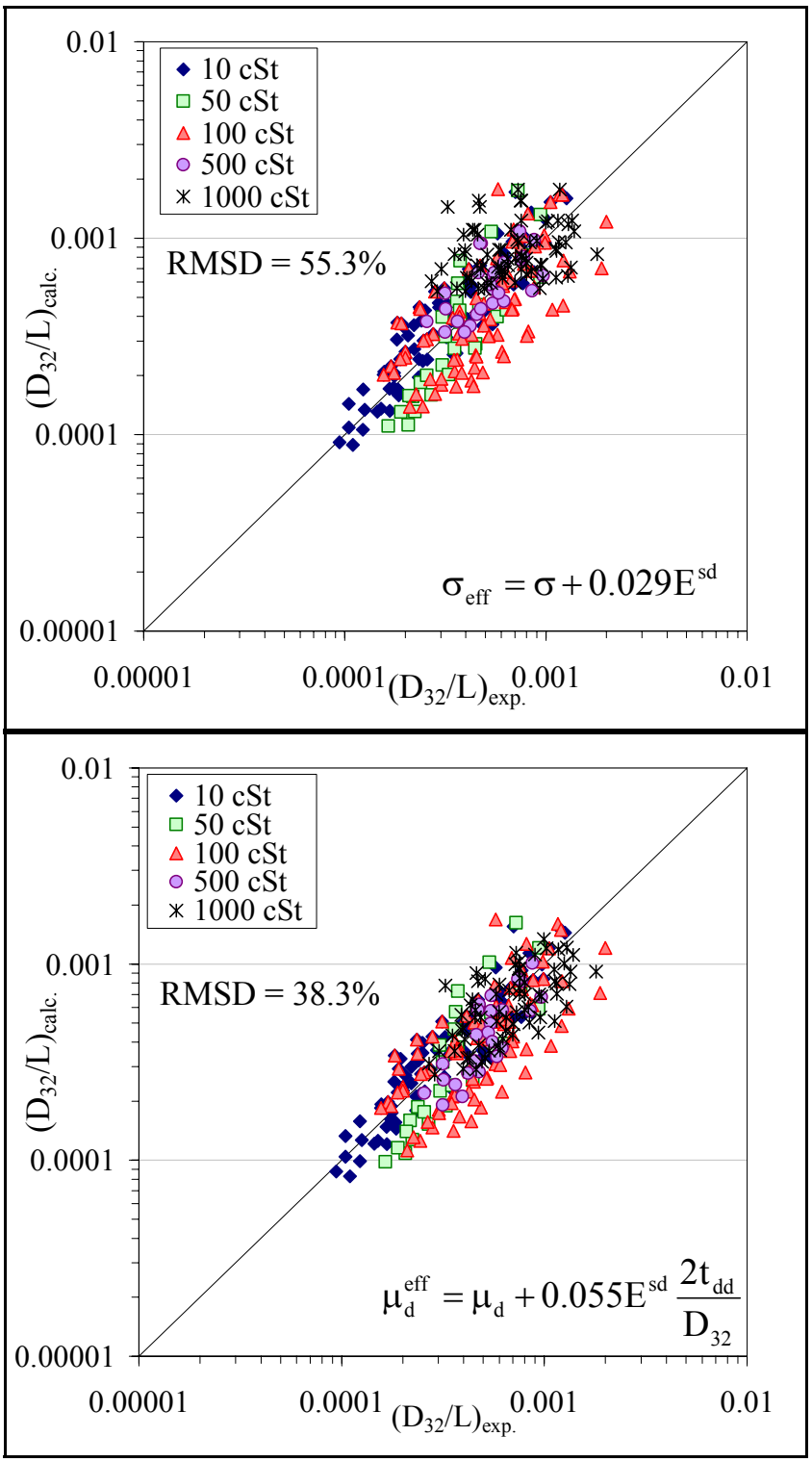

Figure 8.1.2.1- 1. Goodness of fit for the inertial sub-range linear model: top, equation 8.1.2.1-1 (σ_{eff}); bottom, equation 8.1.2.1-2 (μ_d^{eff}).

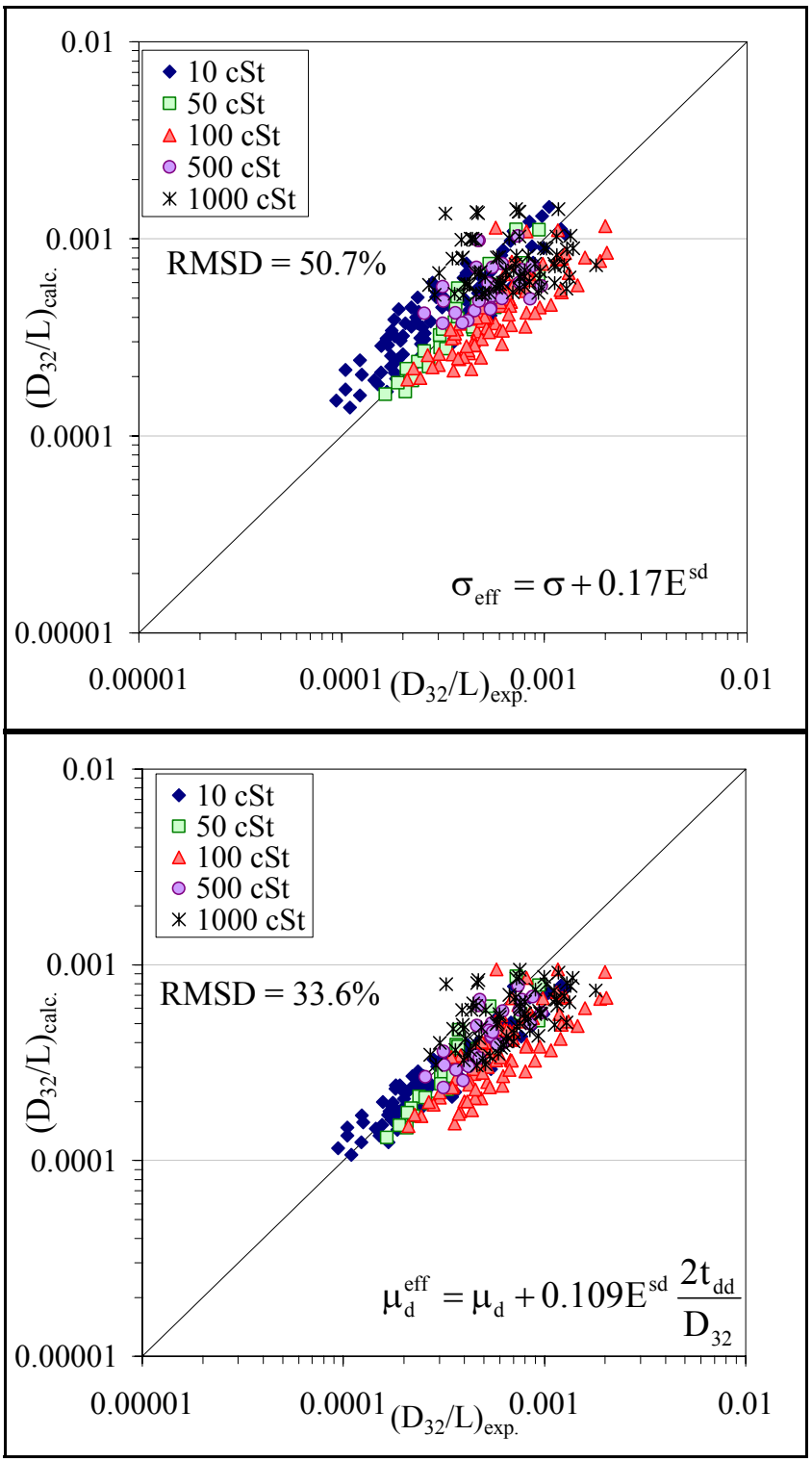

Figure 8.1.2.1- 2. Goodness of fit for the viscous sub-range, inertial stresses, linear model: top, equation 8.1.2.1-3 (σ_{eff}) ; bottom, equation 8.1.2.1-4 (μ_d^{eff}).

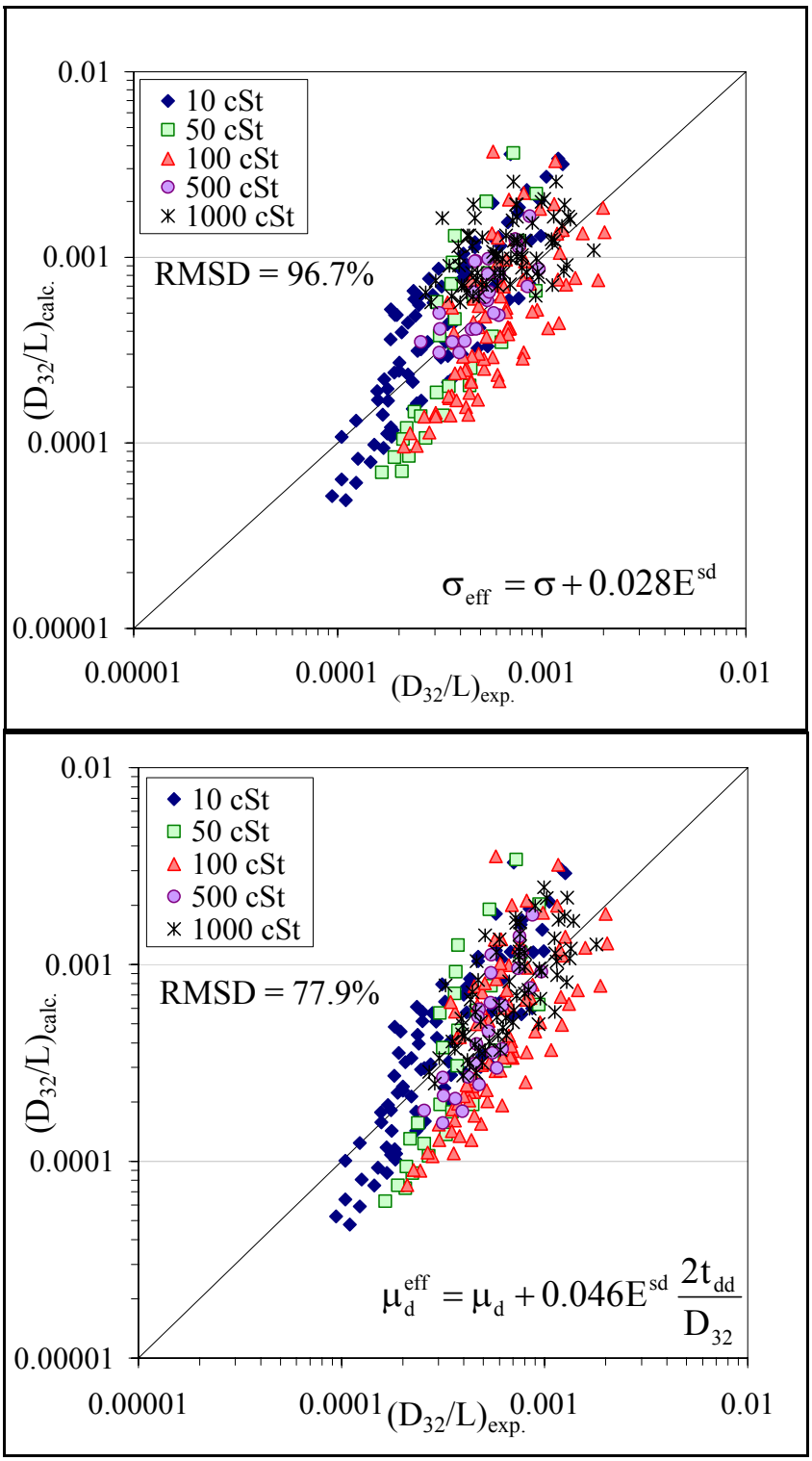

Figure 8.1.2- 3. Goodness of fit for the viscous sub-range, viscous stresses, linear model: top, equation 8.1.2.1-5 (σ_{eff}); bottom, equation 8.1.2.1-6 (μ_d^{eff}).

and the RMSD are 96.7 and 77.9%, respectively.

Several conclusions may be drawn from this set of graphs and equations. First, in all cases, the effective interfacial tension approach yielded considerably worse fits than the effective viscosity approach (RMSD 24 – 51% higher). Therefore, it may be concluded that the observed increase in drop size with surfactant concentration in dilute liquid-liquid dispersions in a rotor-stator mixer, can be better approximated by an increase in the effective dispersed phase viscosity of the system due to changes in interfacial rheology.

Second, the viscous sub-range, viscous stresses model produced prominently worse fits than the other two models, under similar conditions (RMSD 74 – 130% higher). On the other hand, the inertial sub-range and viscous sub-range, inertial stresses models gave fairly similar fits (RMSD within 14%). This is, most likely, due to the fact that the majority of the drops are actually in a region that overlaps the regions of validity of these two models. Figure 8.1.2-4 shows a comparison between the Sauter mean diameter obtained for all experiments and the calculated Kolmogorov microscale (equation 3.2.1-2). Clearly, just a few drops are below the Kolmogorov limit. Most of these correspond to the 10 cSt oil at high surfactant concentration, which were shown in the previous chapter to have sizes that agree with the prediction for sub-Kolmogorov inertial stresses. However, they are just below this limit ($D < \eta$), not in the range where the viscous stresses are predominant ($D << \eta$,). Therefore, they are more likely subject to sub-Kolmogorov inertial stresses (see explanation in section 3.3.2-1). The rest of the drop sizes, while being larger than η, are still roughly within an order of magnitude from it. Considering that equation 3.2.1-2 is meant to provide just an order of magnitude

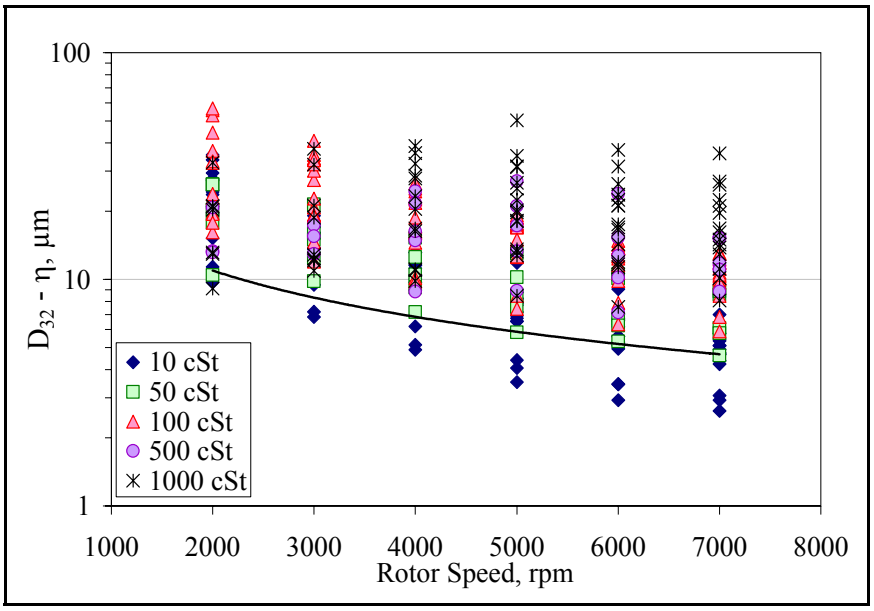

Figure 8.1.2.1- 4. Comparison between the Sauter mean diameter obtained in all experiments and the calculated value of the Kolmogorov microscale (continuous line).

approximation to the size of the small scale eddies in the flow, the drop size range can hardly be considered to be much greater than η. Therefore, all drops are in a range where the continuous phase stresses are still predominantly inertial, but where the effect of the continuous phase viscosity starts to be significant. Thus, they may be slightly better scaled by the equation proposed by Shinnar and Church (1960), equation 3.3.2.1-2, which is the basis for the viscous sub-range, inertial stresses model. Nevertheless, the inertial sub-range model does give a slightly better fit to the largest drops in the data. This should be expected, since these drops are closer to the validity range of this model (L >> D >> η).

Based on these conclusions, the effective interfacial tension approach and the viscous sub-range, viscous stresses model are discarded and will no longer be considered. The differences in RMSD between the inertial sub-range and the viscous sub-range, inertial stresses is very small and, as previously explained, the data is in a size range that

overlaps the validity ranges for both models. Therefore the analysis will be further refined for both of them. As indicated in the previous chapter, the data for 1000 cSt oil, and some for 500 cSt, does not tend to conform to the trends predicted by the mechanistic models. This can also be observed in Figures 8.1.2.1-1 thru -3, where the range of experimental values for the 500 and 1000 cSt oils is contained within the range for the 100 cSt oil. Therefore, for the remainder the this section, only data obtained with the 10 – 100 cSt oils will be taken into the correlations. Calabrese, Wang, and Bryner (1986) took the same approach of limiting their analysis of drop size correlations for stirred tanks to low and moderate viscosities, due to an apparent shift in breakage mechanism. In their case, the transition occurred at a higher viscosity (5000 – 10,000 cP). In this case the transition may have moved towards lower viscosity values due to the higher energy dissipation rate, as previously discussed.

Figures 8.1.2.1-5 shows the data fit for the inertial sub-range model after removing the high viscosity data and recalculating all the adjustable parameters. The equations become:

$(L >> D >> \eta)$ $$\frac{D_{32}}{L} = 0.066 We^{-3/5}\left[1 + 1.30 Vi\left(\frac{D_{32}}{L}\right)^{1/3}\right]^{3/5};$$

$$\mu_d^{eff} = \mu_d + 0.0040 E^{sd}\frac{2t_{dd}}{D_{32}} \qquad (8.1.2.1\text{-}7)$$

and the RMSD reduces to 29.8%. The value of the empirical constants, 0.066 for the Weber number and 1.302 for the viscosity number, are significantly different from those obtained by Phongikaroon (2001) for clean systems in the same rotor-stator mixer with the slotted head: 0.015 and 14.8, respectively; with a 22% RMSD. However, the constant preceding the Weber number is relatively close to that reported by Calabrese, Wang, and

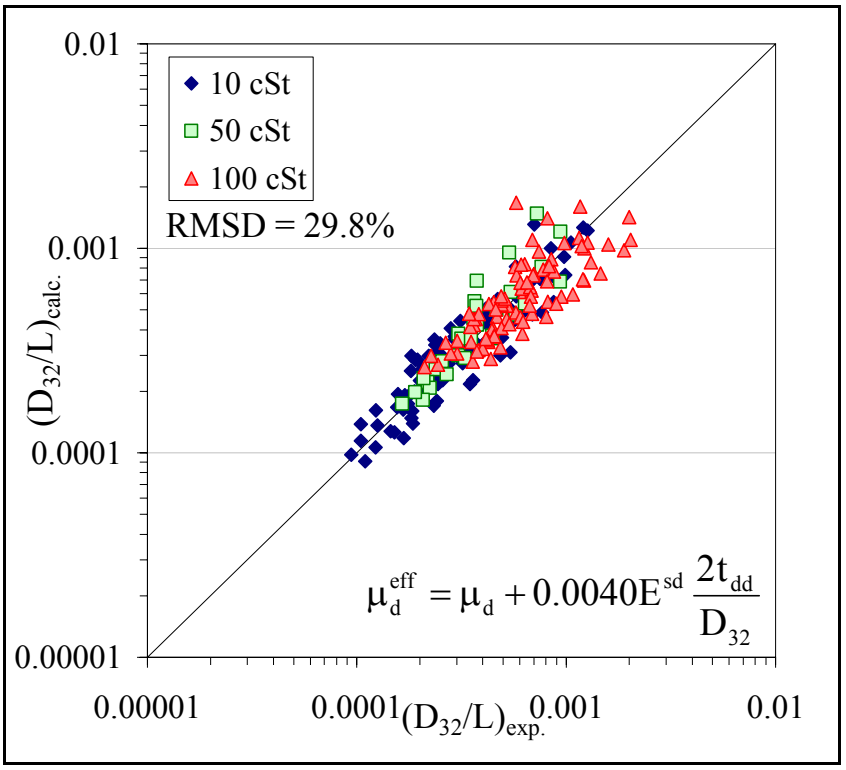

Figure 8.1.2.1- 5. Inertial Sub-range linear model (equation 8.1.2.1-7).

Bryner (1986) for this model in stirred tanks, 0.054. The higher value obtained with surfactant systems may reflect the fact that the drop sizes are, on average, larger than those with obtained under equilibrium, clean interface conditions.

The viscosity number constant, on the other hand, is lower than that for clean systems in both the rotor-stator and stirred tanks (4.42, for the latter). This implies that the effect of the dispersed phase viscosity is relatively lower in the case of surfactant systems, at least in the viscosity range considered. This constant, however, is close to the value of 1.38 obtained by Berkman and Calabrese (1988) for dilute dispersions in a static mixer, using an equivalent version of the model. The Weber number constant in that case was an order of magnitude larger, indicating that the static mixer produces much larger drops, but they seem to follow a similar trend with respect to μ_d as that shown in the

present case. The fact that this constant increased from 0.088, in equation 8.1.2.1-2, indicates that by removing the high viscosity data, the effect of the dispersed phase viscosity becomes more manifest. The reduction in the C_μ constant from the value of 0.055, in equation 8.1.2-2, to 0.0040 may be simply due to the removal of the inaccurately fitted high viscosity data. It must be noted that, even though removing the high viscosity data from the correlation improved its goodness of fit, the RMSD only decreased from 38.3 to 29.8%. Therefore, equation 8.1.2-1 may still be used to estimate mean drop size of high drop viscosity dispersions, as long as the increase in error for the calculated values is deemed acceptable.

Figure 8.1.2.1-6 shows the recalculated model fit for the viscous sub-range, inertial stresses model. The equations obtained from said fit are:

($D < \eta$)

$$\frac{D_{32}}{L} = 0.206\left(We\,Re\right)^{-1/3}\left[1 + 2.31 Vi\, Re^{1/2}\left(\frac{D_{32}}{L}\right)\right]^{1/3};$$

$$\mu_d^{eff} = \mu_d + 0.0085 E^{sd}\frac{2t_{dd}}{D_{32}} \qquad (8.1.2.1\text{-}8)$$

With an RMSD equal to 25.7%. The lower RMSD, compared to the 29.8% obtained with the inertial sub-range model, is consistent with the drops being slightly better correlated by sub-Kolmogorov inertial stresses, as explained before. However, it can be appreciated in the plot, that even though the RMSD is lower and the data points seem more compressed than in figure 8.1.2-5, this model doesn't seem to do a good job fitting the two extremes of the drop size range. The size scatter for the larger drops deviates more from the diagonal (higher deviation from the experimental value) than in the case of the inertial sub-range model. This makes sense from the point of view that these drops are the ones further away from the $D < \eta$ range and, therefore, from the strictly valid range for

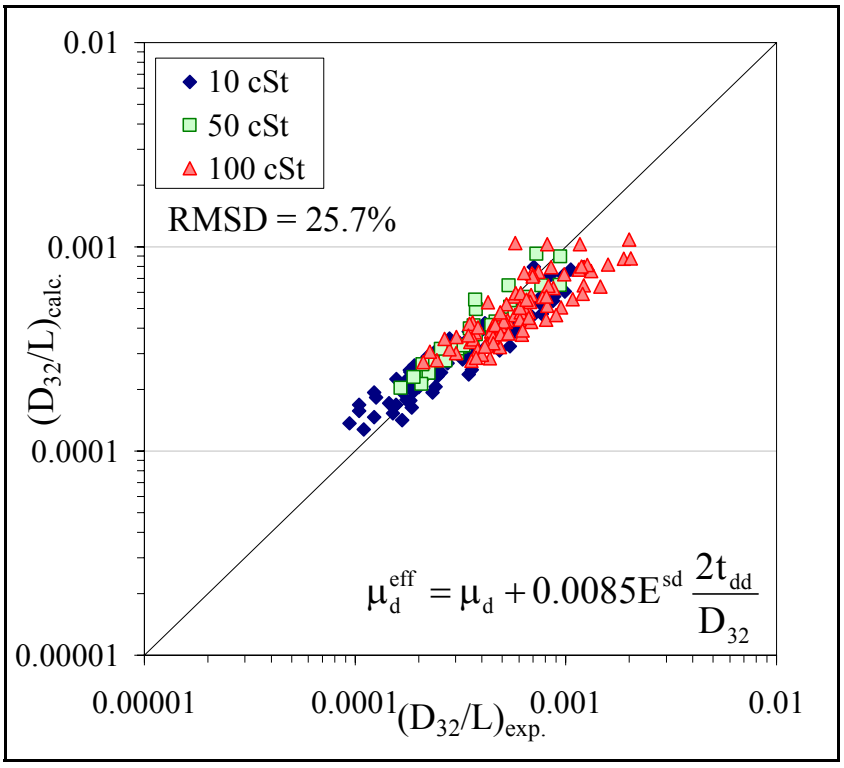

Figure 8.1.2.1- 6. Viscous Sub-range, inertial stresses linear model (equation 8.1.2.1-8)

this model. The apparent deviation in the smaller drop size range is merely compensation for the large deviations observed in the larger drop range, as will be shown later.

Phongikaroon (2001) fit his clean systems data to an equivalent model for the viscous sub-range, inertial stresses, and also found that it fit slightly better that the inertial sub-range model (RMSD of 18%). His Weber and viscosity number constants were 0.061 and 127, respectively. Again, the differences between those constants and the ones in equation 8.1.2.1-8 indicate the production of relatively larger drops and a considerably lower effect of dispersed phase viscosity in the case of surfactant systems. Since this model (equation 8.1.2.1-8) is the one that produces the lowest RMSD value, it will be used as the point of comparison for the next steps of the elimination process. Although this does not mean that the Inertial sub-range model will be ruled out from the rest of the

analysis. Additionally, as in the previous model's case, the removal of high viscosity data improved the correlation (RMSD decreased from 33.6 to 25.7%), but not greatly. Thus equation 8.1.2.1-4 may still be employed in high viscosity cases, with the caveat of a higher error.

Two variations of the viscous sub-range, inertial stresses model were tested. One of them was the use of the eddy lifetime (t_{eddy}), instead of the drop deformation timescale (t_{dd}), as the characteristic time of the deformation. The equations for this case are:

$$\frac{D_{32}}{L} = 0.188\left(We\,Re\right)^{-1/3}\left[1 + 6.19 Vi\, Re^{1/2}\left(\frac{D_{32}}{L}\right)\right]^{1/3};$$

($D < \eta$)

$$\mu_d^{eff} = \mu_d + 0.011 E^{sd}\frac{2t_{eddy}}{D_{32}} \qquad (8.1.2\text{-}9)$$

with an RMSD = 31.7%. Evidently, the goodness of fit is worse, compared to the 25.7% obtained using t_{dd}. In fact, the previously shown models were also tested with t_{eddy} as the characteristic timescale. The RMSD values obtained for the inertial sub-range model with t_{eddy} were either approximately equal to those with t_{dd}: inertial sub-range model with t_{dd}, RMSD = 29.8%, with t_{eddy}, RMSD = 30.0%. Therefore the minimum RMSD for both the inertial and viscous sub-range models was obtained with t_{dd} (25.7%). Consequently, the drop deformation timescale is recommended over the eddy lifetime for the characteristic timescale for data correlation.

The other variation was the use of the spring and dashpot version of the viscous sub-range, inertial stress model (equation 3.3.3.2-3) was also evaluated. The correlation resulting from this fit is:

$$\frac{D_{32}}{L} = 0.245\left(We\,Re\right)^{-1/3}\left[1 - \exp\left(-1.37 Vi'^{-1}\, Re^{-1/2}\left(\frac{D_{32}}{L}\right)^{-1}\right)\right]^{-1/3};$$

(D < η)

$$\mu_d^{eff} = \mu_d + 0.0055E^{sd}\frac{2t_{dd}}{D_{32}} \qquad (8.1.2.1\text{-}10)$$

with an RMSD of 29.3%. Clearly, the use of a more sophisticated model does not guarantee a better correlation .The same conclusion is arrived at when the higher viscosity data is considered: the RMSD increases from 33.6 (Figure 8.1.2.1- 2, bottom). to 34.9%. Therefore, the use of spring and dashpot models is not recommended and will not be continued any further.

8.1.2.2. Low Dispersed Phase Viscosity Limit

The 10 cSt silicone oil data were also analyzed separately to determine if can be correlated with the inviscid versions of the mechanistic models. Figure 8.1.2.2-1 Shows the results for the inertial sub-range: on the left, the general model, and on the right the inviscid limit. The corresponding fitted equations are:

$$\frac{D_{32}}{L} = 0.052We^{-3/5}\left[1 + 6.60Vi\left(\frac{D_{32}}{L}\right)^{1/3}\right]^{3/5};\ \mu_d^{eff} = \mu_d \qquad (8.1.2.2\text{-}1)$$

(L >> D >> η)

$$\frac{D_{32}}{L} = 0.071We^{-3/5} \qquad (8.1.2.2\text{-}2)$$

with RMSD values of 20.7 and 26.7%, respectively. Even though the viscosity is fairly low, the data is better correlated by the general model, which accounts for dispersed phase viscosity effects, rather than by the inviscid model. In stirred tanks, the effect of oil viscosity is usually negligible for viscosities under ~20 cSt. The difference here could be due to the fact that, as previously explained, rotor-stator devices generate considerably larger continuous phase stresses (τ_c), which translate into larger viscous stresses acting to

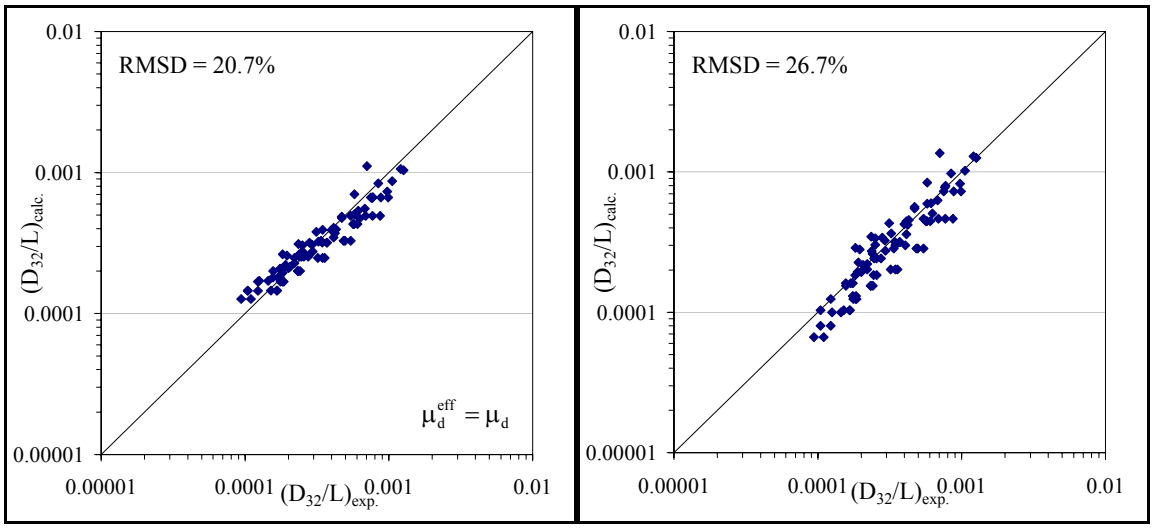

Figure 8.1.2.2- 1. 10 cSt silicone oil data correlated with the general inertial sub-range linear model (left, equation 8.1.2.2-1) and with the inviscid limit of this model (right, equation 8.1.2.2-2).

resist drop deformation ($\tau_d \sim \tau_c^{1/2}$), and therefore the effect of viscosity starts to be observed at lower values of it.

The constant in equation 8.1.2.2-2 (0.071) is greater that the 0.017 obtained by Phongikaroon (2001) and the 0.040 obtained by Francis (1999), both for clean, inviscid systems in rotor-stator mixers. This is consistent with the trend observed in the previous equations. However, the Weber number constant in equation 8.1.2.2-1 (0.052), despite being different from the 0.015 value obtained by Phongikaroon (2001) for viscous drops using this model, is outstandingly close to that obtained by Chen and Middleman (1967) for inviscid fluids (0.053) and the one by Calabrese, Wang, and Bryner (1986) for viscous oils (0.054), both in stirred tanks. The constant preceding the viscosity number is also closer to that for stirred tanks (4.42). In addition, the value obtained for C_μ in this correlation is zero ($\mu_d^{eff} = \mu_d$). Therefore, it seems as though for low viscosities, the

behavior of the rotor-stator resembles that observed for a stirred tanks with higher viscosity oils.

A similar fit is obtained by analyzing the low viscosity data with the viscous sub-range, inertial stresses model. This case is illustrated in Figure 8.1.2.2-2, which corresponds to the following equations:

$$\frac{D_{32}}{L} = 0.261\left(We\,Re\right)^{-1/3}\left[1+0.0013Vi\,Re^{1/2}\left(\frac{D_{32}}{L}\right)\right]^{1/3};\ \mu_d^{eff} = \mu_d + E^{sd}\frac{2t_{dd}}{D_{32}} \quad (8.1.2.2\text{-}3)$$

($D < \eta$)

$$\frac{D_{32}}{L} = 0.299\left(We\,Re\right)^{-1/3} \quad (8.1.2.2\text{-}4)$$

and the RMSD are 20.1 and 27.0, respectively. Remarkably, the low viscosity data can be correlated virtually as well with any of the two general models, even though in this case, the effective viscosity is significantly modified by E^{sd} ($C_\mu = 1$). However, the effect of μ_d^{eff} could be compensated by the notably low viscosity number constant (0.0013). Given that this correlation is the one with the lowest RMSD, it should be the one

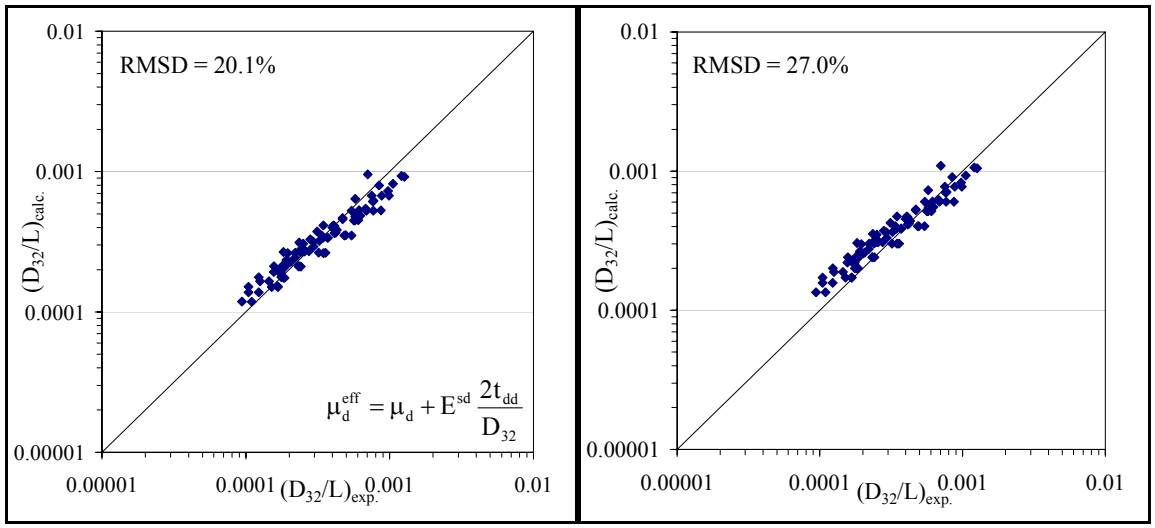

Figure 8.1.2.2- 2. 10 cSt silicone oil data correlated with the general viscous sub-range, inertial stresses, linear model (left, equation 8.1.2.2-3) and with the inviscid limit of this model (right, equation 8.1.2.2-4).

recommended for low dispersed viscosity data ($\mu_d \leq 10$ cP). However, since equation 8.1.2.2-1 provides a practically identical fit and has the advantage that it does not need the surface dilational modulus to fit the data, this is the one recommended for low dispersed phase viscosity cases. The value of the proportionality constant in equation 8.1.2-14 is, again, considerably larger than that obtained by Phongikaroon (2001) for the same model (0.081).

8.1.2.3. Combination of Models

So far, models that were derived assuming that the drops are either in the inertial sub-range ($L >> D >> \eta$) or in the viscous-sub-range ($D < \eta$ or $D << \eta$) have been used to fit the entire data set, despite the fact that it was already shown that values of D_{32} lie between the two sub-ranges (see Figure 8.1.2.1-4). If the data are divided into two sub-sets, one containing those mean drop sizes (D_{32}) larger than the estimated value of the Kolmogorov microscale and the other those that are smaller than η, and each sub-set is correlated by the corresponding model, the accuracy of the correlations can be improved. Figure 8.1.2.3-1 shows the results of this analysis. The resulting equations are:

$$\frac{D_{32}}{L} = 0.055 We^{-3/5}\left[1 + 2.06 Vi\left(\frac{D_{32}}{L}\right)^{1/3}\right]^{3/5}; \quad \mu_d^{eff} = \mu_d + 0.0035 E^{sd}\frac{2t_{dd}}{D_{32}} \quad (8.1.2.3\text{-}1)$$

for $D_{32} > \eta$, which yields an RMSD of 28.5%; and:

$$\frac{D_{32}}{L} = 0.093\left(We\,Re\right)^{-1/3}\left[1 + 24.44\, Vi\, Re^{1/2}\left(\frac{D_{32}}{L}\right)\right]^{1/3};$$

$$\mu_d^{eff} = \mu_d + 0.0032 E^{sd}\frac{2t_{dd}}{D_{32}} \quad (8.1.2.3\text{-}2)$$

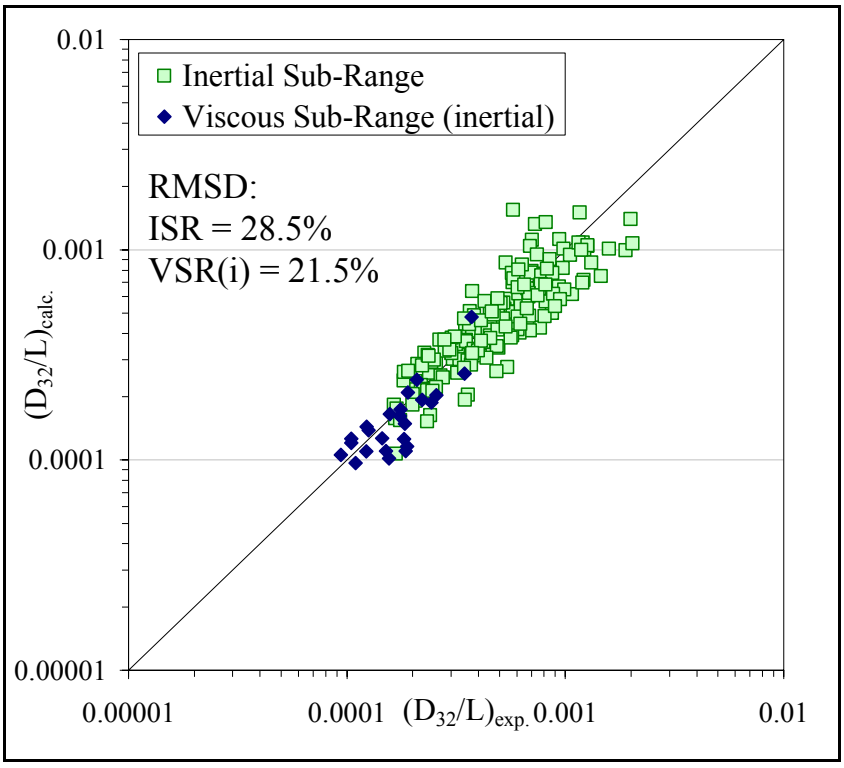

Figure 8.1.2.3- 1. Combination of the inertial sub-range and viscous sub-range, inertial stresses, linear models (equations 8.1.2.3-1 and -2)

for $D_{32} \leq \eta$, with RMSD = 21.5%. As observed, the RMSD decreases slightly for both correlations. Curiously, the Weber number constant in the inertial sub-range equation (8.1.2-15) is practically identical to the value found above by Calabrese, Wang, and Bryner (1986) for clean systems in stirred tanks (0.054). The viscosity number constant in the same equation (2.06) is roughly half of the one reported the same authors (4.42). This could mean that the behavior of a rotor-stator mixer with viscous, surfactant-covered dispersed phases is similar to that for stirred tanks with clean systems, although with a lower dependency on viscosity, as long as an appropriately defined, effective viscosity value is used in the calculation. This agrees with the behavior observed for low viscosities (equation 8.1.2.2-1), for which the appropriate effective viscosity seems to be equal to the nominal dispersed phase viscosity. The lower dependency on dispersed phase

viscosity with respect to the stirred tank case agrees with the observed behavior reported in the section on the effect of viscosity in the previous chapter (Chapter 7, section 7.1.2). Nevertheless, this behavior does not agree with the results of Phongikaroon (2001) for viscous, clean systems in a rotor-stator. Therefore, this conclusion cannot be incontrovertibly made at present. On the other hand, the constants in equation 8.1.2.3-2, 0.093 for the Weber number and 24.44 for the viscosity number, became significantly closer to the ones reported by Phongikaroon (2001) for this model, 0.078 and 56, respectively. Again, is hard to extract a conclusion from this apparent similarity, especially considering that the present values were obtained only with sub-Kolmogorov size data, whereas the ones reported by Phongikaroon (2001) were obtained with data that includes values for D_{32} clearly greater than η.

The fit of this model in the lower extreme of the D_{32}/L range is significantly better than that observed in Figure 8.1.2.1-6. Not necessarily in terms of RMSD, since this only improves slightly, but because the data is more centered around the diagonal. Thus, as previously noted, the apparently poor fit of equation 8.1.2.1-8 in that range is simply caused by the presence of considerably scattered data in the opposite extreme.

It is evident that the values for C_μ in equations 8.1.2.3-1 and -2 are almost the same, 0.0035 and 0.0032. This does not mean, however, that the effective viscosities are the same. In each case, the expressions used to calculate t_{dd} were the ones defined for the appropriate sub-range (equation 3.4-2 for the inertial sub-range and 3.4-3 for the viscous sub-range). This, in addition to producing different numeric values for the timescale, results in slightly different values for E^{sd} for each case, as well (see Figure 6.3-3).

Therefore, there is no reason to believe that the similarity in the adjustable constant is not just coincidence.

It must be noted that the values for the Kolmogorov microscale used in this analysis, even though calculated with the impeller swept volume approach (see Chapter 6, section 6.3), are just approximations. Although, the fact that the RMSD for the correlations of both models improved, indicates that these approximations are, at least, good enough for data correlation.

8.1.3. Clean Systems

In Chapter 7 it was shown how the experimental data obtained from clean systems, in which the continuous phases were methanol solutions, does not seem to behave as predicted by the mechanistic models. However, if this data are fit to the models, the results exhibit similarities to the previously shown surfactant systems. Figure 8.1.3-1 shows the fitting to the three general models: the inertial sub-range and both viscous sub-range models. The equations are:

(L >> D >> η)

$$\frac{D_{32}}{L} = 0.059 We^{-3/5}\left[1 + 0.498 Vi\left(\frac{D_{32}}{L}\right)^{1/3}\right]^{3/5} \qquad (8.1.3\text{-}1)$$

for the inertial sub-range, with an RMSD of 42.5%,

(D < η)

$$\frac{D_{32}}{L} = 0.233\left(We\,Re\right)^{-1/3}\left[1 + 1.19 Vi\, Re^{1/2}\left(\frac{D_{32}}{L}\right)\right]^{1/3} \qquad (8.1.3\text{-}2)$$

for the viscous sub-range, assuming inertial stress (RMSD = 30.0%), and

(D << η)

$$\frac{D_{32}}{L} = 0.0061 We^{-1}\, Re^{1/2}\left[1 + 0.361 Vi\, Re^{-1/4}\right] \qquad (8.1.3\text{-}3)$$

for the viscous sub-range, viscous stress model, which yielded an RMSD of 66.1%. Since

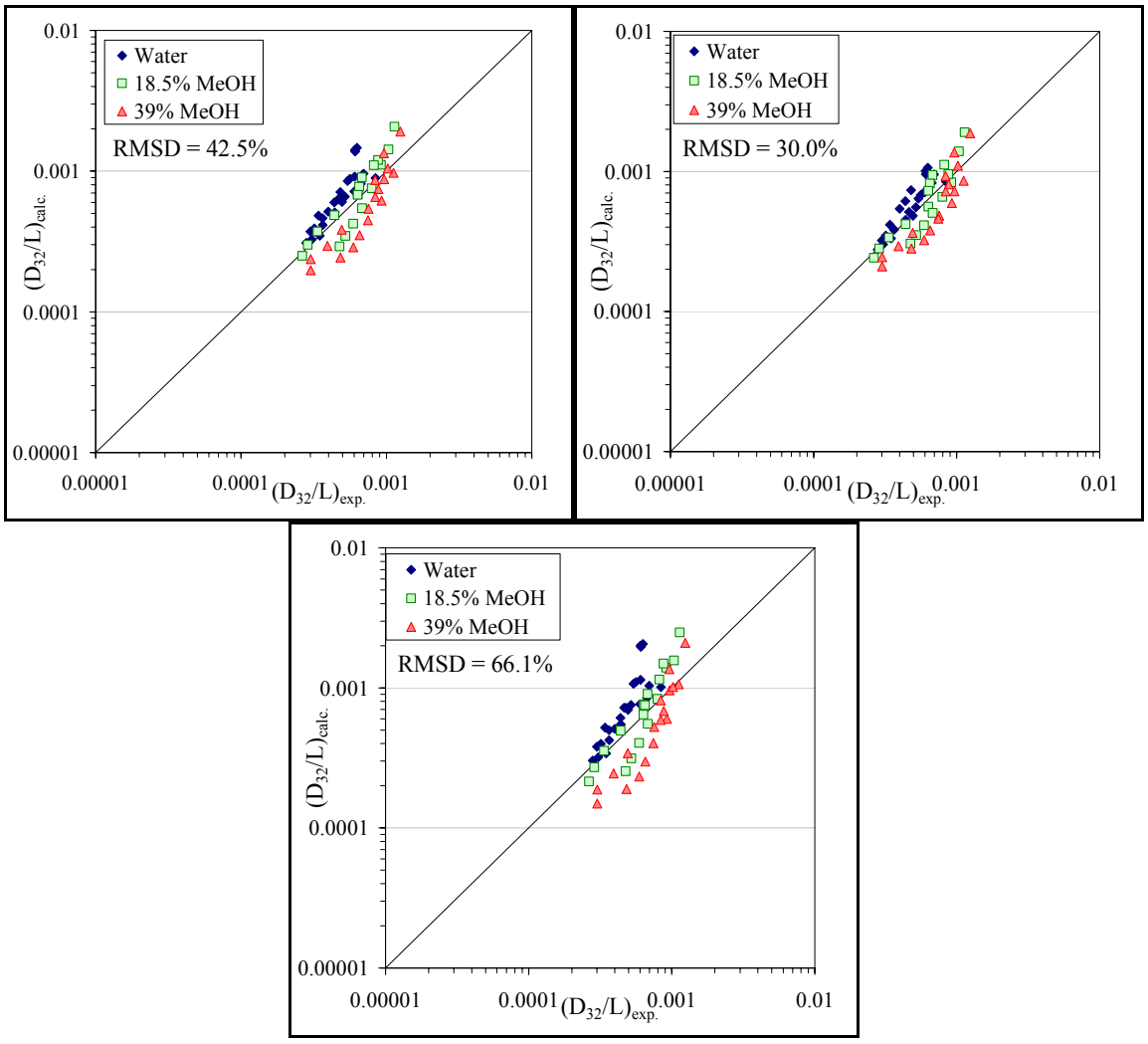

Figure 8.1.3- 1. Correlations for clean systems data. Top, left: inertial sub-range linear model; top, right: viscous sub-range, inertial stress linear model; bottom: viscous sub-range, viscous stress linear model.

data with dispersed phase viscosity in the range 10 – 1000 cSt was included in the preceding model fits, Figure 8.1.3 should be compared to Figures 8.1.2.1-1 thru -3, for surfactant systems.

There are several observations to make about these graphs and equations. First, as in the case of the surfactants systems data, the worst fit (larger RMSD) is attained by the viscous sub-range, viscous stress model and the best corresponds to the viscous sub-

range, inertial stress model. Even the values of the minimum RMSD and the level of scatter in the data are reasonably similar in both cases. Second, the value of the Weber number constant in equation 8.1.3-1 (0.059) is remarkably close to that of equation 8.1.2-15 for surfactant systems and to those obtained for clean systems in stirred tanks (Chen and Middleman 1967; Calabrese, Wang, and Bryner 1986); although the viscosity number constant is an order of magnitude lower than in those cases. Third, both constants in equation 8.1.3-2 are fairly close to those obtained for surfactant systems with the same model when the entire data range is considered (equation 8.1.2-8). All these similarities suggest that, even though the clean systems data set does not conform to all the trends predicted by the mechanistic models, it does follow some of them. Therefore, the fact that the results discussed in the previous chapter cannot yet be fully explained, does not mean that there is a major flaw in this data set. It only means that further studies on this matter are necessary.

Figure 8.1.3-2 shows the clean systems data correlated along with the surfactant data. The entire clean systems data set is above the corresponding Kolmogorov microscale. Therefore, it was correlated with the inertial sub-range model only. The resulting equations are:

$$\frac{D_{32}}{L} = 0.054 We^{-3/5}\left[1+1.81 Vi\left(\frac{D_{32}}{L}\right)^{1/3}\right]^{3/5};\ \mu_d^{eff} = \mu_d + 0.0054 E^{sd}\frac{2t_{dd}}{D_{32}} \quad (8.1.3\text{-}4)$$

for $D_{32} > \eta$, with an RMSD of 32.4% (for $D_{32} \leq \eta$, the equations is still equation 8.1.2.3-2, since there are no new data in this range). Despite the increase in RMSD (from 28.5 to 32.4%), the constants preceding the Weber and viscosity numbers are very close to those in equation 8.1.2.3-1 (0.055 and 2.06, respectively), for surfactant systems alone.

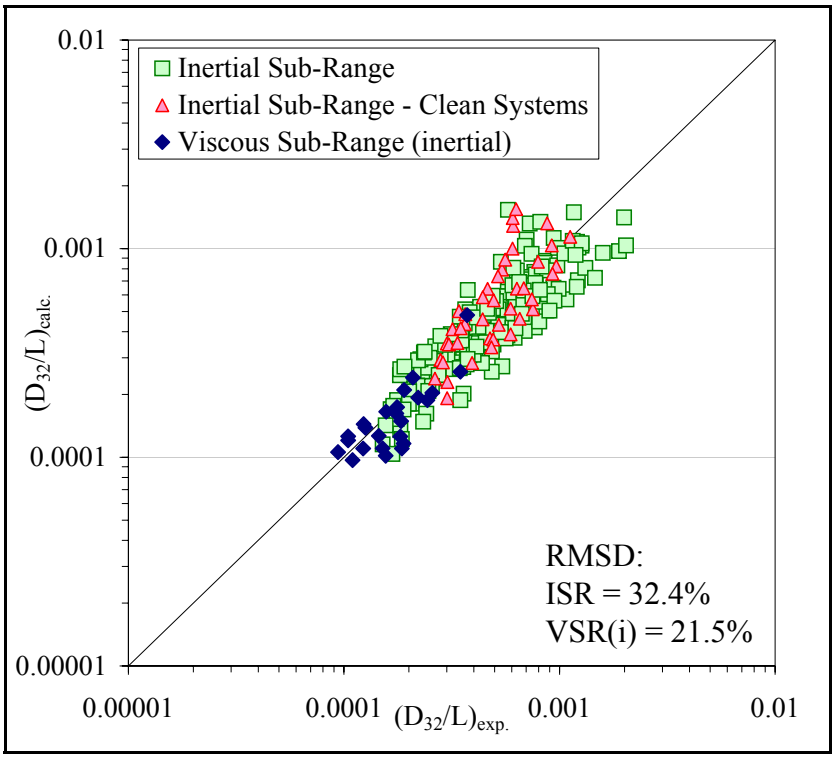

Figure 8.1.3- 2. Correlation for clean and surfactant systems data (equation 8.1.3-4, for the inertial sub-range and 8.1.2.3-2 for the viscous sub-range). $\mu_d \leq 100$ cSt

However, the value for C_μ (0.0054) increased with respect to that for equation 8.1.2.3-1 (0.0035). For the clean systems data the effective dispersed phase viscosity is equal to the nominal dispersed phase viscosity ($E^{sd} = 0$). As a result, this increase is fictitious and could affect the adequacy of the model to fit surfactant data. Therefore, the use of this correlation is not recommended. If the clean systems data is simply correlated with equation 8.1.2.3-1 (shown in Figure 8.1.3-3), the results are almost the same. This way, however, the correlation is not modified and the RMSD remains at 28.5%, if surfactant-containing systems are considered. If the correlation is used for clean systems, the RMSD increases to 32.8%. In conclusion, the correlation for surfactant systems can be used to calculate mean drop sizes for clean systems, as long as the higher error is acceptable. However, it must be noted that the clean systems data shown in Figure 8.1.3-3 is the

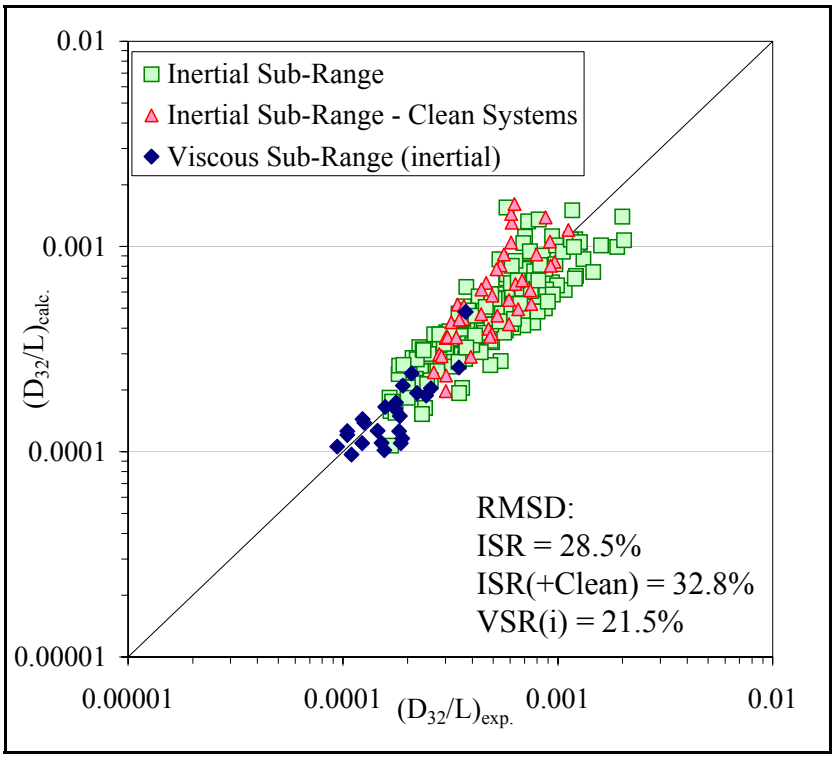

Figure 8.1.3- 3. Clean systems data correlated with the surfactant systems correlation (inertial sub-range, equation 8.1.2.3-1). Viscous sub-range data: equation 8.1.2.3-2. $\mu_d \leq$ 100 cSt

same that was previously shown not to conform to all the trends predicted by the current mechanistic models. Therefore, this correlation may be employed to obtain rough approximations for practical purposes, but its use for data analysis is not advised.

8.2. Drop Size Distribution Correlation

In Chapter 7, it was shown that, despite small variations, all drop size distribution are approximately linear when plotted in log-probability coordinates. This means that all of them are approximately log-normally distributed in volume. Therefore, it would be advantageous if they could be correlated by a single expression. Wang and Calabrese (1986) argued that the functional form of the equilibrium drop size volume distribution of a dispersion may be expressed as a function of the form $F_v(D) = f(D/D_{32})$, where D_{32} is

the Sauter mean diameter of the distribution. In their case, as well as for Chen and Middleman (1967), the distributions were normal in volume, and therefore, they used the normal cumulative distribution function (equation 2.1.4-2) in their analysis. In the present case, the distributions are log-normal in volume. Therefore, the log-normal cumulative distribution function (equation 2.1.4-6) will be used.

In order to correlate the distributions, they have to be normalized by their respective D_{32}. Given the large amount of data generated in this study (367 samples, each with a corresponding DSD), only a selection of DSD were analyzed. This selection consisted in two groups of distributions, of 23 samples each, in which all relevant variables (oil viscosity, surfactant type, surfactant or methanol concentration, and rotor speed) were varied broadly.

The results of the DSD normalization, as well as the fit to equation 2.1.4-2, are presented in Figures 8.2-1 and 8.2-1. The curves are reasonably linear in the 1 – 90% volume range. Comparable broadening at the extremes of the D/D_{32} range were also observed by Wang and Calabrese (1986). They attributed this to scatter in the tails of the individual distributions due to limited drop counts, and not to significant changes in slope. The best fit straight lines in the plots of Figures 8.2-1 and -2 correspond to the equations:

$$F_v\left(\frac{D}{D_{32}}\right)=\frac{1}{2}\left[1+\operatorname{erf}\left(\frac{\ln\left(D/D_{32}\right)-\ln(1.33)}{0.73\sqrt{2}}\right)\right] \tag{8.2-1}$$

for the first sample (Figure 8.2-1), and:

$$F_v\left(\frac{D}{D_{32}}\right)=\frac{1}{2}\left[1+\operatorname{erf}\left(\frac{\ln\left(D/D_{32}\right)-\ln(1.43)}{0.66\sqrt{2}}\right)\right] \tag{8.2-2}$$

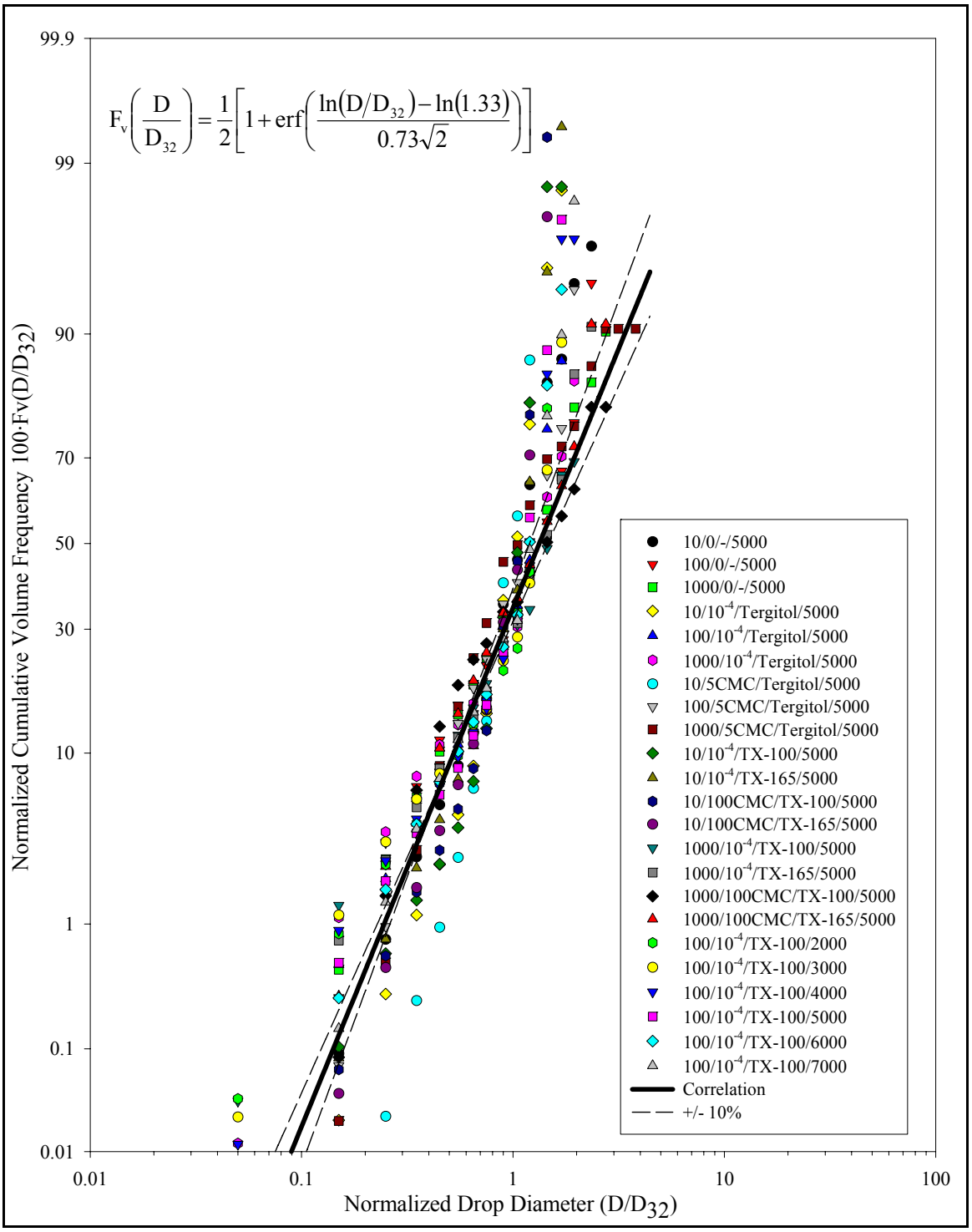

Figure 8.2- 1. Cumulative volume drop size distribution correlation. Legend: Oil viscosity/Surfactant concentration/Surfactant type/Rotor speed. +/- 10%: variation of 10% on values for D_{mM} and σ_0 (parameters of the correlation).

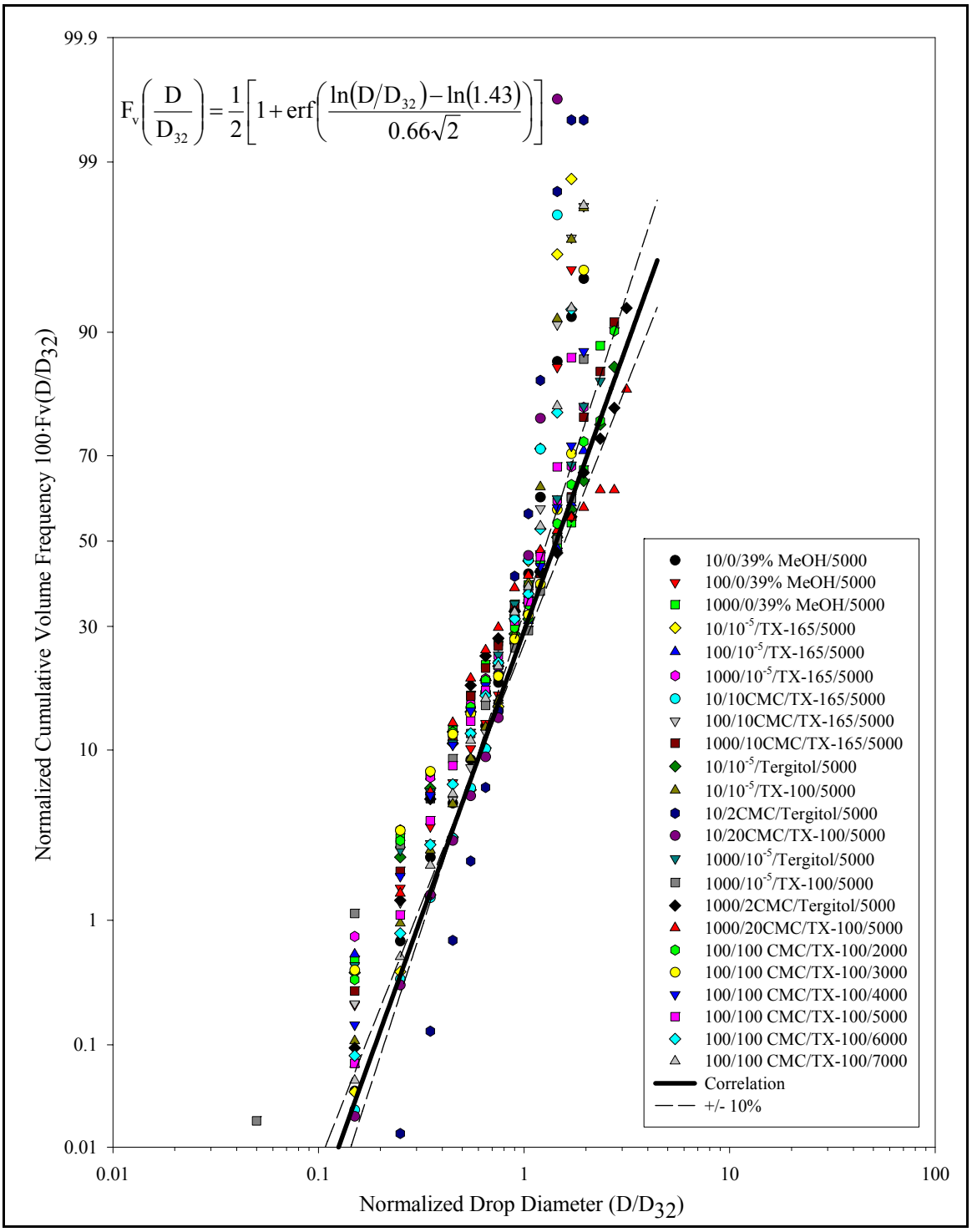

Figure 8.2- 2. Cumulative volume drop size distribution correlation. Legend: oil viscosity/Surfactant or methanol concentration/Surfactant/Rotor speed. +/- 10%: variation of 10% on values for D_{mM} and σ_0 (parameters of the correlation).

for the second one (Figure 8.2-2). The values obtained for the mean normalized drop size, $D/D_{32} = 1.33$ versus 1.43, and for the standard deviation, $\sigma_0 = 0.73$ versus 0.66, are reasonably close. Therefore a single expression is proposed with the average values of these parameters:

$$F_v\left(\frac{D}{D_{32}}\right) = \frac{1}{2}\left[1 + \mathrm{erf}\left(\frac{\ln(D/D_{32}) - \ln(1.38)}{0.695\sqrt{2}}\right)\right] \qquad (8.2\text{-}3)$$

It is important to note that, despite the large deviations in D_{32} from predicted model behavior, the DSD are functionally similar and well normalized by the experimental value of D_{32}. Therefore, equation 8.2-3 is valid over the entire range of the study, provided that D_{32} is appropriately estimated.

The values of D/D_{32} and σ_0 obtained here are slightly larger than those reported by (Phongikaroon 2001) for clean systems in a rotor-stator: 1.25 and 0.613. However, that correlation only considered viscosities up to 100 cSt, which could explain the differences.

8.3. Summary

Experimental mean drop size data were quantitatively analyzed by fitting it to mechanistic models for drop breakup in turbulent flows. These models are based on Kolmogorov's theory of isotropic turbulence and were developed in Chapter 3. The correlation recommended for use with surfactant laden systems and dispersed phase viscositiy in the range 10 – 100 cSt, is that comprised of equations 8.1.2.3-1 and 8.1.2.3-2, for $D_{32} > \eta$ and $D_{32} \leq \eta$, respectively.

To be able to use this correlation, the drop deformation timescale, t_{dd}, must be calculated through equations 3.4-2, for $D_{32} > \eta$, or 3.4-3, for $D_{32} \leq \eta$. These equations

also depend on the surface dilational modulus, E^{sd}, which must be calculated through equation 4.5.2-14, using the appropriate t_{dd} expression as the deformation time, and the corresponding equilibrium adsorption parameters Γ_∞ and a_L (Table 6.1.2-1) and diffusion coefficient, D_{AB} (Table 6.2-1), of the surfactant. All the equations of the correlation (equations 8.1.2.3-1, 3.4-2, and 4.5.2-14, for $D_{32} > \eta$; or 8.1.2.3-2, 3.4-3, and 4.5.2-14, for $D_{32} \leq \eta$) must be solved simultaneously. This can be readily implemented in commercial programming packages such as Matlab.

If the dispersed phase viscosity is low (≤ 10 cSt), equations 8.1.2.3-1 and -2 may be substituted by equation 8.1.2.2-1, which has the advantage that it does not require the calculation of μ_d^{eff}. For dispersed phase viscosity higher than 100 cSt, equations 8.1.2.1-2 and -4 may be used, for $D_{32} > \eta$ and $D_{32} \leq \eta$, respectively, although at the risk of incurring in higher error. Based on the results shown in Figure 8.1.3-3, these same set of equations may be used for clean systems. Although a better fit correlation needs to be developed for this case. Once the value for D_{32} has been calculated, equation 8.2-3 may be used to estimate the functional form of the cumulative volume size distribution.

CHAPTER 9. SUMMARY AND CONCLUSIONS

This chapter provides the major conclusions drawn from this study as well as recommendations for future work. There are many conclusions, given the breadth of this study as demonstrated in the previously presented results. However, the single most important conclusion is that surfactant-induced interfacial rheological properties have a significant influence on drop size. This influence is manifested in different ways, depending on surfactant concentration, dispersed phase viscosity, and rotor speed, and show trends inconsistent with the simplistic assertion that surfactant reduces interfacial tension, and therefore drop size. This finding, as well as the detailed conclusions of the study, will be discussed in the following sections. Furthermore, while the data are specific to rotor-stator mixers, the approaches, findings, and conclusions apply to a broader class of high shear mixing devices.

9.1. Video Microscopy and Image Analysis

- Video microscopy (VM) is a suitable technique for measuring drop size in dilute liquid-liquid dispersions with diameters in the ~ 1 – 200 μm range. Its main disadvantage is the fact that a sample must be withdrawn from the system to perform the analysis. This could destabilize the sample making it no longer representative of the system. However, this disadvantage can be overcome by adding a stabilizing surfactant to the sample. Furthermore, if the system under study already contains surfactants, this stabilization step may not be necessary. This makes VM particularly attractive for the study of drop size in surfactant-laden systems.

- An automated image analysis procedure was developed to facilitate the study of drop sizes of dilute liquid-liquid dispersions through VM. It consist on two separate programs. The first one is a subroutine (macro) written for the Scion Image for Windows image analysis program. It allows extraction of quantitative information from the images of drops obtained through VM. The second is a Microsoft Excel macro designed to analyze this information and convert it into mean drop sizes and discrete drop size distributions. The Scion Image macro is capable of effortlessly analyzing batches of images at a rate of 150 – 180 images/min and the Excel macro performs its analysis in less than 20 seconds. Therefore, the analysis of a sample of ~1000 images can be done in under 5 minutes (rate and times estimates based on performance on a Pentium 4 computer). This represents a considerable improvement over the more time-consuming commonly used manual procedures.

9.2. Interfacial Phenomena

- The pendant drop technique is a suitable technique for the measurement of surface and interfacial tensions for a wide range of liquid interfaces (~ 2 – 72 mN/m). The technique is easy to implement without the need for specialized equipment and provides fairly accurate (within ~5%) and reproducible results. It can also be adapted for measuring dynamic surface tensions. However, for accurate results at short times more sophisticated equipment than that used here would be required.
- An automated image analysis procedure was developed to facilitate the analysis of surface and interfacial tensions via the pendant drop technique. It consists of a Scion Image macro that analyses the drop's shape based on the procedure described by Adamson (1976). Given an appropriate length reference (capillary tube diameter) and

density difference, it is capable of analyzing batches of images of drops and calculating the surface (or interfacial) tension.

- The equilibrium behavior of both the surface and interfacial tension (silicone oil/water interface) in the presence of the nonionic surfactants Tergitol TMN-6, Triton X-100, and Triton X-165 is reasonably well described by the Langmuir – von Szyszkowski equation of state (equation 4.3.1-14), for concentrations below the CMC. This allows characterization of their adsorption behavior with the Langmuir adsorption isotherm (equation 4.3.1-13).

- The equilibrium interfacial tensions of silicone oil/aqueous surfactant systems can be mimicked by silicone oil/aqueous methanol systems by using the appropriate methanol concentration. This, in principle, allows comparison of surfactant-laden and surfactant-free systems at constant equilibrium interfacial tension.

- The dynamic behavior of the surface tension at low concentrations (10^{-5} mol/l) of the aforementioned nonionic surfactants is diffusion controlled. It is well described by the long times approximation of the Ward and Tordai equation (equation 4.4.2-7). This allows estimation of the surfactants' molecular diffusion coefficient from experimental data from the variation of surface tension with time.

- The surface dilational modulus (E^{sd}) is an interfacial rheological property that describes the viscoelastic behavior of an interface due to Marangoni stresses. These stresses are created by the presence of low concentrations of surfactants (~10^{-5} – 10^{-3} mo/l) on a deforming interface. The surface dilational modulus reaches a maximum value at a concentration of surfactant in the bulk solution below the CMC. At this bulk concentration, the concentration of surfactant at the interface is large enough to produce

steep interfacial tension gradients, and thus large Marangoni stresses, when the interface is deformed. However, the adsorption process is not fast enough to relax these stresses (re-establish equilibrium interfacial tension) effectively. E^{sd} may be calculated (equation 4.5.2-14) from equilibrium adsorption parameters and the surfactant diffusion coefficient, as long as an appropriate time scale can be estimated for the interfacial deformation. In this study, appropriate deformation timescales were defined based on Kolmogorov's theory of local isotropic turbulence.

9.3. Effect of Dispersed Phase Viscosity on Drop Size

- For low to moderately high dispersed phase viscosities (10 – 1000 cSt), the mean drop size of dilute liquid-liquid dispersions increases with increasing viscosity. The increase observed for the rotor-stator mixer studied in the present work is, however, less pronounced than that seen in previous studies conducted in stirred tanks and rotor-stator mixers.

- For dispersed phase viscosities above 1000 cSt, the drop size remains approximately constant. This could be explained by a shift to a more extensional flow-like breakage mechanism. Slowly deforming, highly viscous drops are stretched by a succession of short-lived turbulent eddies into a large thread that breaks by capillary instability. This behavior has not been reported for dispersion of similar viscosity oils in stirred tanks. However, this may be due to the fact that drop deformation time scales and eddy lifetimes are closer in magnitude in these devices.

- As the viscosity of the oil increases, the population of small drops in the distribution also increases. This may be due to a larger production of satellite drops

during the breakup of higher viscosity drops. This is consistent with higher viscosity drops being further stretched prior to breakup than lower viscosity drops.

9.4. Effect of Surfactants on Drop Size

- Below the CMC, Marangoni stresses caused by surfactant-induced transient interfacial tension gradients, affect drop size. Mean drop diameters initially increase, rather than decrease, with increasing surfactant concentration. A peak is reached after which the drop size decreases with increasing concentrations, still below CMC.
- The magnitude of the effect of the Marangoni stresses is proportional to the dispersed phase viscosity. The lowest viscosity oil (10 cSt) shows the least effect while the highest viscosity oil (1000 cSt) shows the maximum increase in drop size. This trend is contrary to the effect of viscosity predicted by equation 4.5.2-14, which indicates that a higher E^{sd} is obtained for lower viscosity. However, this may be explained by the relative inability of low viscosity phases to propagate the effect of the Marangoni stresses into the drops.
- At concentrations above the CMC, although the Marangoni stresses are small (E^{sd} becomes negligible), the surfactant still has an effect on drop size. This effect is apparently linked to an increase in surface shear viscosity and depends on dispersed phase bulk viscosity and rotor speed. For low viscosity and high rotor speed, the effect becomes negligible and the drops attain a size consistent with their equilibrium interfacial tension. The same oil at low rotor speed exhibits behavior that is consistent with shear thinning. For high viscosity, the drop size becomes practically independent of rotor speed, this behavior is not readily explainable. However, under these conditions, the linear behavior observed with respect to equilibrium interfacial tension and the increased

production of small drops evidenced in the drop size distribution, agrees with the apparent shift toward a more extensional flow-like breakage mechanism, observed for the high drop viscosity range in clean systems.

- The effect of surfactants in liquid-liquid dispersion is not limited to lowering the interfacial tension and protecting the newly formed drops against coalescence. It also modifies the interfacial rheology of the system which significantly affects the drop size. Therefore, it may not be prudent to "add a little surfactant" to a dispersion when taking experimental drop size data to stabilize it, and simply use the equilibrium interfacial tension to correlate the results.

- A better fundamental understanding on how to quantify the effect of convection on surface rheology is needed. The fact that a diffusion-based approach well correlates the data indicates that convection is not necessarily the dominating transport mechanism, as has sometimes been suggested. From a physicochemical hydrodynamics standpoint, it can be shown that, throughout the wide concentration range considered in this study, diffusion is never negligible as a transport mechanism for surfactant molecules from the bulk phase to the interface.

9.5. Drop Size Correlations

- Mechanistic models for drop breakup in turbulent flows developed for clean systems may be used for correlating mean drop size in surfactant systems, as long as an appropriately defined physical property is used to account for the effect of the surfactant. In the case of viscous drops, a suitable approach is that proposed by Lucassen-Reynders and Kuijpers (1992). It is based on the definition of an effective dispersed phase viscosity, taking into account the surface dilational modulus, the deformation timescale,

and the drop size (equation 8.1.1-1). This approach, however, does not include the effect of the surface shear viscosity, which seems to play a significant role at high surfactant concentrations.

- The mechanistic models used to correlate the experimental drop size data were derived for the different turbulence sub-ranges: the inertial sub-range and the viscous sub-range. In the latter case, two models were developed, one assuming that the predominating disruptive stresses are inertial and one assuming they are viscous in nature. Based on the goodness of fit of the different mechanistic models with experimental data, it can be concluded that the drops are more likely to broken up by inertial stresses due to turbulent pressure fluctuations, rather than by viscous stresses. This makes sense since it was found that the experimental drop size data range overlaps the inertial and viscous sub-ranges. However, the smallest drops sizes remain close to the Kolmogorov microscale (equation 3.2.1-2). Therefore they are more likely subject to sub-Kolmogorov inertial stresses than to viscous stresses, even in this size range.

- The spring and dashpot models, although more sophisticated in that they account for the duration of the disruptive stresses, do not correlate experimental mean drop size data better than the more widely employed linear models. Therefore, the latter are considered more than adequate to correlate the breakage phenomena studied.

- The best choice of a correlation for the Sauter mean diameter (D_{32}) for dilute silicone oil-in-aqueous surfactant dispersions and the methodology to apply it are discussed in Chapter 8, section 8.3.

- A correlation was developed for the functional form of the volume drop size distribution, based on the equation for a continuous log-normal distribution (equation

2.1.4-2). The mean normalized drop diameter was found to be $\overline{D/D_{32}} = 1.38$ and the log-normal standard deviation $\sigma_0 = 0.695$.

9.6. Recommendations for Future Work

- It would be interesting to perform a similar study (similar oil viscosity and surfactant concentration ranges) in a conventional stirred tank (preferably with a Rushton turbine) instead of a rotor-stator mixer. This would allow for a direct comparison between the two mixing devices and determine to what extent the observed effect of surfactants is affected by specific characteristics, namely higher deformation rates, of rotor-stator mixers.

- Further analysis of the behavior of highly viscous drops, both in clean and surfactant systems is required. This would confirm and provide a better understanding of the shift in breakage mechanism towards extensional flow behavior reported in the present study.

- The behavior of clean systems with aqueous methanol as the continuous phase also demands further analysis. In order to eliminate completely the risk of sample destabilization, the use of an in situ drop size measurement technique (such as PDA or the High Magnification Video Probe) is recommended. This would probably require the selection of a different liquid-liquid system (given the low difference in index of refraction that the silicone oil/aqueous methanol system exhibits) and even the development of a different mechanistic theory.

- Since the analysis done here for the effect of the surface dilational modulus is based on estimated values of this property, it is recommended that the data be reanalyzed

with actual values of E^{sd} measured for similar ranges of experimental conditions (oil viscosities and surfactant concentrations). This would confirm the adequacy of the approach presented in this study to represent the effect of surfactants in drop size correlations. Dukhin, Kretzschmar, and Miller (1995) and Edwards, Brenner, and Wasan (1991) provide detailed discussion of available experimental techniques to measure E^{sd}. Some of them, such as those based on the damping of longitudinal or cylindrical waves may be applicable to liquid-liquid interfaces and can achieve deformation timescales of the order of milliseconds.

- The mechanistic models should be further modified to include the surface shear viscosity. This property is difficult to accurately measure or predict, especially for the kind of surfactant used in the present study, but its inclusion would allow for more comprehensive and accurate correlations. Edwards, Brenner, and Wasan (1991), and Miller *et al.* (1996) discuss several experimental technique to measure surface shear viscosity of adsorbed surfactant monolayers. However, these methods are based on planar interfaces. As discussed in Chapter 7, section 7.2.2.1, the results of these methods may not be adequate to describe the interfacial behavior of micron-sized, curved interfaces. Therefore, a new methodology that allows estimation of this property in drops and/or dispersed systems needs to be devised.

- The present study was limited to diffusion-controlled adsorption dynamics. It is recommended to expand the scope of the study to include kinetic-controlled adsorption. This could be accomplished by utilizing ionic surfactants. However, it would require the development of different techniques for the analysis and estimation of dynamic interfacial and rheological properties since the methods employed here (the Ward –

Tordai equation and the Lucassen – van den Tempel approach to the surface dilational modulus) presuppose diffusion-controlled adsorption. Another possibility would be to expand the study to ionic surfactants, but under conditions at which their behavior is also diffusion-controlled (see section 4.4.2). This way the study would still be limited to diffusion-controlled dynamics, but it would be valid for a broader range of surfactant characteristics.

- The effect of convection of surfactant to the drop interface on interfacial rheology needs to be studied. As stated in Chapter 7, section 7.2.4, this implies a significant mathematical difficulty. However, it would provide valuable information to better understand the dynamics of emulsification processes in the presence of surfactants.

APPENDIX A. SURFACTANT PARTITIONING AT THE SILICONE OIL/WATER INTERFACE.

In Chapter 4, the surfactant was assumed to be soluble only in the aqueous phase so it is present only in the continuous phase and the interface. This is usually the situation in liquid-gas systems because surfactants are virtually insoluble in most gas phases. When both phases are liquid, however, the solubility of the surfactant in the oil phase is seldom negligible (Miller, Joos, and Fainerman 1994). As a result, part of the surfactant is transferred across the interface, which may affect the overall adsorption process. Consequently, knowledge of the partitioning properties of the system is required when working with adsorption at liquid-liquid interfaces.

A.1 Partition Coefficient

Surfactant partitioning is characterized by the partition coefficient (Ravera, Ferrari, and Liggieri 2000):

$$k_p = \frac{C_O}{C_W} \tag{A-1}$$

where C_O and C_W are the equilibrium concentrations of surfactant in the oil phase and aqueous phase, respectively. The concentration of surfactants is usually small. Therefore, measuring the concentrations requires the use of sophisticated instrumental analysis methods or indirect methods. One such indirect method is the one proposed by Ravera *et al.* (1997). This method exploits a specific property of surfactants, the relationship between concentration and equilibrium surface tension. Using an adsorption isotherm as a surface tension/concentration calibration curve, the concentration of a given aqueous surfactant solution can be evaluated by measuring its equilibrium surface tension. The

partition coefficient can then be quantified by bringing a volume V_W of aqueous surfactant solution, with initial concentration C_{W0}, in contact with a volume V_O of pure oil for a time long enough to achieve equilibrium (usually days). Then, a sample of the aqueous solution is withdrawn, its surface tension measured, and its equilibrium concentration (C_W) calculated by means of the Langmuir – von Szyszkowski equation (equation 4.3.1-14). Finally, k_p is calculated from a surfactant mass balance:

$$k_P = \frac{V_W}{V_O}\left(\frac{C_{W0}}{C_W} - 1\right) \tag{A-2}$$

It should be noted that in the derivation of the previous mass balance equation, the amount of surfactant adsorbed at the interface was neglected. This is a good assumption only when the interfacial area is small. However, the time required to reach equilibrium is proportional to the in inverse of the interfacial area (Ravera, Ferrari, and Liggieri 2000), hence, the relative volumes of the phases and their container must be chosen carefully to minimize both experimental time and error. One disadvantage of this method is that it is limited to concentrations below the CMC, since beyond this point it the surface tension becomes independent of concentration. However, above the CMC, the concentration of monomeric surfactant remains approximately constant. Therefore, the partition coefficient may be expected to remain constant or, at least, remain at values close to those obtained at the CMC.

A.2 Experimental Method

The method used to quantify the surfactants' partition coefficients was the one previously described, based on Ravera *et al.* (1997). This method consists on the determination of the surface tension of a surfactant solution that has been left in contact

with an oil phase for a long enough period of time for the surfactant to partition into the oil, and for the system to achieve thermodynamic equilibrium. For this purpose, three Tergitol TMN-6 solutions and three Triton X-100 solutions, all at concentrations below the respective CMC, were prepared according to the procedure described in the experimental methods chapter (Chapter 5). Then, 3 ml of each solution was poured into three 18 ml glass vials (a total of 9 vials per surfactant) Next, approximately 6 ml of silicone oils of 10, 100, or 1000 cSt were poured into the vials, so that each vial contained a different combination of surfactant concentration and oil viscosity. The vials were closed and stored in a unperturbed place for about two weeks. After this time, the vials were placed in a thermostatic bath (a glass tank with a heater/recirculator maintaining the temperature constant at 25°C). After 48 hours in this bath, a sample of the surfactant solution was withdrawn from each vial and its surface tension was measured. From this surface tension value the concentration of surfactant remaining in the aqueous phase of the vial was determined. Finally, the partition coefficient was calculated from this concentration and the value of the initial concentration and volume of each of the phases, according to equation A-2.

The partition coefficient of Triton X-165 was not measured since this surfactant's molecule is identical to that of Triton X-100, except for a longer polyethoxylate chain. This makes this X-165 more hydrophilic than X-100, overall, but the hydrophobic part of both is equally attracted to the oil phase. Therefore, the partition coefficient of Triton X-165 should be smaller that that of Triton X-100. No such comparison can be made with Tergitol TMN-6, since the hydrophobic part of this surfactant is different, and it is not easy to determine if it is more or less compatible with the oil phase.

A.3 Results

Figures A-1 and A-2 contain the results for Tergitol TMN-6 and Triton X-100, respectively. As can be seen, negative values were obtained for some cases, in both surfactants. This is evidently an error since negative values of k_p are not physically possible. This could be explained by solubilization of the silicone oil in the aqueous phase. Silicone oils (polidimethylsiloxanes) exhibit interfacial activity when in aqueous solution. Therefore, given the long times allowed for equilibriation (~2 weeks), a significant part of the oil may have dissolved in the aqueous phase. This would result in a lower surface tension for the solution than the one it would attain just by being partially depleted of surfactant. The fact that the 1000 cSt silicone oil is the one least affected (all its k_p values are positive) agrees with this explanation, since this oil would be the least soluble in water due to its higher molecular weight. The 10 cSt oil, on the other hand, is

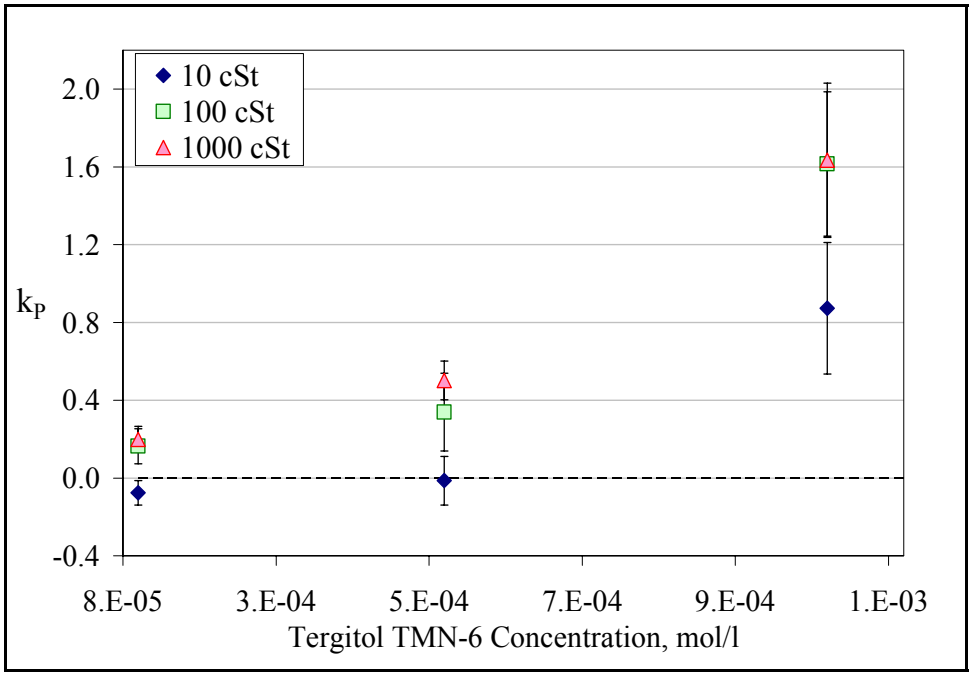

Figure A- 1. Partition coefficient as a function of surfactant bulk concentration for Tergitol TMN-6.

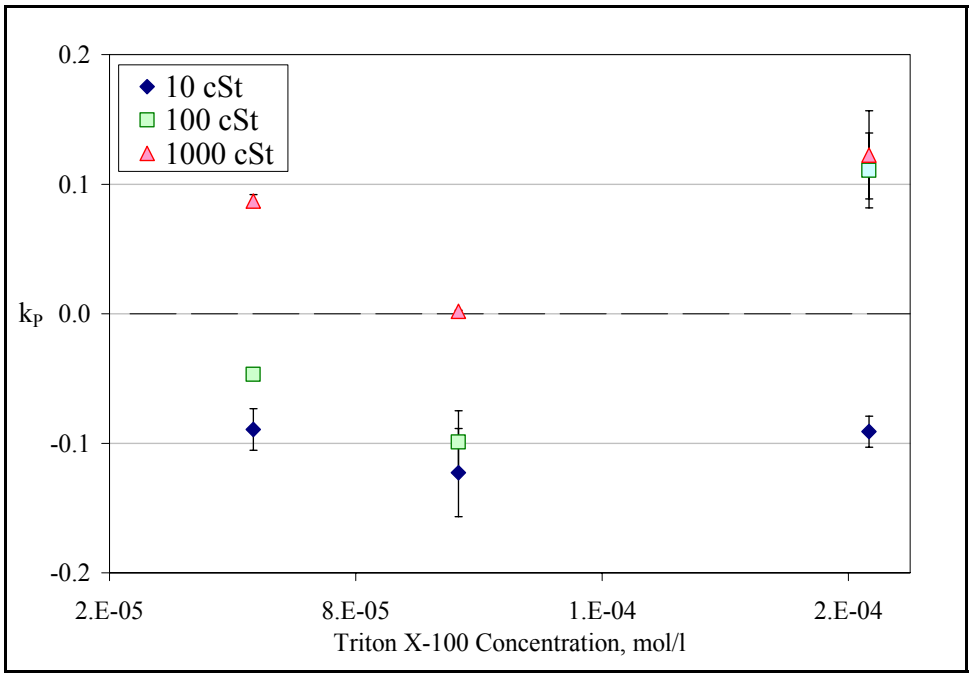

Figure A- 2. Partition coefficient as a function of surfactant bulk concentration for Triton X-100

the one with the largest number of negative values (the only one, in the case of Tergitol) and is the one most likely to have the highest solubility.

As a result, the only assertion that can be made with respect to the partition coefficients is with respect to their apparent order of magnitude. Assuming that the values obtained with the 1000 cSt oil are the ones closest to being correct, the partition coefficient of Tergitol TMN-6 seems to be of O(1), and that of Triton X-100, of O(0.1). Even though k_p increases with concentration for Tergitol, the order of magnitude should remain the same after the CMC (1.73×10^{-3} mol/l) for the reasons already explained.

Given the fact that the phase fraction of the dispersed phases in this study is very low ($\phi = 0.001$), the order of magnitude of the partition coefficient may be all that is needed to determine if partitioning will affect the results. It is needed to ensure that the continuous phase surfactant concentration remains approximately constant during the

dispersion processes. This can be determined from a simple surfactant mass balance. Consider a system of polydisperse oil drops in an aqueous surfactant solution with a volume V_c, as shown in Figure A-3. Before the adsorption process begins (t = 0), the surfactant is present only in the continuous phase, with a concentration equal to C_{W0}. Once the adsorption process reaches equilibrium ($t \rightarrow \infty$), the surfactant is distributed between the continuous phase, the dispersed phase, and the interface, with concentrations C_W, C_O, and Γ_{eq}, respectively. The macroscopic mass balance for this system is given by:

$$\left\{\begin{array}{l}\text{Mass of}\\ \text{surfactant in}\\ \text{cont. phase}\end{array}\right\}_{t=0} = \left\{\begin{array}{l}\text{Mass of}\\ \text{surfactant in}\\ \text{cont. phase}\end{array}\right\}_{Eq} + \left\{\begin{array}{l}\text{Mass of}\\ \text{surfactant in}\\ \text{disp. phase}\end{array}\right\}_{Eq} + \left\{\begin{array}{l}\text{Mass of}\\ \text{surfactant at}\\ \text{interface}\end{array}\right\}_{Eq} \qquad \text{(A-3)}$$

Expressed in terms of the variables already defined, equation A-3 becomes:

$$C_{W0}V_c = C_W V_c + C_O V_d + \Gamma_{eq} A_d \qquad \text{(A-4)}$$

where V_d and A_d are the dispersed phase total volume and area, respectively, and are given by:

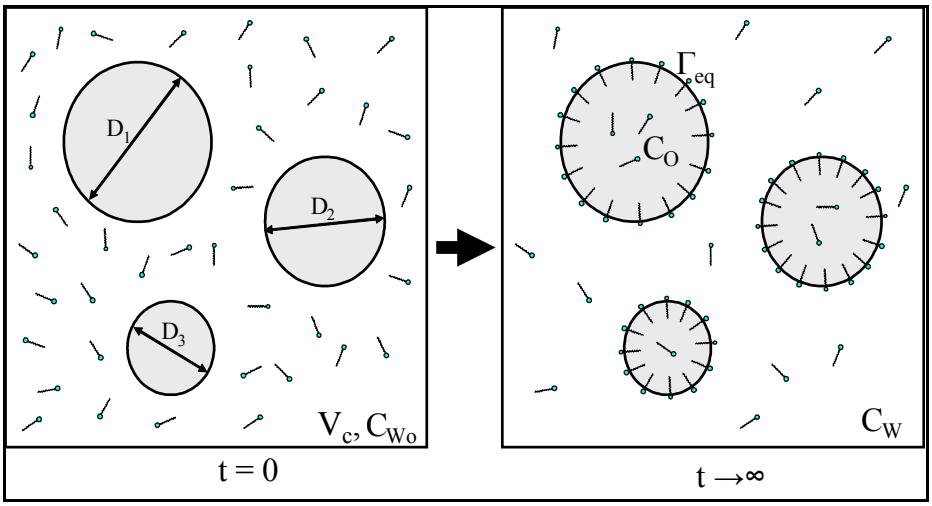

Figure A- 3. Schematic representation of polydisperse oil droplets in a surfactant solution before adsorption begins (left) and at equilibrium (right)

$$V_d = \frac{\pi}{6}\sum_i \frac{n_i}{n} D_i^3 \;\; ; \;\; A_d = \pi \sum_i \frac{n_i}{n} D_i^2 \tag{A-5}$$

Recalling that $k_p = C_O/C_W$ (equation A-1) and the definition of the Sauter mean diameter (D_{32}, equation 2.1.3-8), equation A-4 can be solved for C_W and the expression obtained is:

$$C_W = \frac{C_{W0} - \frac{6\Gamma_{eq}}{D_{32}} \frac{V_d}{V_c}}{1 + k_P \frac{V_d}{V_c}} \tag{A-6}$$

Equation A-6 allows calculation of the concentration of surfactant in the continuous phase once adsorption equilibrium has been reached. In the case of dilute dispersions, V_d/V_c is practically equal to ϕ. Therefore, for $\phi = 0.001$, the partition coefficient would only have a significant effect on the equilibrium continuous phase concentration only if it is of O(100) or greater. Therefore, it can be concluded that, in the present study, the concentration of surfactant in the continuous phase of the dispersions is not significantly affected by surfactant partitioning into the dispersed phase.

In the case of viscous drops, even if the concentration of surfactant inside the drop is of the same order of the concentration in the continuous phase (k_p of O(1)), this is not likely to affect significantly the adsorption dynamics. The diffusion coefficient of surfactants in phases other than water is usually considered proportional to the inverse of the viscosity ratio between said phase and water (Ravera, Ferrari, and Liggieri 2000). In this case, this would make the diffusion coefficient inside the drop 1 to 3 orders of magnitude smaller than that in the continuous phase. Therefore, the behavior of the dynamic interfacial tension and the relaxation of Marangoni stresses are mainly governed by adsorption from the continuous phase.

APPENDIX B. COMPUTER PROGRAM LISTINGS

B.1 Image Analysis

The following program is the Scion Image for Windows macro used to analyze images of drops obtained through the video microscopy technique (see Chapter 2, section 2.2.3.1).

```
procedure Normalize;
var
   min,max,count:integer;
begin
   ResetCounter;
   Measure;
   count:=rCount;
   min :=rMin[count];
   max:=rMax[count];
   KillROI;
   SelectAll;
   AddConstant(-min);
   Max:=Max-min;
   MultiplyByConstant(255/max);
end;

macro 'Measure Particles - VM';
var

i,x,Number,CounterTotal,Mag,figure,background,Threshold:integer;
   Path:string;
begin
   CounterTotal:=0;
   Path:=GetString('Indicate the path in which the images are
stored','C:\Images');
   Number:=GetNumber('Number of images to be analized:',100);
   Mag:=GetNumber('Magnification (10, 20, 43, 60, or 100):',43);
   for i:=000 to Number-1 do begin
      open(Path,'\figure',i:3,'.bmp');
      figure:=PidNumber;
      open(Path,'\Background.bmp');
      background:=PidNumber;
      ImageMath('sub',figure,background,0.5000,128,'result');
      Normalize;
      {ResetCounter;
      Measure;
      Threshold:=round(rMean[rCount]+3*rStdDev[rCount]);
      If Threshold<255 Then SetThreshold(Threshold)
         else SetThreshold(255);}
      Smooth;
      SetThreshold(145);
      SetOptions('Area Major Minor');
```

```
      If Mag=10 Then SetScale(1.197,'µm')
         else If Mag=20 Then SetScale(2.388,'µm')
            else If Mag=43 Then SetScale(5.162,'µm')
               else If Mag=60 Then SetScale(6.958,'µm')
                  else If Mag=100 Then SetScale(11.958,'µm');
      SetParticleSize(5,999999);
      AnalyzeParticles('ignore include reset');
      CounterTotal:=CounterTotal+rCount;
      for x:=1 to rCount do begin
         rUser1[CounterTotal-rCount+x]:=rArea[x];
         rUser2[CounterTotal-rCount+x]:=rMajor[x]/rMinor[x];
      end;
      DisposeAll;
   end;
   SetOptions('User1 User2');
   SetCounter(CounterTotal);
   SetUser1Label('Area');
   SetUser2Label('Maj/Min');
   SetExport('Measurements');
   Export(Path,'\Results.xls');
   PutMessage('Analysis Complete. The results were saved in
',Path,'\Results.xls');
end;
```

B.2 Data Analysis

The following program is the Microsoft Excel macro used to analyze the output of the Scion Image image analysis macro (see Chapter 2, section 2.2.3.2).

```
Sub AnalyzeParticles()
'
' AnalyzeParticles Macro
' Macro recorded 6/12/2002 by Gustavo A. Padron

    f = 1
    a = 1
    x = 0
    Counter = 0

    Rows("1:1").Select
    Selection.Insert Shift:=xlDown
    Range("A1").Select
    ActiveCell.FormulaR1C1 = "Area"
    Range("B1").Select
    ActiveCell.FormulaR1C1 = "Major/minor"
    Range("C1").Select
    ActiveCell.FormulaR1C1 = "Diameter"
    Range("D1").Select
    ActiveCell.FormulaR1C1 = "Diameter(filtered)"
```

```
        Range("E1").Select
        ActiveCell.FormulaR1C1 = "Bin Limits"
        Columns("A:E").Select
        With Selection
            .HorizontalAlignment = xlCenter
            .VerticalAlignment = xlBottom
            .WrapText = False
            .Orientation = 0
            .AddIndent = False
            .IndentLevel = 0
            .ShrinkToFit = False
            .ReadingOrder = xlContext
            .MergeCells = False
        End With
        Columns("B:D").Select
        Selection.NumberFormat = "0.00"
        Columns("A:E").EntireColumn.AutoFit
        Range("A1:E1").Select
        With Selection.Borders(xlEdgeBottom)
            .LineStyle = xlDouble
            .Weight = xlThick
            .ColorIndex = xlAutomatic
        End With

        Do Until a = 0
            x = x + 1
            If Range("A:A").Cells(x) <> "" Then
                Counter = Counter + 1
            Else
                a = 0
            End If
        Loop

        For i = 2 To Counter
           If Range("B:B").Cells(i) < 1.1 Then
              Range("C:C").Cells(i) = ((4 *
Range("A:A").Cells(i)) / 3.14159265359) ^ (1 / 2)
              f = f + 1
              Range("D:D").Cells(f) = ((4 *
Range("A:A").Cells(i)) / 3.14159265359) ^ (1 / 2)
           Else
              Range("C:C").Cells(i) = 0
           End If
        Next i

        Range("E2").Select
        ActiveCell.FormulaR1C1 = "0.1"
```

```
Range("E3").Select
ActiveCell.FormulaR1C1 = "0.2"
Range("E4").Select
ActiveCell.FormulaR1C1 = "0.3"
Range("E5").Select
ActiveCell.FormulaR1C1 = "0.4"
Range("E6").Select
ActiveCell.FormulaR1C1 = "0.5"
Range("E7").Select
ActiveCell.FormulaR1C1 = "0.6"
Range("E8").Select
ActiveCell.FormulaR1C1 = "0.7"
Range("E9").Select
ActiveCell.FormulaR1C1 = "0.8"
Range("E10").Select
ActiveCell.FormulaR1C1 = "1.0"
Range("E11").Select
ActiveCell.FormulaR1C1 = "1.1"
Range("E12").Select
ActiveCell.FormulaR1C1 = "1.3"
Range("E13").Select
ActiveCell.FormulaR1C1 = "1.6"
Range("E14").Select
ActiveCell.FormulaR1C1 = "1.8"
Range("E15").Select
ActiveCell.FormulaR1C1 = "2.1"
Range("E16").Select
ActiveCell.FormulaR1C1 = "2.6"
Range("E17").Select
ActiveCell.FormulaR1C1 = "2.9"
Range("E18").Select
ActiveCell.FormulaR1C1 = "3.4"
Range("E19").Select
ActiveCell.FormulaR1C1 = "4.2"
Range("E20").Select
ActiveCell.FormulaR1C1 = "4.7"
Range("E21").Select
ActiveCell.FormulaR1C1 = "5.5"
Range("E22").Select
ActiveCell.FormulaR1C1 = "6.8"
Range("E23").Select
ActiveCell.FormulaR1C1 = "7.6"
Range("E24").Select
ActiveCell.FormulaR1C1 = "8.9"
Range("E25").Select
ActiveCell.FormulaR1C1 = "11.0"
Range("E26").Select
```

```
        ActiveCell.FormulaR1C1 = "12.3"
        Range("E27").Select
        ActiveCell.FormulaR1C1 = "14.4"
        Range("E28").Select
        ActiveCell.FormulaR1C1 = "17.8"
        Range("E29").Select
        ActiveCell.FormulaR1C1 = "19.9"
        Range("E30").Select
        ActiveCell.FormulaR1C1 = "23.3"
        Range("E31").Select
        ActiveCell.FormulaR1C1 = "28.8"
        Range("E32").Select
        ActiveCell.FormulaR1C1 = "32.2"
        Range("E33").Select
        ActiveCell.FormulaR1C1 = "37.7"
        Range("E34").Select
        ActiveCell.FormulaR1C1 = "46.6"
        Range("E35").Select
        ActiveCell.FormulaR1C1 = "52.1"
        Range("E36").Select
        ActiveCell.FormulaR1C1 = "61.0"
        Range("E37").Select
        ActiveCell.FormulaR1C1 = "75.4"
        Range("E38").Select
        ActiveCell.FormulaR1C1 = "84.3"
        Range("E39").Select
        ActiveCell.FormulaR1C1 = "98.7"
        Range("E40").Select
        ActiveCell.FormulaR1C1 = "122.0"
        Range("E41").Select
        ActiveCell.FormulaR1C1 = "136.4"
        Range("E42").Select
        ActiveCell.FormulaR1C1 = "159.7"

         Application.Run "ATPVBAEN.XLA!Histogram",
ActiveSheet.Range("$D:$D"), "PSD" _
            , ActiveSheet.Range("$E:$E"), False, False,
False, True
            a = 1
        x = 0
        Counter = 0
        TotalParticles = 0

        Do Until a = 0
            x = x + 1
            If Range("A:A").Cells(x) <> "" Then
                Counter = Counter + 1
```

```
            Else
                a = 0
            End If
        Loop

        For x = 2 To Counter - 1
            TotalParticles = TotalParticles +
Range("B:B").Cells(x)
        Next x

        Rows(Counter).Select
        Selection.Delete Shift:=xlUp
        Columns("A:G").Select
        Selection.HorizontalAlignment = xlCenter
        Columns("D:G").Select
        Selection.NumberFormat = "0.0000"
        Rows("1:1").Select
        Selection.Font.Italic = False
        Range("C1").Select
        ActiveCell.FormulaR1C1 = "Di"
        Range("C2").Select
        ActiveCell.FormulaR1C1 = "0.05"
        Range("C3").Select
        ActiveCell.FormulaR1C1 = "=(RC[-2]-R[-1]C[-
2])/2+R[-1]C[-2]"
        Range("C3").Select
        Selection.AutoFill Destination:=Range("C3:C42"),
Type:=xlFillDefault
        Range("C3:C42").Select

        Range("D1").Select
        ActiveCell.FormulaR1C1 = "fn(Di)"
        Range("E1").Select
        ActiveCell.FormulaR1C1 = "fv(Di)"
        Range("F1").Select
        ActiveCell.FormulaR1C1 = "Fn(Di)"
        Range("G1").Select
        ActiveCell.FormulaR1C1 = "Fv(Di)"
        Range("A1:G1").Select
        With Selection.Borders(xlEdgeBottom)
            .LineStyle = xlDouble
            .Weight = xlThick
            .ColorIndex = xlAutomatic
        End With

        Sumfn = 0
        SumDifn = 0
```

```
        SumDi2fn = 0
        SumDi3fn = 0
        SumDi4fn = 0

        For x = 2 To Counter - 1
            Range("D:D").Cells(x) = Range("B:B").Cells(x)
/ TotalParticles 'fn(Di)
            Sumfn = Sumfn + Range("D:D").Cells(x)
            Range("F:F").Cells(x) = Sumfn 'Fn(Di)
            SumDifn = SumDifn + Range("C:C").Cells(x) *
Range("D:D").Cells(x)
            SumDi2fn = SumDi2fn + Range("C:C").Cells(x) ^
2 * Range("D:D").Cells(x)
            SumDi3fn = SumDi3fn + Range("C:C").Cells(x) ^
3 * Range("D:D").Cells(x)
            SumDi4fn = SumDi4fn + Range("C:C").Cells(x) ^
4 * Range("D:D").Cells(x)
        Next x
        D10 = SumDifn
        D32 = SumDi3fn / SumDi2fn
        D43 = SumDi4fn / SumDi3fn

        Sumfv = 0
        Variance = 0

        For x = 2 To Counter - 1
            Range("E:E").Cells(x) = (Range("C:C").Cells(x)
^ 3 * Range("D:D").Cells(x)) / SumDi3fn 'fv(Di)
            Sumfv = Sumfv + Range("E:E").Cells(x)
            Range("G:G").Cells(x) = Sumfv
            Variance = Variance + (Range("C:C").Cells(x) -
D10) ^ 2 * Range("D:D").Cells(x)
        Next x
        StdDev = Variance ^ (1 / 2)

        Range("I1").Select
        ActiveCell.FormulaR1C1 = "Statistical Parameters"
        ActiveCell.Characters(Start:=1,
Length:=22).Font.Size = 16
        Selection.Font.Bold = True
        Selection.Font.Underline = xlUnderlineStyleSingle
        Selection.Font.ColorIndex = 5
        Range("I3").Select
        ActiveCell.FormulaR1C1 = "No of Part."
        Range("I4").Select
        ActiveCell.FormulaR1C1 = "D10="
```

```
        ActiveCell.Characters(Start:=2,
Length:=2).Font.Subscript = True
        Range("I5").Select
        ActiveCell.FormulaR1C1 = "D32="
        ActiveCell.Characters(Start:=2,
Length:=2).Font.Subscript = True
        Range("I6").Select
        ActiveCell.FormulaR1C1 = "D43="
        ActiveCell.Characters(Start:=2,
Length:=2).Font.Subscript = True
        Range("I7").Select
        ActiveCell.FormulaR1C1 = "Variance="
        Range("I8").Select
        ActiveCell.FormulaR1C1 = "Std. Dev.="
        Range("K4").Select
        ActiveCell.FormulaR1C1 = "µm"
        Range("K5").Select
        ActiveCell.FormulaR1C1 = "µm"
        Range("K6").Select
        ActiveCell.FormulaR1C1 = "µm"
        Range("K7").Select
        ActiveCell.FormulaR1C1 = "µm2"
        ActiveCell.Characters(Start:=3,
Length:=1).Font.Superscript = True
        Range("k8").Select
        ActiveCell.FormulaR1C1 = "µm"
        Range("J3").Select
        ActiveCell.FormulaR1C1 = TotalParticles
        Range("J4").Select
        ActiveCell.FormulaR1C1 = D10
        Range("J5").Select
        ActiveCell.FormulaR1C1 = D32
        Range("J6").Select
        ActiveCell.FormulaR1C1 = D43
        Range("J7").Select
        ActiveCell.FormulaR1C1 = Variance
        Range("J8").Select
        ActiveCell.FormulaR1C1 = StdDev
        Range("J4:J8").Select
        Selection.NumberFormat = "0.00"
        Range("C1:D25,F1:F25").Select
        Range("F1").Activate
        Sheets("PSD").Select
        Rows("1:10").Select
        Selection.Insert Shift:=xlDown
        Range("I11:K18").Select
        Selection.Cut Destination:=Range("A1:C8")
```

```
        Range("H12").Select
        ActiveCell.FormulaR1C1 = "=RC[-4]*100"
        Range("H12").Select
        Selection.AutoFill Destination:=Range("H12:K12"),
Type:=xlFillDefault
        Range("H12:K12").Select
        Selection.AutoFill Destination:=Range("H12:K52"),
Type:=xlFillDefault
        Range("H12:K52").Select
        ActiveWindow.SmallScroll Down:=-14
        Selection.NumberFormat = "0.0000"
        Range("H11").Select
        ActiveCell.FormulaR1C1 = "fnx100"
        Range("I11").Select
        ActiveCell.FormulaR1C1 = "fvx100"
        Range("J11").Select
        ActiveCell.FormulaR1C1 = "Fnx100"
        Range("K11").Select
        ActiveCell.FormulaR1C1 = "Fvx100"
        Range("G11").Select
        Selection.AutoFill Destination:=Range("G11:K11"),
Type:=xlFillFormats
        Range("G11:K11").Select
        Range("C10:K10").Select
        Selection.Borders(xlDiagonalDown).LineStyle =
xlNone
        Selection.Borders(xlDiagonalUp).LineStyle = xlNone
        Selection.Borders(xlEdgeLeft).LineStyle = xlNone
        Selection.Borders(xlEdgeTop).LineStyle = xlNone
        With Selection.Borders(xlEdgeBottom)
            .LineStyle = xlContinuous
            .Weight = xlMedium
            .ColorIndex = xlAutomatic
        End With
        Selection.Borders(xlEdgeRight).LineStyle = xlNone
        Selection.Borders(xlInsideVertical).LineStyle =
xlNone
        Columns("H:K").Select
        Range("H3").Activate
        With Selection
            .HorizontalAlignment = xlCenter
            .VerticalAlignment = xlBottom
            .WrapText = False
            .Orientation = 0
            .AddIndent = False
            .IndentLevel = 0
            .ShrinkToFit = False
```

```
            .ReadingOrder = xlContext
            .MergeCells = False
        End With
        ActiveWindow.LargeScroll Down:=-1
        Rows("7:7").Select
        Selection.Insert Shift:=xlDown
        Range("A7").Select
        ActiveCell.FormulaR1C1 = "Dmax="
        ActiveCell.Characters(Start:=2,
Length:=3).Font.Subscript = True
        Range("C7").Select
        ActiveCell.FormulaR1C1 = "µm"
        DMax =
Application.WorksheetFunction.Max(Worksheets("Results").Ran
ge("D:D"))
        Range("B7").Select
        ActiveCell.FormulaR1C1 = DMax
        Range("A1").Select
        Style = vbOKOnly + vbInformation
        Response = MsgBox("Particle Size Distribution
Analysis Complete", Style, "Particle Analysis")

    End Sub
```

B.3 Pendant Drop Image Analysis

The following program is the Scion Image for Windows macro used to analyze images of drops taken for pendant drop analysis (see Chapter 5, section 5.1.2).

```
procedure Normalize;
var
   min,max,count:integer;
begin
   ResetCounter;
   SetOptions('Major Minor');
   Measure;
   count:=rCount;
   min :=rMin[count];
   max:=rMax[count];
   KillROI;
   SelectAll;
   AddConstant(-min);
   Max:=Max-min;
   MultiplyByConstant(255/max);
   killROI;
end;

macro 'Pendant Drop Measurement';
```

```
var

Number,n,y,x,i,Value,Counter,xmin,xmax,ymax,depix,dspix,yds,yneed
le,j,k,xneedlemin,xneedlemax,xdsmin,xdsmax,Needlepix,Bond:integer
;

Needlemm,DeltaRho,PixmmCF,de,ds,S,LnOneoverH,OneoverH,Sigma:real;
   Path,Name:string;
begin
   SetPrecision(4);
   Path:=GetString('Indicate the path in which the images are
stored','C:\Frame Grabber');
   Name:=GetString('Name of the image(s)','Drop');
   Number:=GetNumber('Number of images to be analized:',1);
   DeltaRho:=GetNumber('Density difference (in
Kg/m3):',995.877,3);
   Needlemm:=GetNumber('Needle width (in mm):',1.27);
   for n:=1 to Number do begin
      open(Path,'\',Name,n:1,'.bmp');
      Counter:=1;
      ResetCounter;
      Normalize;
      Smooth;
      filter('sobel');
      SetThreshold(135);
      MakeBinary;
      Outline;
      for y:=0 to 479 do begin
         for x:=0 to 639 do begin
            value:=GetPixel(x,y);
          If value>0 then begin
                rX[Counter]:=x;
                rY[Counter]:=y;
                Counter:=Counter+1;
                ShowMessage(Counter);
            end;
         end;
      end;
      SetOptions('X-Y Center User1 User2');
      SetCounter(Counter-1);
      xmin:=640;
      xmax:=0;
      ymax:=0;
      for i:=1 to Counter-1 do begin
         if rX[i]<xmin then xmin:=rX[i];
         if rX[i]>xmax then xmax:=rX[i];
         if rY[i]>ymax then ymax:=rY[i];
      end;
      depix:=xmax-xmin;
      yds:=ymax-depix;
      yneedle:=15;
      j:=1;
      k:=1;
      for i:=1 to Counter-1 do begin
         if rY[i]=yds then begin
            rUser1[j]:=rX[i];
            j:=j+1;
         end;
```

```
         if rY[i]=yneedle then begin
            rLength[k]:=rX[i];
            k:=k+1;
         end;
      end;
      xneedlemin:=640;
      xneedlemax:=0;
      xdsmin:=640;
      xdsmax:=0;
      for i:=1 to j-1 do begin
         if rUser1[i]<xdsmin then xdsmin:=rUser1[i];
         if rUser1[i]>xdsmax then xdsmax:=rUser1[i];
      end;
      for i:=1 to k-1 do begin
         if rLength[i]<xneedlemin then xneedlemin:=rLength[i];
         if rLength[i]>xneedlemax then xneedlemax:=rLength[i];
      end;
      Needlepix:=xneedlemax-xneedlemin;
      PixmmCF:=Needlemm/Needlepix;
      de:=depix*PixmmCF;
      dspix:=xdsmax-xdsmin;
      S:=dspix/depix;
      LnOneoverH:=ln(0.3152)-2.6072*ln(S);
      OneoverH:=exp(LnOneoverH);
      Sigma:=(DeltaRho*9.8*(de*0.001)*(de*0.001)*OneoverH)*1000;
      Bond:=0.25*(1/OneoverH);
      rMajor[n+1]:=de;
      rMinor[n+1]:=sigma;
      rUser2[n+1]:=Bond;
      if n<Number Then Dispose;
   end;
   for i:=1 to Number do begin
      rMajor[i]:=rMajor[i+1];
      rMinor[i]:=rMinor[i+1];
      rUser2[i]:=rUser2[i+1];
   end;
   SetCounter(Number);
   SetPrecision(3);
   SetOptions('Major Minor User2');
   SetMajorLabel('de (mm)');
   SetMinorLabel('IT (nN/m)');
   SetUser2Label('Bond No.');
   Dispose;
   ShowResults;
   PutMessage('Analysis Complete.');
end;
```

B.4 Mechanistic Model Evaluation

The following program is the Matlab program used to solve the linear mechanistic model equations coupled with the surface dilational modulus equation, for surfactant

systems, in all turbulent sub-ranges (see Chapter 8, section 8.1.1). A similar program was used for the spring and dashpot models. The only difference is the model equations.

```
% Mechanistic Model Evaluation for Surfactant Systems - Linear Models
(mmsurf.m)

% - Initial Data and Physical Properties Input -
clear
format short g
mm=input('Select Mechanistic Model, 1) Inertial S-R, 2) Viscous S-R
(i), 3) Viscous S-R (v): ');
op1=input('Select 1) No Surface Dilation, 2) Effective Interfacial
Tension, 3) Effective Dispersed Phase Viscosity: ');
op2=input('Select 1) Drop Stretching Timescale, 2) Eddy Lifetime: ');
md=[0.00935 0.048 0.0964 0.4845 0.97]; % - Dispersed Phase Viscosities
(Pa*s)
mc=0.00092; % - Continuous Phase Viscosity (Pa*s)
rd=[935 960 964 969 970]; % - Dispersed Phase Densities (kg/m^3)
rc=997.045; % - Continuous Phase Density (kg/m^3)
C=[1e-5 1e-4 1e-3 3.44e-3 8.60e-3 1e-5 1e-4 6.04e-4 6.04e-3 3.02e-2 1e-
5 1e-4 9.26e-4 4.63e-3 4.63e-2]; % - Surfactant Conc. (mol/l)
Gi=[2.429 2.429 2.429 2.429 2.429 3.099 3.099 3.099 3.099 3.099 2.048
2.048 2.048 2.048 2.048]*1e-6; % - Surf. Excess C. (mol/m^2)
aL=[1.21 1.21 1.21 1.21 1.21 1.5 1.5 1.5 1.5 1.5 .604 .604 .604 .604
.604]*1e-6; % - Langmuir Parameter (mol/l)
seq=[.0337 .0193 .0056 .0027 .0027 .0296 .0146 .0056 .0056 .0056 .0309
.0208 .0118 .0118 .0118]; % - Eq. Interfacial T. (N/m)
e=[57.483 150.909 391.984 584.712 968.501 1891.907]; % - Turbulent
Kinetic Energy Dissipation Rate (m^2/s^3)
D=[8.1 8.1 8.1 8.1 8.1 5.02 5.02 5.02 5.02 5.02 1.15 1.15 1.15 1.15
1.15]*1e-10; % - Diffusivities (m^2/s)
A=input('Constant A: ');
B=input('Constant B: ');
if op1==2 Cs=input('Constant Cs: '); end
if op1==3 Cm=input('Constant Cm: '); end
L=0.028; % - Rotor Diameter (m)
R=8.31451; % - Ideal Gas Constant (J/(mol*K))
T=298; % - Absolut Temperature (K)
D32exp=[19.70 20.33 16.14 0 0; 16.09 14.98 19.32 0 0; 16.15 10.5 15.94
24.96 28.7; 12 10.23 18.67 21.06 20.16; 9.05 10.09 12.64 15.3 14.29; 7
8.56 13.07 15.26 16.16; 23.62 26.31 22.82 0 0; 17.19 21.42 20.75 0 0;
11.19 15.26 16.22 21.68 0; 8.19 13.01 17.67 27.08 31.54; 6.73 10.52
14.8 23.87 26.36; 5.77 8.85 10.36 15.2 35.93; 15.22 26.24 23.8 20.73
21.08; 9.47 16.01 19.13 17.36 18.73; 6.19 12.55 16.08 14.82 16.73; 4.4
8.57 12.56 17.3 13.57; 3.45 6.67 9.85 12.69 11.31; 2.93 6.11 8.45 11.77
10.11;11.37 17.8 19.61 13.33 13.15; 7.19 12.43 11.98 12.93 12.81; 4.9
9.19 10.12 16.3 10.99; 3.52 7.54 8.46 13.32 13.26; 2.93 6.26 7.87 10.19
11.95; 2.63 5.79 6.83 11.05 11.12; 9.7 10.43 19.44 13.16 9.1; 6.83 9.83
14.61 15.52 10.9; 5.15 7.17 9.78 8.83 9.86; 4.06 5.85 7.43 8.91 8.46;
3.44 5.32 6.34 7.16 7.56; 3.07 4.61 5.9 8.82 8.06; 35.39 0 32.64 0 0;
21.4 0 27.48 0 0; 13.15 0 21.73 0 36.13; 11.81 0 17.12 0 35.06; 7.01 0
13.78 0 21.17; 5.46 0 10.16 0 21.07; 27.31 0 55.84 0 0; 17.54 0 34.22 0
0; 11.56 0 24.49 0 0; 8.25 0 18.79 0 50.39; 6.18 0 13.74 0 37.17; 5.09
0 10.71 0 27; 24.35 0 52.86 0 0; 13.83 0 34.03 0 0; 8.98 0 22.85 0 0;
6.54 0 16.96 0 26.66; 4.94 0 12.36 0 31.47; 4.66 0 11.89 0 26.1; 21.51
```

```
0 36.84 0 20.9; 15.17 0 30.12 0 12.37; 10.04 0 22.53 0 16.35; 6.74 0
17.33 0 18.16; 5.11 0 13.61 0 16.98; 4.23 0 12.23 0 13.8; 19.31 0 17.77
0 12.94; 13.57 0 19.01 0 12.13; 9.71 0 14.54 0 11.09; 6.53 0 12.64 0
12.74; 5.2 0 10.67 0 11.66; 4.69 0 10 0 12.89; 33.75 0 0 0 0; 21.64 0
32.21 0 0; 13.16 0 17.07 0 27.88; 8.76 0 16.94 0 25.18; 6.58 0 14.21 0
21.17; 5.11 0 9.65 0 16.82; 29.52 0 0 0 0; 19.09 0 35.42 0 0; 11.55 0
23.14 0 38.74; 7.85 0 18.2 0 31.32; 6.63 0 13.71 0 22.41; 5.35 0 12.93
0 22.4; 27.71 0 56.89 0 0; 16.95 0 40.86 0 37.75; 10.41 0 26.53 0
32.32; 7.7 0 19.19 0 22.35; 5.61 0 13.73 0 23.65; 4.74 0 11.8 0 19.6;
24.67 0 44.45 0 32.8; 16.03 0 33.62 0 32.08; 10.38 0 25.15 0 23.29;
7.17 0 17.48 0 19.74; 5.6 0 12.71 0 17.49; 4.91 0 11.18 0 14.96; 20.99
0 33.23 0 20.33; 15.76 0 22.7 0 21.13; 9.65 0 18.71 0 20.42; 6.9 0
14.97 0 18.03; 5.29 0 11.54 0 16.53; 4.37 0 10.49 0 14.25];
D32Lexp=D32exp*1e-6/L;

% - Model Evaluation -

for x=1:15 % - Continuous Phases
   for y=1:5 % - Dispersed Phases
      results(1,y)=round(md(y)*1e6/rd(y));
      D32o=[15 15 15 15 15 15]*1e-6; % - Initial Drop Diameter Values
(m)
      D32Lo=D32o/L;
      error=[100 100 100 100 100 100];
      for i=1:6 % - Rotor Speeds
         if op1==1 % - No Surface Dilational Modulus
            seff=seq(x);
            mdeff=md(y);
            N=(i+1)*1000;
            We=(rc*((N/60)^2)*L^3)/seff;
            Vi=((mdeff*(N/60)*L)/seff)*((rc/rd(y))^(1/2));
            Re=(rc*(N/60)*L^2)/mc;
            while error(i)>0.001
               if mm==1 % - Inertial Sub-Range
                  D32L(i)=A*(We^(-
3/5))*((1+B*Vi*(D32Lo(i)^(1/3)))^(3/5));
               elseif mm==2 % - Sub-Kolmogorov (Inertial)
                  D32L(i)=(A*(Re*We)^(-
1/3))*((1+B*Vi*(Re^(1/2))*D32Lo(i))^(1/3));
               else
                  disp('Invalid Model Selection - No VSR(v) model for
this Esd Option');
               end
               error(i)=(abs(D32Lo(i)-D32L(i))/D32Lo(i))*100;
               D32Lo(i)=D32L(i);
               %disp(error(i));
            end
            results(i+1,y)=D32L(i);
         end
         if op1==2 % - Surface Dilation Through Effective Interfacial
Tension
            mdeff=md(y);
            Esd=0.005; % - Initial Value of Surface Dilational Modulus
            N=(i+1)*1000;
            Re=(rc*(N/60)*L^2)/mc;
            while error(i)>0.001
               seff=seq(x)+Cs*Esd;
```

```
                We=(rc*((N/60)^2)*L^3)/seff;
                Vi=((mdeff*(N/60)*L)/seff)*((rc/rd(y))^(1/2));
                if mm==1 % - Inertial Sub-Range
                   D32L(i)=A*(We^(-
3/5))*((1+B*Vi*(D32Lo(i)^(1/3)))^(3/5));
                   D32o(i)=D32L(i)*L;
                   if op2==1 % - Drop Stretching Timescale

Esd=(R*T*Gi(x)*C(x)/aL(x))/(1+sqrt(D(x)*mdeff/rc)*(aL(x)*1000/Gi(x))*((
C(x)/aL(x)+1)^2)*(e(i)^(-1/3))*(D32o(i)^(-1/3)));
                   elseif op2==2 % - Eddy Lifetime

Esd=(R*T*Gi(x)*C(x)/aL(x))/(1+sqrt(D(x))*(aL(x)*1000/Gi(x))*((C(x)/aL(x
)+1)^2)*(e(i)^(-1/6))*(D32o(i)^(1/3)));
                   end
                elseif mm==2 % - Viscous Sub-Range (inertial)
                   D32L(i)=A*((Re*We)^(-
1/3))*((1+B*Vi*(Re^(1/2))*D32Lo(i))^(1/3));
                   D32o(i)=D32L(i)*L;
                   if op2==1 % - Drop Stretching Timescale

Esd=(R*T*Gi(x)*C(x)/aL(x))/(1+(sqrt(D(x)*mdeff*mc)/rc)*(aL(x)*1000/Gi(x
))*((C(x)/aL(x)+1)^2)*(e(i)^(-1/2))*(D32o(i)^-1));
                   elseif op2==2 % - Eddy Lifetime

Esd=(R*T*Gi(x)*C(x)/aL(x))/(1+sqrt(D(x))*((mc/rc)^(1/4))*(aL(x)*1000/Gi
(x))*((C(x)/aL(x)+1)^2)*(e(i)^(-1/4)));
                   end
                elseif mm==3 % - Viscous SubRange (viscous)
                   D32L(i)=A*(We^-1)*(Re^(1/2))*(1+B*Vi*(Re^(-1/4)));
                   D32o(i)=D32L(i)*L;
                   if op2==1 % - Drop Stretching Timescale

Esd=(R*T*Gi(x)*C(x)/aL(x))/(1+(sqrt(D(x)*mdeff)/((mc*rc)^(1/4)))*(aL(x)
*1000/Gi(x))*((C(x)/aL(x)+1)^2)*(e(i)^(-1/4)));
                   elseif op2==2 % - Eddy Lifetime

Esd=(R*T*Gi(x)*C(x)/aL(x))/(1+sqrt(D(x))*((rc/mc)^(1/8))*(aL(x)*1000/Gi
(x))*((C(x)/aL(x)+1)^2)*(e(i)^(-1/8))*(D32o(i)^(1/2)));
                   end
                else
                   disp('Invalid Model Selection');
                end
                error(i)=(abs(D32Lo(i)-D32L(i))/D32Lo(i))*100;
                D32Lo(i)=D32L(i);
                %disp(error(i));
             end
             results(i+1,y)=D32L(i);
          end
          if op1==3 % - Surface Dilation Through Effective Dispersed
Phase Viscosity
             seff=seq(x);
             Esd=0.005; % - Initial Value of Surface Dilational Modulus
             N=(i+1)*1000;
             while error(i)>0.001
                if mm==1
                   if op2==1
```

```
                    mdeff=md(y)*(1+Cm*(2*Esd/rc)*(e(i)^(-
2/3))*(D32o(i)^(-5/3)));
                elseif op2==2
                    mdeff=md(y)+Cm*2*Esd*(e(i)^(-1/3))*(D32o(i)^(-
1/3));
                end
            elseif mm==2
                if op2==1
                    mdeff=md(y)*(1+Cm*(2*Esd*mc/rc^2)*(e(i)^-
1)*(D32o(i)^-3));
                elseif op2==2
                    mdeff=md(y)+Cm*2*Esd*sqrt(mc/rc)*(e(i)^(-
1/2))*(D32o(i)^-1);
                end
            elseif mm==3
                if op2==1
                    mdeff=md(y)*(1+Cm*(2*Esd/sqrt(mc*rc))*(e(i)^(-
1/2))*(D32o(i)^-1));
                elseif op2==2
                    mdeff=md(y)+Cm*2*Esd*((rc/mc)^(1/4))*(e(i)^(-
1/4));
                end
            end
            We=(rc*((N/60)^2)*L^3)/seff;
            Vi=((mdeff*(N/60)*L)/seff)*((rc/rd(y))^(1/2));
            Re=(rc*(N/60)*L^2)/mc;
            if mm==1 % - Inertial Sub-Range
                D32L(i)=A*(We^(-
3/5))*((1+B*Vi*(D32Lo(i)^(1/3)))^(3/5));
                D32o(i)=D32L(i)*L;
                if op2==1 % - Drop Stretching Timescale

Esd=(R*T*Gi(x)*C(x)/aL(x))/(1+sqrt(D(x)*mdeff/rc)*(aL(x)*1000/Gi(x))*((
C(x)/aL(x)+1)^2)*(e(i)^(-1/3))*(D32o(i)^(-1/3))); % - Drop Stretching
Timescale
                elseif op2==2 % - Eddy Lifetime

Esd=(R*T*Gi(x)*C(x)/aL(x))/(1+sqrt(D(x))*(aL(x)*1000/Gi(x))*((C(x)/aL(x
)+1)^2)*(e(i)^(-1/6))*(D32o(i)^(1/3))); % - Eddy Lifetime
                end
            elseif mm==2 % - Viscous Sub-Range (Inertial)
                D32L(i)=A*((Re*We)^(-
1/3))*((1+B*Vi*(Re^(1/2))*D32Lo(i))^(1/3));
                D32o(i)=D32L(i)*L;
                if op2==1 % - Drop Stretching Timescale

Esd=(R*T*Gi(x)*C(x)/aL(x))/(1+(sqrt(D(x)*mdeff*mc)/rc)*(aL(x)*1000/Gi(x
))*((C(x)/aL(x)+1)^2)*(e(i)^(-1/2))*(D32o(i)^-1)); % - Drop Stretching
Timescale
                elseif op2==2 % - Eddy Lifetime

Esd=(R*T*Gi(x)*C(x)/aL(x))/(1+sqrt(D(x))*((mc/rc)^(1/4))*(aL(x)*1000/Gi
(x))*((C(x)/aL(x)+1)^2)*(e(i)^(-1/4))); % - Eddy Lifetime
                end
            elseif mm==3 % - Viscous SubRange (viscous)
                D32L(i)=A*(We^-1)*(Re^(1/2))*(1+B*Vi*(Re^(-1/4)));
                D32o(i)=D32L(i)*L;
```

```
                    if op2==1 % - Drop Stretching Timescale

Esd=(R*T*Gi(x)*C(x)/aL(x))/(1+(sqrt(D(x)*mdeff)/((mc*rc)^(1/4)))*(aL(x)
*1000/Gi(x))*((C(x)/aL(x)+1)^2)*(e(i)^(-1/4)));
                    elseif op2==2 % - Eddy Lifetime

Esd=(R*T*Gi(x)*C(x)/aL(x))/(1+sqrt(D(x))*((rc/mc)^(1/8))*(aL(x)*1000/Gi
(x))*((C(x)/aL(x)+1)^2)*(e(i)^(-1/8))*(D32o(i)^(1/2)));
                    end
                else
                    disp('Invalid Model Selection');
                end
                error(i)=(abs(D32Lo(i)-D32L(i))/D32Lo(i))*100;
                D32Lo(i)=D32L(i);
                %disp(error(i));
             end
             results(i+1,y)=D32L(i);
          end
       end
    end
    if x==1 disp('Tergitol TMN-6'); end
    if x==6 disp('Triton X-100'); end
    if x==11 disp('Triton X-165'); end
    disp(results);
    for k=1:6
       Totalresults(k+(x-1)*6,:)=results(k+1,:);
    end
end
wk1write('test.xls',Totalresults);
for x=1:90
    for y=1:5
       if D32Lexp(x,y)==0
          DiffSq(x,y)=0;
       else
          DiffSq(x,y)=((D32Lexp(x,y)-Totalresults(x,y))/D32Lexp(x,y))^2;
       end
    end
end
RMS=100*sqrt(sum(sum(DiffSq))/306);
disp(RMS);
```

REFERENCES

Adamson, A. W. 1976. *Physical Chemistry of Surfaces*. Third edition. New York: Wiley-Interscience.

Alderliesten, M. 1990. Mean Particle Diameters.1. Evaluation of Definition Systems. *Particle & Particle Systems Characterization* 7 no. 4: 233-241.

Alderliesten, M. 1991. Mean Particle Diameters.2. Standardization of Nomenclature. *Particle & Particle Systems Characterization* 8 no. 3: 237-241.

Ali, A. M., H. H. S. Yuan, D. S. Dickey and G. B. Tatterson. 1981. Liquid Dispersion Mechanisms in Agitated Tanks.1. Pitched Blade Turbine. *Chemical Engineering Communications* 10 no. 4-5: 205-213.

Arai, K., M. Konno, Y. Matunga and S. Saito. 1977. Effect of dispersed phase viscosity on the maximum stable drop size for break-up in turbulent flow. *Journal of Chemical Engineering of Japan* 10: 325-330.

Arce, A., A. Blanco, A. Soto and I. Vidal. 1993. Densities, Refractive-Indexes, and Excess Molar Volumes of the Ternary-Systems Water Plus Methanol Plus 1-Octanol and Water Plus Ethanol Plus 1-Octanol and Their Binary-Mixtures at 298.15 K. *Journal of Chemical and Engineering Data* 38 no. 2: 336-340.

Becher, P. and S. Trifiletti. 1973. Nonionic Surface-Active Agents.12. Effect of Solvent on Thermodynamics of Micellization. *Journal of Colloid and Interface Science* 43 no. 2: 485-490.

Bentley, B. J. and L. G. Leal. 1986. An experimental investigation of drop deformation and breakup in steady, two-dimensional linear flows. *Journal of Fluid Mechanics* 167: 241-283.

Berkman, P. D. and R. V. Calabrese. 1988. Dispersion of viscous liquids by turbulent flow in a static mixer. *AIChE Journal* 34 no. 4: 602-609.

Bernard, P. S. and J. M. Wallace. 2002. *Turbulent Flow*. Hoboken, New Jersey: John Wiley & Sons, Inc.

Bonfillon, A. and D. Langevin. 1993. Viscoleasticity of monolayers at oil-water interfaces. *Langmuir* 9: 2172-2177.

Bourne, J. R. and J. Baldyga. 1994. Drop Breakup in the Viscous Subrange - a Source of Possible Confusion. *Chemical Engineering Science* 49 no. 7: 1077-1078.

Brown, D. E. and K. Pitt. 1972. Drop Size Distribution of Stirred Non-Coalescing Liquid-Liquid System. *Chemical Engineering Science* 27 no. 3: 577-583.

Calabrese, R. V. 2001. Research needs and opportunities in fluid mixing technology. *Chemical Engineering Research & Design* 79 no. A2: 111-112.

Calabrese, R. V., T. P. K. Chang and P. T. Dang. 1986. Drop Breakup in Turbulent Stirred-Tank Contactors.1. Effect of Dispersed-Phase Viscosity. *AIChE Journal* 32 no. 4: 657-666.

Calabrese, R. V., C. Y. Wang and N. P. Bryner. 1986. Drop Breakup in Turbulent Stirred-Tank Contactors.3. Correlations for Mean Size and Drop Size Distribution. *Aiche Journal* 32 no. 4: 677-681.

Chang, T. P. K., Y. H. E. Sheu, G. B. Tatterson and D. S. Dickey. 1981. Liquid Dispersion Mechanisms in Agitated Tanks.2. Straight Blade and Disk Style Turbines. *Chemical Engineering Communications* 10 no. 4-5: 215-222.

Chatzi, E. G., C. J. Boutris and C. Kiparissides. 1991. Online Monitoring of Drop Size Distributions in Agitated Vessels.2. Effect of Stabilizer Concentration. *Industrial & Engineering Chemistry Research* 30 no. 6: 1307-1313.

Chatzi, E. G., A. D. Gavrielides and C. Kiparissides. 1989. Generalized-Model for Prediction of the Steady-State Drop Size Distributions in Batch Stirred Vessels. *Industrial & Engineering Chemistry Research* 28 no. 11: 1704-1711.

Chen, H. T. 1966. Drop Size Distribution in Agitated Tanks. Ph. D. thesis, University of Rochester.

Chen, H. T. and S. Middleman. 1967. Drop Size Distribution in Agitated Liquid-Liquid Systems. *Aiche Journal* 13 no. 5: 989-995.

Chen, J. and K. J. Stebe. 1996. Marangoni retardation of the terminal velocity of a settling droplet: The role of surfactant physico-chemistry. *Journal of Colloid and Interface Science* 178 no. 1: 144-155.

Clark, M. M. 1988a. Drop Breakup in a Turbulent-Flow.1. Conceptual and Modeling Considerations. *Chemical Engineering Science* 43 no. 3: 671-679.

Clark, M. M. 1988b. Drop Breakup in a Turbulent-Flow.2. Experiments in a Small Mixing Vessel. *Chemical Engineering Science* 43 no. 3: 681-692.

Coulaloglou, C. A. and L. L. Tavlarides. 1976. Drop Size Distributions and Coalescence Frequencies of Liquid- Liquid Dispersions in Flow Vessels. *Aiche Journal* 22 no. 2: 289-297.

Coulaloglou, C. A. and L. L. Tavlarides. 1977. Description of Interaction Processes in Agitated Liquid-Liquid Dispersions. *Chemical Engineering Science* 32 no. 11: 1289-1297.

Crowe, C., M. Sommerfeld and Y. Tsuji. 1997. *Multiphase Flows with Droplets and Particles*. Boca Raton: CRC Press.

Danov, K. D., P. A. Kralchevski and I. B. Ivanov. 2001. Dynamic Processes in Surfactant-Stabilized Emulsions. In *Encyclopedic Handbook of Emulsion Technology*, edited by J. Sjöblom. New York, Macel Dekker, Inc.

Danov, K. D., D. S. Valkovska and P. A. Kralchevsky. 2002. Adsorption relaxation for nonionic surfactants under mixed barrier-diffusion and micellization-diffusion control. *Journal of Colloid and Interface Science* 251 no. 1: 18-25.

Das, P. K. 1996. Prediction of maximum stable diameter of viscous drops in a turbulent dispersion. *Chemical Engineering & Technology* 19 no. 1: 39-42.

Davies, J. T. 1987. A Physical Interpretation of Drop Sizes in Homogenizers and Agitated Tanks, Including the Dispersion of Viscous Oils. *Chemical Engineering Science* 42 no. 7: 1671-1676.

Diamant, H. and D. Andelman. 1996a. Kinetics of surfactant adsorption at fluid-fluid interfaces. *Journal of Physical Chemistry* 100 no. 32: 13732-13742.

Diamant, H. and D. Andelman. 1996b. Kinetics of surfactant adsorption at fluid/fluid interfaces: Non-ionic surfactants. *Europhysics Letters* 34 no. 8: 575-580.

Diamant, H., G. Ariel and D. Andelman. 2001. Kinetics of surfactant adsorption: the free energy approach. *Colloids and Surfaces a-Physicochemical and Engineering Aspects* 183: 259-276.

Djabbarah, N. F. and D. T. Wasan. 1982. Relationship between Surface Viscosity and Surface-Composition of Adsorbed Surfactant Films. *Industrial & Engineering Chemistry Fundamentals* 21 no. 1: 27-31.

Dong, C. D., C. T. Hsu, C. Y. Chiu and S. Y. Lin. 2000. A study on surfactant adsorption kinetics: Effect of bulk concentration on the limiting adsorption rate constant. *Langmuir* 16 no. 10: 4573-4580.

Dukhin, S. S., G. Kretzschmar and R. Miller. 1995. *Dynamics of Adsorption at Liquid Interfaces*. Amsterdam: Elsevier.

Edwards, D. A., H. Brenner and D. T. Wasan. 1991. *Interfacial Transport Processes and Rheology*. Boston: Butterworth-Heinemann.

Edwards, D. A. and D. T. Wasan. 1988a. Surface Rheology.2. The Curved Fluid Surface. *Journal of Rheology* 32 no. 5: 447-472.

Edwards, D. A. and D. T. Wasan. 1988b. Surface Rheology.3. Stress on a Spherical Fluid Surface. *Journal of Rheology* 32 no. 5: 473-484.

Eggleton, C. D. and K. J. Stebe. 1998. An adsorption-desorption-controlled surfactant on a deforming droplet. *Journal of Colloid and Interface Science* 208 no. 1: 68-80.

Erni, P., P. Fischer, E. J. Windhab, V. Kusnezov, H. Stettin and J. Lauger. 2003. Stress- and strain-controlled measurements of interfacial shear viscosity and viscoelasticity at liquid/liquid and gas/liquid interfaces. *Review of Scientific Instruments* 74 no. 11: 4916-4924.

Evans, D. F. and H. Wennerström. 1999. *The Colloidal Domain*. Second edition. New York: Wiley-VCH.

Fainerman, V. B., A. V. Makievski and R. Miller. 1994. The Analysis of Dynamic Surface-Tension of Sodium Alkyl Sulfate-Solutions, Based on Asymptotic Equations of Adsorption Kinetic-Theory. *Colloids and Surfaces a-Physicochemical and Engineering Aspects* 87 no. 1: 61-75.

Fainerman, V. B., R. Miller and A. V. Makievski. 1995. Reorientation of Polyethylene-Glycol Octylphenyl Ether in Nonequilibrium Adsorption Layers at the Water/Air Interface - Role of Molecular-Weight and Temperature. *Langmuir* 11 no. 8: 3054-3060.

Ferri, J. K. and K. J. Stebe. 2000. Which surfactants reduce surface tension faster? A scaling argument for diffusion-controlled adsorption. *Advances in Colloid and Interface Science* 85 no. 1: 61-97.

Flick, E. W. 1993. *Industrial Surfactants*. Second edition. Noyes Publications.

Francis, M. K. 1999. The development of a novel probe for the in situ measurement of particle size distributions, and application to the measurement of drop size in rotor stator mixers. Ph. D. thesis, University of Maryland.

Gandhi, K. S. and R. Kumar. 1990. An Elongational Flow Model for Drop Breakage in Stirred Turbulent Dispersions. *Chemical Engineering Science* 45 no. 9: 2998-3001.

Gibbs, J. W. 1878. On the equilibrium of heterogeneous substances. *Transactions of the Connecticut Academy, III*: 108-204, 343-524.

Göbel, J. G. and G. R. Joppien. 1997. Dynamic interfacial tensions of aqueous triton X-100 solutions in contact with air, cyclohexane, n-heptane, and n-hexadecane. *Journal of Colloid and Interface Science* 191 no. 1: 30-37.

Griffin, W. C. 1949. Classification of Surface-Active Agents by "HLB". *Journal of The Society of Cosmetic Chemists* 1: 311-326.

Griffin, W. C. 1954. Calculation of HLB Values of Non-Ionic Surfactants. *Journal of The Society of Cosmetic Chemists* 5: 249-256.

Gupta, L. and D. T. Wasan. 1974. Surface Shear Viscosity and Related Properties of Adsorbed Surfactant Films. *Industrial & Engineering Chemistry Fundamentals* 13 no. 1: 26-33.

Hajiloo, A., T. R. Ramamohan and J. C. Slattery. 1987. effect of interfacial viscosities on the stability of a liquid thread. *Journal of Colloid and Interface Science* 117 no. 2: 384-393.

Hansen, F. K. and H. Fagerheim. 1998. The influence of oil phase on the adsorption of non-ionic surfactants investigated by the automatic sessile drop method. *Colloids and Surfaces a-Physicochemical and Engineering Aspects* 137 no. 1-3: 217-230.

Hansen, S., G. W. M. Peters and H. E. H. Meijer. 1999. the effect of surfactant on the stability of a fluid filament embedded in a viscous fluid. *Journal of Fluid Mechanics* 382: 331-349.

Hanus, L. H. and H. J. Ploehn. 1999. Conversion of intensity-averaged photon correlation spectroscopy measurements to number-averaged particle size distributions. 1. Theoretical development. *Langmuir* 15 no. 9: 3091-3100.

Heisenberg, W. 1948. On the Theory of Statistical and Isotropic Turbulence. *Proceedings of the Royal Society of London Series a-Mathematical and Physical Sciences* 195 no. 1042: 402-406.

Hesketh, R. P., A. W. Etchells and T. W. F. Russell. 1991. Experimental observations of bubble breakage in turbulent flow. *Industrial & Engineering Chemistry Research* 30 no. 5: 835-841.

Hiemenz, P. C. and R. Rajagopalan. 1997. *Principles of Colloid and Surface Chemistry*. Third edition. New York: Marcel Dekker, Inc.

Hinze, J. O. 1955. Fundamentals of the Hydrodynamic Mechanism of Splitting in Dispersion Processes. *Aiche Journal* 1 no. 3: 289-295.

Horozov, T. and L. Arnaudov. 2000. Adsorption kinetics of some polyethylene glycol octylphenyl ethers studied by the fast formed drop technique. *Journal of Colloid and Interface Science* 222 no. 1: 146-155.

Hu, Y. T. and A. Lips. 2003. Estimating surfactant surface coverage and decomposing its effect on drop deformation. *Physical Review Letters* 91 no. 4: 044501-1-044501-4.

Janssen, J. J. M., A. Boon and W. G. H. Agterof. 1994a. Droplet Break-up in Simple Shear-Flow in the Presence of Emulsifiers. *Colloids and Surfaces a-Physicochemical and Engineering Aspects* 91: 141-148.

Janssen, J. J. M., A. Boon and W. G. M. Agterof. 1994b. Influence of Dynamic Interfacial Properties on Droplet Breakup in Simple Shear-Flow. *Aiche Journal* 40 no. 12: 1929-1939.

Janssen, J. J. M., A. Boon and W. G. M. Agterof. 1997. Influence of dynamic interfacial properties on droplet breakup in plane hyperbolic flow. *Aiche Journal* 43 no. 6: 1436-1447.

Janssen, J. M. H. and H. E. H. Meijer. 1993. Droplet Breakup Mechanisms - Stepwise Equilibrium Versus Transient Dispersion. *Journal of Rheology* 37 no. 4: 597-608.

Janssen, L. P. B. M. and M. M. C. G. Warmoeskerken, Eds. 1987. *Transport Phenomena Data Companion*, Edward Arnold/Delftse Uitgevers Maatschappij.

Jiang, Q., Y. C. Chiew and J. E. Valentini. 1992. Damping of cylindrical propagating capillary waves on monolayer-covered surfaces. *Langmuir* 8: 2747-2752.

Kissa, E. 1999. *Dispersions. Characterization, Testing and Measurement*. New York: Marcel Dekker.

Kolmogorov, A. N. 1941. The Local Structure of Turbulence in Incompressible Viscous Fluid for Very Large Reynolds Numbers. *Proceedings of the Royal Society of London Series a- Mathematical Physical and Engineering Sciences* 434 no. 1890: 9-13.

Kolmogorov, A. N. 1949. On the breakage of drops in a turbulent flow. In *Selected works of A. N. Kolmogorov. Volume I: Mathematics and Mechanics*, edited by V. M. Tikhomirov. Dordrecht, Kulwer Academic Publishers.

Konno, M., K. Arai and S. Saito. 1982. The effect of stabilizer on coalescece of dispersed drops in suspension polymerization of styrene. *Journal of Chemical Engineering of Japan* 15 no. 2: 131-135.

Koshy, A., T. R. Das and R. Kumar. 1988. Effect of Surfactants on Drop Breakage in Turbulent Liquid Dispersions. *Chemical Engineering Science* 43 no. 3: 649-654.

Koshy, L., A. H. Saiyad and A. K. Rakshit. 1996. The effects of various foreign substances on the cloud point of Triton X 100 and Triton X 114. *Colloid and Polymer Science* 274 no. 6: 582-587.

Kresta, S. M. and R. S. Brodkey. 2004. Turbulence in Mixing Applications. In *Handbook of Industrial Mixing: Science and Practice*, edited by E. L. Paul, V. A. Atiemo-Obeng and S. M. Kresta. Hoboken, New Jersey, John Wiley & Sons.

Krope, A. and J. Krope. 2001. Surfactant drag reducing flow. Proceedings of the 37th Heat Transfer and Fluid Mechanics Institute, Held in California State University, Sacramento edited by F. H. Reardon and T. D. Ngo.

Kuriyama, M., M. Ono, H. Tokanai and H. Konno. 1996. Correlation of transient sizes of highly viscous drops in dispersion process in liquid-liquid agitation. *Chemical Engineering Research & Design* 74 no. A4: 431-437.

Lagisetty, J. S., P. K. Das, R. Kumar and K. S. Gandhi. 1986. Breakage of Viscous and Non-Newtonian Drops in Stirred Dispersions. *Chemical Engineering Science* 41 no. 1: 65-72.

Langevin, D. 2000. Influence of interfacial rheology on foam and emulsion properties. *Advances in Colloid and Interface Science* 88 no. 1-2: 209-222.

Lee, J. M. and Y. Soong. 1985. Effects of Surfactants on the Liquid Liquid Dispersions in Agitated Vessels. *Industrial & Engineering Chemistry Process Design and Development* 24 no. 1: 118-121.

Leng, D. E. and R. V. Calabrese. 2004. Immiscible Liquid-Liquid Systems. In *Handbook of Industrial Mixing: Science and Practice*, edited by E. L. Paul, V. A. Atiemo-Obeng and S. M. Kresta. Hoboken, New Jersey, John Wiley & Sons.

Levich, V. G. 1962. *Physicochemical Hydrodynamics*. Englewood Cliffs, N.J.: Prentice Hall, Inc.

Lide, D. R., Ed. 1999. *CRC Handbook of Chemistry and Physics*. Boca Raton, CRC Press.

Lin, S. Y., H. C. Chang and E. M. Chen. 1996. The effect of bulk concentration on surfactant adsorption processes: The shift from diffusion-control to mixed kinetic diffusion control with bulk concentration. *Journal of Chemical Engineering of Japan* 29 no. 4: 634-641.

Lin, S. Y., K. McKeigue and C. Maldarelli. 1990. Diffusion-Controlled Surfactant Adsorption Studied by Pendant Drop Digitization. *Aiche Journal* 36 no. 12: 1785-1795.

Loglio, G., U. Tesei, R. Miller and R. Cini. 1991. Dilational Viscoelasticity of Fluid Interfaces - the Diffusion-Model for Transient Processes. *Colloids and Surfaces* 61: 219-226.

Lucassen-Reynders, E. H., Ed. 1981. *Anionic Surfactants. Physical Chemistry of Surfactant Action*. Surfactant Science Series. New York, Marcel Dekker, Inc.

Lucassen-Reynders, E. H. 1994. Competitive Adsorption of Emulsifiers.1. Theory for Adsorption of Small and Large Molecules. *Colloids and Surfaces a-Physicochemical and Engineering Aspects* 91: 79-88.

Lucassen-Reynders, E. H., A. Cagna and J. Lucassen. 2001. Gibbs elasticity, surface dilational modulus and diffusional relaxation in nonionic surfactant monolayers. *Colloids and Surfaces a-Physicochemical and Engineering Aspects* 186 no. 1-2: 63-72.

Lucassen-Reynders, E. H. and K. A. Kuijpers. 1992. The Role of Interfacial Properties in Emulsification. *Colloids and Surfaces* 65 no. 2-3: 175-184.

Lucassen-Reynders, E. H. and D. T. Wasan. 1993. Interfacial Viscoelasticity in Emulsions and Foams. *Food Structure* 12 no. 1: 1-12.

Lucassen, J. and M. van den Tempel. 1972. Dynamic Measurements of Dilational Properties of a Liquid Interface. *Chemical Engineering Science* 27 no. 6: 1283-1291.

Mathieu, J. and J. Scott. 2000. *An Introduction to Turbulent Flow*. Cambridge: Cambridge University Press.

Middleman, S. 1998. *An Introduction to Fluid Dynamics*. New York: John Wiley & Sons, Inc.

Miller, R., P. Joos and V. B. Fainerman. 1994. Dynamic Surface and Interfacial-Tensions of Surfactant and Polymer-Solutions. *Advances in Colloid and Interface Science* 49: 249-302.

Miller, R., R. Wustneck, J. Kragel and G. Kretzschmar. 1996. Dilational and shear rheology of adsorption layers at liquid interfaces. *Colloids and Surfaces a-Physicochemical and Engineering Aspects* 111 no. 1-2: 75-118.

Milliken, W. J. and L. G. Leal. 1994. The Influence of Surfactant on the Deformation and Breakup of a Viscous Drop - the Effect of Surfactant Solubility. *Journal of Colloid and Interface Science* 166 no. 2: 275-285.

Milliken, W. J., H. A. Stone and L. G. Leal. 1993. The Effect of Surfactant on the Transient Motion of Newtonian Drops. *Physics of Fluids a-Fluid Dynamics* 5 no. 1: 69-79.

Mu, J. H., G. Z. Li, W. C. Zhang and Z. W. Wang. 2001. Determination of the second CMCs of dodecyl polyoxyethylene polyoxypropylene ether by the methods of cloud point, fluorescence, and viscosity. *Colloids and Surfaces a-Physicochemical and Engineering Aspects* 194 no. 1-3: 1-6.

Myers, D. 1992. *Surfactant Science and Technology*. Second edition. New York: VCH Publishers.

Myers, K. J., M. F. Reeder and D. Ryan. 2001. Power draw of a high-shear homogenizer. *Canadian Journal of Chemical Engineering* 79 no. 1: 94-99.

Myers, K. J., M. F. Reeder, D. Ryan and G. Daly. 1999. Get a fix on high-shear mixing. *Chemical Engineering Progress* 95 no. 11: 33-42.

Nambiar, D. K. R., R. Kumar, T. R. Das and K. S. Gandhi. 1992. A New Model for the Breakage Frequency of Drops in Turbulent Stirred Dispersions. *Chemical Engineering Science* 47 no. 12: 2989-3002.

Nambiar, D. K. R., R. Kumar, T. R. Das and K. S. Gandhi. 1994. Two-zone model of breakage frequency of drops in stirred dispersions. *Chemical Engineering Science* 49 no. 13: 2194-2198.

Padron, G. A. 2001. Measurement and comparison of power draw in batch rotor-stator mixers. M.Sc. Thesis, University of Maryland.

Paine, A. J. 1993. Error-Estimates in the Sampling from Particle-Size Distributions. *Particle & Particle Systems Characterization* 10 no. 1: 26-32.

Patist, A., J. R. Kanicky, P. K. Shukla and D. O. Shah. 2002. Importance of micellar kinetics in relation to technological processes. *Journal of Colloid and Interface Science* 245 no. 1: 1-15.

Paul, E. L., V. A. Atiemo-Obeng and S. M. Kresta. 2004. Introduction. In *Handbook of Industrial Mixing: Science and Practice*, edited by E. L. Paul, V. A. Atiemo-Obeng and S. M. Kresta. Hoboken, New Jersey, John Wiley & Sons.

Perry, R. H. and D. W. Green, Eds. 1999. *Perry's Chemical Engineers' Handbook on CD-ROM*, McGraw-Hill.

Phongikaroon, S. 2001. Effect of dispersed phase viscosity and interfacial tension on drop size distribution in a batch rotor-stator mixer. Ph. D. thesis, University of Maryland.

Pozrikidis, C. 1994. Effects of Surface Viscosity on the Finite Deformation of a Liquid-Drop and the Rheology of Dilute Emulsions in Simple Shearing Flow. *Journal of Non-Newtonian Fluid Mechanics* 51 no. 2: 161-178.

Qiao, L. and A. J. Easteal. 1998. The interaction between triton X series surfactants and poly (ethylene glycol) in aqueous solutions. *Colloid and Polymer Science* 276 no. 4: 313-320.

Randolph, A. D. and M. A. Larson. 1971. *Theory of Particulate Processes: Analysis and Techniques of Continuous Crystallization*. New York: Academic Press.

Ravera, F., M. Ferrari and L. Liggieri. 2000. Adsorption and partitioning of surfactants in liquid-liquid systems. *Advances in Colloid and Interface Science* 88 no. 1-2: 129-177.

Ravera, F., M. Ferrari, L. Liggieri, R. Miller and A. Passerone. 1997. Measurement of the partition coefficient of surfactants in water/oil systems. *Langmuir* 13 no. 18: 4817-4820.

Ravera, F., L. Liggieri and R. Miller. 2000. Molecular orientation as a controlling process in adsorption dynamics. *Colloids and Surfaces a-Physicochemical and Engineering Aspects* 175 no. 1-2: 51-60.

Ray, A. 1971. Solvophobic Interactions and Micelle Formation in Structure Forming Nonaqueous Solvents. *Nature* 231 no. 5301: 313-315.

Rillaerts, E. and P. Joos. 1982. Rate of Demicellization from the Dynamic Surface Tensions of Micellar Solutions. *Journal of Physical Chemistry* 86 no. 17: 3471-3478.

Sadhal, S. S., P. S. Ayyaswamy and J. N. Chung. 1996. *Transport Phenomena with Drops and Bubbles*. New York: Springer.

Sæther, Ø. 2001. Video-enhanced Microscopy Investigation of Emulsion Droplets and Size Distributions. In *Encyclopedic Handbook of Emulsion Technology*, edited by J. Sjöblom. New York, Macel Dekker, Inc.

Sharma, S. K., A. N. Goswami and B. S. Rawat. 1991. Effect of Surfactants on Drop Breakage in O/W Emulsions in Liquid Membrane Separations. *Indian Journal of Technology* 29 no. 5: 254-258.

Shinnar, R. 1961. On the Behaviour of Liquid Dispersions in Mixing Vessels. *Journal of Fluid Mechanics* 10 no. 2: 259-275.

Shinnar, R. and J. M. Church. 1960. Statistical Theories of Turbulence In. Predicting Particle Size in Agitated Dispersions. *Industrial and Engineering Chemistry* 52 no. 3: 253-256.

Sobotka, Z. 1984. *Rheology of matrials and engineering structures*. Amsterdam: Elsevier.

Sprow, F. B. 1967. Distribution of Drop Sizes Produced in Turbulent Liquid-Liquid Dispersion. *Chemical Engineering Science* 22 no. 3: 435-442.

Stebe, K. J., S. Y. Lin and C. Maldarelli. 1991. Remobilizing Surfactant Retarded Fluid Particle Interfaces.1. Stress-Free Conditions at the Interfaces of Micellar Solutions of Surfactants with Fast Sorption Kinetics. *Physics of Fluids a-Fluid Dynamics* 3 no. 1: 3-20.

Stone, H. A. 1990. A Simple Derivation of the Time-Dependent Convective-Diffusion Equation for Surfactant Transport Along a Deforming Interface. *Physics of Fluids a-Fluid Dynamics* 2 no. 1: 111-112.

Stone, H. A., B. J. Bentley and L. G. Leal. 1986. An Experimental-Study of Transient Effects in the Breakup of Viscous Drops. *Journal of Fluid Mechanics* 173: 131-158.

Stone, H. A. and L. G. Leal. 1990. The Effects of Surfactants on Drop Deformation and Breakup. *Journal of Fluid Mechanics* 220: 161-186.

Taylor, G. I. 1932. *Proceedings of the Royal Society of London Series A-Mathematical and Physical Sciences* 131: 41.

Taylor, G. I. 1935. Statistical Theory of Turbulence. *Proceedings of the Royal Society of London Series A-Mathematical and Physical Sciences* 151: 421-478.

Teipel, U. and N. Aksel. 2001. Adsorption behavior of nonionic surfactants studied by drop volume technique. *Chemical Engineering & Technology* 24 no. 4: 393-400.

Van den Bogaert, R. and P. Joos. 1979. Dynamic Surface Tensions of Sodium Myristate Solutions. *Journal of Physical Chemistry* 83 no. 17: 2244-2248.

van Doorn, E., C. M. White and K. R. Sreenivasan. 1999. The decay of grid turbulence in polymer and surfactant solutions. *Physics of Fluids* 11 no. 8: 2387-2393.

Van Dyke, M. 1982. *An album of fluid motion*. Stanford: The Parabolic Press.

Varadaraj, R., J. Bock, S. Zushma, N. Brons and T. Colletti. 1991. Effect of Hydrocarbon Chain-Branching on Interfacial Properties of Monodisperse Ethoxylated Alcohol Surfactants. *Journal of Colloid and Interface Science* 147 no. 2: 387-395.

Wallace, J. M. and U. Piomelli. 2001. ENME656 Physics of Turbulence. Class Notes. Department of Mechanical Engineering, University of Maryland. College Park.

Walstra, P. 1983. Formation of Emulsions. In *Encyclopedia of Emulsion Technology*, edited by P. Becher. New York, Marcel Dekker, Inc. 1.

Walstra, P. 2003. *Physical Chemistry of Foods*. New York: Marcel Dekker, Inc.

Walstra, P. and P. E. A. Smulders. 1998. Emulsion Formation. In *Modern Aspects of Emulsion Science*, edited by B. P. Binks. Cambridge, The Royal Society of Chemistry.

Wang, C. Y. and R. V. Calabrese. 1986. Drop Breakup in Turbulent Stirred-Tank Contractors.2. Relative Influence of Viscosity and Interfacial-Tension. *Aiche Journal* 32 no. 4: 667-676.

Ward, A. F. H. and L. Tordai. 1946. Time-Dependence of Boundary Tensions of Solutions.1. The Role of Diffusion in Time-Effects. *Journal of Chemical Physics* 14 no. 7: 453-461.

Wasan, D. T., L. Gupta and M. K. Vora. 1971. Interfacial Shear Viscosity at Fluid-Fluid Interfaces. *Aiche Journal* 17 no. 6: 1287-1295.

Weiss, J., C. Canceliere and D. J. McClements. 2000. Mass transport phenomena in Oil-in Water emulsions containing surfactant micelles: Ostwald ripening. *Langmuir* 16 no. 17: 6833-6838.

Zhang, N., R. V. Calabrese and J. W. Gentry. 1992. Fundamental properties of interlaced Fibonacci sequences and their potential in describing particle breakage. *Journal of Aerosol Science Proceedings of the 1992 European Aerosol Conference, Sep 07-11 1992* 23 no. Suppl 1: S193-S196.

Zholob, S. A., V. B. Fainerman and R. Miller. 1997. Dynamic adsorption behavior of polyethylene glycol octylphenyl ethers at the water/oil interface studied by a dynamic drop volume technique. *Journal of Colloid and Interface Science* 186 no. 1: 149-159.